# Laboratory simulation and numerical modelling of the kinematics of oceanic internal waves

by

Alastair John Martin

Doctor of Philosophy
The University of Edinburgh
1997

## Abstract

Internal waves are known to occur in most ocean areas, especially the deep ocean where stable stratification is often found. While engineering operations have hitherto largely been confined to well-mixed shallow seas (such as the North Sea), new petroleum discoveries have prompted a move into areas (e.g. west of Shetland) where internal waves are more likely to be a problem. The implications of internal waves for safety in offshore operations have been raised by Osborne, Burch and Scarlett (1978) and by Bole, Ebbesmeyer and Romea (1994). The presence of internal waves in sea areas of current interest to the UK offshore industry has been confirmed by Sherwin (1991).

While many aspects of internal wave behaviour have been extensively studied (e.g., Thorpe, 1975), very few measurements of detailed wave kinematics have been performed. Using an advanced flow measurement technique, this study provides measurements of internal wave kinematics in the laboratory and comparisons with non-linear wave theory.

The extensive literature on internal waves is reviewed from the viewpoint of offshore engineering. Then, extending the Stokes expansion presented by Thorpe (1968), a non-linear model for internal waves in a continuously stratified fluid, suitable for numerical solution, is derived. The long wave theory of Benjamin (1966) is also discussed. The experimental facilities are described, and the velocity measurement technique (Particle Image Velocimetry) is discussed in the context of stratified flow measurement. Errors in the measurements are discussed, and an upper bound of about 9% is found to apply to the bulk of the flow, with larger errors (up to 17%) in the interface. The results of the experiments are presented alongside comparisons with the numerical predictions. The implications of the results for offshore engineering are discussed with special reference to loading effects.

It is concluded that second order Stokes theory is able to predict the velocities in large amplitude short internal waves within around 16% on average, although in the extremes the measured velocities can be up to 40% above predictions. The kinematics of large amplitude long waves are underpredicted by linear theory to a factor of up to 2 for the horizontal components, and 4 for the vertical components. These disparities warrant the use of more advanced methods of prediction in engineering applications.

# Declaration

This thesis has been composed by myself and, except where stated, the work contained in it is my own.

---

Alastair Martin
February, 1997

# Acknowledgments

I would like to thank the following people for their contribution to this thesis: Bill Easson, my supervisor, whose support and advice were invaluable throughout the project; Tom Bruce, who taught me the basics of the measurement technique and advised on many aspects of the project, as did Jonathan Whale (who also read part of the manuscript), David Skyner, Michael Jakobsen, Duncan Anderson and many others. Peter Woodhead and Richard Yemm contributed especially to the design of the wavemaker and control system, and the wave height gauge design is largely due to Douglas Rogers. Jean-Baptiste Richon and Heather Earnshaw were involved with the experiments on the light guide. The help of all of the technicians in the Mechanical Engineering Workshop is gratefully acknowledged, especially Laird Parker, who built most of the wave tank and wavemaker.

The support and encouragement of Don Smith and Colin Grant is gratefully acknowledged, as is the kind interest of Jim Bole, Jung Daruvala and the other members of the North West Approaches Group, and many helpful conversations with Alan Evans, John Grue, Peter Davies and Nadine Thompson.

This work was funded by the Health and Safety Executive (HSE) through the Marine Technology Support Unit (MaTSU), as part of a joint project with the Department of Civil Engineering at the University of Dundee and the Department of Physics and Astronomy at the University of Edinburgh. Their support is gratefully acknowledged.

I would like to thank my family for their solid support and understanding throughout. Finally, I would like to thank my wife, Norma, without whose constant encouragement, understanding and patience this thesis would not have been completed. This thesis is dedicated to her.

# Contents

# List of Figures

# List of Tables

# Chapter 1

# Introduction

> Thule[1] was also seen, previously hidden by snow and winter; but *the sea is said to be tough and hard for the rowers* [sed mare pignum et grave remigontibus] and to be little stirred by the winds...[2]

> The steerman...commanded the oars to be got out and the galley-slaves to be forced on with hard blows. But the galley did not move from the spot... Then a man named Catelano, told the captain...to have three monks removed from the deck of the galley and averred that the galley would then immediately begin to move; and when the captain had had them removed, the galley certainly did begin to speed like an arrow.
>
> Then all the men were about to throw these three poor fellows into the sea...[3]

> Pliny [the Naturalist] narrates that a ship, carrying the boys of noble families, who by order of Periander the despot should be castrated, was checked on her way, though she had all sails set. The cause was attributed to a species of mollusc (*Murex*), which by affixing itself to the vessel, stopped her speed and thus saved the boys.[4]

These and other ancient accounts were all quoted by Ekman (1904) as stories which, unknown to their writers, may have been caused by the phenomenon known as *dead*

[1] Probably Norway.

[2] Tacitus, *Agricola*, chapter 10; on the geography of Britain.

[3] From Bartolomeo Crescentio Romano (1607), *Nautica Mediterranea*

[4] *Historia naturalis*, book IX, chapter 41

*water*. As well as monks and shellfish the authors attributed the vexing and inexplicable drag experienced by their vessels to submerged magnetic rocks and supernatural forces. However, Ekman showed that dead water was caused by internal wave motions in the boundary between relatively light fresh surface water (entering the sea from rivers) and the denser, more salty water underneath.

An enormous variety of internal wave phenomena exist in nature. As Turner (1973) says,

> Natural bodies of fluid such as the atmosphere, the oceans and lakes are characteristically stably stratified: that is, their mean (potential) density decreases as one goes upwards, in most regions and for most of the time. When they are disturbed in any way, internal waves are generated.

Stratification in the ocean can be the result of differences in temperature or in salinity. Haloclines (layers where salinity increases with depth) can result from river outflow, but the ocean thermoclines (layers through which temperature decreases with depth), which may be seasonal or permanent, are more common and, because of their scale, more able to support large wave motions. Usually both salinity and temperature vary with depth, not always in the same sense; a general density increase with depth is termed a pycnocline.

Thermoclines are formed by the interaction of different water masses in the ocean, by surface heating (which may be seasonal), and by the confinement of surface wave induced mixing to the upper layer of the ocean. There is also an abundance of forcing mechanisms; one major energy input is from the interaction of tides with bottom topography.

## 1.1 Motivation for the present study

In 1976, in the Andaman Sea west of Thailand, Osborne, Burch and Scarlet (1978) discovered large amplitude internal solitary waves propagating on a thermocline. The wave heights were around 60m and the drillship (Discoverer 534) on which they were working was swept some distance off station. Bole, Ebbesmeyer and Romea (1994) reported equipment damage caused by internal waves in an oil field in the South China Sea. Meanwhile, in the deep water in the North West Approaches west of Shetland,

oil companies have found themselves working in areas which may also be susceptible to internal wave activity.

The present study was funded by the United Kingdom Health and Safety Executive, who were concerned to investigate the possible impact of internal waves in the North West Approaches on operations there. To this end, this study proceeded with the following aims:

1. To make measurements of the kinematics of periodic internal waves in a laboratory tank with the aim of discovering the conformance between measured internal waves and mathematical models;
2. To extend the measurements to a variety of stratification conditions, wave amplitudes and frequencies;
3. To consider the possible implications of internal waves for offshore engineering and the loading of offshore structures.

At the start of the project, advanced flow measuring techniques had only rarely been applied to stratified flows, and in fact the kinematics of internal waves had only been studied using comparatively primitive techniques. It was found during the work that the theories which were available for internal wave kinematics did not apply particularly well to the cases which could be studied in the laboratory tank (for example, the Boussinesq approximation is frequently applied; the kinematics of waves in a Boussinesq fluid would not be easy to measure in the laboratory).

In the light of these considerations, the objectives of this project are summarised below.

1. To present a broad literature review and attempt to describe the possible effects of internal waves on offshore engineering;
2. To design and construct a laboratory facility suitable for the measurement of the properties of a variety of internal wave types;
3. To adapt an existing Particle Image Velocimetry system to the measurement of internal wave kinematics;
4. To measure the kinematics and other properties of periodic internal waves of various amplitudes and frequencies in different stratification conditions;

5. To extend the existing theoretical models into forms suitable for comparison with the experimental results;

6. To assess the implications of the results for offshore engineering, with reference to fluid loading and to the North West Approaches.

Chapter 2 is a review of the literature on internal waves, and of the theories of surface and internal waves which might be useful in predicting internal wave kinematics. Chapter 3 presents two of these theories (Stokes waves and Korteweg-de Vries solitary waves). The Stokes theory is extended to third order without the Boussinesq approximation, and a numerical method for solution of this and the KdV theory is described. The experimental equipment is described in chapter 4 except for the velocity measuring equipment. This is dealt with separately in chapter 5.

The programme of experiments and the results are presented in chapter 6 and compared to the theoretical models. This chapter also contains some numerical experiments and some comparisons with ocean scale measurements. Chapter 7 discusses the implications of the findings of chapter 6 in the context of offshore engineering, and presents some calculations of fluid loading. The particular relevance of the work to the North West Approaches is also discussed. The main conclusions of the project are summarised in chapter 8.

The work described here was part of a joint project, conducted between the Department of Mechanical Engineering and the Department of Physics and Astronomy at the University of Edinburgh and the Department of Civil Engineering at the University of Dundee. The project was funded by the Health and Safety Executive through the Marine Technology Support Unit.

# Chapter 2

# Review of the literature

The literature on internal waves is introduced with a brief description of early work on dead water. The parallel development of mathematical theories for surface and internal waves is discussed, emphasising the much broader range of phenomena associated with the latter. This is then enlarged with a review of the many types of internal wave behaviour, including generation and dissipation processes. Finally the implications of internal waves for offshore engineering are introduced.

## 2.1 First discoveries

Norwegian seamen have long known about the great increase in drag which a ship could experience where the sea was covered with a thin layer of fresh water. This phenomenon was named dead water. The Norwegian explorer Fridtjorf Nansen, on his three year exploration of the Arctic Ocean and North Pole, encountered many areas of dead water, and took some basic measurements.

The discovery and first serious study of internal waves, conducted by Walfrid Ekman, arose from communications on the subject between Nansen and Ekman's former teacher, Vilhelm Bjerknes. Bjerknes suggested that the drag was associated with energy radiated away from the ship by internal waves generated by the ship on the density interface. He passed his theory on to Ekman, whose subsequent work quickly confirmed the hypothesis. The quotations at the start of chapter 1 were taken from Ekman's treatise (Ekman, 1904).

Ekman sought evidence for dead water internationally, advertising for accounts in 36 foreign newspapers. He concluded that "dead water may occur at every place where fresh-water flows out over the sea, but that for some reason or other it is comparatively seldom met with beyond Scandinavia..."

Dead water was certainly the first practical manifestation of internal waves to be discovered. The advent of modern ships, which travel at supercritical speeds, has shifted interest away from dead water. However, the discovery of important wave-driven effects in the fields of meteorology and oceanography has ensured that understanding of internal waves has continued to advance.

## 2.2 Development of theories of surface and internal waves

The early development of the theory of water waves is largely associated with the names of Sir George Biddel Airy, John Scott Russell and Sir George Gabriel Stokes. These three researchers between them posed the problem of long waves of permanent form, which remained unsolved for several years. Stokes developed the theory on which much current engineering design is based. Russell is quoted at the outset of any treatise on solitary waves, and Airy's linear wave theory is still useful over a range of water depths.

### 2.2.1 Stokesian theories

Stokes' approach to surface waves was to include non-linear effects by means of a perturbation expansion (Stokes, 1847). By this method he showed that waves could be represented as a sum of harmonics, the relative importance of the higher harmonics increasing with the height of the wave. He took the expansion to second order for general waves, and to third order for short waves. At third order he found a correction to the dispersion relation.

Stokes' solution was carried analytically to fifth order in 1961 by Skjelbreia and Hendrickson (Dean and Dalrymple, 1991). The complicated analytic coefficients are available in tabulated form (Hallam et al., 1978), and it is in this form that they are used for design. However, even Stokes V becomes inadequate as waves approach their breaking limit, and computational methods of generating higher order coefficients, such as Dean's streamfunction method (Dean and Dalrymple, 1991), must be used.

At the same time as he developed his perturbation method for surface waves, Stokes also developed a linear theory for waves on the interface between two immiscible fluids (he gave as an example the case of water over mercury). However, a perturbation expansion for interfacial waves or for internal waves (in a continuously stratified fluid) was not carried out for over a century.

Thorpe (1968b), who carried out the Stokesian analysis, expressed surprise that it had taken so long for finite amplitude internal waves to be investigated in this way. He suggested that the lack of experimental data with which to compare the approximate models may have discouraged researchers from developing such models. Thorpe's method, which will be used in section 3.4, introduces the non-linearity in the equation of motion (the vorticity equation, one form of which is given in equation 3.11), while Stokes had a linear governing equation (the Laplace equation for the velocity potential) and the non-linearity entered through the surface boundary conditions.

Making the Boussinesq approximation (section 3.3.4), Thorpe was able to extract analytic streamfunction profiles to second order for short waves in particular density profiles (including the important tanh profile). Some of his more important (in the present context) findings were:

- In continuous stratification of whatever form, internal waves may be present in a number of modes. The streamfunction profile, from which the wave shape is extracted, is always an eigenfunction of a Sturm-Liouville type equation, where the corresponding eigenvalue is the phase speed of the particular mode.

  Each mode is characterised by the number of changes in sign of the horizontal velocity through the depth of the fluid. Thus an interface of finite thickness between two fluids is capable of supporting a wide variety of forms of disturbance for a given frequency of excitation. This means in practise that internal wave energy can be transferred from low modes to high by resonant interaction, and this may be an important element in the dissipation of internal wave energy in the ocean (Thorpe, 1975; Turner, 1973).

  The existence of many possible internal modes in a stratified fluid is one of the most important ways in which internal waves differ from surface waves. In a continuously stratified ocean, the modes theory implicitly allows the existence of internal wave "rays" (section 2.3.1), which propagate vertically as well as horizontally. Thus while surface wave energy is necessarily confined to the surface layer of the ocean, internal wave energy has a "free run" at all depths, subject to the local stratification.

- In certain conditions, including a linear density profile, the second order stream-function vanishes and the linear solution is valid to second order. However, the second order density provides a correction to the sinusoidal wave shape, so that near the surface, the wave crests are flattened, and near the sea bed, the wave troughs are flattened (figure 2.1). This is in agreement with ocean observations made by La Fond (Turner, 1973).

- There is no second order correction to the phase velocity of the wave in deep water with a tanh density profile. This is in agreement with Stokes' discovery that the correction to the phase speed was found only at third order for surface waves.

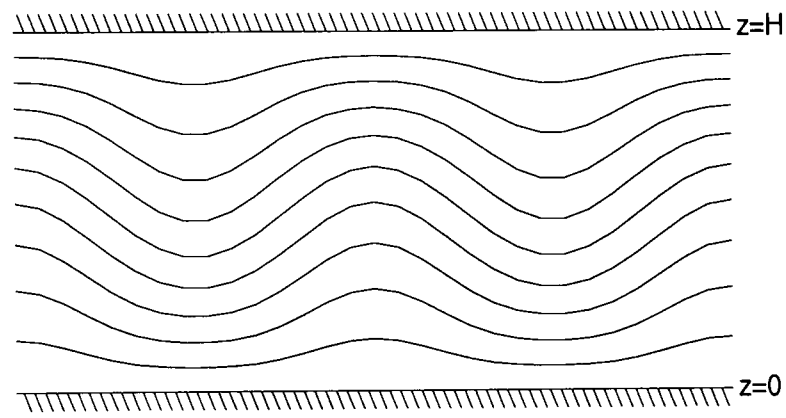


Figure 2.1: *Isopycnals for the first mode internal wave in a linearly stratified domain bounded by planes at $z = 0$ and $z = H$ (after Thorpe, 1968b)*

### 2.2.2 Long waves

#### Solitary waves

The first recorded observation of a solitary wave was Russell's famous encounter with a wave generated by the sudden stopping of a boat in a canal in 1834 (Miles, 1980). Russell pursued the "singular and beautiful phenomenon" on horseback for a couple of miles, watching its height slowly diminish. Russell subsequently recreated the solitary wave in the laboratory.

Russell's waves were subject to a gradual decrease in amplitude over time as they propagated. He attributed this to adhesion of the fluid to the walls of the channel (Stokes, 1847). Stokes, on the basis that the linearised equations had no solitary wave solutions, suggested that in fact the attenuation was an "essential characteristic of a

solitary wave", and in agreement with Airy, proposed that a long shallow water wave could not propagate without change of form.

The problem was resolved independently by Boussinesq and by Rayleigh in the 1870s (Lamb, 1952). Their theoretical descriptions and that of Korteweg and De Vries (1895) has guided understanding of finite amplitude long waves since. The so-called KdV theory shows how, at third order in amplitude, the tendency of a disturbance to attenuate by dispersion (low frequency components travel more quickly than high frequency ones) is exactly balanced by amplitude effects, whereby high parts of the wave travel faster than the rest, tending to steepen the wave. Thus certain types of long waves can propagate without change of form.

The importance of such waves stems from Zabusky and Kruskal's discovery in 1965 that such waves (which they christened *solitons*), far from being peculiarities, are more likely to arise than not from a wide range of physical disturbances (Miles, 1980). In fact, with knowledge of the form of the initial disturbance, it is possible to predict the number and forms of the packet of solitary and sinusoidal waves which must evolve from it mathematically (Osborne and Burch, 1980).

Miles' (1980) detailed review of solitary wave theory is complemented by a more descriptive introduction by Herman (1992). It should be noted that KdV theory is available in a variety of refinements, including the Finite Depth equation and a higher order KdV equation (Koop and Butler, 1981).

KdV solitons are weakly non-linear, and the intense current interest is more concerned with fully non-linear solitary waves (e.g., Evans, 1996a and 1996b, and Grue, private communication) whose shapes can be far from the $\mathrm{sech}^2$ shape of Boussinesq and Rayleigh.

### Cnoidal waves

The other vital contribution to wave theory which Korteweg and De Vries made in their 1895 paper was the discovery of *cnoidal* waves. The term cnoidal comes from the notation for the Jacobian elliptic function cn which is used to describe the wave shape. Definitions of this function are seldom found in water wave texts, but one is given by Bowman (1953). Cnoidal waves are an important class of regular shallow water waves whose crests are significantly steeper, taller and narrower than their troughs. Mathematically they may be seen as an intermediate step between solitary waves and

Stokes waves. Practically they are an intermediate step between deep water Stokes waves and waves breaking on a beach. Their characteristics for engineering purposes are again tabulated by Hallam et al. (1978).

As for Stokes waves, long internal waves waited for several decades before being subjected to the theoretical treatment received by surface waves. Long (1956) dealt with solitary waves in two-fluid systems, and later (1965) discovered some classes of solitary waves in special cases of continuous stratification which could not exist when the Boussinesq approximation was made. Benjamin (1966) derived the properties of KdV solitary and cnoidal waves for a continuously stratified fluid, without the Boussinesq approximation.

As before, the range of phenomena possible on the sea surface is only a subset of that possible within the interior of a stratified ocean. In terms of solitary and other long waves, this includes such effects as the following:

- A new class of solitary wave, possible only within stratified fluids, was described by Benjamin (1967), and also by Ono (1975). While KdV solitary waves require to be long compared to the water depth in order to exist, the Benjamin-Ono waves (or *algebraic solitary waves*) need only be long compared to the thickness of the density interface. There is a strong case for suspecting that such waves would be found on the ocean thermocline, although Koop and Butler (1980), as well as Osborne and Burch (1980), have found KdV theory to be more useful in practise.

- The analysis of solitary and cnoidal internal waves can be reduced to an eigenvalue problem, as was true for sinusoidal waves. This implies again that various modes are possible. Hence the laboratory observations of second mode Benjamin waves as travelling bulges on a density interface by Davis and Acrivos (1967).

- Russell, working in a shallow surface wave flume, was never able to create a solitary wave of depression, but only of elevation. KdV theory in the context of internal waves means that solitary waves are only possible if the density interface is nearer to either the sea surface or the sea bed. In the former case, the solitary waves are of depression, and in the latter case they are of elevation. This raises the interesting question of what happens when a solitary wave in a shallow thermocline encounters a reduction in the overall water depth, so that the two layer depths become equal. It is generally believed that the solitary wave can no longer propagate, and the resulting redistribution of energy has been nicknamed "soliton

fission". Djordjevic and Redekopp (1978), Evans (1996b) and others, have suggested ways in which this energy might be redistributed, and experiments have been conducted by Helfrich and Melville (1986).

### Internal tides and seiches

Another important class of long internal wave covers internal tides and seiches. The former are waves whose periods are equal to the tidal forcing period, while the latter cover waves whose length is comparable to the horizontal extent of the domain in which they occur.

Tidal forces excite not only surface displacement in the oceans (barotropic mode) but also displacement of surfaces of constant density (baroclinic mode). On smaller scales, wind shear can have the same effect, causing internal seiches in lakes. Due to the reduced gravitational restoring forces, the resulting displacement of the pycnoclines can be much greater than that of the sea surface (Stevens and Imberger, 1996).

As for barotropic tides, internal tides distant from topography may be analysed with infinitessimal long wave theory (Airy theory), but close to shelf-breaks non-linearity becomes significant. The transformation of a strong linear tide into a bore as the water depth decreases is apparent in the River Severn. A similar effect in an internal tide was observed by Holloway et al. (1997) on the Australian North West Shelf. As before, however, baroclinic motions are often far more complex than the associated barotropic motions; modes and rays being some of the extra properties which require consideration.

Some of the many field observations of internal tides and seiches which have been made are discussed along with other field observations in section 2.3.2.

## 2.3 A smørrebrødsbord of internal wave phenomena

### 2.3.1 Modes and rays in continuous stratification

The ability of internal waves to exhibit modal behaviour was introduced in section 2.2.1 and is demonstrated mathematically in section 3.4. In the study of infinitesimal waves in continuous stratification, a linear ordinary differential equation (equation 3.40) results.

Where the wave motions essentially fill the whole fluid domain, boundary conditions are applied and various modes of oscillation (eigenfunctions) can be extracted. This is the case when the waves propagate along a relatively thin interface.

Another way of attacking the problem is to allow the waves to propagate away from an isolated disturbance. The mathematics is identical, but the observed behaviour is very different. For a given frequency of excitation $\omega$, the waves propagate away from the source, maintaining an angle $\theta$ to the *vertical* given by

$$\omega = N \cos\theta \tag{2.1}$$

where $N$ is the buoyancy frequency.

Waves of this kind were generated by Mowbray and Rarity (1967) in a linearly-stratified ($N$ = constant) salt solution. Thomas and Stevenson (1972) provide a rather clearer explanation of what is going on in these waves. Figure 2.2 is a diagram based on the latter paper.

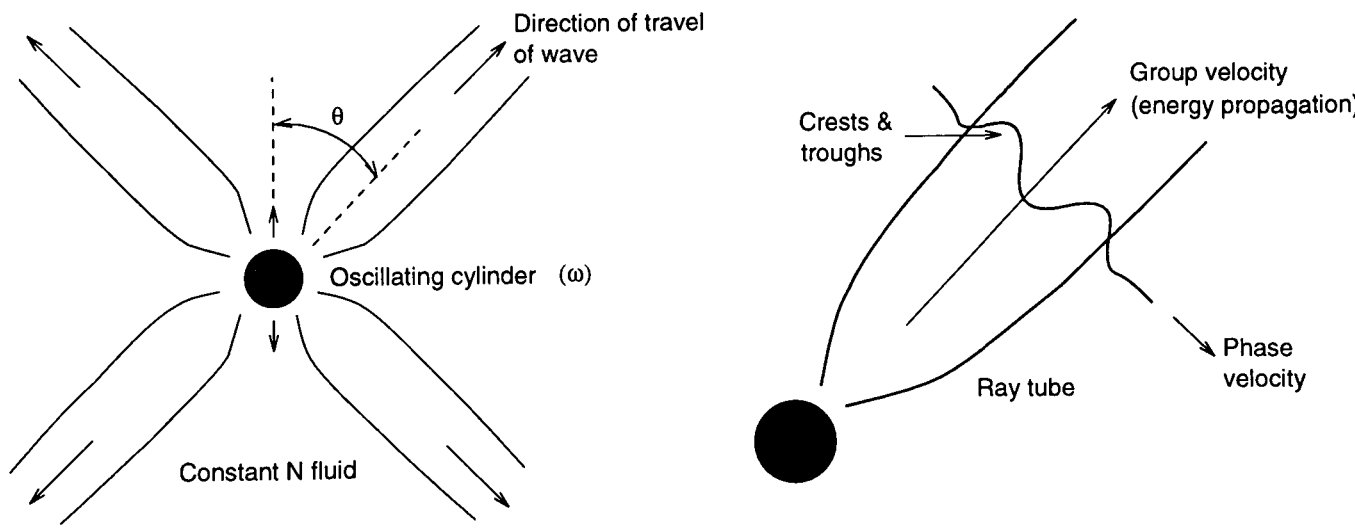


Figure 2.2: *Internal wave "rays", after Thomas & Stevenson (1972)*

The angle $\theta$ given above is the direction of propagation of energy, and the group velocity $\mathbf{c_g}$ (now a vector) is in that direction. The phase velocity (propagation of crests) is at right angles to the direction of energy propagation.

The direction of propagation of a wave is a function only of its frequency and the local stratification. A wave reflected at a solid boundary will maintain its angle $\theta$ to the vertical, rather than to the solid boundary. These facts raise a number of different

mechanisms by which internal wave energy can be transmitted and dissipated, some of which are illustrated in figure 2.3.

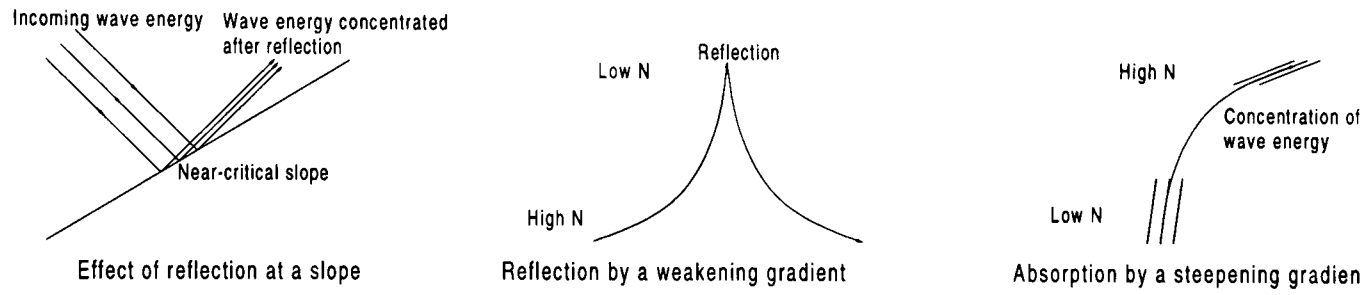


Figure 2.3: *Some internal wave ray processes (after Turner, 1973)*

- Should a wave be reflected from a sloping boundary whose slope angle is close to the wave propagation angle, the wave energy may become concentrated on reflection into a much smaller volume. Such a slope is termed *critical*. Gilbert and Garrett (1989) found that enhancement is particularly significant from convex boundaries, and less significant from concave ones. Such enhancement could well cause significant localised diapycnal mixing.

- A ray propagating into a region of weaker density gradient (reduced $N$) will decrease its angle to the vertical $\theta$ in accordance with 2.1. At the level where $\omega = N$, reflection may take place. Thus the wave may be able to follow a horizontal wave guide.

- On the other hand, a ray propagating into a region of higher density gradient will increase its angle to the vertical. At a level where $\omega/N \rightarrow 0$ the wave may become unstable and break.

- The ability of rays to carry wave energy vertically is important in shear flows, such as frequently occur in the atmosphere, and also in the ocean. For example, a wave generated by flow over a mountain may propagate upwards. If the flow is sheared, the wave may encounter a region where its phase velocity is equal to the mean flow velocity. At such a level (termed a *critical layer*), the wave may break and the energy be absorbed by the mean flow (Booker and Bretherton, 1967; Turner, 1973).

- Wave rays in a closed basin are subject to focusing and resonance (seiching), as shown by Maas and Lam (1995). This happens on the assumption of a reasonably high reflection coefficient, but does not depend on a particular type of stratification. Even when a resonance (in which ray paths fold exactly back on themselves

after reflections at the boundaries) is not encountered, multiple reflections can focus energy into particular regions. These regions may be distant from boundaries, excitation sources, critical slopes and critical layers.

Despite the ubiquitous nature of internal wave rays, first mode short internal waves are still of great importance on the ocean thermocline. This is because rays propagating through the weakly stratified ocean depths must be of relatively low frequency, while on the strongly stratified ocean thermocline, high frequency waves can propagate.

Woods (1968) measured and indeed photographed a wide variety of internal wave activity in the summer thermocline of the Mediterranean Sea around Malta. He observed internal wave breaking by wave-driven shear instability (section 2.3.5), and was able to show how waves on the thermocline interact with the detailed structure in the stratification.

### 2.3.2 Internal tides and seiches

As mentioned in section 2.2.2, where both barotropic and baroclinic oscillation modes are subject to the same forcing, the baroclinic mode undergoes much greater displacement than the barotropic mode. Such forcing may be tidal or sustained wind shear.

Sherwin (1988) and Sherwin et al. (1996) have investigated internal tides in both linear and non-linear forms with particular reference the European continental shelf. One conclusion from the latter paper was that the enhanced currents near the sea bed may have considerable significance for offshore engineering. Dealing specifically with the Færoe-Shetland Channel (section 7.3.3), Sherwin (1991) showed that a strong internal tide, with energy spread across the first six modes, was generated by the barotropic tide over the Wyville-Thomson Ridge. Within the channel the motions remained linear, but around the edges of the channel, solitary waves or bores might occur. Sherwin's analysis included the effect of the earth's rotation, which is significant especially for the first mode.

The work of Baines (e.g. Baines, 1983; Baines and Fang, 1985) has shown that energy from internal tides can be passed into other types of internal waves, including (esp. the earlier paper) wave rays (section 2.3.1). The transmission of internal wave energy throughout the ocean depth by rays has apparently not been dealt with from an engineering perspective.

Internal seiches have been studied by Stevens and Imberger (1996) in the laboratory, and in Loch Ness by Thorpe et al. (1972). The forcing is generally wind stress. Stevens and Imberger found a variety of modes being generated by the wind shear, while in Loch Ness the seiche was manifested as a travelling surge.

### 2.3.3 Waves created by obstacles

Into this category certainly falls the phenomenon of dead water dealt with by Ekman (1904). This phenomenon was revisited by Tulin, Wang and Yao (1993) who performed a numerical investigation of non-linear waves generated supercritically, which is more relevant to modern ship design than classical subcritical dead water.

A related piece of recent work is the experimental (PIV) study by Spedding, Browand and Fincham (1996). Although they were more interested in the turbulent structure of wakes, they were able to capture some aspects of the kinematics of the internal waves which must, necessarily, attend any object moving through a stratified fluid.

A more classical problem is that of lee waves behind fixed obstacles on a boundary, e.g., a mountain (on land or submarine). Study of these waves began in 1939 (Queney, 1955). Theoretical and experimental work by Long (1952, 1953, 1954 & 1955) showed how lee waves can form internal hydraulic jumps and trapped rotors.

SODAR measurements by Helmis et al. (1996) have shown that lee waves East of the Hymettos mountain in Attica produce frequent, intense localised disturbances. The waves can become hydraulic jumps, with downdrafts that reach ground level. Similar measurements were performed by Ralph et al. (1992) in southern France.

### 2.3.4 Solitary internal waves

The term "long wave" in the present context refers mainly to solitary and cnoidal waves, including KdV waves (solitons), which are long compared to the water depth; Benjamin-Ono waves, which are long compared to some other depth parameter; and cnoidal waves, which bridge the gap between KdV solitary waves and sinusoidal waves.

Of great importance here are the many field studies which have provided evidence of solitary waves propagating on the ocean thermocline (Osborne and Burch, 1980; Osborne et al., 1978). These researchers found KdV solitary waves propagating along

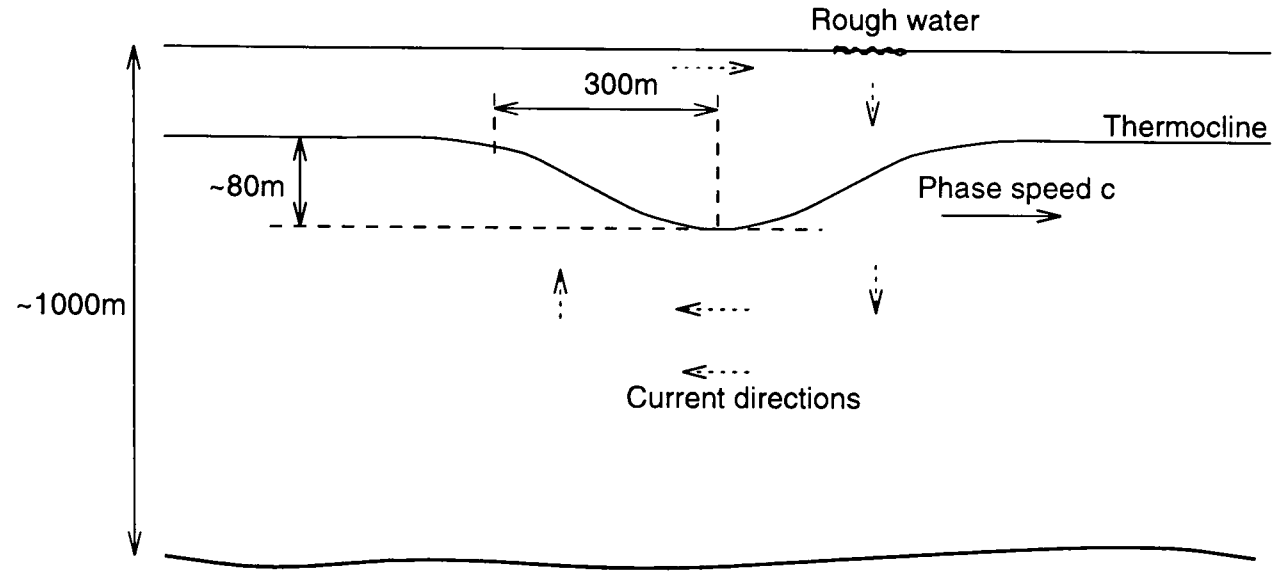


Figure 2.4: *Scales in the Andaman Sea internal solitary waves*

a relatively shallow thermocline in the Andaman Sea, off Thailand. A sketch of the scales of these waves is given in figure 2.4. This figure explains the concern which Osborne et al. felt towards conducting offshore drilling operations in the presence of these waves.

With a similar engineering interest, Bole et al. (1994) found large amplitude solitary waves being refracted round Pratas Island in the South China Sea. The internal wave climate was so strong in the area in which drilling operations were planned that a "soliton early warning system" had to be considered.

Bole et al. invoked KdV theory to describe the measured waves, as did Osborne and Burch. Although KdV theory for internal solitary waves requires (in the two-layer approximation) that both layer depths be finite (Benjamin, 1966), Osborne and Burch found that even in the great depths of the Andaman Sea the KdV approach was adequate. However, the necessarily restricted range of measurements which can be made in a field study meant that neither of these studies can be taken to show that KdV theory is a better predictor of internal waves kinematics than Benjamin-Ono for the same parameters, or indeed the fully non-linear models of Evans (1996a) and others.

An attempt to identify the domains of applicability of the various internal wave models (KdV, modified KdV, Finite Depth and Benjamin-Ono) was made by Koop and Butler (1981). For the whole range of their experimental results, they found that classical KdV and higher order KdV were the best predictors of internal solitary wave behaviour, even in the ranges where they expected Benjamin-Ono or finite depth theory to perform better. Segur and Hammack (1982) reached similar conclusions. It is significant that

Koop and Butler performed their experiments in a two-fluid system (Freon and water), while Segur and Hammack performed theirs in stratified saline solution.

The mathematical permanence of solitary waves has long been of interest, as has the deterministic nature of KdV solitary wave evolution from an arbitrary initial disturbance. The studies cited above show that internal solitary waves do indeed travel over immense distances. Practical solitary waves in other fields (such as soliton light waves in fibre optic cables) have shown that this permanence can be a true physical effect (Herman, 1992). A study by Apel, Holbrook and others (Apel et al., 1985; Apel et al., 1975; Liu et al., 1985) into solitary internal waves in the Sulu Sea showed that dissipation of wave energy by Reynolds stresses was significant. Nevertheless, the mathematical evolution behaviour is reproduced in the ocean.

The Andaman Sea and Sulu Sea studies, along with Perry and Schimke (1965), all showed how large amplitude internal waves can dramatically affect the surface wave climate. A long internal wave will exert a considerable influence on the surface kinematics. Downwelling occurs in front of the wave trough, and upwelling behind it (figure 2.4). In regions of downwelling, surface wave energy is focused into narrow rough bands ("rips") which extend the length of the internal wave trough, and in the upwelling regions the surface wave energy is spread out. Thus an internal solitary wave is preceded by a rip and succeeded by calm water.

This property of internal waves allowed various of the above researchers to estimate the extents of their internal waves from satellite photographs. A large-scale experiment in the New York Bight (Gasparovic et al., 1988) had as its aim the correlation of observed surface wave enhancement with measured internal waves. The surface rips were detected using (among other methods) airborne synthetic aperture radar.

Although the first mode Benjamin-Ono wave has proved elusive, second mode waves have been successfully made in the laboratory by Davis and Acrivos (1967), and more recently by Stamp and Jacka (1995). It seems likely that such waves would be encountered on the ocean thermocline, especially since the thermocline is typically diffuse.

None of the above authors have felt that a description in terms of cnoidal waves would be appropriate for their observations.

### 2.3.5 Wave generation and dissipation

From an oceanographic point of view, processes of internal wave generation, propagation and dissipation are vital to any attempt to understand the ocean's energy budget and internal transactions of heat, salt, turbulence, oxygen and nutrients. From an engineering point of view, an understanding of wave generation and propagation is important for attempts to predict the wave climate at a particular location, and wave dissipation is important in predicting the appearance of otherwise unexpected packets of turbulent mixing.

The processes which play a role in the global (oceanographic) calculation are reviewed by Thorpe (1975). The preceding discussion was partly intended to show that internal wave processes are so varied that mesoscale predictions need to be made on a phenomenon-by-phenomenon and locality-by-locality basis. Nevertheless, Thorpe's discussion helps to classify some of the phenomena of interest.

1. *Generation processes*

   - Generation by irregular topography is probably the generation mechanism most invoked to explain waves observed in the ocean. Tidal flow over a submarine ridge or mountain can generate packets of internal solitary waves on the ocean thermocline by a process demonstrated by Maxworthy (1979), and by Lee and Beardsley (1974).

     Stratified flow over an obstacle produces a trapped lee wave or possibly a hydraulic jump, as in the atmospheric case. However, the oscillatory nature of tidal flow causes the lee wave or jump to become periodically detached, and the resulting disturbance, propagating against the slackening tide, evolves into a train of solitary waves most commonly regarded as being of the KdV type (Osborne and Burch, 1980; Apel et al., 1985). Figure 2.5 is a sketch of Maxworthy's experiment.

     Recent laboratory experiments by Kleuser (1996) have suggested that second mode Benjamin-Ono solitary waves may be generated in a diffuse thermocline by the same mechanism, though there is as yet no proof of this.

     Irregular topography can create many other forms of waves. Where stratification is not confined to a thin thermocline, but is continuous, internal waves will propagate vertically upwards from an obstacle in a flow, and possibly be advected horizontally by the flow, which may well be sheared (Turner, 1973).

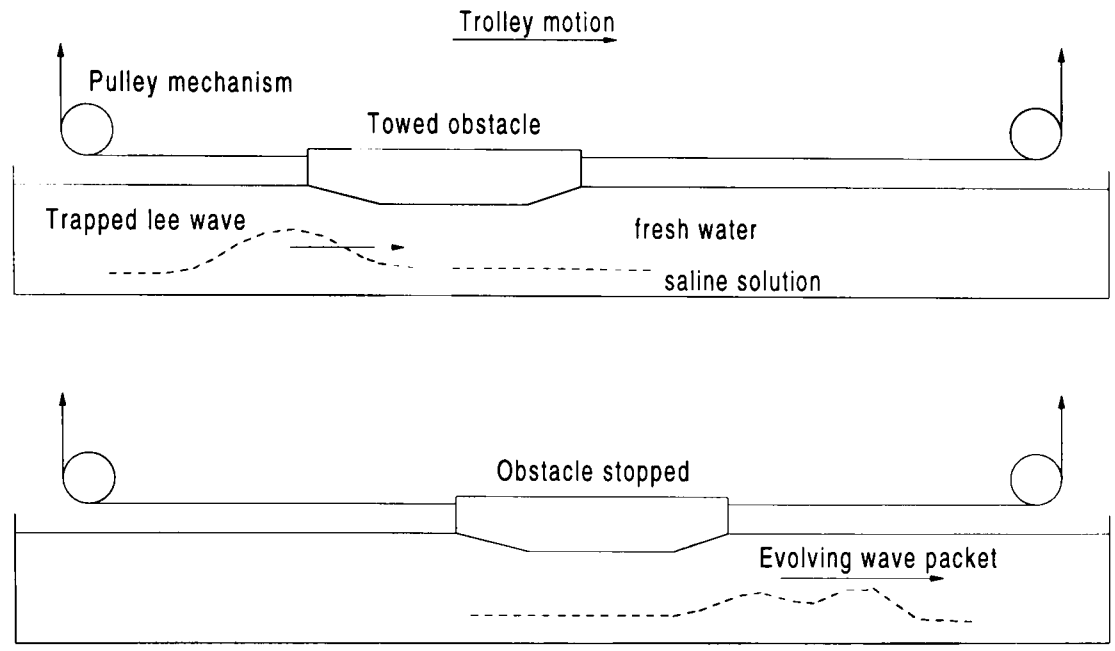


Figure 2.5: *A two-dimensional sketch of Maxworthy's (1979) three-dimensional experiment on solitary wave generation by tides*

- Atmospheric disturbances can generate internal waves directly. Thorpe cites two main mechanisms: a travelling pressure field and a travelling stress field. By a travelling pressure field a moving weather system may be understood, but a ship can also be classified as such. A travelling stress field corresponds to wind shear, and was investigated recently by Stevens and Imberger (1996), and earlier by Thorpe et al. (1972). Both of these studies were concerned with confined (inland) bodies of water.
- Resonant interaction between pairs of surface waves can create internal waves. Thorpe showed how interaction coefficients may be calculated for given pairs of surface wave fronts at given angles. The highest coefficients are at small separation angles.
- Hammack (1980) investigated the generation of baroclinic tsunami, by which may be understood earthquake-driven long internal waves. As for other surface/internal internal wave systems, the amplitude of the baroclinic mode greatly exceeded that of the barotropic mode, with the phase speed following the opposite relation.
- Other generation mechanisms are instability in the ocean's Ekman boundary layer, and parametric instability coupled with tidal forcing. Interactions between internal waves can transfer energy between modes and between wavenumbers.

- Viscous attenuation, which on oceanic scales must be considered to include Reynolds' stresses, occurs because of the shear associated with internal waves. LeBlond (1966) concluded that short waves (length < 100m) are strongly damped in any basin, while (long) internal tides would propagate in deep basins over distance of order 1000km. The accuracy of these calculations, LeBlond acknowledged, depends entirely on the accuracy of the assumed values of eddy viscosity.

  It should be noted that Osborne and Burch (1980), as well as Bole et al. (1994) were able to measure large amplitude solitary waves great distances from their assumed generation sites.

- Shear instability is an amplitude-related wave breaking mechanism. The stability of a shear layer at a crest or trough of an internal wave is measured by the local gradient Richardson number $Ri$, as shown jointly by Miles (1961) and Howard (1961). A sufficient condition for *stability* is that

$$Ri = \frac{N^2}{(\partial u/\partial z)^2} = -\frac{g\,\partial\rho/\partial z}{\rho(\partial u/\partial z)^2} > \frac{1}{4} \tag{2.2}$$

  The velocity shear $\partial u/\partial z$ is proportional to the density gradient $\partial\rho/\partial z$, but since velocity shear appears squared on the bottom line, waves on thin interfaces are less stable than equivalent waves on thick interfaces. Nevertheless, instability may still be found in fluids with linear stratification (e.g. McEwan 1983a,b).

  Shear instability results in the growth of Kelvin-Helmholtz billows in the shear layer, which perform diapycnal mixing (figure 2.6).

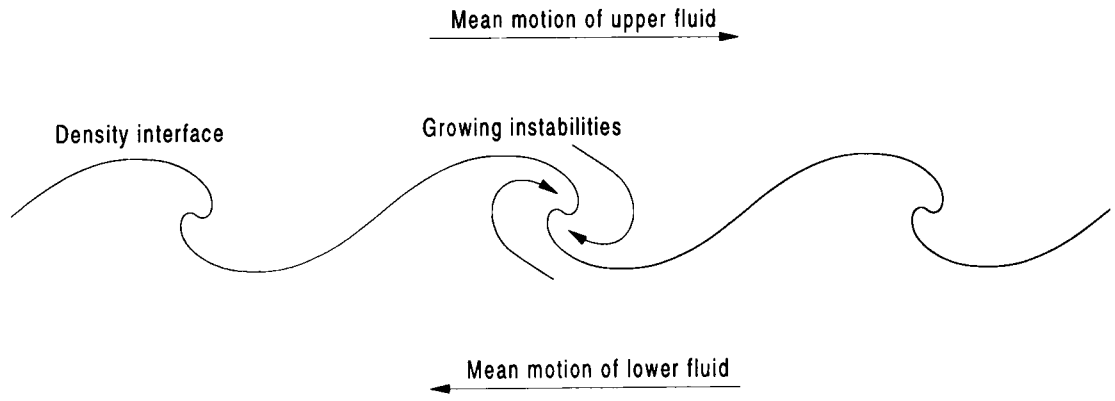


Figure 2.6: *Kelvin-Helmholtz billows*

Shear instability has been widely studied. Among the most important papers on its relationship to internal waves are Woods' (1967) field study of

waves and billows on the ocean thermocline, and Thorpe's (1968b) theoretical and experimental treatise, in which he calculated the gradient Richardson number for internal waves in a tanh density profile.

- Thorpe (1978) found another breaking mechanism for internal waves in a shear flow. The crests of the waves become "cusped", and wisps of fluid are drawn into the upper fluid, where they can remain, even though they are statically unstable. Possibly related behaviour was seen near the nodes of standing internal waves (Thorpe, 1968c).

  Marginal effects such as these ("Holmboe") instabilities, as well as the previous Kelvin-Helmholtz billows, were treated numerically by Smyth and Peltier (1991), and in further experiments by Taylor (1992). Taylor, in agreement with Woods, found that the result of the mixing created by the instabilities was fine structure on the interface.

  The work of McEwan (1983a,b) is significant not least because it is possibly the first published record of velocity measurements in internal waves. McEwan used streak photography to calculate the velocity shear, and hence the gradient Richardson number, in waves driven to breaking in a continuously stratified fluid. He found that the condition $Ri < 1/4$ was true only in a few isolated locations within a breaking wave.

- Mention has already been made (section 2.3.1) of critical layer absorption, critical slopes, and propagation of waves into regions of different background stratification. Shoaling of internal waves is also significant, as seen from the experiments of Nadine Thompson (Easson et al., 1993). An image from one of these experiments is reproduced in figure 2.7.

Ultimately, the dissipation of internal wave energy takes place by a combination of viscous attenuation (in which Reynolds stresses must be included) in the shear layers, viscous dissipation through the production of turbulence, and modification of the stratification through turbulent diapycnal mixing. This latter method is unique to stratified flow, and is a consequence of the fact that destroying the stratification in a fluid by mixing raises the fluid's centre of gravity, which means that work must be done against gravity.

The bimodal nature of turbulent energy dissipation in a stratified fluid is characterised by the flux Richardson number $Rf$ (Turner, 1973), which offers a measure of mixing efficiency. Turner shows that, in general, the majority of the mixing energy is lost in Reynolds' stresses, and only a fraction ($\leq 0.2$) works against gravity.

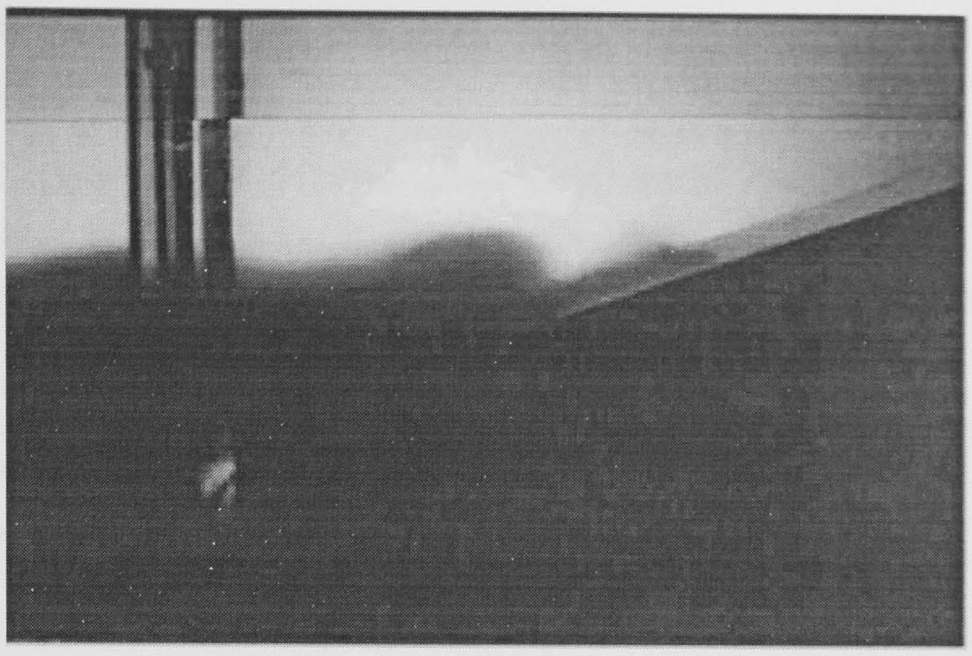

Figure 2.7: *Internal wave breaking on a sloping beach (due to Nadine Thompson, University of Dundee)*

## 2.4 Internal waves in the context of offshore engineering

Following on from the preceding discussion, several points of particular relevance to offshore engineering can be made.

1. Internal waves are ubiquitous phenomena. The required conditions of stratification are found in one form or another in most bodies of water, and all the deep oceans. Nor is there any shortage of generation mechanisms or forcing. Furthermore, the variety of forms which they may take is much wider than might be supposed by simple extrapolation from surface waves.

2. The vertical excursions made by fluid elements during the passage of internal waves is likely to be much greater than that of surface waves, even if both are forced by the same event (e.g. an earthquake, wind shear or tidal forcing). However, the frequencies of oscillation, and hence the phase speeds and internal velocities, are correspondingly lower.

3. The vast majority of internal wave research has been conducted by oceanographers, meteorologists, physicists and mathematicians. Their emphasis has generally either been on the role of internal waves in macro-scale processes such as ocean energy budgets, or in fundamental understanding of smaller scale events. While this work has certainly laid a firm foundation for an engineering discussion, only a few people have tackled internal waves from the point of view of the

engineer. Among these are Bole et al. (1994), Osborne et al. (1978) and Sherwin et al. (1996).

4. Internal waves may be studied in terms of spectra, in the same way as surface waves. Work on internal wave spectra was commenced by oceanographers Christopher Garrett and Walter Munk (Garrett and Munk, 1975) who were looking for eddy transport coefficients for energy through the ocean thermocline. Their model spectrum (first offered as GM72 and subsequently revised several times on the basis of new data) could conceivably be used to predict "worst case" waves in much the same way as surface wave spectra are used.

5. Internal waves can affect engineering operations in many different ways. The most studied are internal solitary waves (Bole et al., 1994; Osborne et al., 1978; see also the Oil & Gas Journal, 1979), which can have a potentially serious effect on activities near or even on the surface. Sherwin et al. (1996) make the point that internal tides can impact on operations near the sea bed. Uninvestigated as yet is the possibility that internal wave rays could prove dangerous, not least for their ability to deliver packets of intense turbulence to unexpected locations. Secondary effects include the concentration of surface wave energy into rough bands, which is a signature of internal solitary waves, and increased scour and sediment transport on the sea bed. Internal waves are cited in the design guidelines of the Department of Energy (1990) as a potential source of difficulty for deep water operations.

6. The kinematics of internal waves have been less studied than their other aspects, such as wave shapes, generation and breaking processes, macro energy budgets, characteristic spectra, etc. This is partly because of the expense of obtaining detailed kinematic measurements in the field, and the difficulty of obtaining them in the laboratory. Thus the effects of, for example, non-linearity have been tested against wave shape predictions, but not against velocity predictions.

The following chapters aim to redress some of this imbalance by providing kinematic models and testing them against laboratory measurements, and where possible by couching the findings in engineering terms.

# Chapter 3

# Theoretical description of internal waves

The equations of motions for stratified flows are presented and the vorticity equation is derived for a two-dimensional incompressible fluid. Using dimensional analysis, it is shown that neither the Boussinesq approximation nor the assumption of linearity can be justified for the range of parameters in the experiments, although to second order viscosity can be neglected. A perturbation expansion similar to that of Thorpe (1968b) is carried out to third order, but without the Boussinesq approximation. A means of obtaining numerical solutions to the resultant equations is described. The non-Boussinesq long wave theory due to Benjamin (1966) is also presented and a means of solution described.

## 3.1 Introduction

The purpose of this chapter is to investigate and expand existing internal wave theories so that they may be used for comparison with the experimental results. Two main classes of theory are used, in accordance with the main classes of experiment which were conducted. These are: short wave theory, which uses a Stokes expansion, and long wave theory, which uses the description by Korteweg and de Vries (1895).

In discussing surface waves, this classification of "short" and "long" is widely accepted. Amongst mathematicians and engineers the same view is generally taken for internal

waves. However, from an oceanographic point of view, the longest waves of interest are internal tides, and Korteweg-deVries type solitary waves are in fact regarded as relatively short. This study does not deal with internal tides and so the former terminology will be adhered to.

It should also be pointed out that Korteweg-de Vries theory was originally developed for surface waves, and various adaptations of it are available for internal waves. Benjamin (1966) provides Korteweg-de Vries theory in forms suitable for any type of stratification. The two-layer form is most often encountered in the literature (e.g. Bole et al. 1994; Osborne and Burch, 1980), but it will be seen that Benjamin's continuous stratification form is also straightforward to use.

## 3.2 Derivation of the governing equation

Derivations for the equations governing motion in a stratified fluid can be found in various texts, e.g., LeBlond and Mysak (1978), Arnsten (1990) and Phillips (1977). Phillips' concise derivation of equations for continuous stratification in the linear inviscid limit is the most accessible. Arnsten presents this and the derivation for the two-layer case in the greatest detail. Dalrymple and Liu (1978), investigating the surface-wave driven motion of a soft seabed, present the linearised viscous two-layer case. Thorpe (1968b) makes use of, but does not derive, the non-linear inviscid case.

All of the above writers use the Boussinesq approximation, while some acknowledge that it may not be valid for many practical cases. The significance of this approximation is discussed by Long (1965), and its role in the present study is reviewed in section 3.3.4.

The derivation given in this section makes no approximations other than that of two-dimensional incompressible flow over a flat bottom in the absence of Coriolis forces. Further approximations are made on the basis of scaling arguments in section 3.3, and subsequently by means of a Stokesian perturbation expansion (section 3.4).

### 3.2.1 Equations of motion

A definition sketch of the continuously stratified case is shown in figure 3.1.

Following (in part) Arnsten (1990), three equations of motion are available. These are the equation of mass conservation

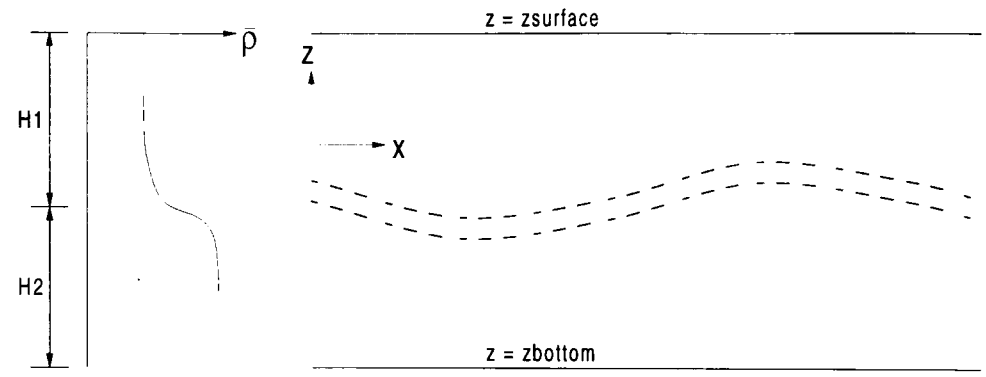


Figure 3.1: *Definition sketch of the continuously stratified domain. Note the arbitrary position origin, which in the experimental results is set to the camera origin*

$$\frac{\partial \rho}{\partial t} + \frac{\partial (\rho u)}{\partial x} + \frac{\partial (\rho w)}{\partial z} = 0 \tag{3.1}$$

from which follows the relation for incompressibility

$$\frac{\partial u}{\partial x} + \frac{\partial w}{\partial z} = 0 \tag{3.2}$$

and finally the Navier-Stokes (momentum) equations

$$\left.\begin{aligned} \frac{\partial u}{\partial t} + u\frac{\partial u}{\partial x} + w\frac{\partial u}{\partial z} &= -\frac{1}{\rho}\frac{\partial p}{\partial x} + \nu\left(\frac{\partial^2 u}{\partial x^2} + \frac{\partial^2 u}{\partial z^2}\right) \\ \frac{\partial w}{\partial t} + u\frac{\partial w}{\partial x} + w\frac{\partial w}{\partial z} &= -\frac{1}{\rho}\frac{\partial p}{\partial z} - g + \nu\left(\frac{\partial^2 w}{\partial x^2} + \frac{\partial^2 w}{\partial z^2}\right) \end{aligned}\right\} \tag{3.3}$$

### 3.2.2 Derivation

Again following Arnsten, the density is expanded as a static density profile $\overline{\rho}(z)$ and a small fluctuation $\tilde{\rho}(x, z, t)$ which is due to the wave motion

$$\rho = \overline{\rho}(z) + \tilde{\rho}(x, z, t) \tag{3.4}$$

From this point on, it is more convenient to use the subscript notation for the derivatives, except where the quantity is a function of one variable only, where the primed

notation is used (e.g. $d\overline{\rho}/dz \equiv \overline{\rho}'$). The streamfunction $\psi(x,z,t)$ is introduced in place of the velocity

$$u = -\psi_z, \quad w = \psi_x \tag{3.5}$$

The sign convention is that of Massey (1989), and is the opposite of Thorpe's (1968b). Equation 3.1 is expanded using 3.4 and 3.5 to yield

$$\tilde{\rho}_t + \overline{\rho}'\psi_x + \tilde{\rho}_z\psi_x - \tilde{\rho}_x\psi_z = 0$$

$$\tilde{\rho}_t + \overline{\rho}'\psi_x - \mathrm{J}(\tilde{\rho},\psi) = 0 \tag{3.6}$$

where $\mathrm{J}(p,q)$ represents the Jacobian derivative

$$\mathrm{J}(p,q) = q_z p_x - q_x p_z \tag{3.7}$$

Equation 3.6 will be referred to as the buoyancy equation. Its derivative with respect to $x$ will be required below

$$\tilde{\rho}_{tx} + \overline{\rho}'\psi_{xx} - \mathrm{J}(\tilde{\rho},\psi)_x = 0 \tag{3.8}$$

The vorticity equation is derived from the Navier-Stokes equation firstly by cross-differentiation and elimination of the pressure $p$

$$\begin{aligned}
&\rho[(\psi_{xt} - \psi_z\psi_{xx} + \psi_x\psi_{zx})_x + (\psi_{zt} - \psi_z\psi_{zx} + \psi_x\psi_{xx})_z] + g\rho_x \\
= \;& -\rho_x(\psi_{xt} - \psi_z\psi_{xx} + \psi_x\psi_{zx}) + \rho_z(\psi_{zt} - \psi_z\psi_{zx} + \psi_x\psi_{zz}) \\
&+ \nu[(\rho\nabla^2\psi_x)_x - (\rho\nabla^2\psi_z)_z]
\end{aligned} \tag{3.9}$$

$$\begin{aligned}
&\rho\nabla^2\psi_t + g\rho_x = \rho\mathrm{J}(\nabla^2\psi,\psi) \\
&- \rho_x[\psi_{xt} - \mathrm{J}(\psi_x,\psi)] - \rho_z[\psi_{zt} - \mathrm{J}(\psi_z,\psi)] \\
&+ \rho\nu[\nabla^2\psi_{xx} - \nabla^2\psi_{zz}] + \nu[\rho_x\nabla^2\psi_x - \rho_z\nabla^2\psi_z]
\end{aligned} \tag{3.10}$$

The governing equation is then found by differentiating equation 3.10 with respect to $t$ and substituting for $\tilde{\rho}_{xt}$ from equation 3.8, yielding

$$\left.\begin{aligned}
&\nabla^2\psi_{tt} - \frac{g\overline{\rho}'}{\rho}\psi_{xx} = Q_v + Q_b + Q_d + Q_\nu \\
&Q_v = \mathrm{J}(\nabla^2\psi, \psi)_t \\
&Q_b = -\frac{g}{\rho}\mathrm{J}(\tilde{\rho}, \psi)_x \\
&Q_d = \frac{1}{\rho}\left\{\rho_t[\mathrm{J}(\nabla^2\psi, \psi) - \nabla^2\psi_t] + (\rho_x[\mathrm{J}(\psi_x, \psi) - \psi_{xt}] + \rho_z[\mathrm{J}(\psi_z, \psi) - \psi_{zt}])_t\right\} \\
&Q_\nu = \nu[\nabla^2\psi_{xx} - \nabla^2\psi_{zz}]_t + \frac{\rho_t\nu}{\rho}[\nabla^2\psi_{xx} - \nabla^2\psi_{zz}] + \frac{\nu}{\rho}[\rho_x\nabla^2\psi_x - \rho_z\nabla^2\psi_z]_t
\end{aligned}\right\} \tag{3.11}$$

This equation is a form of the vorticity equation referred to by Thorpe (1968b) and LeBlond and Mysak (1978). In this equation, the meanings of the terms are as follows

- $\nabla^2\psi_{tt}$ is the non-zero vorticity (section 3.3.5);
- $g\overline{\rho}'/\rho\psi_{xx}$ is the restoring buoyancy force, which at first order drives the vorticity (Turner, 1973);
- $Q_v$ represents the non-linear velocity terms which are rejected when the Navier-Stokes equations are linearised;
- $Q_b$ contains the non-linear terms which come from the buoyancy equation;
- $Q_d$ contains those terms which are rejected in the Boussinesq approximation;
- $Q_\nu$ represents the viscous terms (some of which are non-linear, and some of which are rejected in the Boussinesq case).

### 3.2.3 Boundary conditions

At the bottom boundary, the condition of zero vertical velocity applies. In the inviscid case, no condition on the horizontal velocity is imposed. Therefore

$$\psi(x, z_{bottom}, t) = 0 \tag{3.12}$$

On the free surface, the approximation of zero vertical velocity is made (the so-called "rigid lid" case). A justification for this choice is given in section 3.3.6. This means that

$$\psi(x, z_{surface}, t) = 0 \tag{3.13}$$

The kinematic free surface boundary condition which is applied to surface waves (Dean and Dalrymple, 1991) states that any fluid on the surface remains there as the wave passes. This condition translates into a rather different prescription for internal waves. The relation which will be referred to as the *kinematic equation* states that fluid on an isopycnal remains on that isopycnal; i.e. there is no mixing or diffusion. This can be stated as

$$\eta_t - \psi_z \eta_x - \psi_x = 0 \tag{3.14}$$

where $\eta(x, z, t)$ is the vertical displacement of a streamline from its rest position $(x, z)$. This equation enables the evaluation of the wave shape from the streamfunction, and will also be used in the Taylor expansion of the vertical co-ordinate (section 3.4.2).

## 3.3 Dimensional analysis and scaling

### 3.3.1 Dimensional analysis

The purpose of this section is to assess the relative importance of the various terms in equation 3.11. Since the eventual goal is a prediction of the kinematics based on the wave parameters, a logical way to proceed is with a dimensional analysis based on the functional dependence

$$u = \phi(a, k, \omega, g', \rho, H, \mu, \delta) \tag{3.15}$$

Here $a$ and $\omega$ are the amplitude and frequency of the driving disturbance, $k$ is the generated wavenumber, $g'$ is the reduced gravitational acceleration, $\rho$ is the density, $H$ is a water depth scale, $\mu$ is the dynamic viscosity, and $\delta$ is the interface thickness parameter.

Three fundamental dimensions are expressed in the above dependence (mass, length and time), and there are eight independent variables, therefore the problem must be wholly defined by $8 - 3 = 5$ dimensionless parameters. This can be expressed as

$$\Pi_1 = \phi(\Pi_2, \Pi_3, \Pi_4, \Pi_5, \Pi_6) \tag{3.16}$$

Choosing $k$ and $\omega$ as the principal variables, the dimensionless groups can be found

$$\Pi_1 = u\omega^b k^d, \;\; \Pi_2 = g'\omega^e k^f, \;\; \Pi_3 = \mu\rho^e\omega^h k^i, \;\; \Pi_4 = H^l k^m, \;\; \Pi_5 = a^n k^p, \;\; \Pi_6 = k^q\delta^r \tag{3.17}$$

By equating powers of each of the dimensions mass, length and time to zero in each dimensionless group, the indices can be found

$$\Pi_1 = uk/\omega, \;\; \Pi_2 = g'k/\omega^2, \;\; \Pi_3 = \frac{\mu k^2}{\rho\omega}, \;\; \Pi_4 = kH, \;\; \Pi_5 = ak, \;\; \Pi_6 = k\delta \tag{3.18}$$

Using $c = \omega/k$ and $\nu = \mu/\rho$, this can be expressed as

$$\frac{u}{c} = \phi\left(\frac{g'}{c^2k}, \frac{\nu k}{c}, kH, ak, k\delta\right) \tag{3.19}$$

The first independent group is a kind of inverse Froude number for the internal wave, effectively indicating the steepness which a sinusoidal wave would have under these conditions. The second is an inverse Reynolds number. The last three relate the wavelength to the water depth, wave amplitude and interface thickness respectively.

### 3.3.2 Nondimensional governing equation

To make use of the above result in practise, it is necessary to search for the independent dimensionless groups in the governing equation (3.11), as demonstrated by Dean and Dalrymple (1991) for the case of surface waves. This is done by non-dimensionalising according to the following scheme

$$x = \hat{x}/k, \;\; z = \hat{z}/k, \;\; t = \hat{t}/kc, \;\; \psi = ac\hat{\psi}, \;\; \rho = \rho_0\hat{\rho} \tag{3.20}$$

where $\hat{x}$, $\hat{z}$, etc. denote dimensionless variables, and $\rho_0$ is a mean undisturbed density. Derivatives of the density scale differently, since the maximum density change against any co-ordinate is equal to the density difference between the upper and lower fluid. For example, if the static density profile is a tanh function

$$\begin{aligned} \overline{\rho} &= \rho_0 \left(1 - \alpha \tanh\left(\frac{z}{\delta}\right)\right) \\ \overline{\rho}' &= -\frac{1}{\delta}\rho_0 \,\alpha \,\mathrm{sech}^2\left(\frac{z}{\delta}\right) \end{aligned} \tag{3.21}$$

Thus derivatives of the density are $O(\alpha)$. The density fluctuation $\hat{\tilde{\rho}}$ is determined using the first order of the Stokes expansion (section 3.4) of the buoyancy equation (3.6)

$$\begin{aligned} \tilde{\rho}_1 &= -\frac{1}{c}\overline{\rho}'\psi_1 \\ \Rightarrow \tilde{\rho} &= -\frac{ac\alpha k}{c}\hat{\overline{\rho}}'\hat{\psi} \\ \Rightarrow \tilde{\rho} &= (ak\,\alpha)\hat{\tilde{\rho}} \end{aligned} \tag{3.22}$$

For the rest of this section the hat notation is dropped for clarity. Substituting these results into equation 3.11 and retaining only leading order in each term yields the following, after dividing by $ac^3k^4$

$$\left.\begin{aligned} \nabla^2\psi_{tt} - \left(\frac{g'}{c^2k}\right)\frac{\overline{\rho}'}{\rho}\psi_{xx} &= Q_v + Q_b + Q_d + Q_\nu \\ Q_v &= (ak)\,\mathrm{J}(\nabla^2\psi, \psi)_t \\ Q_b &= \left(\frac{g'}{c^2k}\right)(ak)\,\frac{1}{\rho}\mathrm{J}(\tilde{\rho}, \psi)_x \\ Q_d &= -\alpha\frac{\overline{\rho}'}{\rho}\psi_{ztt} \\ Q_\nu &= \left(\frac{\nu k}{c}\right)[\nabla^2\psi_{xx} - \nabla^2\psi_{zz}]_t \end{aligned}\right\} \tag{3.23}$$

### 3.3.3 Non-linearity

The left hand side of equation 3.23 is $O(1)$. The non-linear velocity terms $Q_v$ are of order $ak$, while the non-linear buoyancy terms $Q_b$ are of order $ak$ divided by the Froude number $c^2k/g'$.

The parameter $\epsilon = ak$ is a measure of the wave steepness, and it is the parameter frequently used in the Stokes expansion (e.g. Longuet-Higgins, 1953). In the laboratory waves discussed here, it is $O(10^{-1})$. Therefore non-linear velocity terms will be important in the analysis. Note that $\epsilon$ is one of the dimensionless groups of equation 3.19.

In the Stokes expansion of section 3.4, $\epsilon$ is chosen as the expansion parameter. It is important to note, however, that a different scheme for non-dimensionalising equation 3.11 would have led to a different choice of expansion parameter. Where the water depth is important (in shallow water waves), the suggestion of LeBlond and Mysak (1978) of $a/H$ as the expansion parameter might be preferable. However, in the waves studied in the experiments, this parameter is found to be $O(1)$ for the shallow water cases, and so the series would not converge. Furthermore, at the outset of a Stokes expansion it seems more likely that the expansion will be successful for short waves than for long, in which cnoidal or solitary wave solutions may be required.

Well-known results for surface waves (Ursell, 1953) back up the assertion that the Stokes expansion will perform less well for long waves than for short. The effects of depth on the Stokes expansion are expressed as the Ursell parameter, proportional to

$$\frac{3}{8}\frac{ak}{k^3H^3} < 1 \tag{3.24}$$

for the expansion to converge (Dean and Dalrymple, 1991). This parameter expresses an important aspect of long wave theory, which is discussed further in section 3.5.

Dean and Dalrymple point out that convergence of the series is not a sufficient condition for meaningful results. If the second order term is large, and the expansion is truncated at second order, the troughs in the theoretical surface wave profile may develop an anomalous bump. That the wave should have a single crest for each cycle may be used as a criterion for the maximum wave height which may be represented. Dean and Dalrymple show that this reduces to

$$3\frac{ak}{k^3H^3} < 1 \tag{3.25}$$

This condition is eight times more stringent than 3.24.

For internal waves, using a two-layer approximation with upper and lower layer depths $H_1$ and $H_2$, the depth $H$ would be replaced by $H_1 H_2/(H_1 + H_2)$. This reduces to $H_1$ in the case of a shallow thermocline in deep water.

### 3.3.4 The Boussinesq approximation

Recalling the derivation of the vorticity equation, the left-hand side of equation 3.10 can be rearranged with the substitution for density from equation 3.4

$$(\overline{\rho} + \tilde{\rho})\nabla^2\psi_t + g\tilde{\rho}_x \tag{3.26}$$

This illustrates how, in the inertia terms, the density always occurs in the combination $(\overline{\rho} + \tilde{\rho})$, while in the gravity (buoyancy) term, it occurs as $\tilde{\rho}$ only. Thus in the inertia term the density fluctuation appears as a correction, while in the buoyancy term it dominates.

The Boussinesq approximation relies on regarding the density as a constant in all of the inertia terms at the outset. Thus derivatives of density are set to zero wherever they are not in combination with gravity. In the derivation of section 3.2.2, these terms (except for those involving viscosity) are collected into the quantity $Q_d$.

$Q_d$ has been shown to be of the order of $\alpha$, which is a measure of the density difference across the interface. In the ocean $\alpha = O(10^{-3})$, while in the laboratory tank $\alpha = O(10^{-1}) = O(\epsilon)$. Since $\alpha$ can be regarded as a measure of the validity of the Boussinesq approximation, it can be concluded that this approximation is valid in the ocean to third order, while in the laboratory it is valid to first order only.

As Long (1965) pointed out, the retention of terms of order $\epsilon$ cannot be justified in such circumstances if the Boussinesq approximation is to be made, since the linear approximation is of the same order. Long showed that such inconsistency actually prevented the discovery of certain types of solitary waves, which are non-linear but cannot exist in the Boussinesq case. In the analysis of section 3.4, the Boussinesq approximation will not be made for the laboratory waves.

### 3.3.5 Viscous effects

The viscous term $Q_\nu$ is shown by equation 3.23 to be $O(Re^{-1})$, where $R\epsilon = c/\nu k$ is a Reynolds number based on the wave motion (Dore, 1970). Since $R\epsilon = O(10^5)$ in the laboratory, viscosity can be neglected in the bulk of the flow. However, the choice of length scale may have masked aspects of the flow which are governed by viscosity. To inspect the motion in thin regions of the flow, the vertical co-ordinate is rescaled

$$z = \delta' \hat{z} \tag{3.27}$$

If $\delta'$ represents a layer of thickness $\sim$ 1mm near to a fixed boundary, then it is found (as for surface waves; Dean and Dalrymple, 1991) that $Q_\nu = O(1)$. Thus in thin boundary layers the motion is governed by viscosity.

On the other hand, if $\delta' = 2\delta \sim 40$mm, using the thickness of the density interface as a vertical lengthscale, then $Q_\nu = O(10^{-2})$. Therefore, except in very thin interfaces, viscous effects only become important at third (or at worst second) order.

At larger scales, such as may be encountered in the ocean, Reynolds' stresses become more important than those due to molecular viscosity. One way of dealing with this is to estimate an *eddy viscosity*, using which the Reynolds' stresses may be treated in the same way as laminar viscous stresses. Massey (1989) argues against this on the basis that the eddy viscosity cannot be accurately known. A discussion of the use of eddy viscosity in internal waves is given by LeBlond (1966). The estimate for the eddy viscosity $K_m$ in oceanic solitary internal waves given by Helfrich and Melville (1986) is $K_m \simeq 10^{-4}$–$10^{-3}\mathrm{m}^2/\mathrm{s}$.

Using Helfrich and Melville's larger value, the Reynolds number of Osborne and Burch's (1980) Andaman Sea waves is $O(10^6)$. Using the interface thickness lengthscale $\delta$, a Reynolds number of $O(10^4)$ is obtained. Thus viscous effects can be expected to be negligible in the oceanic interface to third order.

In view of the intense shear at the interface, it may appear surprising that viscous effects do not govern the flow there. Strong shear in one co-ordinate, such as that found at the crests and troughs of internal waves, necessitates the existence of a non-zero vorticity $\zeta$, given by

$$\zeta = -\nabla^2 \psi \tag{3.28}$$

The above scaling arguments show that equation 3.11 is driven by vorticity. That this may occur even in an inviscid fluid may be shown by recalling Lord Kelvin's vorticity theorem (as stated by Prandtl, 1952, p.56)

> *In a homogeneous frictionless fluid the circulation along a closed fluid line remains constant as time goes on.*

The condition of homogeneity is essential, as both Prandtl and Lamb (1932, art. 17) emphasise, and Kelvin's theorem may not be applied to a heterogeneous fluid.

In the case of *interfacial waves*, a different argument must be used. The two fluids must be treated as homogeneous fluids separated by a movable but impermeable boundary, and in each fluid the motion may be regarded as potential flow (Arnsten, 1990). In the potential flow approach the vorticity is confined to a discontinuity at the interface, where its value is infinite.

In reality the interface acts like a solid boundary, adjacent to which there will be a viscous boundary layer (Harrison, 1908). The fact that this boundary layer is present in the centre of the most active region of the flow explains why experiments involving two imiscible fluids (e.g. Koop and Butler, 1981; Leone et al., 1982) suffer from much greater viscous attenuation than do experiments performed on a diffuse interface. The solid boundaries of the laboratory tank, being in less active regions, do less to attenuate the wave.

### 3.3.6 The rigid lid boundary condition

On the free surface, one might assume either zero vertical velocity (the so-called "rigid lid" case), or apply a dynamic free surface boundary condition. The former undoubtedly makes the mathematics easier. Three justifications can be made in favour of the former. Firstly, Phillips (1977) has shown that the validity of the rigid lid assumption depends on the condition $\omega^2/gk \ll 1$, which is satisfied in the laboratory, and even more so in the ocean. Secondly, in most of the experiments, the buoyancy frequency was zero near the surface, and where this was not so, the wave frequency was low. Thus the vertical motions near the surface can be supposed small. Thirdly, no vertical motions were

observed by eye in the laboratory tests (except where the wavemaker was accidentally started impulsively) and due to the meniscus effect which affects wire wave gauges, no equipment was available which would measure surface displacements which were not visible to the eye.

## 3.4 A Stokes expansion for internal waves

### 3.4.1 Perturbation expansion

The following Stokes expansion follows the formulation of Thorpe (1968b), although here the Boussinesq approximation is not made, and numerical solutions are sought for general cases (Thorpe started from the Boussinesq approximation and found analytic solutions for special cases up to second order). A further refinement is that the vertical co-ordinate $z$ is expanded in a Taylor series.

The perturbation expansion will at all times be truncated at third order. This is because the scaling arguments have shown that viscous effects become important at this order, and there will be no justification for preceding beyond it without inclusion of the viscous terms. In fact it will be seen that for many of the waves studied, even the third order cannot be used. The expansion outlined below is not able to cover viscous effects. In addition, without the Boussinesq approximation, the expressions become extremely cumbersome even at second order.

Equation 3.11 contains two dependent variables: the density fluctuation $\tilde{\rho}$ and the streamfunction $\psi$. These are expressed as a perturbation expansion in the wave steepness parameter $\epsilon$, along with the wave shape $\eta$

$$\left.\begin{aligned} \tilde{\rho} &= \sum_{m=1}^{M} \epsilon^m \tilde{\rho}_m \\ \psi &= \sum_{m=1}^{M} \epsilon^m \psi_m = \sum_{m=1}^{M} \epsilon^m \Psi_m(z+\eta) e^{mjk(x-ct)} \\ \eta &= \sum_{m=1}^{M} \epsilon^m \eta_m = \sum_{m=1}^{M} \epsilon^m H_m(z) e^{mjk(x-ct)} \end{aligned}\right\} \tag{3.29}$$

Thus the streamfunction and the wave shape are expanded in terms of a depth profile ($\Psi_m(z)$ and $H_m(z)$ respectively) multiplied by a harmonic oscillatory term[1]. Here, as

[1] According to engineering practise, $j$ is used instead of $i$ in the complex exponentials

before, $k$ is the wavenumber and $c$ is the phase speed. Note that the dependent variable $z + \eta$ is used in the streamfunction profiles instead of $z$; this follows Benjamin (1966).

### 3.4.2 Application of the Taylor series and the kinematic equation

The unknown wave shape $\eta(x, z, t)$ in the streamfunction is removed by expanding $\psi(x, z, t)$ as a Taylor series in $\eta$, rejecting terms which will appear smaller than third order.

$$\left.\begin{aligned}
\psi_1 &= \Psi_1(z)e^{jk(x-ct)} + \eta\Psi_1'(z)e^{jk(x-ct)} + \frac{\eta^2}{2}\Psi_1''(z)e^{jk(x-ct)} \\
\psi_2 &= \Psi_2(z)e^{2jk(x-ct)} + \eta\Psi_2'(z)e^{2jk(x-ct)} \\
\psi_3 &= \Psi_3(z)e^{3jk(x-ct)}
\end{aligned}\right\} \tag{3.30}$$

After substitution for $\eta$ from equation 3.29, $\psi_m$ is found in terms of $\Psi_m$ and $H_m$

$$\left.\begin{aligned}
\psi_1 &= \Psi_1 e^{jk(x-ct)} \\
\psi_2 &= \left[\Psi_2 + H_1\Psi_1\right]e^{2jk(x-ct)} \\
\psi_3 &= \left[\Psi_3 + \Psi_1'H_2 + \Psi_1'H_1H_1' + \frac{1}{2}\Psi_1''H_1 + \Psi_2'H_1\right]e^{3jk(x-ct)}
\end{aligned}\right\} \tag{3.31}$$

where $\Psi_1$, $H_1$, etc., are functions of $z$ only.

The displacement profiles $H_m$ are expressed in terms of the streamfunction profiles $\Psi_m$ by substitution of 3.31 into the kinematic equation 3.14. Although $H_1$, $H_1'$ and $H_2$ appear in the expressions for $\psi_2$ and $\psi_3$, they can be eliminated by collecting coefficients, solving the lower orders first and substituting for the low order expressions when required. This yields explicit expressions for the displacement profiles.

$$\left.\begin{aligned}
H_1 = &\ -\frac{1}{c}\Psi_1 \\
H_2 = &\ -\frac{1}{c}\Psi_2 + \frac{1}{2c^2}\Psi_1\Psi_1' + \frac{1}{c^2}\Psi_1^2 \\
H_3 = &\ -\frac{1}{c}\Psi_3 + \frac{1}{2c^2}\Psi_1\Psi_1'' + \frac{5}{3c^2}\Psi_1'\Psi_2 - \frac{7}{3c^3}\Psi_1^2\Psi_1' \\
&\ -\frac{11}{6c^3}(\Psi_1')^2\Psi_1 + \frac{1}{3c^2}\Psi_1\Psi_2' + \frac{1}{c^2}\Psi_1\Psi_2''
\end{aligned}\right\} \tag{3.32}$$

Thus once the streamfunction profiles are known, the vertical displacement $\eta(x, z, t)$ of an element of fluid from its rest position $(x, z)$ can be calculated.

### 3.4.3 The buoyancy equation

The density fluctuation $\tilde{\rho}_m$ may be found for each order $m$ by substituting the perturbation expansion for $\tilde{\rho}$ and $\psi$ (equation 3.29) into the buoyancy equation (3.6), and collecting coefficients of the expansion parameter $\epsilon$.

Collecting coefficients for the first order case ($\epsilon^1$), the Jacobian in 3.6 vanishes and the buoyancy equation becomes

$$\tilde{\rho}_{1t} = -\overline{\rho}'\psi_{1x} = -jk\overline{\rho}'\Psi_1 e^{jk(x-ct)} \tag{3.33}$$

This equation is integrated with respect to $t$ to find the buoyancy fluctuation

$$\tilde{\rho}_1 = \frac{\overline{\rho}'}{c}\Psi_1 e^{jk(x-ct)} + f_1(x, z) \tag{3.34}$$

as found by Thorpe (1968b).

The unknown constant of integration $f_1(x, z)$ can be dealt with as follows. First, it may be assumed that at first order, the density fluctuation must be periodic in both $x$ and $t$, if it is periodic at all. Since $f_1$ is not a function of $t$, it may be concluded that $f_1 = f_1(z)$ only.

Secondly, at first order it may be assumed that the density fluctuation integrated over one wave period is zero, i.e., elements of fluid return to their rest positions after the passage of the wave. Integration of equation 3.34 with this in mind gives

$$f_1(z) = 0 \tag{3.35}$$

Thorpe showed that the vorticity equation (in the Boussinesq approximation) gives $f_1 = f_1(z)$, and gave an energy argument for setting $f_1(z) = 0$ in the general case.

By collecting coefficients of $\epsilon^2$ and substituting for $\tilde{\rho}_1$ from 3.34 the second order density fluctuation can be found

$$\tilde{\rho}_2(x,z,t) = \left( -\frac{\overline{\rho}'}{c}\Psi_2 + \frac{\Psi_1^2\overline{\rho}' + \frac{1}{2}\overline{\rho}''\Psi_1^2}{c^2} \right) e^{2jk(x-ct)} + f_2(x,z) \tag{3.36}$$

No assumption is made about the form of $f_2(x,z)$. For the third order fluctuation, coefficients of $\epsilon^3$ are collected and $\tilde{\rho}_1$ and $\tilde{\rho}_2$ are replaced with the appropriate expressions

$$\begin{aligned} \tilde{\rho}_3(x,z,t) = & \left( -\frac{\overline{\rho}'\Psi_3}{c} + \frac{\overline{\rho}'\Psi_2\Psi_1' + \frac{1}{2}\overline{\rho}'\Psi_1''\Psi_1 + \overline{\rho}'\Psi_1\Psi_2' + \overline{\rho}''\Psi_1\Psi_2}{c^2} \right. \\ & \left. - \frac{\overline{\rho}'\Psi_1^2\Psi_1' - \frac{1}{2}\overline{\rho}'\Psi_1\Psi_1'^2 - \overline{\rho}''\Psi_1^3 - \frac{1}{6}\overline{\rho}''\Psi_1^3}{c^3} \right) e^{3jk(x-ct)} \\ & - \left( \frac{f_{2z}\Psi_1}{c} + \frac{j f_{2x}\Psi_1'}{kc} \right) e^{jk(x-ct)} + f_3(x,z) \end{aligned} \tag{3.37}$$

As Thorpe (1968b) pointed out, the forms of $f_2$ and $f_3$ are completely unknown, except that they must vanish on the horizontal boundaries of the domain.

For there to be a non-zero $x-$component in $f_2$ then there must be a change in the stratification along the length of the domain through which the wave travels. This could be the case if the wave were causing some form of non-linear mass transport, as occurs for surface waves (Stokes, 1847; Longuet-Higgins, 1953).

Mass transport certainly occurs in internal waves. Dore (1970) has investigated the situation in *interfacial* waves, and found, as did Longuet-Higgins for surface waves, that a non-zero viscosity greatly enhances the "Stokes drift", i.e., the mass transport which is calculated from the inviscid Stokes solution. The Stokes drift is $O(\epsilon^2)$ compared to the first order term; i.e., it is third order. A non-zero viscosity enhances this by a factor proportional to the square root of the Reynolds number.

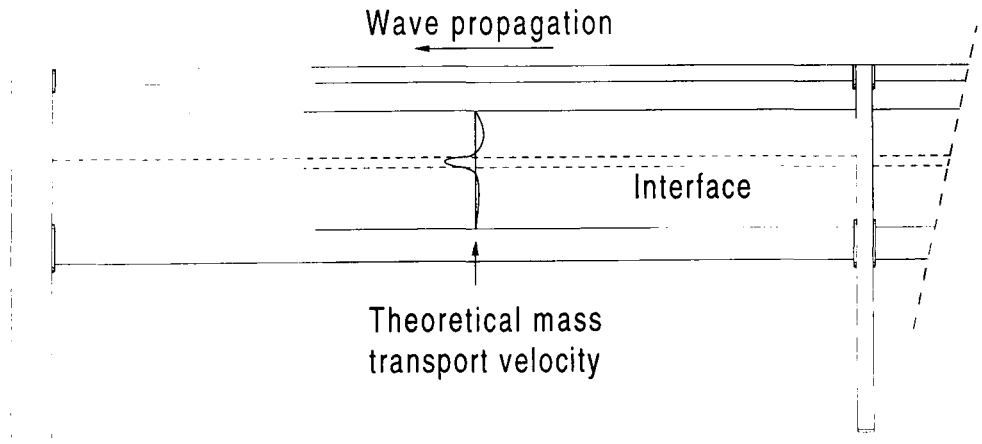


Figure 3.2: *Theoretical mass transport velocity*

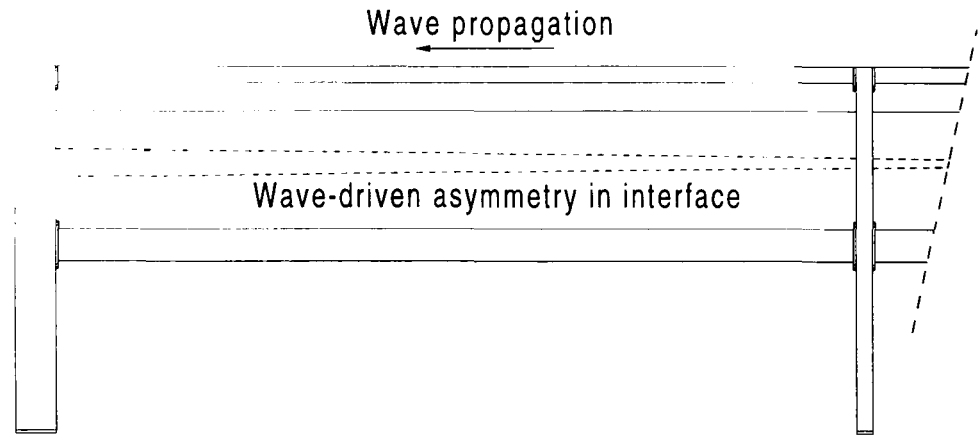


Figure 3.3: *Possible effect of "mass transport" in a confined tank*

Dore's analysis dealt with a two-layer fluid and with a horizontally unbounded domain. The effect of the tank end walls must be considered for the laboratory case. Figure 3.2 shows how the fluid is expected to behave. In surface waves, Longuet-Higgins shows that the net flow is forward at the surface and backward at the sea bed. Dore shows that the net flow in interfacial waves is forward near the interface and backward in the fluid interior.

For the case of surface waves in a laboratory tank, any mass transport will be expressed as a circulation in the tank. With stratification, this is impossible as any circulation will be resisted by buoyancy forces. Therefore, it is supposed that the tendency of the waves to give rise to a net mass flux will be resisted in the tank by means of modification to the background stratification. This modification might take the form of a thickening of the interface at the beach end of the tank, and a thinning of the interface near the wavemaker. A static head is thus set up along the tank which resists the forward mass transport in the interface. The situation is shown in figure 3.3. If the waves should cease, this static head would collapse, giving rise to a weak gravity current, or possibly a mode 2 seiche. In some of the larger amplitude experiments, a clear reverse gravity current did indeed follow the cessation of the waves.

Equipment was not available in the laboratory tests which would enable the testing of this hypothesis. Ideally, at least three density probes would take a large number of density profiles during the experiment, and an average interface thickness would be calculated. However, even with this information it would not necessarily be possible to observe the build-up of the static head. This is because wave energy dissipation at the beach may be associated with a small amount of diapycnal mixing, which would locally thicken the interface and drive a gravity current. Mixing was observed to occur at the wavemaker for some of the larger amplitude experiments. Separation of the mass-transport driven head from that created by mixing would be very difficult.

A further problem is that Dore's analysis would probably require considerable modification, because, as was shown in section 3.3.5, the influence of viscosity in a continuously stratified fluid is less than in a two-layer fluid. Faced with these practical and mathematical difficulties, it would seem necessary to proceed with an approximation, and note that for the unbounded case of the open ocean, a modification to the theory may be required. The approximation is

$$f_2(x,z) = f_3(x,z) = 0 \tag{3.38}$$

The terms involving $f_2(x,z)$ and $f_3(x,z)$ will be retained in the analysis which follows in order to observe the effect of neglecting them.

### 3.4.4 The first order equation

Stokes (1847) found that the phase velocity of surface waves calculated from linear theory receives a correction at third order. It is expected that something similar will happen for internal waves in continuous stratification. Anticipating this, Thorpe (1968b) suggested a perturbation expansion for the phase speed, which did not require to be implemented in the event because the linear phase velocity turned out to be correct to second order, as expected. Here the expansion will be made *a priori*

$$c = c_0 + \sum_{m=1}^{M} \epsilon^m c_m \tag{3.39}$$

This expression, along with the expressions for the streamfunction (equations 3.29 and 3.31) and those for the density fluctuation (equations 3.29, 3.34, 3.36 and 3.37) are substituted into the vorticity equation 3.11. Here it is understood that $Q_\nu = 0$ (section 3.3.5) and $f_1 = 0$ (section 3.4.3).

Terms smaller than third order are rejected, and expressions which enable the first, second and third order streamfunction profiles to be found are obtained. The first order equation is obtained by equating coefficients of $\epsilon^1$

$$\Psi_1'' + \frac{\overline{\rho}'}{\overline{\rho}}\Psi_1' + \left(-\frac{g\overline{\rho}'}{c_0^2\overline{\rho}} - k^2\right)\Psi_1 = 0 \tag{3.40}$$

All of the coefficients of $\epsilon^1$ are also coefficients of $e^{jk(x-ct)}$, which becomes a common factor and cancels out.

If the Boussinesq approximation is made, the term in $\Psi_1'$ vanishes, and Thorpe's (1968b) first order equation is obtained. The quantity $-g\overline{\rho}'/\overline{\rho}$ is equal to $N^2$, where $N$ is the buoyancy frequency.

The non-linear vorticity equation has thus been reduced to a linear ordinary differential equation, which is second order and homogeneous (no forcing function). In special cases of stratification it may be solved analytically.

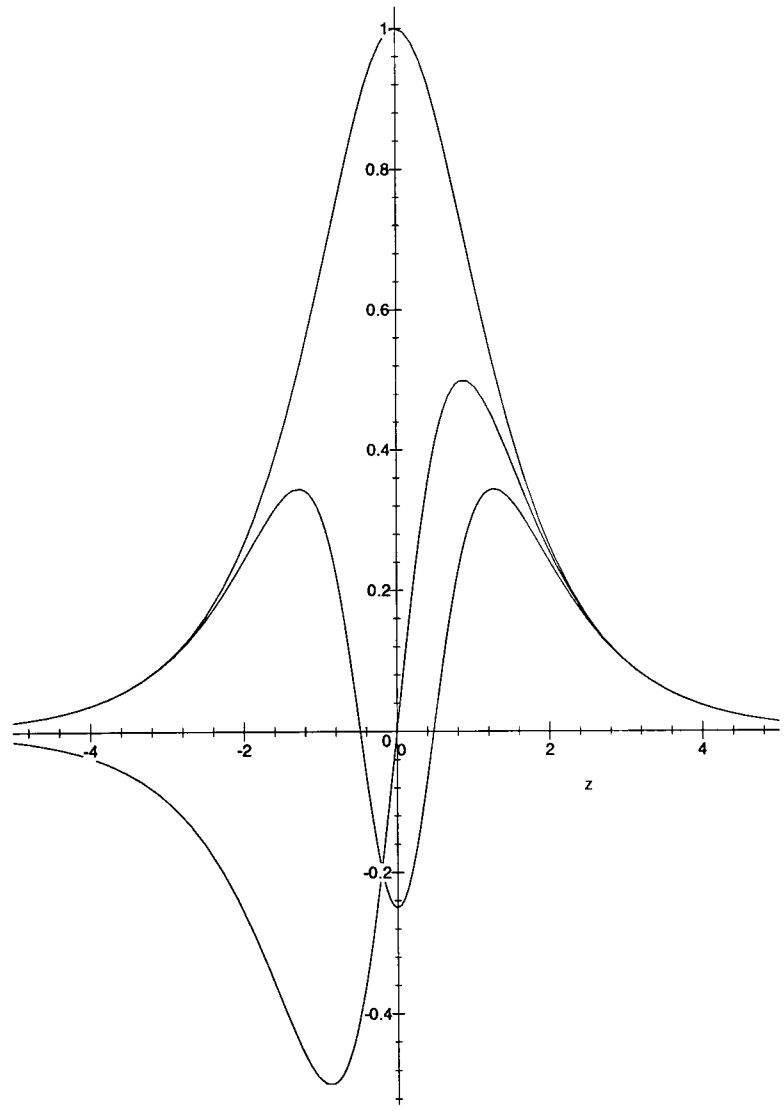


Figure 3.4: *The first three eigenfunctions of a short wave in a tanh density profile*

Equation 3.40 is a Sturm-Liouville or eigenvalue problem. Solutions to this equation take the form of eigenfunctions $\Psi_1(z)$ with corresponding eigenvalues $c_0^2$, assuming that the wavenumber $k$ is given. This means that for an infinite number of discrete special values of $c_0^2$ there exists a corresponding mode shape $\Psi_1(z)$. For the current purposes, the lowest mode is always sought, which is the mode with the largest phase speed $c_0$.

Figure 3.4 shows the streamfunction mode shapes for the first few modes in a tanh density profile, with infinite vertical extent. This is one of the analytic cases of Thorpe (1968b).

### 3.4.5 The second and third order equations

Equating coefficients of $\epsilon^2$ in the vorticity equation gives the following

$$\begin{aligned}\Psi_2'' + \frac{\overline{\rho}'}{\overline{\rho}}\Psi_2' + \left(-\frac{g\overline{\rho}'}{c_0^2\overline{\rho}} - 4k^2\right)\Psi_2 = \\ \frac{g\overline{\rho}'^2}{2c_0^3\overline{\rho}^2}\Psi_1^2 + \frac{\overline{\rho}'}{2c_0\overline{\rho}}\left(\Psi_1'^2 - \Psi_1\Psi_1''\right) \\ + \frac{g\overline{\rho}'}{c_0^3\overline{\rho}}\Psi_1^2 + \frac{2}{c_0}\Psi_1'^2 - \frac{\overline{\rho}'^2}{2c_0\overline{\rho}^2}\Psi_1\Psi_1' - \frac{2k^2}{c_0}\Psi_1^2\end{aligned} \tag{3.41}$$

$$\frac{gc_1\overline{\rho}'}{2c_0^3\overline{\rho}}\Psi_1 = 0 \tag{3.42}$$

Equation 3.41 contains the second-order terms proportional to $e^{2jk(x-ct)}$. It is again a linear second order ordinary differential equation, but this time it is inhomogeneous, with a forcing function formed from the first order eigenfunction.

The additional equation (3.42) contains the terms proportional to $e^{jk(x-ct)}$. As was expected, the only solution to this equation is

$$c_1 = 0 \tag{3.43}$$

Thus there is no second order correction to the phase speed.

The third order equation is formed in the same way, by equating coefficients of $\epsilon^3$. The coefficients of $e^{3jk(x-ct)}$ are grouped in equation 3.44, and the coefficients of $e^{jk(x-ct)}$ are grouped in equation 3.45. There are no coefficients of $e^{2jk(x-ct)}$.

$$
\begin{aligned}
&\Psi_3'' + \frac{\overline{\rho}'\Psi_3'}{\overline{\rho}} + \left(-\frac{g\overline{\rho}'}{c_0^2\overline{\rho}} - 9k^2\right)\Psi_3 = \\
&-\frac{1}{c_0}\left(-\frac{\overline{\rho}'^2\Psi_1'^2}{\overline{\rho}^2} + \frac{\Psi_1'^2\overline{\rho}''}{\overline{\rho}} + \frac{2}{3}\frac{\Psi_1\overline{\rho}'^2\Psi_2'}{\overline{\rho}^2} + \frac{4}{3}\frac{\Psi_1'\overline{\rho}''\Psi_2}{\overline{\rho}} + 2\frac{\Psi_1'\overline{\rho}''\Psi_2'}{\overline{\rho}} + \frac{1}{2}\frac{\overline{\rho}'^3\Psi_1\Psi_1'}{\overline{\rho}^3} - \frac{1}{3}\frac{\Psi 1\overline{\rho}''\Psi_2'}{\overline{\rho}}\right. \\
&\quad -\frac{\overline{\rho}'\Psi_1\Psi_1'\overline{\rho}''}{\overline{\rho}^2} + \frac{\Psi_1\Psi_1''\overline{\rho}''}{\overline{\rho}} + \frac{\overline{\rho}'\Psi_1'\Psi_1''}{\overline{\rho}} + \frac{\overline{\rho}'\Psi_1\Psi_2'''}{\overline{\rho}} + \frac{5}{3}\frac{\overline{\rho}'\Psi_1''\Psi_2}{\overline{\rho}} - \frac{1}{2}\frac{\overline{\rho}'^2\Psi_1\Psi_1''}{\overline{\rho}^2} + \frac{1}{2}\frac{\overline{\rho}'\Psi_1'''\Psi_1}{\overline{\rho}} \\
&\quad +\frac{1}{2}\frac{\Psi_1\Psi_1'\overline{\rho}'''}{\overline{\rho}} + \frac{\overline{\rho}'^3\Psi_1\Psi_2'}{\overline{\rho}^3} + \frac{1}{3}\frac{\overline{\rho}'\Psi_1\Psi_2''}{\overline{\rho}} + 2\frac{\overline{\rho}'\Psi_1'\Psi_2''}{\overline{\rho}} + \frac{\Psi_1'\overline{\rho}'\Psi_2'}{\overline{\rho}} + \frac{1}{3}\frac{\overline{\rho}'^2\Psi_1'\Psi_2}{\overline{\rho}^2} - \frac{\overline{\rho}'^2\Psi_1\Psi_2''}{\overline{\rho}^2} \\
&\quad -2\frac{\overline{\rho}'\Psi_1\overline{\rho}''}{\Psi_2'}\overline{\rho}^2 - 2\frac{\overline{\rho}'^2\Psi_1'\Psi_2'}{\overline{\rho}^2} + \frac{\Psi_1\overline{\rho}'''\Psi_2'}{\overline{\rho}} + 2\frac{\Psi_1\overline{\rho}''\Psi_2''}{\overline{\rho}} - \left(\frac{\Psi_1\overline{\rho}'\Psi_2}{\overline{\rho}} + 12\frac{\overline{\rho}'\Psi_1\Psi_2'}{\overline{\rho}} + 8\Psi_1'\Psi_2'\right. \\
&\quad \left.\left.+\frac{9}{2}\frac{\overline{\rho}'\Psi_1\Psi_1'}{\overline{\rho}} + 2\Psi_2'\Psi_1 + 4\Psi_1\Psi_2'' + \Psi_1'^2 + \frac{1}{2}\Psi_1''\Psi_1 - 4\Psi_1'\Psi_2\right)k^2 + \left(32\Psi_1\Psi_2 + 4{\Psi_1}^2\right)k^4\right) \\
&-\frac{1}{c_0^2}\left(-4\Psi_1''^2\Psi_1 - 8\Psi_1''\Psi_1'^2 - 4\Psi_1'''\Psi_1'\Psi_1 - \frac{4}{3}\Psi_1'\Psi_1''\Psi_1 + \frac{1}{2}\frac{\Psi_1^2\Psi_1''\overline{\rho}'''}{\overline{\rho}} + \frac{1}{6}\frac{\Psi_1'\Psi_1^2\overline{\rho}'''}{\overline{\rho}} - \frac{13}{2}\frac{\Psi_1'^3\overline{\rho}'}{\overline{\rho}}\right. \\
&\quad -\frac{1}{2}\frac{\Psi_1\Psi_1'^2\overline{\rho}'''}{\overline{\rho}} + \frac{1}{2}\frac{\Psi_1^2\Psi_1^{\mathrm{IV}}\overline{\rho}'}{\overline{\rho}} + \frac{\Psi_1\Psi_1^2\overline{\rho}'\Psi_1'\overline{\rho}'''}{\overline{\rho}^2} + \frac{\Psi_1^2\Psi_1'''\overline{\rho}''}{\overline{\rho}} + \frac{\Psi_1'\Psi_1\Psi_1'''\overline{\rho}'}{\overline{\rho}} - \frac{1}{2}\frac{\overline{\rho}'\Psi_1'\Psi_1^2\overline{\rho}''}{\overline{\rho}^2} \\
&\quad -\frac{5}{3}\frac{\overline{\rho}'^2\Psi_1'\Psi_1^2}{\overline{\rho}^2} - 4\frac{\Psi_1'^2\overline{\rho}'\Psi_1}{\overline{\rho}} + \frac{1}{2}\frac{\overline{\rho}'^3\Psi_1'\Psi_1^2}{\overline{\rho}^3} - \frac{2}{3}\frac{\Psi_1^2\overline{\rho}''\Psi_1'}{\overline{\rho}} - \frac{19}{6}\frac{\Psi_1'^2\Psi_1\overline{\rho}''}{\overline{\rho}} + 5\frac{\overline{\rho}'\Psi_1\Psi_1'^2\overline{\rho}''}{\overline{\rho}^2} \\
&\quad +\frac{\Psi_1^2\overline{\rho}''^2\Psi_1'}{\overline{\rho}^2} - 4\frac{\overline{\rho}'^3\Psi_1\Psi_1'^2}{\overline{\rho}^3} + 2\frac{\overline{\rho}'^4\Psi_1^2\Psi_1'}{\overline{\rho}^4} - 4\frac{\overline{\rho}'^2\Psi_1^2\Psi_1'\overline{\rho}''}{\overline{\rho}3} + 3\frac{\Psi_1'^2\Psi_1\overline{\rho}'^2}{\overline{\rho}^2} - \frac{\Psi_1^2\overline{\rho}'^3\Psi_1''}{\overline{\rho}^3} \\
&\quad +\frac{\overline{\rho}'\Psi_1^2\Psi_1''\overline{\rho}''}{\overline{\rho}^2} + 2\frac{\overline{\rho}'^2\Psi_1\Psi_1'\Psi_1''}{\overline{\rho}^2} - \frac{1}{2}\frac{\Psi_1\Psi_1''^2\overline{\rho}'}{\overline{\rho}} - \frac{7}{3}\frac{\overline{\rho}'\Psi_1^2\Psi_1''}{\overline{\rho}} + \frac{1}{6}\frac{\Psi_1^2\overline{\rho}'^2\Psi_1''}{\overline{\rho}^2} - \frac{\Psi_1'^2\Psi_1''\overline{\rho}'}{\overline{\rho}} \\
&\quad +\frac{1}{6}\frac{\Psi_1^2\overline{\rho}'\Psi_1'''}{\overline{\rho}} + \frac{1}{6}\frac{\Psi_1^2\overline{\rho}''\Psi_1''}{\overline{\rho}} - 7\frac{\Psi_1'\overline{\rho}'\Psi_1\Psi_1''}{\overline{\rho}} + 2\frac{\overline{\rho}'^2\Psi_1'^3}{\overline{\rho}^2} - \frac{\Psi_1'^3\overline{\rho}''}{\overline{\rho}} + \left(4\frac{\Psi_1'^2\overline{\rho}'\Psi_1}{\overline{\rho}} + \frac{4}{3}\Psi_1'\Psi_1^2\right. \\
&\quad \left.-4\frac{\overline{\rho}'\Psi_1^2\Psi_1''}{\overline{\rho}} + 4\Psi_1^2\Psi_1'' + \frac{\Psi_1^3\overline{\rho}'}{\overline{\rho}} + \frac{4}{3}\frac{\overline{\rho}'\Psi_1^2\Psi_1'}{\overline{\rho}} - 4\frac{\overline{\rho}'^2\Psi_1'\Psi_1^2}{\overline{\rho}^2} + 25\Psi_1'^2\Psi_1\right)k^2 - 13k^4\Psi_1^3\Big) \\
&-\frac{1}{c_0^3}\left(\left(8\frac{\Psi_1\Psi_2 g\overline{\rho}'}{\overline{\rho}} + 4\frac{\Psi_1^2 g\overline{\rho}'}{\overline{\rho}}\right)k^2 + \frac{\overline{\rho}'^2\Psi_1\Psi_2' g}{\overline{\rho}^2} + 2\frac{\overline{\rho}'^2\Psi_1'\Psi_2 g}{\overline{\rho}^2} - \frac{1}{2}\frac{g\overline{\rho}'\Psi_1''\Psi_1}{\overline{\rho}} - \frac{g\Psi_1\overline{\rho}'^2\Psi_2}{\overline{\rho}^2}\right. \\
&\quad -\frac{\Psi_1'^2 g\overline{\rho}'}{\overline{\rho}} - \frac{1}{2}\frac{\Psi_1^2 g\overline{\rho}'''}{\overline{\rho}} - \frac{\overline{\rho}'^3\Psi_1\Psi_2 g}{\overline{\rho}^3} + 2\frac{\overline{\rho}'\Psi_1\Psi_2 g\overline{\rho}''}{\overline{\rho}^2} - \frac{1}{2}\frac{\overline{\rho}'^3\Psi_1^2 g}{\overline{\rho}^3} - \frac{g\Psi_1\overline{\rho}''\Psi_2}{\overline{\rho}} \\
&\quad -\frac{g\overline{\rho}'\Psi_1'\Psi_2}{\overline{\rho}} - 2\frac{\Psi_1\Psi_1' g\overline{\rho}''}{\overline{\rho}} - \frac{\Psi_1\Psi_2 g\overline{\rho}'''}{\overline{\rho}} - 2\frac{\Psi_1\Psi_2' g\overline{\rho}''}{\overline{\rho}} + \frac{\overline{\rho}'\Psi_1^2 g\overline{\rho}''}{\overline{\rho}^2} - 2\frac{\Psi_1'\Psi_2 g\overline{\rho}''}{\overline{\rho}} \\
&\quad \left.+\frac{3}{2}\frac{\overline{\rho}'^2\Psi_1\Psi_1' g}{\overline{\rho}^2} - 2\frac{\Psi_1'\Psi_2' g\overline{\rho}'}{\overline{\rho}} - 2\frac{\Psi_2'\Psi_1 g\overline{\rho}'}{\overline{\rho}} - \frac{g\overline{\rho}'\Psi_1\Psi_2''}{\overline{\rho}}\right) \\
&-\frac{1}{c_0^4}\left(\left(14\frac{\Psi_1^3 g\overline{\rho}'}{\overline{\rho}} + 4\frac{g\Psi_1^3\overline{\rho}'^2}{\overline{\rho}^2}\right)k^2 + 3\frac{g\overline{\rho}'\Psi_1'^2\Psi_1}{\overline{\rho}} + 4\frac{\overline{\rho}'^2\Psi_1^3 g\overline{\rho}''}{\overline{\rho}^3} - \frac{3}{2}\frac{\overline{\rho}'^3\Psi_1^3 g}{\overline{\rho}^3} - \frac{7}{6}\frac{g\Psi_1^3\overline{\rho}'''}{\overline{\rho}}\right. \\
&\quad -2\frac{\overline{\rho}'^4\Psi_1^3 g}{\overline{\rho}^4} + \frac{5}{2}\frac{\overline{\rho}'\Psi_1^3 g\overline{\rho}''}{\overline{\rho}^2} + \frac{19}{3}\frac{g\overline{\rho}'\Psi 1\prime\Psi_1^2}{\overline{\rho}} - 2\frac{\Psi_1^2\Psi_1'' g\overline{\rho}'}{\overline{\rho}} - 6\frac{\Psi_1^2 g\overline{\rho}'\Psi_1'\overline{\rho}''}{\overline{\rho}^2} \\
&\quad +\frac{g\Psi_1^3\overline{\rho}'^2}{\overline{\rho}^2} - 3\frac{\Psi_1 g\Psi_1'^2\overline{\rho}'^2}{\overline{\rho}^2} + \frac{g\Psi_1^3\overline{\rho}''}{\overline{\rho}} - 3\frac{\Psi_1'\Psi_1^2 g\overline{\rho}''}{\overline{\rho}} + 5\frac{\overline{\rho}'^3\Psi_1^2 g\Psi_1'}{\overline{\rho}^3} - \frac{\Psi_1^2 g\overline{\rho}'^2\Psi_1''}{\overline{\rho}^2} \\
&\quad \left.-\frac{\Psi_1^3 g\overline{\rho}'\overline{\rho}'''}{\overline{\rho}^2} - \frac{13}{6}\frac{\Psi_1'\Psi_1^2 g\overline{\rho}'^2}{\overline{\rho}^2} - \frac{\Psi_1^3 g\overline{\rho}''^2}{\overline{\rho}^2}\right) - \frac{1}{c_0^6}\left(3\frac{\Psi_1^3 g^2\overline{\rho}'^2}{\overline{\rho}^2}\right)
\end{aligned}
\tag{3.44}
$$

$$\frac{\Psi_1' f_{2z}}{\overline{\rho}} - \frac{\overline{\rho}'\Psi_1' f_2}{\overline{\rho}^2} + \frac{jk\Psi_1 f_{2x}}{\overline{\rho}}$$
$$+\frac{1}{c_0^2}\left(-\frac{g f_{2z}\Psi_1}{\overline{\rho}} + \frac{jg f_{2xz}\Psi_1}{k\overline{\rho}} - \frac{jg f_{2x}\Psi_1'}{k\overline{\rho}} + \frac{\overline{\rho}'\Psi_1 g f_2}{\overline{\rho}^2} - \frac{g f_{2xx}\Psi_1'}{k^2\overline{\rho}}\right) \qquad (3.45)$$
$$+\frac{2c_2\Psi_1 g\overline{\rho}'}{c_0^3\overline{\rho}} = 0$$

Equation 3.44 is an inhomogeneous equation of the same type as 3.41. From the other equation (3.45), it can be seen that a third order correction $c_2$ to the phase speed $c$ may now enter, as expected. However, the approximation made in section 3.4.3 was that $f_2(x,z) = 0$. The correction to the phase speed is seen to depend on $f_2(x,z)$ and so, continuing with the approximation, it is assumed that

$$c_2 = 0 \qquad (3.46)$$

and that $c = c_0$ is a sufficiently good approximation to the phase speed of the wave.

The implication of these assertions and the analysis is that when there is no non-linear mass transport term, the phase speed remains linear. Whether this is merely a spurious result of the approximations taken, or an essential part of the behaviour of internal waves in a closed tank, remains to be seen.

### 3.4.6 Implementation of the Stokes solution

Neglecting the viscous term, the fully non-linear vorticity equation (3.11) and the buoyancy equation (3.6) were programmed into a symbolic manipulation package (Maple V release 3.0 for MS-Windows) on a personal computer. This package was used to perform symbolic calculations. The results for the Taylor expansion of $\psi$ (equations 3.31 and 3.32) were substituted into the vorticity and buoyancy equations to obtain firstly the buoyancy fluctuations $\tilde{\rho}_{1-3}(x,z,t)$ (equations 3.34, 3.36 and 3.37), and finally the ordinary differential equations for the streamfunction profiles $\Psi_{1-3}(z)$ (equations 3.40, 3.41 and 3.44).

The ordinary differential equations, which are all second order, were reduced to pairs of first order ordinary differential equations by substitution, e.g. for the first order equation

$$\left.\begin{aligned} \Psi_1' &= A_1 \\ A_1' + \frac{\overline{\rho}'}{\overline{\rho}}\Psi_1' + \left(-\frac{g\overline{\rho}'}{c_0^2\overline{\rho}} - k^2\right)\Psi_1 &= 0 \end{aligned}\right\} \tag{3.47}$$

where $A_1(z)$ is a new variable.

The linear problem has been expressed as a system of two coupled first order linear ordinary differential equations in the unknowns $A_1(z)$ and $\Psi_1(z)$, with one further unknown, the phase speed $c_0$, which is the eigenvalue. To incorporate this into the system, a third equation is added

$$c_0' = 0 \tag{3.48}$$

The boundary conditions, from section 3.2.3, are

$$\Psi_1(z_1) = \Psi_1(z_2) = 0 \tag{3.49}$$

where $z_{1,2}$ are the top and bottom boundaries respectively. The arbitrary amplitude of the eigenfunction $\Psi_1(z)$ provides the final boundary condition.

Press et al. (1994) recommend this formulation as a means of solving eigenvalue problems, and suggest a "shooting" method for solution. In this method, the boundary value problem described above is transformed into an initial value problem by changing the boundary prescriptions, for example

$$\begin{aligned} \Psi_1(z_1) &= 0 \\ A_1(z_1) &= p \\ A_1'(z_1) &= q \end{aligned} \tag{3.50}$$

Here $p$ is a guess for the starting slope of the function, and $q$ is an arbitrary starting value for the second derivative (set to unity). From this starting point, the equations were integrated by a 4th order adaptive stepsize Runge-Kutta method, and the value of $\Psi_1$ at the end point $z_2$ was found. The value of $p$ was adjusted until the required boundary condition at $z_2$ was satisfied. This adjustment was performed using a Newton-Raphson

method, modified to ensure convergence when the starting guess was distant from the root. Both of these routines ('C' functions) were taken from Press et al. (1994).

An infinite number of modes are possible, but only the first mode was sought. Hence, the number of flow reversals in the derivative of $\Psi_1$ was calculated and the starting guess $p$ modified if the wrong mode had been found. Thereafter, the solution was scaled so that the amplitude of the wave was correct.

The second and third order equations were not eigenvalue problems, since they possessed a forcing term, and the value of $c$ was already known. For each, a pair of coupled first order equations had to be solved to match two boundary conditions, thus the magnitudes were also constrained.

These equations could not be reliably solved using the shooting method. Convergence for these equations seemed to be far more finely balanced, and as the correct starting guess $p$ was approached, instabilities were sometimes observed to appear in the function. They were solved using the more complicated method of finite differences, again using a routine by Press et al. (1994).

## 3.5 Long wave theory for internal waves

### 3.5.1 The long wave paradox

The long wave paradox mentioned in chapter 2 is an important part of the theory of surface and internal waves. The paradox, and its resolution, is best expressed with the Ursell parameter for surface waves (Ursell, 1953)

$$\mathcal{U} = \frac{a\lambda^2}{h^3} \tag{3.51}$$

This parameter actually first appeared in Stokes' (1847) discussion of non-linear waves in deep water, to differentiate between his theory and Airy's non-linear shallow water theory. For Stokes' deep water expansion to converge, he required that $\mathcal{U} \ll 1$, whereas Airy's theory required $\mathcal{U} \gg 1$. The former prescription implies great depth, in which the vertical and horizontal motions are of equal magnitude. The latter condition implies that the vertical accelerations are insignificant. With this prescription Airy found that finite amplitude waves would tend to steepen, so that a long finite amplitude wave of

permanent form was impossible. This effect has been termed *amplitude dispersion*, to distinguish it from *frequency dispersion* which by spreading out the spectral components of a wave reduces its steepness.

The paradox is therefore the conflict between Boussinesq and Rayleigh's discovery of solitary wave solutions to the equations of motion (Lamb, 1932) together with Russell's (1845) convincing experiments, and Airy's prediction that a weakly non-linear long wave could not propagate without change of form.

The weakness of the Airy theory is its neglect of the vertical accelerations, which restricts it to long infinitesimal waves. Ursell showed that the intermediate case, where $\mathcal{U} \sim 1$, gave the Boussinesq equation, which has a solitary wave solution (Lamb, 1932). Korteweg and de Vries (1895) showed that solitary waves arise when the effects of amplitude dispersion and frequency dispersion balance one another exactly, and it is now known that such a condition may occur readily in many types of wave motions. Benjamin (1966) points out that the prescription $\mathcal{U} = 1$ implies this same condition.

### 3.5.2 Solitary internal waves

Benjamin (1966) applied long wave theory to internal waves, following a different derivation to that of the rest of this chapter. His theory will be used without modification, and his derivation will not be repeated here. Benjamin's analysis neglects the possible effects of the earth's rotation, as was done in the preceding sections. It should be noted, as Thorpe (1968b) points out, that long waves on ocean scales are more likely to be influenced by Coriolis forces than are short waves.

Using a frame of reference moving with the wave, Benjamin arrives at the same eigenvalue problem as was encountered in the Stokes expansion (equation 3.40), but with the wavenumber $k = 0$

$$\frac{d}{dz}\left(Q_n \frac{d\phi_n}{dz}\right) - g\frac{d\rho}{dz}\phi_n = 0 \tag{3.52}$$

where the subscript $n$ represents the mode number, $Q_n = \rho c_n^2$, $\rho$ is the density, $\phi_n$ is the eigenfunction and $c_n$ is the phase speed of the $n$th mode. This equation expands to

$$\frac{d^2\phi_n}{dz^2} + \frac{1}{\rho}\frac{d\rho}{dz}\frac{d\phi_n}{dz} - \frac{g}{\rho c_n^2}\frac{d\rho}{dz}\phi_n = 0 \tag{3.53}$$

which is clearly related to equation 3.40. The second term vanishes in the Boussinesq approximation, but this approximation is known to be invalid for long waves (Long, 1965). The eigenvalue problem essentially gives the solution to the infinitesimal long wave problem, and since it is posed in the same way as before, the same methods of solution can be used.

Benjamin arrives at the following long wave solution

$$\begin{aligned} \eta(x,z) &= \frac{\epsilon J \phi_n}{K}\text{sech}^2\left(\frac{(\epsilon J)^{1/2}x}{2I^{1/2}}\right) \\ I &= \int_{z_1}^{z_2} Q\phi_n^2 dz \\ J &= \int_{z_1}^{z_2} \gamma_n \left(\frac{d\phi_n}{dz}\right)^2 dz \\ K &= \int_{z_1}^{z_2} Q_n \left(\frac{d\phi_n}{dz}\right)^3 dz \end{aligned} \tag{3.54}$$

in which $\epsilon$ is a small parameter of the wave height, $\epsilon\gamma_n = \rho(c^2 - c_n^2)$, $c$ is the actual phase speed of the wave (in fixed co-ordinates), and $Q = \rho c^2$. The domain is bounded above and below by $z_1$ and $z_2$.

Properties of the three quantities $I$, $J$ and $K$ are as follows: $I > 0$ always; $J > 0$ for supercritical waves (as solitary waves are) while $J < 0$ for subcritical waves; and the sign of $K$ denotes whether the wave is one of elevation or of depression. For a shallow thermocline in dep water, $K < 0$, since the solitary wave is one of depression. The small parameter $\epsilon$ cancels out, as does the arbitrary constant multiplying the mode shape $\phi_n$.

Benjamin found this result using the separation of variables $\zeta(x,z) = f(x)\phi_n(z)$ and expanding the equations of motion to third order in $\epsilon$. Here $\eta = \epsilon\zeta$. He noted a weakness in this approach in that using the independent variable $z$ in $\phi_n$ rather than the dependent variable $z + \eta$ appeared to restrict the validity of the solution to very small $\epsilon$. However, by performing a Taylor expansion

$$\begin{aligned}\zeta &= f(x)\phi(z+\epsilon\zeta) \\ &= f\phi + \epsilon f^2\phi\phi' + \epsilon^2 f^3\left(\tfrac{1}{2}\phi^2\phi'' + \phi\phi'^2\right) + \ldots\end{aligned} \tag{3.55}$$

and repeating the substitution, he found that the terms neglected in the simpler calculation were all of order $\alpha\epsilon$ smaller than the largest terms retained, where $\alpha$ is the fractional density difference. He concluded that equation 3.54, which was obtained using the simpler substitution, was valid if $\alpha\epsilon$ was small. He recommended that the Taylor expansion 3.55 be used with the initial form of the wave determined by equation 3.54. This was done here for both the wave shape and the kinematics.

### 3.5.3 Implementation of solitary wave solution

Solutions for the first mode only ($n = 1$) will be sought. In order to eliminate the unknown constants, the following substitutions will be introduced

$$\begin{aligned} I &= \kappa^2 c^2 I^*; & I^* &= \int_{z_1}^{z_2} \rho\hat{\phi}_1^2 dz \\ \epsilon J &= \kappa^2(c^2 - c_1^2)J^*; & J^* &= \int_{z_1}^{z_2} \rho\left(\frac{d\hat{\phi}_1}{dz}\right)^2 dz \\ K &= \kappa^3 c_1^2 I^*; & K^* &= \int_{z_1}^{z_2} \rho\left(\frac{d\hat{\phi}_1}{dz}\right)^3 dz \end{aligned} \tag{3.56}$$

where $\hat{\phi}_1$ is the first mode eigenfunction $\phi_1$, normalised to have a maximum amplitude of unity, and $\kappa$ is the arbitrary amplitude of $\phi_1$.

Equation 3.54 now becomes

$$\eta(x,z) = \frac{c^2 - c_1^2}{c_1^2}\frac{J^*}{K^*}\mathrm{sech}^2\left(\left(\frac{c^2 - c_1^2}{c^2}\frac{J^*}{I^*}\right)^{1/2}\frac{x}{2}\right) \tag{3.57}$$

which is entirely in terms of known quantities, except the phase speed $c$. The eigenvalue $c_1$ and the eigenfunction $\hat{\phi}_1$ are obtained in the same way as for the Stokes solution (section 3.4), and then $I^*$, $J^*$ and $K^*$ can be calculated. The wave height is found by setting $x = 0$

$$H_w = \frac{c^2 - c_1^2}{c_1^2} \frac{J^*}{K^*} \tag{3.58}$$

and it can be seen that only the infinitesimal wave ($H_w \to 0$) has $c = c_1$.

For a more accurate representation of the wave shape, Benjamin's recommendation (3.55) is followed, and a Taylor expansion of $\eta$ is performed. To simplify matters, a lengthscale $L$ is defined

$$L = 2\left(\frac{c^2}{c^2 - c_1^2}\frac{I^*}{J^*}\right)^{1/2} \tag{3.59}$$

The Taylor expansion for the wave shape is as follows

$$\begin{aligned}\eta(x,z) = \quad & H_w\hat{\phi}_1 \mathrm{sech}^2\left(\frac{x}{L}\right) + H_w^2\hat{\phi}_1\frac{d\hat{\phi}_1}{dz}\mathrm{sech}^4\left(\frac{x}{L}\right) \\ & + H_w^3\left[\frac{1}{2}\frac{d^2\hat{\phi}_1}{dz^2} + \hat{\phi}_1\left(\frac{d\hat{\phi}_1}{dz}\right)^2\right]\mathrm{sech}^6\left(\frac{x}{L}\right)\end{aligned} \tag{3.60}$$

which can be evaluated explicitly. The velocities are found from the streamfunction by means of the kinematic equation 3.14. A substitution is made as follows for the streamfunction

$$\begin{aligned}\psi(x,z) = \quad & \Psi_0(z) + H_w\Psi_1(z)\mathrm{sech}^2\left(\frac{x}{L}\right) \\ & + H_w^2\Psi_2(z)\mathrm{sech}^4\left(\frac{x}{L}\right) + H_w^3\Psi_3(z)\mathrm{sech}^6\left(\frac{x}{L}\right)\end{aligned} \tag{3.61}$$

Since the frame of reference moves with the wave at the phase speed $c$, the first streamfunction profile $\Psi_0$ is known from the boundary condition at infinity, while the other streamfunction profiles $\Psi_{1-3}$ are found by equating coefficients of $\mathrm{sech}^2(x/L)$, after substituting for $\eta$ and $\psi$ in the kinematic equation.

$$
\begin{aligned}
\Psi_0(z) &= cz \\
\Psi_1(z) &= -c\hat{\phi}_1 \\
\Psi_2(z) &= -\frac{1}{2}c\hat{\phi}_1^2\frac{d\hat{\phi}_1}{dz} \\
\Psi_3(z) &= -c\left[\frac{1}{2}\frac{d^2\hat{\phi}_1}{dz^2} + \frac{1}{3}\hat{\phi}_1\left(\frac{d\hat{\phi}_1}{dz}\right)^2 - \frac{1}{6}\hat{\phi}_1\frac{d}{dz}\left(\hat{\phi}_1\frac{d\hat{\phi}_1}{dz}\right)\right]
\end{aligned}
\tag{3.62}
$$

Thus once $\hat{\phi}_1$ is known all of the other quantities can be computed directly.

## 3.6 Summary

It has been shown that analytical extension of Stokes theory to third order without the Boussinesq approximation is possible, though complex. In chapter 6, use will be made of first, second and third order theories in order to assess their usefulness in predicting internal wave kinematics. Comparisons between measured and theoretical kinematics are made in section 6.2.5 to second order (see for example figures 6.7 to 6.11). Assessment of the effect of including second and third order components are made in section 6.6.2.

The Korteweg-de Vries theory described above is used alongside linear theory to predict the kinematics of the longer waves in chapter 6. Comparisons with long wave theory are made in section 6.4 (see for example figures 6.25 and 6.29). It is found that the theories are not as broadly applicable as might be hoped. Chapter 7 discusses the implications of using these theories in an engineering context.

# Chapter 4

# Experimental equipment

The aims and objectives of the laboratory experiments are reviewed and some preliminary tests are described. The mechanical design of the wave tank and wavemaker is discussed, followed by a description of the electronic and software aspects of the control and data collection system. The design and performance of the wave height gauges and the density probe is presented, including corrections to the readings of the aspirating density probe. The chapter concludes with a brief review of the tank, wavemaker and instrumentation.

## 4.1 Aims and objectives of the experiments

The aim of the experimental programme was to provide accurate measurements of the kinematics of regular internal waves under a range of known conditions. The specific objectives which arose from this aim were:

1. To generate stable stratification in a fluid in a laboratory tank;
2. To have accurate knowledge of the form of density stratification in the tank;
3. To generate trains of regular internal waves in the stratified fluid using a sinusoidal paddle motion of well defined frequency and amplitude;
4. To measure the shapes of the resultant internal waves;
5. To measure the fluid particle velocities within the internal waves.

Virtually no experimental equipment, other than a laser, was available at the start of the project; nor had forced internal waves been produced in any of the University departments connected with the project. Therefore, before designing and building the equipment it was necessary to run feasibility tests to determine the type of wave tank and wavemaker which would be needed. These tests are described in section 4.2.

Despite the project's "standing start" in terms of equipment, there was considerable expertise in surface waves and in velocity measurement using particle image velocimetry at the University of Edinburgh (e.g., Greated et al., 1992). Measurements in a variety of other buoyancy driven flows had previously been conducted at the University of Dundee. Some of the methods used are described by Davies (1992).

The equipment needed for the project was as follows:

1. A laboratory tank and a stratification system;
2. A computer controlled wave generator;
3. Wave height gauges;
4. A traversing probe for measuring the density profile in the tank;
5. Velocity measurement equipment.

This chapter deals with all of the experimental apparatus with the exception of the velocity measuring equipment, which is discussed in chapter 5.

## 4.2 Preliminary tests

In order to find the best method of generating internal waves and measuring wave shapes and density profiles, preliminary experiments were conducted in existing tanks in both Edinburgh University and Dundee University. The Dundee tests were conducted by the collaborators in the project. Neither of these tanks were suitable for kinematic measurements; the Dundee tank was too short and the Edinburgh tank had a steel base. However, these tanks did allow testing of basic wavemaker paddle shapes, and observation of the behaviour of different internal waves.

An early conclusion of these tests was that it is not difficult to set up a laboratory tank with a stable, near two-layer stratification, using fresh and salty water. Additionally, nearly any disturbance near the interface will set up progressive internal waves.

These conclusions were very encouraging. Some of the instability modes described in section 2.3.5 were also observed, especially resonance due to finite interface thickness.

Different paddle shape and motion tests were conducted at each site. Since some hardware for the task was already available in Dundee, paddles moving in a linear vertical oscillation were tested there. In Edinburgh, paddles rotating about a pivot were tested. Various shapes were tested in each site. At the time, no reliable means of measuring the wave heights was available, so the performance of each paddle shape was judged qualitatively on the basis of the amount of local mixing generated. Besides upsetting the stratification, mixing at the paddle was a sign that energy was not being efficiently transmitted to the wave. The smoothness of the wave shapes was also observed.

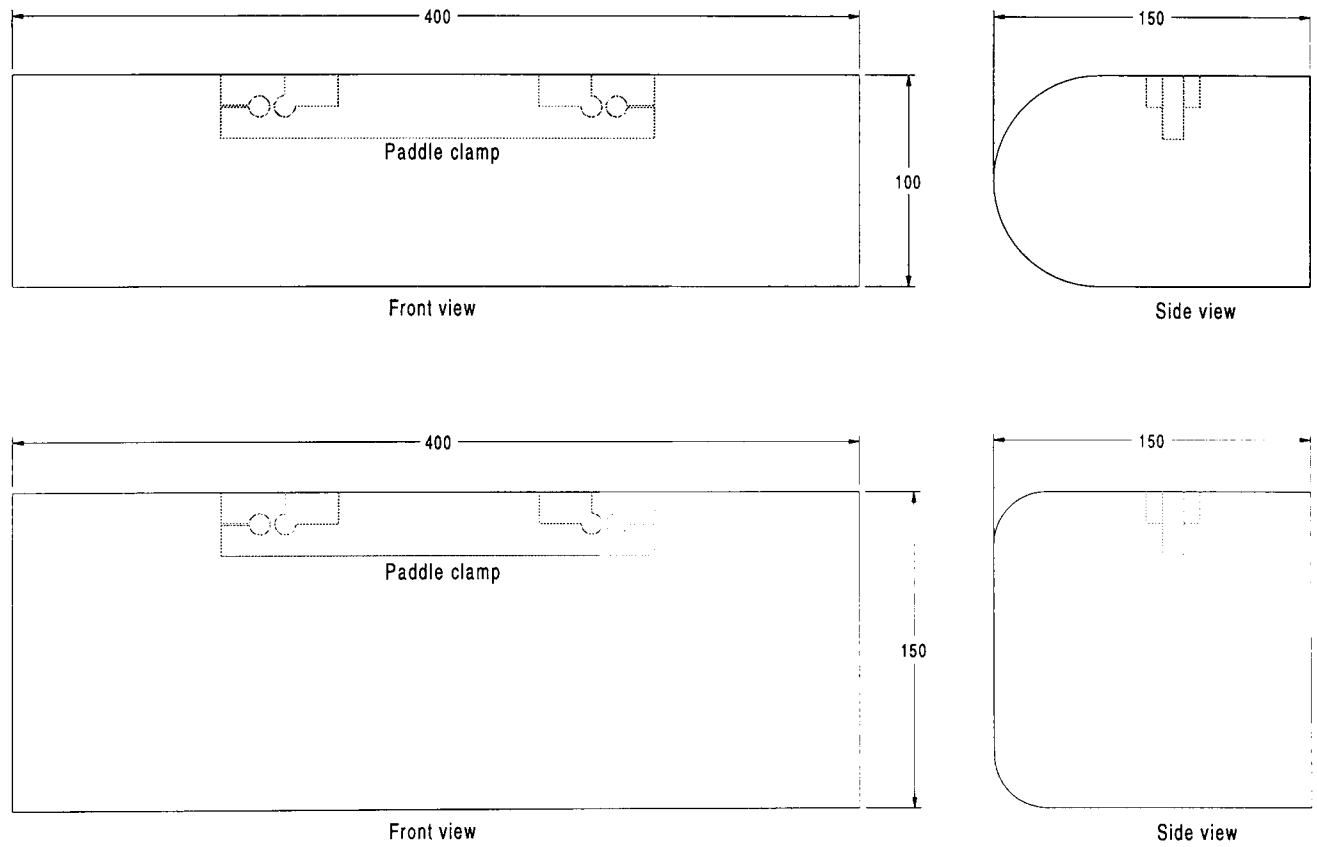


Figure 4.1: *Paddles used in the tests. Top: original paddle; bottom: larger paddle.*

From these tests, a vertically oscillating D-shaped paddle (figure 4.1) was selected as being the most effective over a range of frequencies and stratification conditions. The figure shows two sizes; the first size was that chosen from the preliminary tests, while the second was constructed when it was desired to generate larger waves (the taller face of the larger paddle generated less mixing than the smaller paddle when the amplitude was high). It was later decided that the paddles should be neutrally buoyant, so that they would not rise to the surface of the water when the power to the wavemaker was switched off.

## 4.3 Laboratory tank

The laboratory tank was designed on the basis that its primary function was to allow the study of the kinematics of internal waves using Particle Image Velocimetry (PIV). Velocities in internal waves are low compared to those in surface waves, and the PIV technology which was available at the time was not well suited to the measurement of very low velocities. These considerations meant that a relatively large tank would be required to allow the full range of wave conditions to be studied using PIV. The resulting design specification for the laboratory tank was as follows:

- The tank should be long enough to allow waves of reasonable length ($\lambda$ up to 2–3m) to propagate;
- The tank should be wide enough that wall effects should be negligible;
- The depth of water should be sufficient to allow all depth regimes to be studied, up to $\lambda/h < 1$;
- The overall volume of the tank should not be so great as to create an excessive consumption and storage requirement for saline solution; nor should the stratification of the tank take more than two or three hours;
- Compatibility with existing and future wave tanks in the University should be preserved where possible, in order to allow the sharing of equipment and facilities between projects;
- The tank should be small enough to fit into a certain laboratory area (which was not known at the start of the design but which was decided before the design was completed);
- The tank walls and base should be optically clear to allow the use of a particle image velocimetry system;
- For the same reason, the tank base had to be a minimum of 0.7m above the laboratory floor;
- The total cost should not exceed £4,500, including the stratification system. This figure was based on an estimate of the requirements of other aspects of the project. In fact the expenditure on the tank and stratification system was about half this figure. This was fortunate as the estimated expenditure on other items was exceeded.

### 4.3.1 Selection of wall and base material

The requirement that the tank walls and base be optically clear essentially defined the basic configuration, and the dimensions, early in the process. Glass was immediately selected as the base and wall material, as it combined optical clarity with scratch resistance, high stiffness ($\sim 70GPa$; equal to that of aluminium) and low cost. Optical plastics such as perspex (acrylic) or polycarbonate suffer from low stiffness ($\sim 3GPa$), low scratch resistance, and high cost.

Having selected glass as the primary load-bearing material, the options for tank dimensions became clearer. In the first place, panes of glass of length greatly in excess of 3m were difficult to obtain. In the second place, the required thickness of glass was a strong function of water depth, while the cost per unit area increased dramatically with increasing thickness.

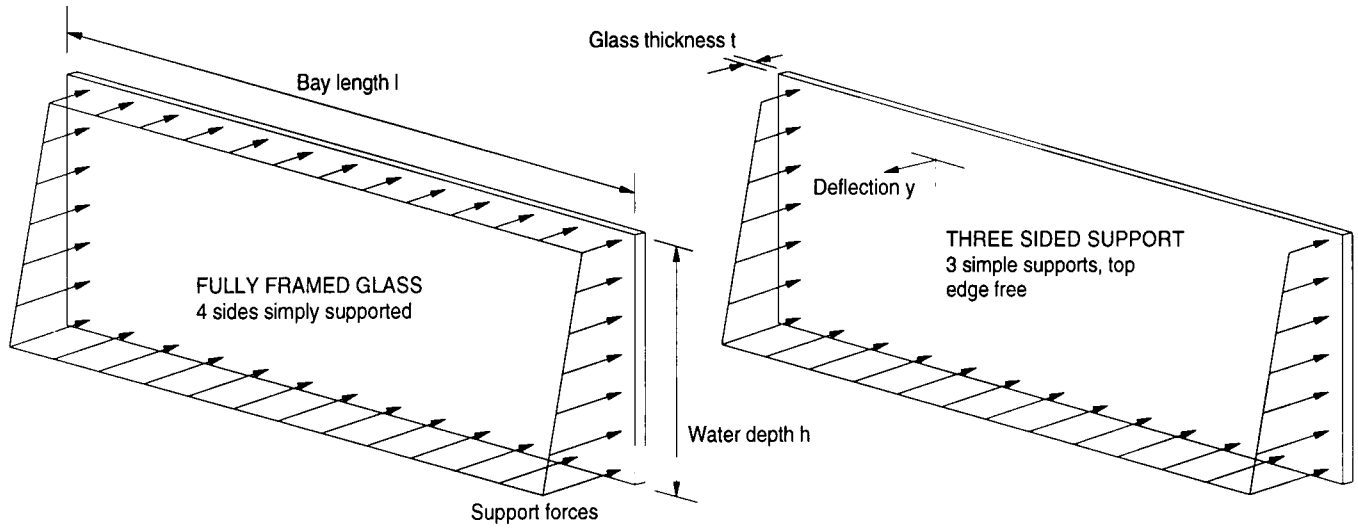


Figure 4.2: *Side glass support options*

Figure 4.2 shows the relevant quantities in the stress calculation for the glass sides and base. For the tank sides, the options were to support the glass along all four edges ("fully framed" case) or to leave the top edge free. The latter case resulted in a much higher stress in the glass. As optical access to the very top layers of the tank was not a priority, the fully framed arrangement was adopted.

With the glass fully framed, the glass thickness was governed by the water depth rather than by the length of the bays, so it was advantageous to have the bays as long as possible, minimising the number of intermediate supports which would interfere with observation. Therefore the bay length was set at 3m (slightly shorter than the longest easily available sheet of glass).

The overall length of the tank was set at a nominal 6m, as there would have been some difficulty in accommodating a longer tank.

The maximum stress ($\sigma_{max}$) and deflection ($y_{max}$) for a rectangular flat plate with four edges simply supported, under the loading case shown in figure 4.2. are given by (Roark, 1989, table 26, case 1e)

$$\left.\begin{aligned} \sigma_{max} &= \frac{0.38\rho g h^3}{t^2} \\ y_{max} &= \frac{0.07\rho g h^5}{E t^3} \end{aligned}\right\} \qquad (4.1)$$

where $\rho$ is the water density, $g$ is the gravitational acceleration, $t$ is the plate thickness and $E$ is modulus of elasticity of the plate.

| Thickness | $\sigma_{max}(MPa)$ | | | Price/$m^2$ | |
|---|---|---|---|---|---|
| (mm) | $h = 0.55$m | $h = 0.60$m | $h = 0.65$m | Haran | G.&J. Rae |
| 10 | 6.8 | 8.9 | 11.3 | £62 | £28 |
| 12 | 4.7 | 6.2 | 7.8 | £68 | £37 |
| 15 | 3.0 | 3.9 | 5.0 | £157 | - |
| 19 | 1.9 | 2.5 | 3.1 | - | - |
| 25 | 1.1 | 1.4 | 1.8 | £220 | - |

Table 4.1: *Glass selection choices*

Table 4.1 shows the options for glass thickness, including prices from two of the suppliers at the time (January 1993). A safe working stress of $\sigma_{max} = 7MPa$ for (standard) annealed float glass[1]. was adopted. The cost cutoff point was clearly a water depth $h$ =0.6m, which gave a glass thickness of 12mm. A minor increase in depth would have pushed the glass thickness up to 15mm and increased the glass cost by a factor of 4, for little obvious gain.

In the chosen configuration, the maximum deflection of the walls was kept below 0.5mm. If acrylic had been used, a deflection of 5mm would have been expected.

It was decided that a standard tank width of $b = 0.4$m would be used wherever appropriate (following an existing tank) for future tanks. This width was believed to be adequate to avoid wall effects, and gave a glass thickness 12mm for the base.

[1]This figure was suggested by Mr John Hellsby of Pilkington Glass Ltd

The tank end walls (figure 4.3) were to be the connection points for filling and draining plumbing. These were made from 15mm thick PVC sheet. An entry port was cut in each plates just below the level of the tank base. The ports were closed by removable entry covers to which all pipework could be attached. The possible future need to cut into the tank end walls *in situ* or remove the end walls for machining was thereby obviated.

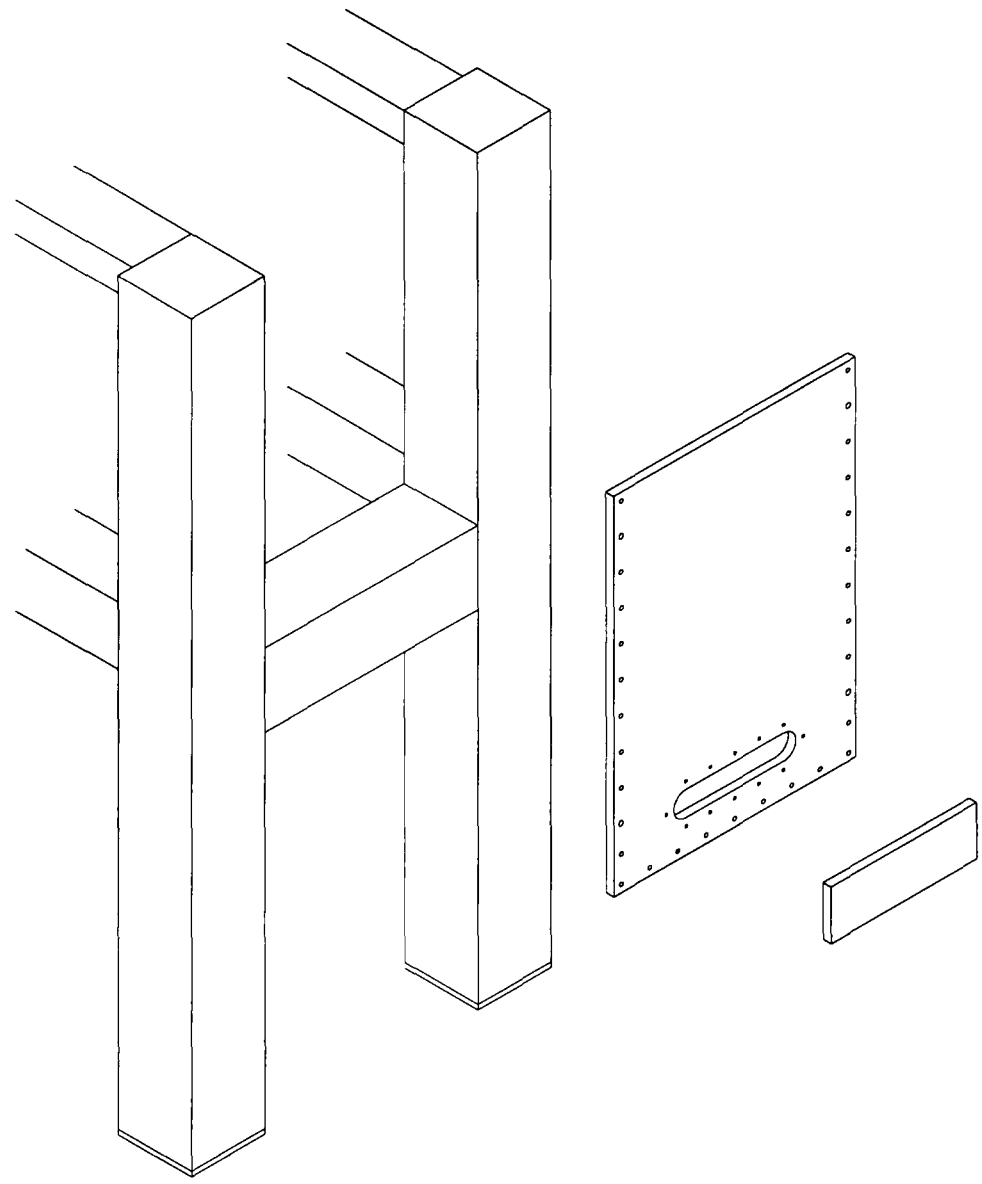

Figure 4.3: *Isometric assembly view of one of the tank end plates*

Nominal gaps of 5mm were left between panes of glass, and between the end wall and the glass, to allow silicone rubber seals to be made. This relatively large gap was specified to reduce the tendency of the seals to break due to slight deflections of the structure during filling. In the event, the dimensional tolerance on the glass was such that in certain places the gaps were rather smaller. Nevertheless, sealing was successful on the first attempt except for the four bottom corners.

### 4.3.2 Design of supporting structure

The design of the support structure was based on tanks designed by Dr David Skyner and Mr Tom Bruce, in the Department of Physics and Astronomy at the University of Edinburgh. Mild steel was chosen for the main support structure, because of its high strength/cost ratio and ease of welding. An inner structure of HE30 aluminium alloy angle, fastened to the steel frame, supported the glass. Extruded aluminium angle was chosen over steel angle because its superior dimensional consistency made it easier to align. Packing between the steel frame and the aluminium angle allowed fine tuning of the alignment before the glass was inserted.

Stress concentrations in the glass were avoided by interposing solid neoprene rubber strips between the aluminium and the glass. The rubber strips were bonded to the aluminium inner frame, and the glass to the rubber strips, using a high strength double-sided adhesive tape. A cross-section of the whole arrangement is shown in figure 4.4.

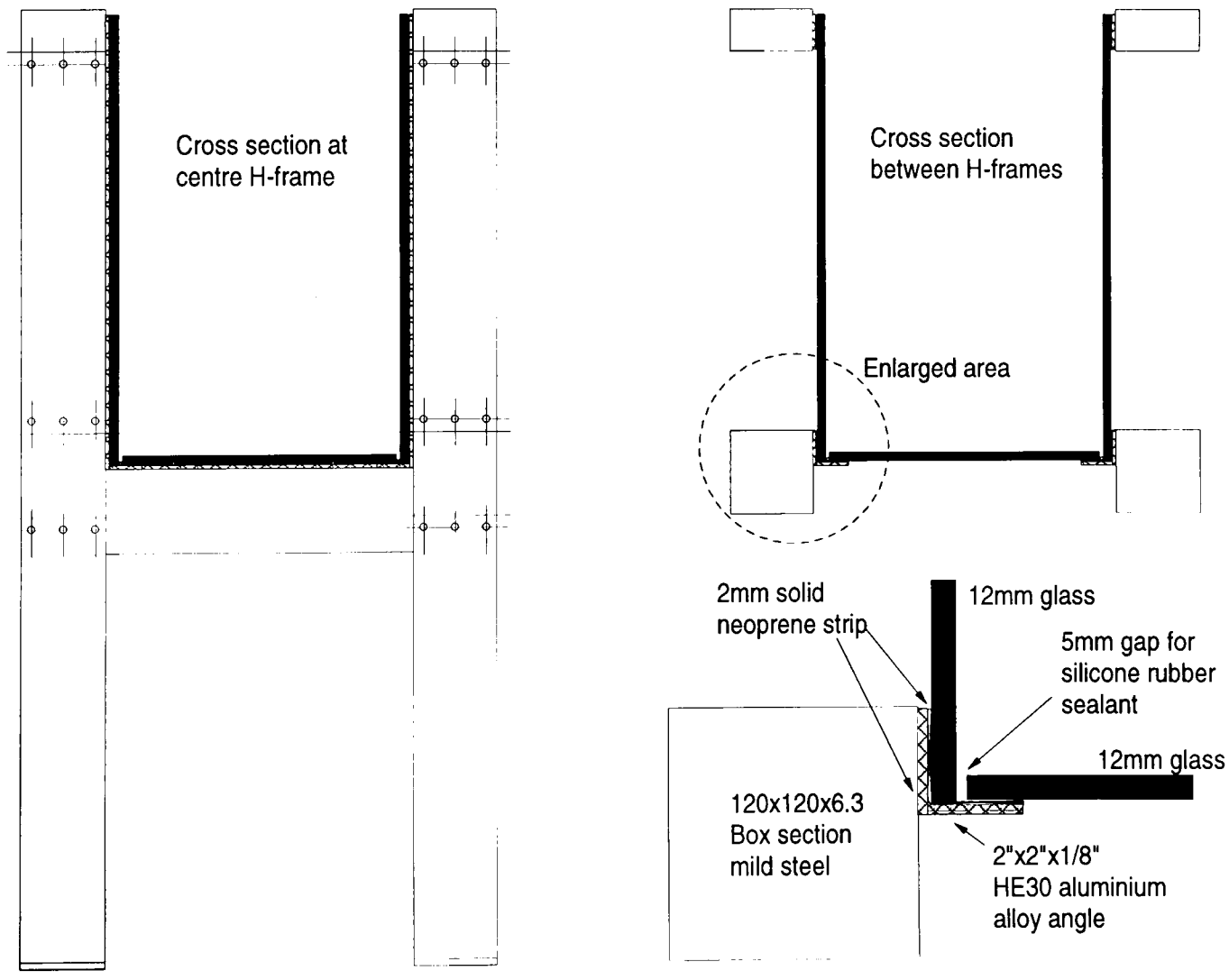


Figure 4.4: *Cross-sections of the wave tank*

A potential worry with the use of rubber strips to support the glass was that the rubber might compress under load, leading to a deflection which might break the seals. An experiment revealed that the rubber compression would be less than 1%.

It can be seen in the figure that the base glass rests on the edges of the aluminium angle, rather than fitting under the side glass. Although this arrangement results in a theoretically higher bending moment at the root of the angle, several factors mitigated in its favour, notably

- in either arrangement, slight bowing of the glass would tend to concentrate most of the load onto the outside edge of the angle, removing any comparative advantage,
- the arrangement chosen gives a solid support to the side glass, making the task of assembly much easier, and
- with this arrangement any pane of glass can be removed without necessitating the removal of another.

Simple stress calculations showed that 1/8" thick HE30 aluminium angle would be sufficient to carry the load.

Specifications for the steel support structure were governed by the requirement that deflections should not exceed 1mm when the tank was filled to the top. This was chosen to ensure the integrity of the seals, to avoid modulation of the internal waves by a varying channel width, and to reduce the flexibility in width required from any close-fitting equipment which was to be placed into the tank.

An isometric sketch of the steel structure is shown in figure 4.5. The tank is comprised of three welded H-sections separated by longitudinal beams. The function of the H-sections is to support the glass and to resist the static load applied by the water. The central H-section is required to separate the tank into discrete individually glazed bays.

| Part | Box dimensions (mm) | Wall thickness (mm) |
|---|---|---|
| End H-sections | $150 \times 150$ | 6.3 |
| Central H-section | $120 \times 60$ | 5 |
| Top side beams | $120 \times 60$ | 5 |
| Bottom side beams | $120 \times 120$ | 6.3 |

Table 4.2: *Steel specifications*

Separation of the tank length into bays allows the use of easily obtainable lengths of glass, and decreases the stiffness requirement for the longitudinal beams, whose deflection goes with the third power of beam length.

Calculation of the individual deflections of the longitudinal beams is straightforward: however, the actual deflection of the beams is increased by twist in the end H-sections. A sketch of the moments which cause this twist is shown in figure 4.6. Twist of the central H-section was not an issue since twisting moments applied from one side were balanced by moments applied from the other.

The steel chosen for the tank construction is listed in table 4.2. Box section steel was used throughout. The tight deflection requirement led to a structure whose strength is far in excess of that required to support the load.

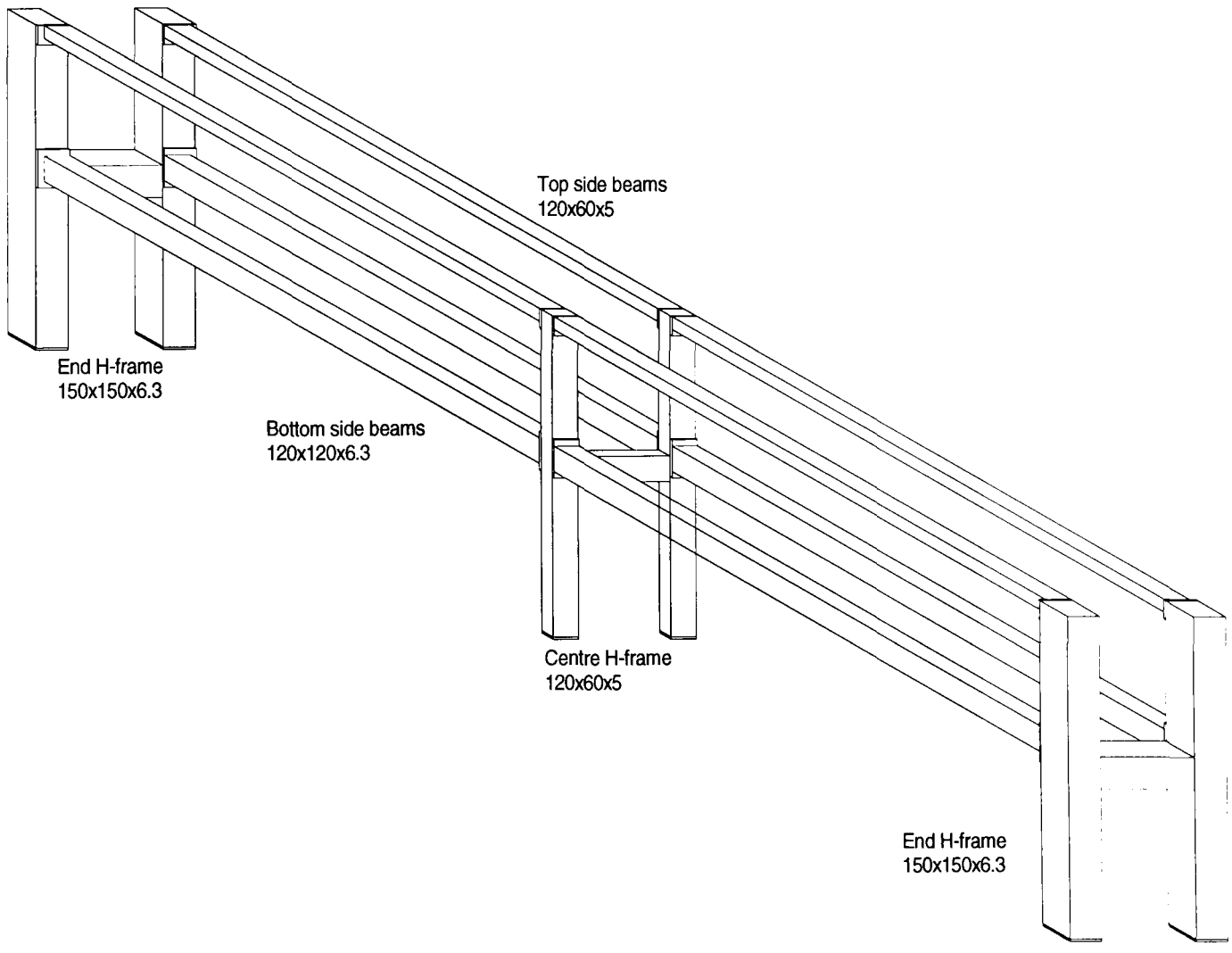


Figure 4.5: *An isometric view of the steel support structure*

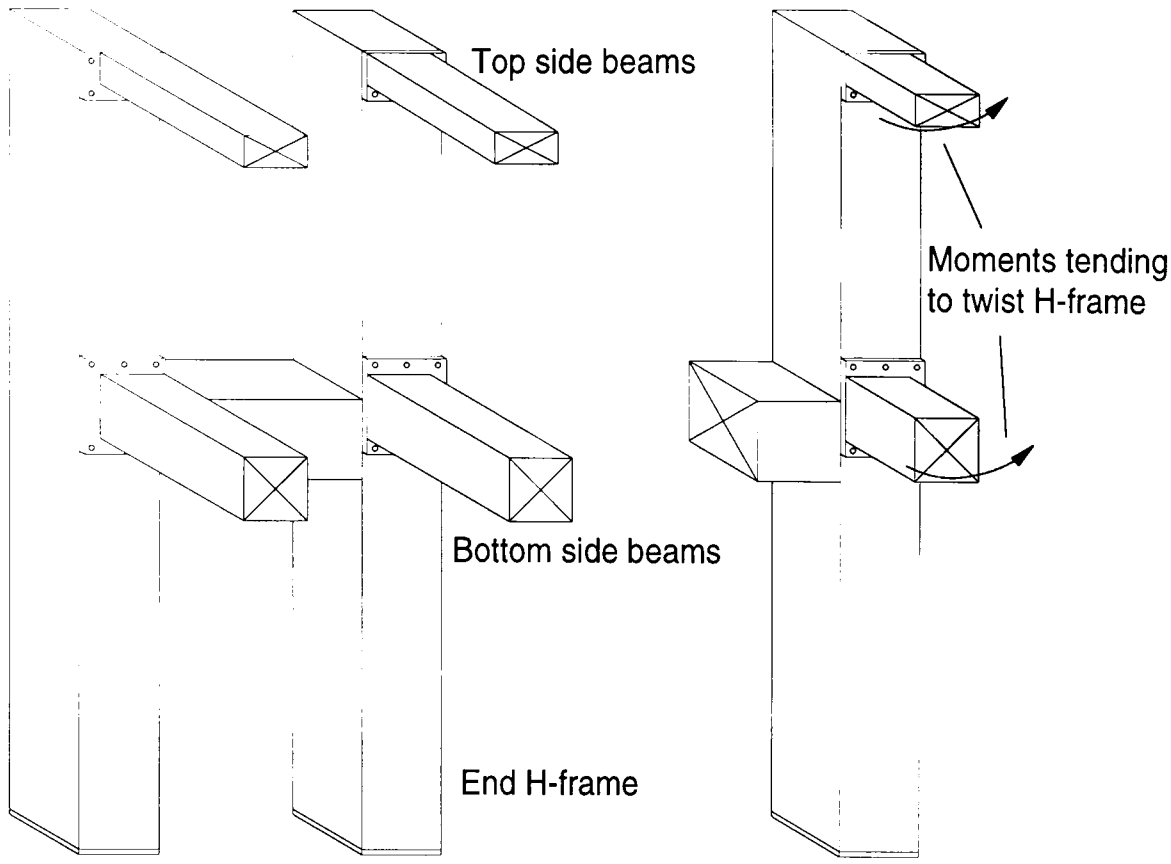


Figure 4.6: *Moments tending to twist the end H-section*

### 4.3.3 Stratification system

The requirements for the stratification system were that it should be able to produce nominally two-layer and more general density profiles. Control over the form of the density profile, especially the thickness of the interface, was considered important. Additionally, it was considered desirable that the saline solution should be conserved after experiments. This necessitated the provision of a reservoir and some form of filtering system, since the recycled water would become dirty after many uses.

The capacity of the wave tank is $1.53\text{m}^3$. A stratification system was required which could store a volume of saline solution equal to a reasonable fraction of this. As the tank would never be filled completely with saline solution, it was not considered necessary to store the full volume; however, the ability to store more than one solution was considered an advantage.

Two storage reservoirs of capacity $0.98\text{m}^3$ each, which had formed part of a previous experimental tank, were available. Two small pumps were also available. A system for stratifying the tank and storing saline solution was devised and modified during the project. The final stratification system is shown in figure 4.7. The stratification system functions as follows:

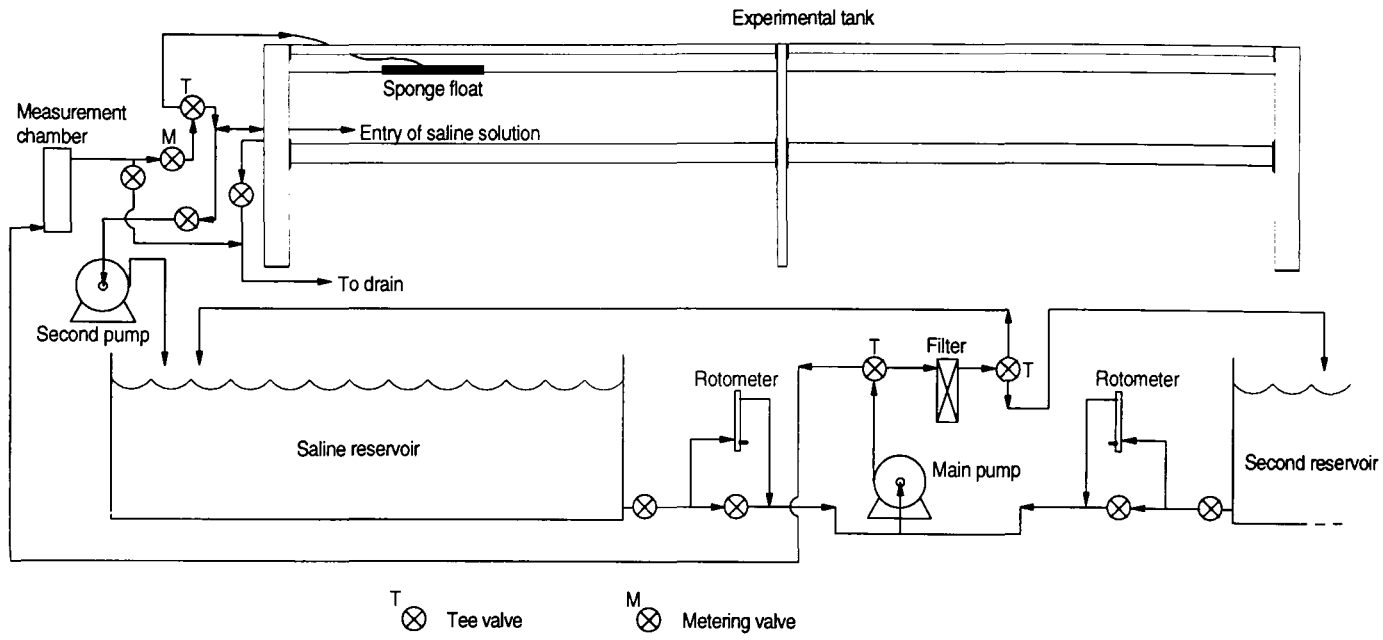


Figure 4.7: *The final system for storage of saline solution and stratification of the tank*

1. *Reservoir recirculating system*—One reservoir was selected as the saline storage tank. In this tank, saline solution was prepared, mixed, filtered and stored. The outlet of this tank was fed to the inlet of one of the pumps. This pump assisted in the function of filtering and mixing. The output from pump could be diverted either to the experimental tank, or back into the reservoir via a filter. Thus the pump could be used to fill the experimental tank, or to mix or clean the saline solution in storage.

   The return pipe from the filter to the reservoir entered the reservoir at the top, distant from the reservoir outlet. By this means, when mixing or filtering was in progress, a constant slow circulation was set up which prevented the fluid in the reservoir from itself becoming stably stratified. Filtering was done routinely for a few hours before every experimental run, and whenever saline solution was being prepared. The constant circulation helped to ensure that the salt dissolved properly.

2. *Stratification for two-layer cases*—The case most commonly studied was where two layers of differing densities were separated by a relatively thin interface, on which the waves propagated. For these cases, the tank was partially filled with fresh water and saline solution was slowly bled in underneath. Two alternative schemes were used for introducing the saline under the fresh water:

   - A baffle was placed at the bottom of one end of the tank behind which saline was introduced;

- Saline was pumped along a pipe which ran along the side of the tank. Four small downward-pointing holes, covered by profiled baffles, allowed the saline to escape under the fresh water.

There was little difference in performance between the two methods. In practise, the thickness of the interface appeared to be controlled by the absolute density difference and the time taken to fill the tank, which is determined by the flow rate. The limit for the flow rate was the onset of shear instability (figure 2.6) at the inlet. The interface tended to diffuse through time, and the rate of diffusion is a strong function of the interface thickness. Thus the interface tended to reach a stable thickness of the order of 20–30mm over the 2–3 hours which were spent filling the tank.

The water was drawn from the saline storage tank by the pump, and the flow was controlled using a metering valve.

3. *Tank draining*—After experiments, the saline solution was drained back into the reservoir, via the same inlet pipe which had been used to fill the tank. The baffles in the flow path created resistance to the flow so that draining took a considerable time. The second pump was employed to speed the process. The fresh water was discarded.

4. *Stratification for linear density profiles*—Some of the experiments were carried out with a linear density profile in part of the water column. For these experiments, it was necessary to be able to vary the salinity of the water being introduced into the tank continuously.

   For this purpose, the second reservoir was filled with fresh water. A system of valves allowed the main pump to draw water from either of the reservoirs, either directly or through two flow meters. The flow in the meters was adjusted differentially during filling, so that a controlled mixture was obtained. Good mixing of the two fluid streams was ensured by the impeller of the pump.

   The method of filling, for these experiments, was to partially fill the experimental tank with saline solution, and bleed a mixture of controlled salinity onto the surface, through a sponge float. By making timed adjustments to the rotameters, a stepped decrease in the density of the saline entering the tank was achieved. These fine steps diffused into a smooth increase in density with depth after a few hours.

   A clear measuring chamber was placed in the pipe before the entry into the experimental tank. The intention was to place a hygrometer in the chamber so

that the density of the fluid could be monitored continuously. It was found that this was not necessary.

The system described above was arrived at after many trials and errors. Alternative methods of managing the stratification in a laboratory tank were considered. Some of the possible variations are listed below.

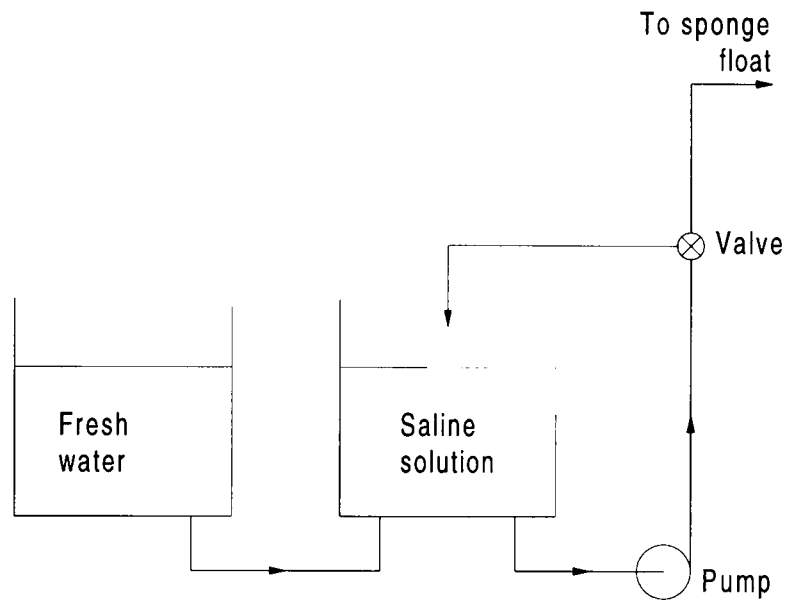


Figure 4.8: *The double bucket method for creating a linear stratification*

- *Double bucket system*—A common means of producing linear stratification in a laboratory tank is the double bucket system, shown in figure 4.8. The first bucket contains saline solution and the second fresh water. A pipe connects the two buckets. Saline solution is drawn from the first bucket by a pump. A small portion of the solution is fed into the laboratory tank via a sponge float, while the rest is fed back into the first bucket. This forced return flow creates turbulent mixing and maintains a uniform density in the first bucket. As the level drops in the first bucket, fresh water flows under gravity from the second bucket. By this means a linear decrease in the concentration of salt over time in the first bucket is obtained. Hence a linear density profile (for small densities) is obtained in the laboratory tank.

  The success of this method in producing linear density profiles depends on the effectiveness of mixing in the first bucket. Unfortunately, the volume of water required was such that a much larger pump would have been required to ensure effective mixing in the reservoir.

- *Tilting tank system*—For the production of two-layer and other profiles, Thorpe (1968a) has used a tilting tank (figure 4.9). The tank is first half filled with saline solution in the vertical position, then fresh water is fed on top of the saline,

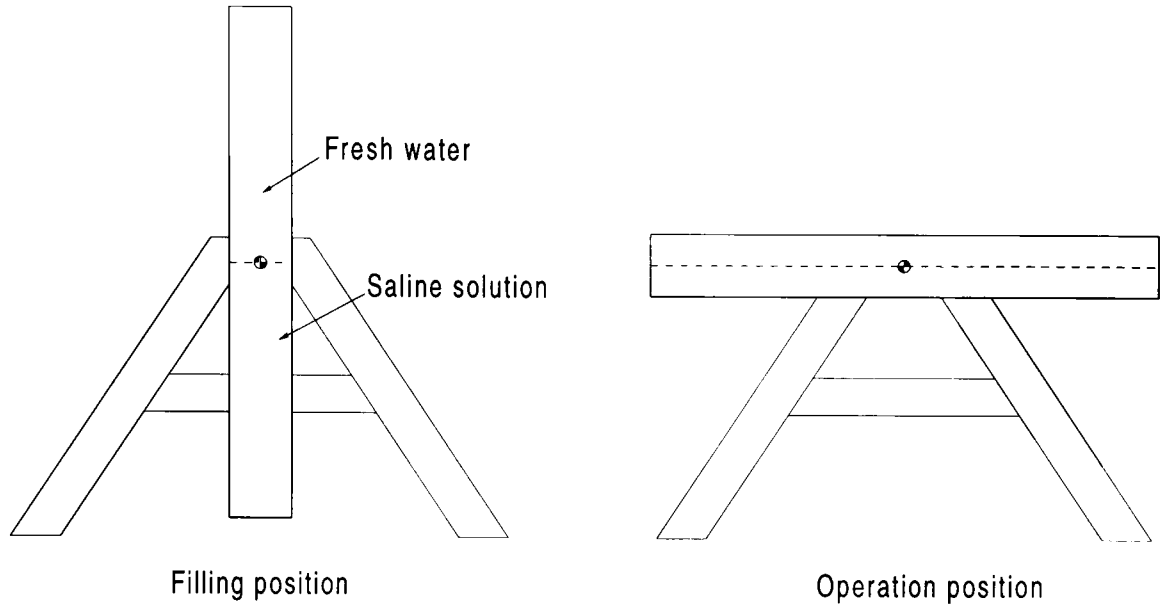


Figure 4.9: *Thorpe's tilting tank method of creating stratification*

creating an interface. When the tank is slowly tilted to the horizontal position, buoyancy forces create a shear flow which results in the two layers stretching out along the length of the tank. The interface between the fluids is stretched by this mechanism and becomes very thin. The tank must be tilted slowly in order to avoid shear instabilities.

Unfortunately, the shear volume of water required for the experiments, coupled with the need for a large number of ancillary devices in or near the flow (wave gauges, density probes, wavemaker, illumination equipment) made the use of a tilting tank almost impossible for these experiments.

- *Computer controlled system*—One idea which was considered at the outset was to replace the two rotameters with solenoid valves, which would then be driven by a computer, to which a density probe could be coupled. By alternately opening and closing the solenoid valves (on a timescale of a few seconds), a mixture of saline and fresh water would be obtained. By controlling the relative open and closed times of the valves, in a manner similar to switched-mode power supplies, the density of the effective mixture could be controlled. It was envisaged that the measuring chamber would act as a "low-pass filter" by smoothing out the high frequency changes in density produced by the alternation of the valves.

  Although such a system would in principle be able to create any density profile in a controlled manner, practical problems prevented it from being implemented. A major difficulty was that low cost solenoid valves required a certain minimum pressure drop (greater than the depth of water in the reservoir) in order for them to open. This was to be supplied by the pump; however, while the flow was blocked the pump would either stall or draw air in through the seals, so that it

would require re-priming before it would draw fluid. In such a situation the valves could not be relied upon to open at the correct time.

If the reservoirs were to be placed above the level of the experimental tank, a gravity feed rather than a pump feed could be used to stratify the tank. In this case solenoid valves could be used and computer control over the density profile would be feasible.

## 4.4 Wave generator

Following from the conclusions of section 4.2, the specification for the wave generator, including the control electronics, computer interface and software, were as follows:

1. The wave generation mechanism was to be the vertical oscillation of a paddle of selectable size and shape.

2. The motion of the paddle was to be controlled by a computer, which would be able to create periodic or non-periodic motions.

3. Oscillation excursions of up to ±100mm, at frequencies up to 1Hz, were required, along with the ability to produce very low frequency motions.

4. The paddle motion was to be sufficiently free from vibration and jerks that no waves other than at the desired frequencies were produced.

5. The control electronics, computer interface and software were to simultaneously perform the tasks of wave generation, data collection and control of ancillary equipment.

6. Safety features should be present in the system which would protect the user, the wave generator itself, and the tank in the event of a malfunction.

7. The overall cost of the wavemaker, including the drive electronics and computer, should be less than £3,000. (The final figure was substantially more than this.)

It was clear from the outset that some form of closed loop control would be needed to produce a paddle oscillation that was sufficiently free from unwanted vibrations and jerks and that followed the desired motion closely. Several points about the selection of closed loop control system are important:

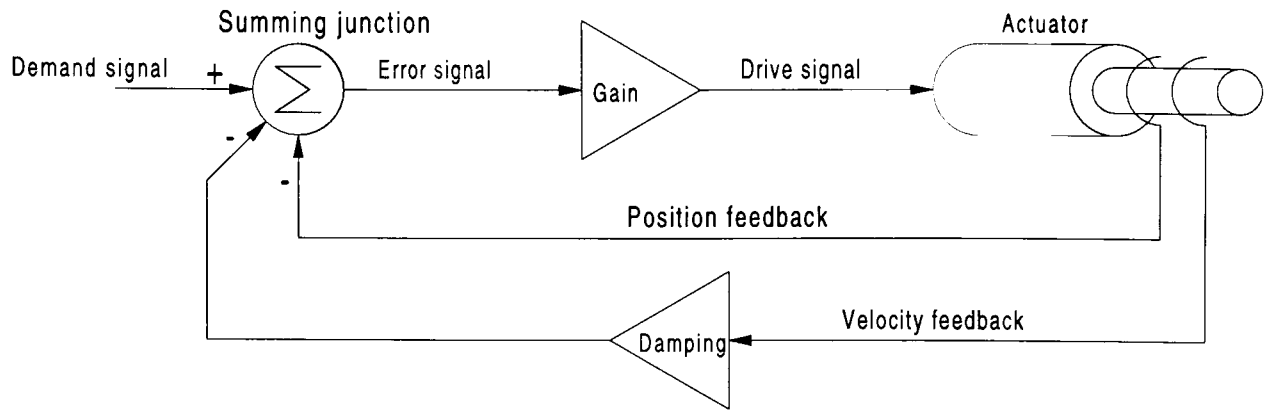


Figure 4.10: *Basic control system schematic*

- *Characteristics of closed-loop control*—Closed loop control systems (figure 4.10) function by measuring a quantity which is to be controlled (e.g., position, force, velocity) and comparing it to a *demand* signal (the required position, force or velocity). The difference (or *error signal*) between the demand and the measured value is multiplied by a *gain* and applied to an actuator (such as an electric motor). The actuator serves to bring the measured variable closer to the demand variable, reducing the error signal. Thus the measurement device provides *negative feedback* which tends to bring the error signal to zero.

  Most control systems control the motion of objects with finite inertia. This gives them a tendency to oscillate about the demand variable, and can lead to instability. The solution is to provide a second feedback signal which is normally a factor of the derivative of the first. Where position is being controlled, the derivative is the velocity, which can be measured using using a tachometer or evaluated electronically. The derivative fraction is known as the *damping factor*.

  A closed loop control system would allow the wavemaker paddle to perform any motion within the bandwidth and physical constraints of the hardware.

- *Position control*—The simplest choice for the controller was to control the paddle position. This is a choice commonly made for surface wavemakers, though it is not always the best one. Position control allows the user to move the paddle in any desired motion. However, no compensation is made for poor matching of the paddle motion to the "correct" motion for the wave at that frequency, other than subsequent adjustments made by the user to the demand signal. Nor is the wavemaker capable of absorbing reflected waves.

- *Force and velocity feedback*—Absorbing wavemakers, described in more detail by Skyner (1992) use a different strategy. An electric motor drives a (surface) wavemaker via a load cell, which measures force. A tachometer measures velocity, which acts as a form of damping (though it is not the derivative of the force).

The use of force feedback allows the wave control system to attempt to absorb incoming reflected waves. This is done by prior measurement of the frequency-dependent characteristic impedance of the water, and adjustment of the control electronics to match the wavemaker's "impedance" (as seen by an incoming wave) to that of the water. None of the wave is then reflected back.

Force feedback was not adopted for the internal wave generator for three reasons:

1. All practical force sensors (piezo-electric, strain etc) suffer from drift, which means that a lower limit must be placed on their operating bandwidth, i.e., their outputs must be high-pass filtered. The minimum operating frequency is adequate for surface gravity waves (frequency range 0.2–2Hz in laboratory tanks), but not for internal waves, whose frequency range could be an order of magnitude lower.

2. The forces on a paddle generating surface waves are strongly dominated by two factors: the *added mass*, which corresponds to the mismatch between the wave motion and the paddle motion, and *added damping* or *radiation impedance*, which corresponds to the energy transferred to the radiated wave. Where no other major component is present, absorbing wavemakers can be made to work reasonably well.

   Calculations of the forces which would be exerted on a paddle generating internal waves (section 4.4.1) showed that the fluid drag on the paddle would be a significant component. Under these circumstances it was felt that force feedback would not function well.

3. Matching the paddle response to the water response is only practical when the water response is constant. With the different stratification and depth conditions which were envisaged in the internal waves tests, the radiation condition of the water would have to be measured before every experimental run.

### 4.4.1 Paddle load

A nominal design bandwidth of 1Hz was desired. The required force on the paddle was estimated based on worst-case assumptions, and the simplification of a cylindrical paddle. Newman (1977) defines three forces which act on a body in waves:

- The drag force $F_d$, which is in phase with the paddle motion, and is defined by

$$F_d = \frac{1}{2} C_d \rho A u |u| \tag{4.2}$$

where $\rho$ is the fluid density, $A$ is the projected area of the body, and $u$ is the body velocity. $C_d$, the drag coefficient, takes a worst-case value of 2.

- The added mass contribution or inertia force, $F_m$, acts 90° out of phase with the body motion. It represents the force required to accelerate a volume of fluid around the body, and is defined by

$$F_m = C_m \rho V \frac{du}{dt} \tag{4.3}$$

where $V$ is the displaced volume of the body, and the added mass coefficient $C_m$ takes on a worst-case value of 2.

- The added damping contribution $F_b$ represents the force required to generate wave energy. It is defined by

$$F_b = C_b u \tag{4.4}$$

Here $C_b$ is a coefficient which depends on the wave frequency, water density and paddle dimensions. It is given in graphical form by Newman (1977) for surface waves. In these conditions the coefficient takes values ranging from about 1–30kg/s. For simplicity, and since a conservative design was sought, the coefficient was used directly. The coefficient for internal waves was expected to be lower.

The force components are summed to produce a total force:

$$F = \sqrt{(F_b + F_d)^2 + F_m^2} \tag{4.5}$$

Figure 4.11 shows the contributions of these forces to the total force at various frequencies. The design force of 40N at 1Hz is marked on the figure. At this frequency, the inertia term dominates.

### 4.4.2 Mechanical design options

The design of the mechanical parts was governed by considerations of stability in the control system. This was due to the fact that the neutrally buoyant paddles (section 4.2)

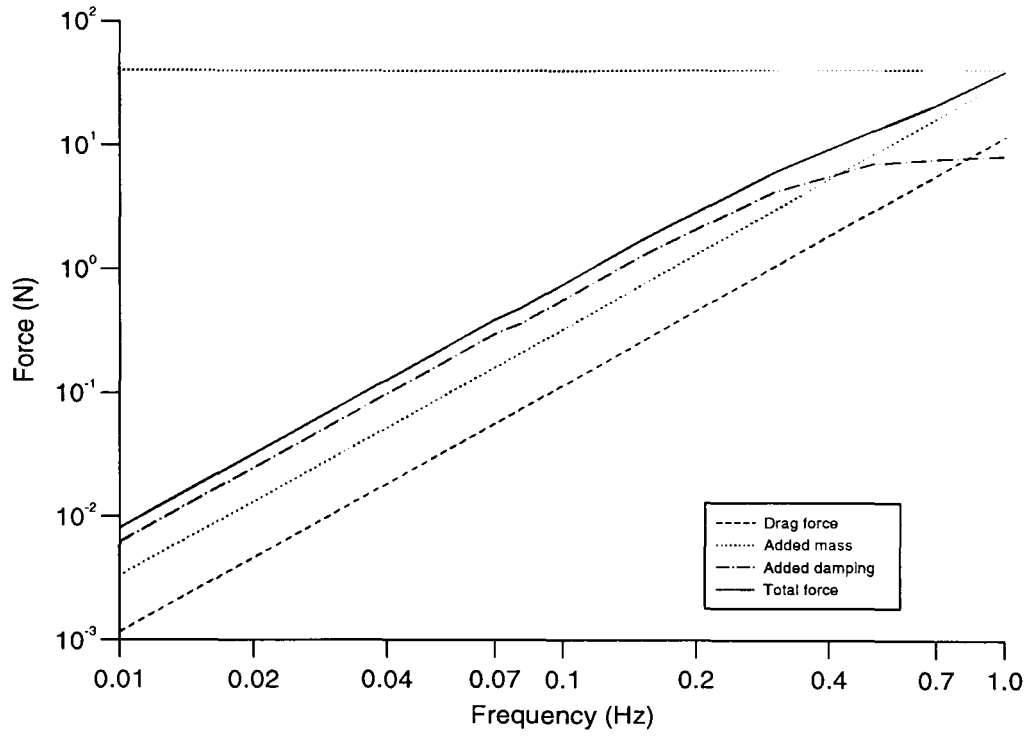


Figure 4.11: *Forces acting on the paddle*

would have high inertias, and so would have to be driven with high gain and high damping. Stiffness in the drive train and in the wavemaker support structure was therefore of the greatest importance.

Other important considerations were lost motion, stiction and kinematics. Lost motion ("play", or "backlash") introduces nonlinearity into the response of a controlled element and can result in violent vibrations. "Stiction" (or starting friction) is a feature of journal bearings and some transmission elements and can have similar results.

The principal kinematic concern was that the drive system should properly constrain the correct number of degrees of freedom. A solid body has six degrees of freedom. One was to be controlled (the paddle motion) and so five had to be constrained. This was done by providing five rigid points of contact, with force components pressing the paddle structure against all five. The lines of action were arranged so that there was no redundancy.

After the preliminary experiments, it was decided that a vertical motion driven by an electric motor would be the best solution. The class of drive system then had to be settled:

- *Linkage drive*—Rotational motions, via the use of linkages, can be used to approximate linear motions. A classical example is James Watt's steam engine linkage.

- *Flexible element transmission*—Toothed belts, V-belts, metal bands and wire rope (Bowden cable) are all commonly used for driving linear motions. For very precise motions metal bands are superior performers.

- *Rack and pinion*—A gear wheel driving a toothed bar is a popular linear drive, although it is principally recommended for very high load situations. Toothed systems suffer from lost motion unless they are preloaded in one direction.

- *Friction drive*—Not commonly chosen because of fear of slipping, a direct friction drive can be a very high stiffness linear solution. Lost motion is entirely absent and stiction is confined to the bearings.

From this list three contenders were selected on the basis of zero lost motion, minimal stiction, stiffness and practicality: metal band drives, wire rope drives and friction drives. Examples of previous uses[2] of each are shown in figure 4.12. The linkage drive was rejected because in order to obtain an adequate approximation to a linear motion long linkage elements would be needed, raising concerns about inertia, stiffness and cost. V-belts and toothed belts were rejected on the basis of low stiffness and high stiction, and concerns about lost motion made rack and pinion drives unacceptable.

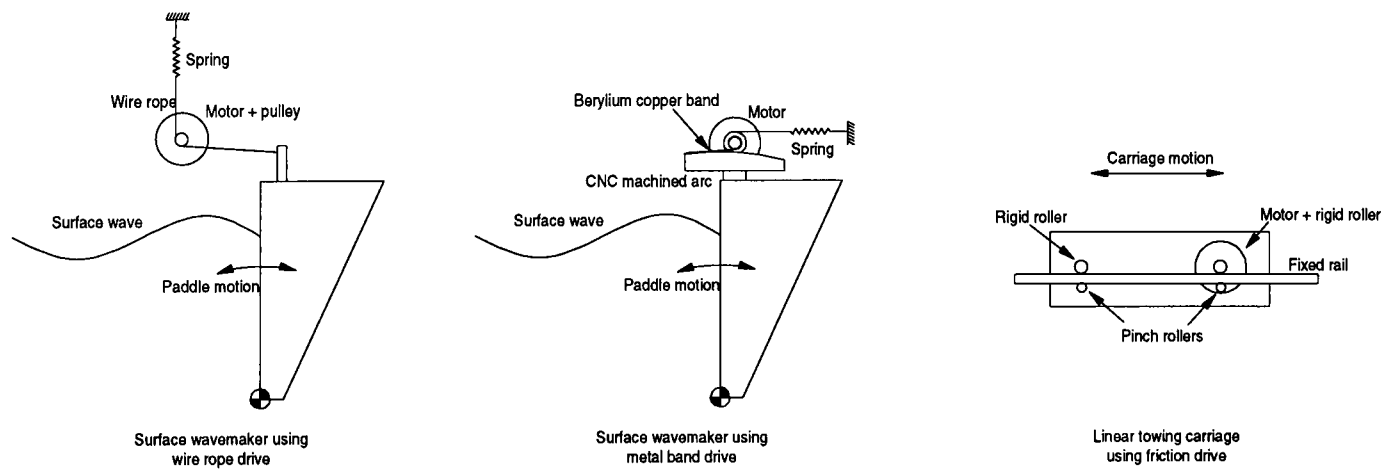


Figure 4.12: *Examples of the use of wire rope, metal band and friction drives*

A wire rope drive can easily be configured as a linear motion device, while a friction drive is better suited to linear motion than to rotation. Metal band drives have been used as linear motion devices, but their greatest advantages are lost. In the rotational situation shown in the figure, the metal band is stretched across an arc of the same radius and centre as the motion being generated. Thus all but a very short length of

[2]All of these uses were developed by the Wave Power Group at the Department of Mechanical Engineering, the University of Edinburgh. The wire rope and metal band wavemakers were developed by Professor Stephen Salter and the friction drive carriage by Dr Richard Yemm.

the band is in contact with a solid object at all times. This serves to dramatically increase the natural frequency of the band, greatly increasing stability. However, as the band cannot be supported in this way in linear motion, this advantage is lost. The metal band thus performs no better than a wire rope.

A wire rope based design was developed, but it became clear that the rope would need to be under be under very high tension to offer stability. Such a high tension would inevitably increase the stiction effects at the pulleys, and would pose a potential hazard.

Faced with this difficulty, it was necessary to investigate the practicality of a friction drive. The calculations are given in section 4.4.3. It was found that the implementation of the friction drive would be straightforward.

### 4.4.3 Friction drive design

An assembly drawings of the friction drive system designed is given in figure 4.13. The details of the design borrowed heavily from an existing towing carriage designed and built in the department (Yemm, 1995).

The paddle forms the bottom of a square frame, whose motion is constrained in all degrees of freedom except vertical translation. The frame sides are vertical rods and the frame is completed at the top by a crossbar. The friction drive roller is connected to the motor shaft and bears directly onto one of the vertical rods. The friction at the contact point between these two elements drives the paddle in a vertical motion.

The choice of materials in contact at the friction point was determined by the following factors:

- *Coefficient of friction*—this had to be sufficiently high that the required force could be applied to the paddle;
- *Stress concentrations*—the Hertzian stress at the contact point was a function of the elastic moduli of the materials; stiffer materials exhibiting higher contact stresses;
- *Corrosion*—The use of metals in submerged parts of the wavemaker would be acceptable only where corrosion protection or corrosion resistance could be guaranteed;

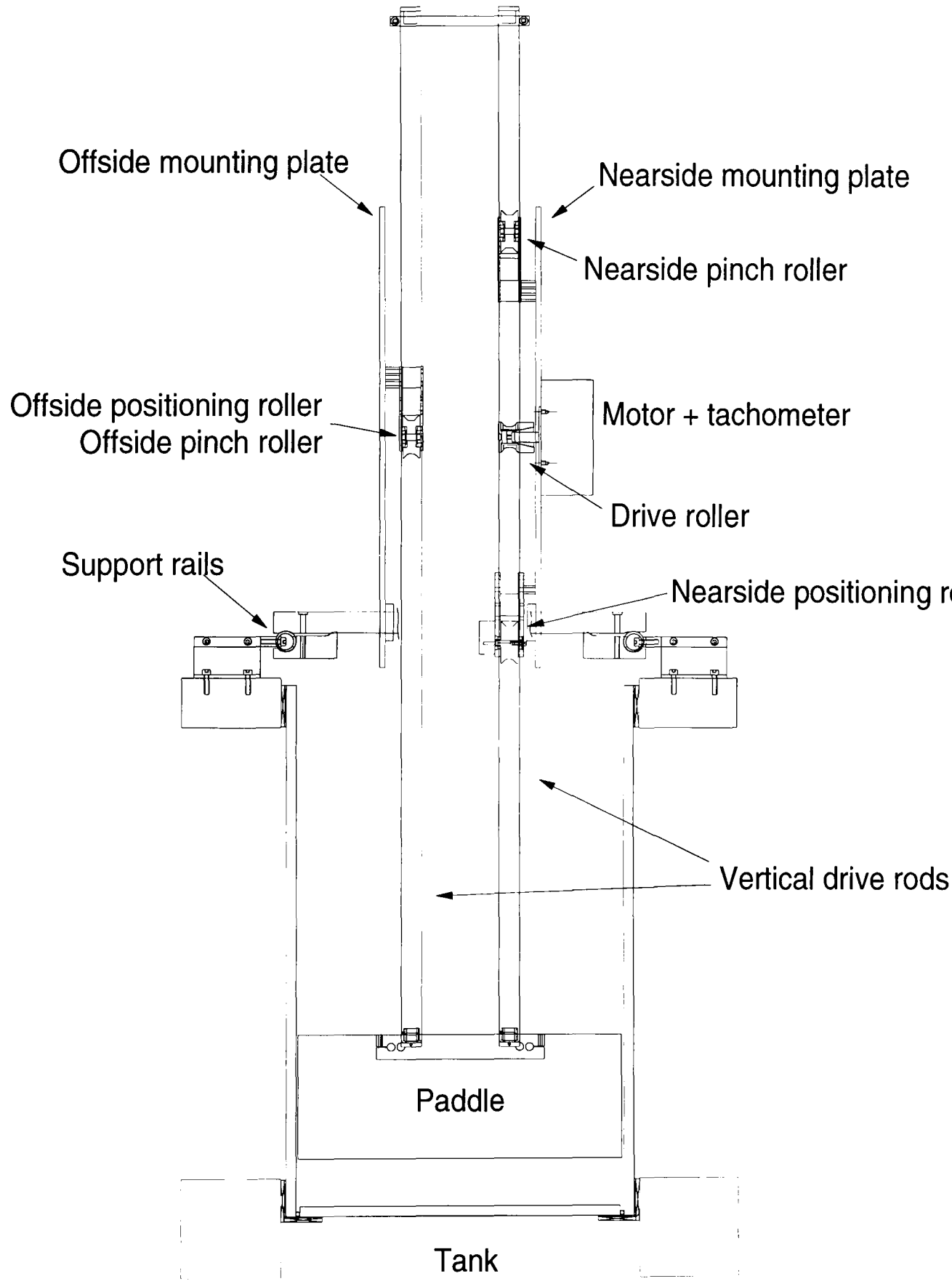


Figure 4.13: *Simplified end view of the friction drive system*

| Material combination | Surface condition | Friction coefficient |
|---|---|---|
| Metal-metal | Unlubricated, not cleaned | 0.2–0.4 |
| Nonmetal-nonmetal | Unlubricated | 0.4–0.9 |
| Metal–nonmetal | Unlubricated | 0.4–0.6 |
| Aluminium-mild steel | Clean | 0.5 |
| Most polymers-mild steel | Clean | 0.5 |
| General surface | Thick lubricating film | 0.1-0.5 |

Table 4.3: *Friction coefficients for various combinations of materials (Crandall et al., 1978; Neale, 1973)*

- *Stiffness and inertia*—it was desirable that the inertia of the moving parts be as low as possible, although the system inertia would most probably be governed by the paddle. On the other hand, the stiffness of the vertical rods would be of importance in governing the bandwidth of the wavemaker.

The friction coefficients for various combinations of materials are listed in table 4.3. It was assumed that the surfaces would be free of oil or grease but would not always be "clean". Therefore, for metal-metal contacts a safe friction factor of 0.2 was chosen, while for contacts involving one or two nonmetals, a friction factor of 0.4 was used.

The load predictions discussed in section 4.4.1 gave a design drive force of 40N. Using a V-roller design (figure 4.16), two contact points were obtained, halving the normal force required. For metal-metal contacts, the force per contact point was 100N, while for metal-nonmetal or nonmetal-nonmetal it was 50N. However, the compressive contact stresses were basically governed by the elastic moduli of the two materials (Roark, 1989, table 33, case 3). Variation of stress with load went by a power of 1/3. Reaction forces at the nearside positioning and nearside pinch rollers (figure 4.15) were half the force at the drive roller (by static equilibrium).

Relevant material properties are given in table 4.4. The resultant compressive contact stresses are listed in table 4.5. These calculations, compared against the material properties, can only be regarded as giving a first approximation of likelihood of failure. The calculated contact stresses are compressive and are being compared against the tensile strengths of anisotropic materials. Furthermore, the damage stress at a Hertzian contact point may be much greater than the elastic limit, since the stress is highly localised (Roark, 1989).

| Material | Tensile strength | Young's modulus | Density | Corrosion | Machinability |
|---|---|---|---|---|---|
| Anodised HE30 aluminium alloy | 600MPa | 70GPa | 2800kg/m$^3$ | Corrodes | Excellent |
| Stainless steel 304 | 600MPa | 216GPa | 7930kg/m$^3$ | May corrode | Good |
| Stainless steel 316 | 600MPa | 216GPa | 7930kg/m$^3$ | Resists | Poor |
| Carbon fibre/ epoxy rod (strong direction) | 450MPa | 17GPa | 1600kg/m$^3$ | Resists | n/a |
| Carbon fibre/ epoxy rod (weak direction) | 170MPa | 11GPa | 1600kg/m$^3$ | Resists | n/a |
| Acrylic | 60MPa | 3GPa | 1190kg/m$^3$ | Resists | Good |

Table 4.4: *Properties of the materials considered for the friction drive*

| Drive rod material | Roller material | Load | Contact stress |
|---|---|---|---|
| Stainless steel | Aluminium alloy | 100N | 470MPa |
| Stainless steel | Aluminium alloy | 50N | 380MPa |
| Carbon fibre | Aluminium alloy | 50N | 120MPa |
| Carbon fibre | Aluminium alloy | 25N | 94MPa |
| Carbon fibre | Acrylic | 50N | 47MPa |
| Carbon fibre | Acrylic | 25N | 38MPa |

Table 4.5: *Contact stresses for the various roller/drive rod material pairs considered*

In the end pragmatism played a deciding role in material choice. Corrosion resistant 316 grade stainless steel was expensive and difficult to machine. HE30 aluminium alloy would certainly have corroded severely, even after anodising. On the other hand, carbon fibre reinforced epoxy rods were available in convenient lengths (requiring no machining), and combined high stiffness with very low density. Further, with one non-metal in the drive train the lower contact force (50N) could be used at the drive roller.

The roller material was a choice between aluminium alloy and a polymer, e.g., acrylic. On the nearside pinch and nearside positioning rollers, the contact stress was sufficiently low to allow the use of aluminium rollers. The higher stress at the drive roller raised doubts about the durability of the carbon fibre rods. However, if a low modulus material such as acrylic were used, concern would be raised over the durability of the acrylic. Furthermore, if slip were to occur at the drive roller damage to the drive rods might be more severe if a harder material were used.

It was decided that replacement of the drive rods would be more inconvenient than replacement of segments of the drive roller. A "sandwich" drive roller was designed which had replaceable acrylic contact pieces, and is shown in figure 4.14. It was intended that if the contact pieces failed they could be replaced with a different polymer (Nylon, PVC) or with aluminium.

In retrospect, the inhomogeneity of the carbon fibre rods exerted a great influence over performance. At the aluminium alloy rollers, the rods tended to polish the rollers, presumably by the action of the hard fibres. The acrylic drive roller was sufficiently durable until slip occurred, as it did several times during testing. On slip, the acrylic wore quickly, and debris began to eat into the epoxy base of the rods as well as the acrylic itself. However, in normal operation, the drive proved more than capable of performing to specification without slip.

### 4.4.4 Drive motion kinematics and wavemaker mounting

Kinematic location of the drive rod assembly was considered essential in ensuring good performance. This location method ensures that the position of a solid body is fixed by a single rigid point of contact for each degree of freedom which is to be constrained. Forces are applied which keep the solid body in contact with the contact points. The members which apply the forces play no role in constraining the solid body, therefore they must have a degree of flexibility.

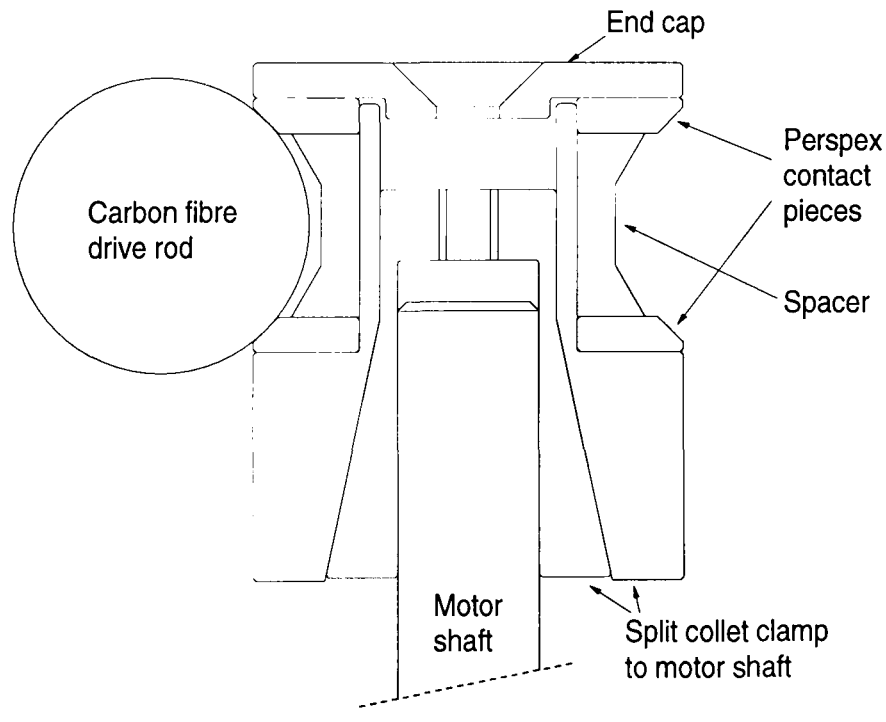


Figure 4.14: *Design of the drive roller*

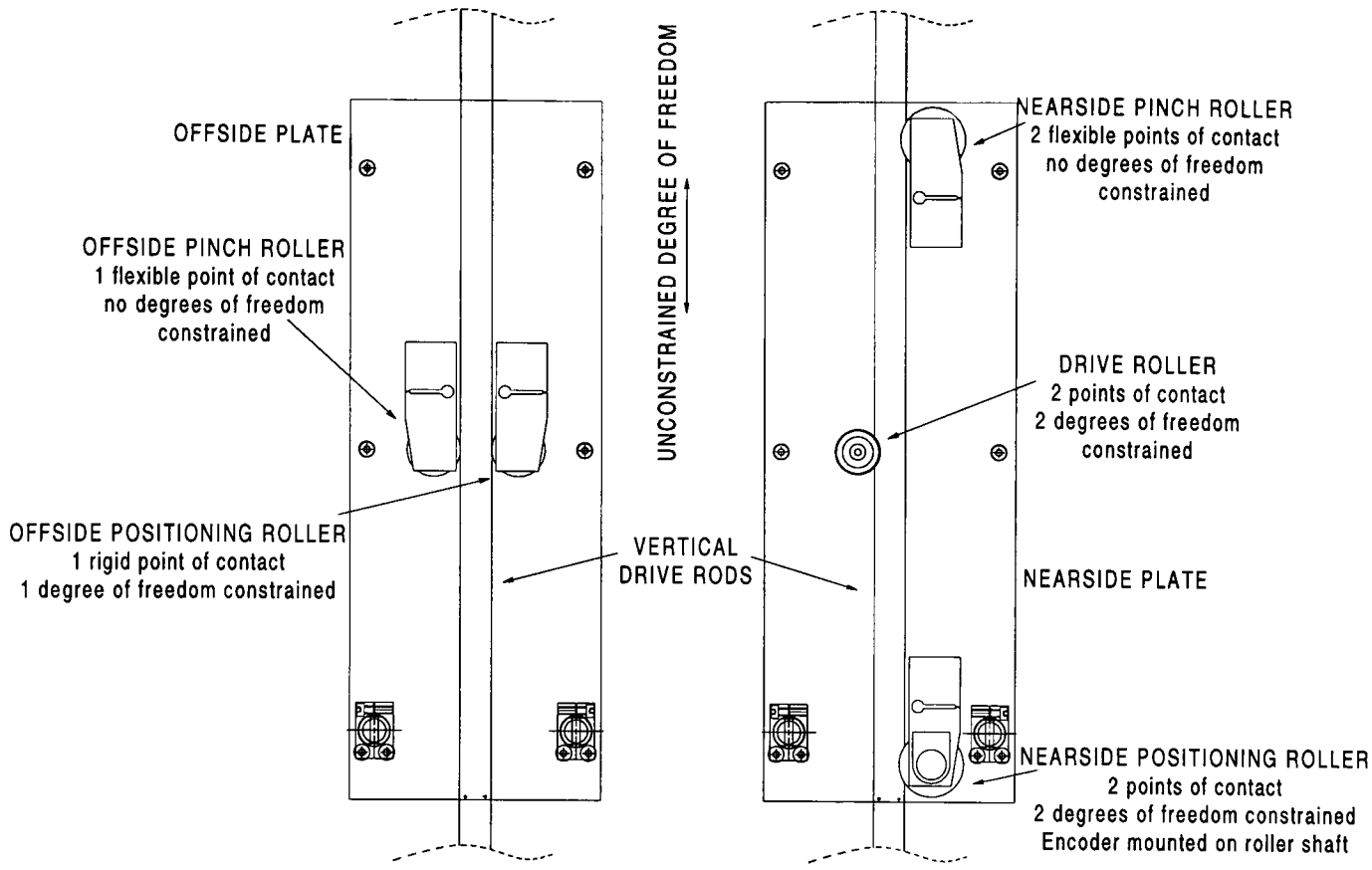


Figure 4.15: *"Open sandwich" view of the arrangement of the pinch and kinematic positioning rollers on the two side plates*

Figure 4.15 shows the scheme which was adopted. Here, "flexible" points of contact refer to the points through which the constraining forces are applied. The two pinch rollers each have as many degrees of flexibility as they do contact points, and so play no role in locating the drive rod assembly.

The different rollers, which are virtually identical to those designed by Yemm (1995), are shown on figure 4.16. The drive roller and the nearside positioning roller are both V-rollers, each with two points of contact. Neither exhibit any axial play (preloaded bearings were employed in the nearside positioning roller) or transverse flexibility, although the transverse position of the nearside positioning roller is adjustable. The nearside pinch roller is also a V-roller, but it possesses axial play and transverse flexibility (it is pressed against the drive rod by a spring) and so applies only a force to press the rod against the nearside positioning roller and the drive roller. A V-roller is used to reduce the contact stress.

The four degrees constrained by the nearside plate are: pitch and roll rotations of the paddle, and cross-tank ($y$, sway) and along-tank ($x$, surge) translations. Yaw rotation is constrained by the offside positioning roller, a flat roller which acts on the offside

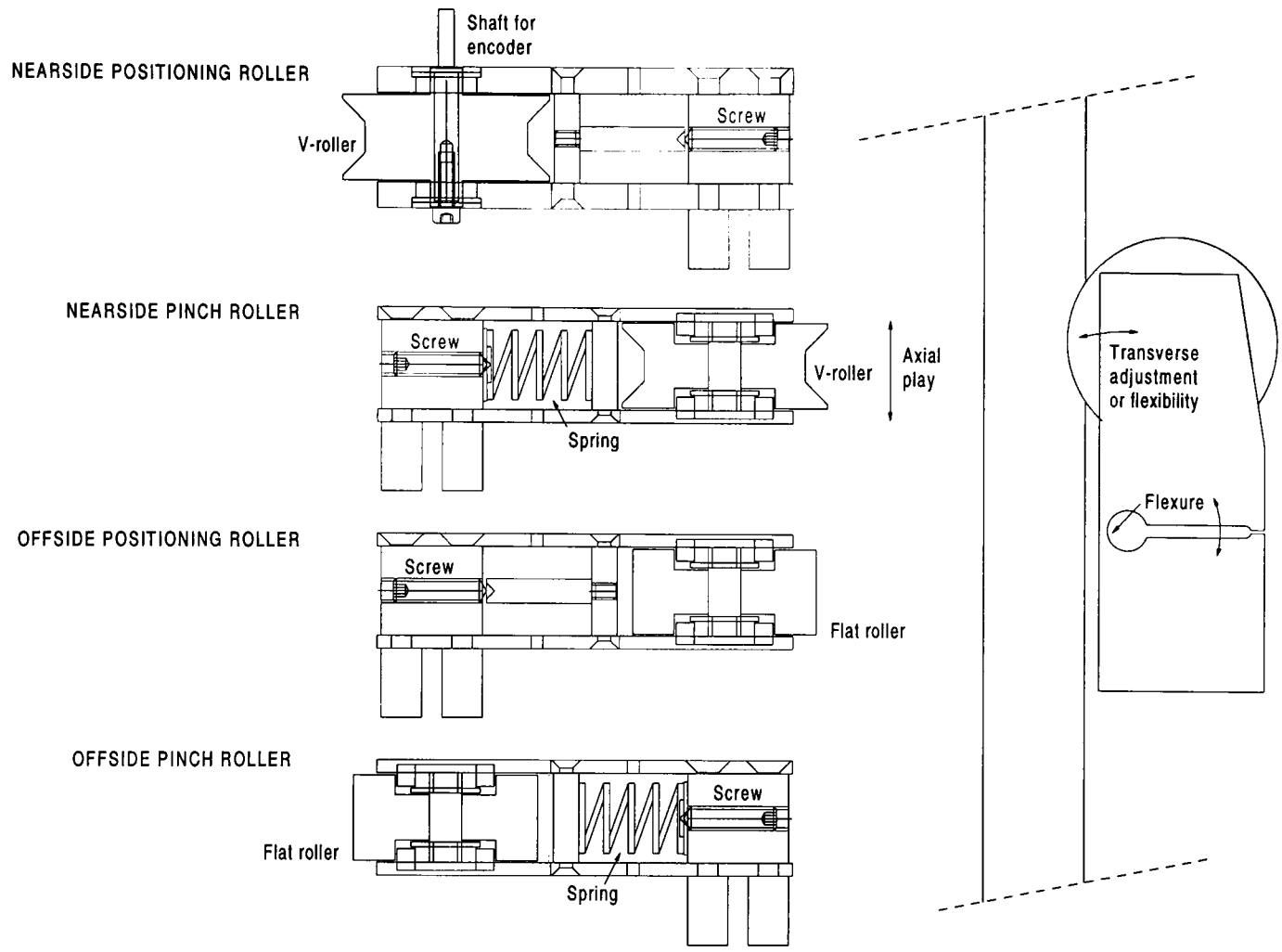


Figure 4.16: *Positioning and pinch rollers*

drive rod. The offside pinch roller, also flat, applies a force to press the offside drive rod against the offside positioning roller.

The positioning rollers possess a small degree of transverse adjustability. A flexure allows the roller to hinge towards the drive rod, and a screw is used to make this movement. The pinch rollers have a similar structure, but a spring in front of the screw is used to attain adjustment of force rather than adjustment of position. The position of the drive roller on the shaft is adjustable by loosening the split collet and sliding it along the shaft. The three adjustments allow the three paddle rotations (pitch, roll and yaw) to be set finely.

Figure 4.13 shows the mounting of the wavemaker frame onto the tank. Rails made of 1" stainless steel tubes run along the length of the tank and allow the wavemaker and any other equipment at any point along the tank. Two mounting tubes straddle the tank and the wavemaker side plates are fastened to these. The remaining adjustments (in $x$ and $y$) are made by moving the mounting tubes relative to the rails and to the wavemaker respectively. In the figure, the transverse cylinders which clamp together

the offside and nearside plates are omitted for clarity, and the mounting tubes are shown cut away.

After the wavemaker had been constructed, its frequency response was assessed. Figure 4.17 shows the result. It is seen that the 1Hz specification is met. At about 10Hz an instability is seen; this corresponds to pitch vibration in the paddle. There was no excitation source for this mode during the experiments, and it was not observed.

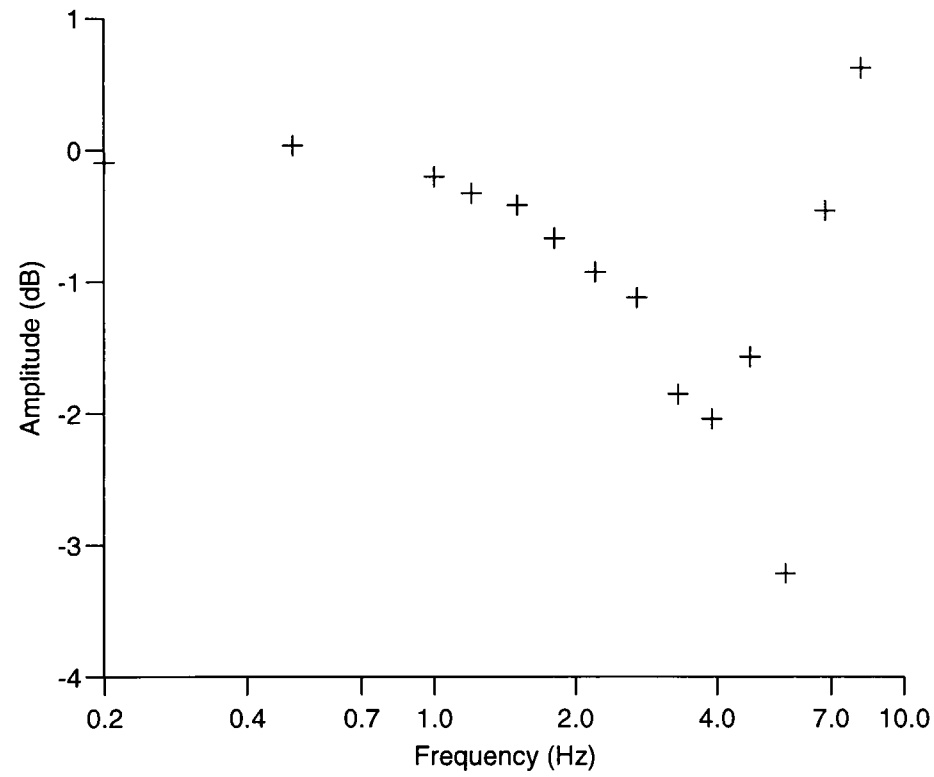


Figure 4.17: *Amplitude response of the wavemaker in fresh water with the large paddle*

## 4.5 Computer control and data collection system

A control system of the type shown in figure 4.10 was implemented using a mixture of electronic hardware and computer software. Hardware and software for data collection were implemented in combination with this. The goals for the whole system were as follows:

- *Control system*

  - The drive was obviously capable of damaging itself or the tank or injuring the operator. It was therefore necessary to build safety and self-protection features into the drive.
  - It was planned to use several different paddle shapes during the experiments. Since the gain and damping parameters of the control system might be different for each paddle, it was considered desirable to make setting of these parameters as easy as possible.
  - The possibility of using the control system to control a completely different drive (such as a towing carriage) was considered. This again suggested that setting of the parameters should be straightforward.
  - It was important that the system be usable without the computer, so that (e.g.) during testing the drive could be run from a signal generator or other signal source, while during experiments the signal could be produced by the computer.

- *Data collection system*

  - Multiple channels of data (from several wave height gauges and/or density probes) were to be read into the computer during experiments.
  - The offset and gain of each signal was to be adjustable.
  - Diagnostic information about the paddle motion was to be available alongside the wave height gauges.

- *Computer and software*

  - The system was to be controlled by a standard IBM compatible PC.
  - The program was required to play out a choice of either a sinusoidal signal or a pre-prepared time series.
  - Simultaneous with the signal generation, the program was required to read and store the information from the various analogue input channels.
  - The whole system was to be as extensible as possible, to allow both for unforeseen requirements and future projects.

### 4.5.1 Control and data acquisition hardware

Figure 4.18 is a simplified block diagram of the system which was constructed for the task. A more complete block diagram, showing the internal workings of the devices, is shown in in figure A.6. The roles of the various items shown are as follows.

1. The **computer** housed the two interface cards and was used to compile and run the software which performed control and data collection. A network connection (installed later in the project) allowed transfer of data files to other machines.

2. Two **input-output** cards were purchased for the PC. The first was a PCL-812PG, which was connected to the Edinburgh Designs interface box. This card contained:

   - 2 × 12-bit analogue outputs;
   - 16 × 12-bit analogue inputs;
   - 16 digital outputs;
   - 16 digital inputs;
   - one programmable timer.

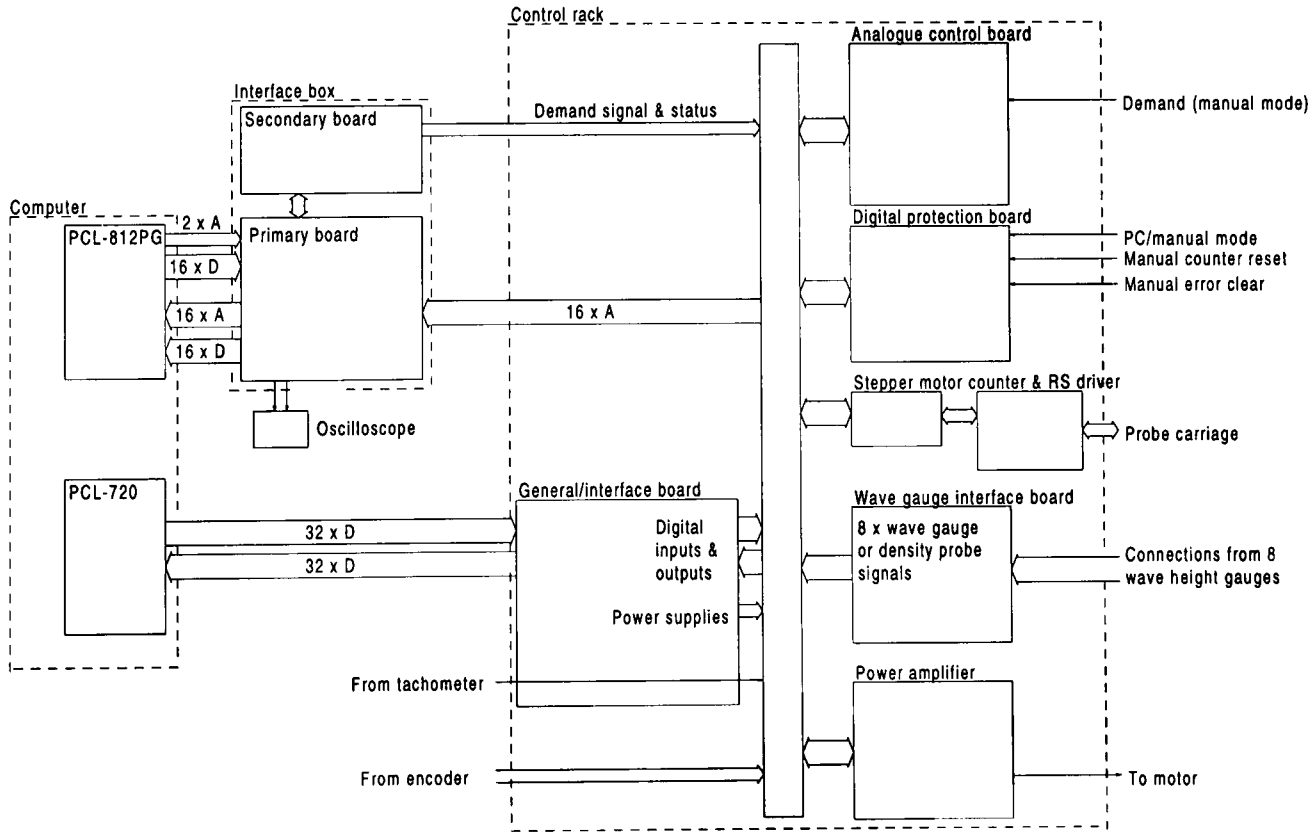


Figure 4.18: *Simplified block diagram of the control and data collection electronics*

The second card, a PCL-720, was connected to the general interface board within the control rack. The card contained:

- 32 digital outputs;
- 32 digital inputs;
- 3 programmable timers.

3. An Edinburgh Designs **interface box**, intended for interfacing with surface wavemakers, was purchased. The PCL-812PG card was connected directly to this box. The box contained two circuit boards: a primary board and a secondary board. The secondary board was responsible for conditioning of the signal which was played out to the wavemaker. The communication channels were connected to the primary board and were used as follows:

   - One of the two analogue output channels was passed to the secondary board for playing out through the wavemaker.
   - Sixteen analogue inputs were received at the back panel of the interface box and passed to the PCL-812PG card via filters. The control rack reserved the first four analogue inputs for reporting the state of the wavemaker.
   - The digital outputs were used to switch and scale the analogue output. The analogue output amplitude could be controlled from 0% to 255% of the signal value, by placing the relevant 8-bit binary number on the output channels.
   - The digital inputs were used to monitor the state of the output circuitry on the secondary card.
   - The programmable timer on the PCL-812PG card was used by the control program to synchronise and pace the experiment.

4. A **control rack** was designed and constructed to drive the wavemaker and receive the various inputs. A Eurorack system with a part-width backplane was used.

   In total, six boards were used in the rack. Five of these were plugged into the backplane: a general power/interface board, an analogue control board, a digital protection board, a wave height gauge data collection board, and a stepper motor drive board. The remaining board was the power amplifier, which could not be connected directly to the backplane.

5. The **general power/interface board** had three functions: to connect the digital inputs and outputs provided by the PCL-720 card to the backplane in a safe manner (using tri-state buffers); to distribute power at low (regulated) voltage to

the other boards on the backplane, and to connect the output of the tachometer to the backplane. A schematic for this board is shown in figure A.5 in the appendix.

6. A block diagram of the **analogue control board** is seen in figure A.6. This board communicates almost entirely via the backplane. The schematic is shown in figure A.3 in the appendix. The role of this board is to take the position demand signal from the computer or the front panel, combine it with the measured position of the paddle and the measured velocity of the paddle, and create a drive signal for the power amplifier.

   There are two control loops available on this board. One of the loops is used when the computer is running; it takes its demand signal from the computer and has gain and damping parameters set by software. The other loop, used when the computer is not running, takes its demand signal from the front panel, and has gain and damping parameters set there as well.

   Signals from the rotary position encoder on the wavemaker are decoded and used to generate the position signal. The tachometer output (velocity signal) enters the backplane via the power/interface board.

   For the computer control loop, two digital-to-analogue converters (DACs) in multiplication mode set the "gain" and "damping" control parameters, which are obtained through the digital outputs from the PCL-720 card. For the stand-alone loop (without the computer), front-panel trimming potentiometers are used to set the gain and damping parameters. There are two summing junctions to create the two error signals. The required error signal is selected by a digitally-operated analogue switch.

   Whichever signal is selected is passed through a filter (to make the system stable and remove noise) and a final fixed gain stage, and is then placed once more on the backplane. This drive signal is connected directly to the power amplifier.

7. A schematic of the **digital protection board** is shown in figure A.4 in the appendix. A block diagram of this board is given in figure A.6. This board communicates via the backplane, and with the user via front-panel switches.

   The function of this board is to prevent the paddle from operating accidentally or when a fault is present, and to deactivate the paddle should a fault occur. The board recognises two modes of operation: PC mode and manual mode, which are selected by the user on a front panel switch. In PC mode, the computer is responsible for resetting the counter, clearing error conditions, activating the paddle and setting gain and damping parameters. In manual mode, the front

panel switches, adjustments and connections perform these functions, and the output of the computer is ignored.

The digital protection board guards against a number of possible faults. These are:

- *Out of range*, detected by an optical switch which operates if the paddle is too high or low in the tank;
- *Interlock*, which is a series circuit incorporating panic buttons on the front panel and on the wavemaker;
- *Amplifier error*, the self-diagnostic feature of the power amplifier;
- *Kill*, a panic button on the interface box;
- *Power-up delay*, a circuit which prevents the system from entering an unsafe state accidentally at switch-on;
- *Watchdog*, a circuit which detects a software crash on the computer (this line is ignored if the system is in manual mode);
- *Over speed*, a circuit which compares the velocity signal to a preset maximum velocity;
- *Slip*, a circuit which detects differences between the measured velocity to the derivative of the measured position signal.

All of the error signals are combined so that the power amplifier cannot be enabled if any error condition is present, and so that should any error condition appear, the power amplifier will be disabled. In addition, the circuit only permits enabling of the amplifier if the "drive" signal being applied to the power amplifier input is below a preset level.

Electrical noise was a serious problem for the digital circuit, causing false triggering at all points which were connected to the outside world. The main noise source was the power amplifier, and the noise was fed into the circuit both directly and via the tachometer (which being attached to the motor shaft was able to pick up noise from the amplifier).

By interfacing the tachometer to the rest of the circuit using the differencing amplifier shown in figure A.5, noise from the tachometer was reduced. Direct transmission of noise was reduced by careful implementation of shielding and grounding procedures (Horowitz & Hill, 1989). The sensitivity of the digital board to noise was reduced by replacing the standard 74LS family of TTL logic chips with the more modern 74HC and 74HCT families.

8. The **power amplifier** was a Euroamp/8 servo amplifier purchased from Printed Motors Ltd., the manufacturers of the motor. The amplifier had the following features:

   - 10A maximum continuous drive current;
   - Switched-mode current drive (52kHz switching frequency);
   - Self-protect circuits;
   - Enable and error lines.

   Switched mode amplifiers are more efficient than linear amplifiers. However, since they operate by switching high currents at high frequencies into an inductive load, they generate significant electrical noise. This was the main noise source affecting the other circuits. Aside from the measures described above, the generated noise was reduced by fitting an extra choke to the amplifier board.

   Once all of the noise reduction measures described had been implemented, the system functioned reliably.

9. Measurements were made via a **wave height gauge interface board**. A schematic of this board is shown in figure A.2. Up to eight wave height gauges (or aspirating density probes) could be connected to front panel sockets, which also supplied power to the wave gauge driver boards. Each of the eight inputs corresponded to one analogue input to the PC. Since the first four analogue inputs (numbers 0–3) were reserved for wavemaker diagnostics, channels 4–11 were connected to this board. The final four channels (12–15) were reserved for future expansion.

   As described in section 4.6.2, the wave gauges had two outputs, described as "clean" and "dirty". The former produced a filtered, self-zeroing signal while the latter still required demodulation.

   Two signal paths through the gauge interface board were provided for each analogue input channel, as seen in figure A.6. The first was connected to the "clean" output of the wave gauge, and passed the signal directly to the appropriate analogue input channel. The second was connected to the "dirty" output, and performed rectification and filtering, as well as providing adjustable offset and gain, before passing the signal to the analogue input channel. The desired signal for each channel was selected using switches on the gauge interface board.

10. The **stepper motor drive board** was used to drive the density probe vertically through the water for taking density profiles. A schematic of the system is shown in figure A.7. The driver/position counter makes use of a proprietary (RS) stepper

driver to provide current drive for the motor phases. Additional electronics sets the frequency of the internal oscillator on the RS driver, and measures the position of the probe by inference from the clock and direction signals.

### 4.5.2 Control software

A software kernel for the wavemaker drive program was written, in the form of a C++ library, by Mr Peter Woodhead. Making use of the features of this library, the kernel was extended by the author to include all of the features required for control and data collection.

C++ header files, giving synopses of the contents of the library written by Mr Woodhead, are included in appendix B.1. Header files for the extensions to the software kernel are included in appendix B.2. Appendix B.3 contains the source code for the experiment driver program `exrun`. A brief set of instructions for extending the software kernel was written at the time for the benefit of future users of the library; it is included in appendix B.4.

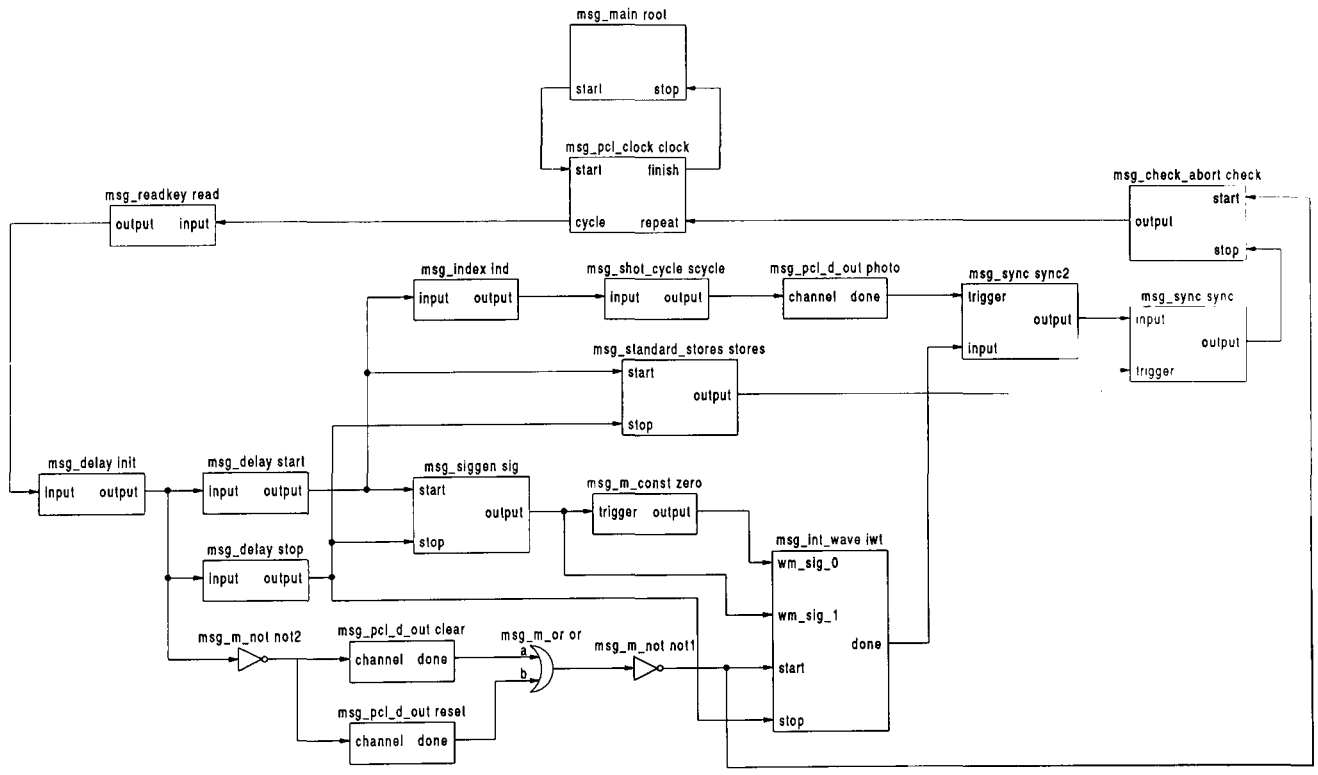


Figure 4.19: *Block diagram of the message-passing part of the program* `exrun`. *The program is shown in sine wave mode, with camera triggering at fixed times.*

The software follows a message-passing paradigm, making use of the object-oriented features of the C++ language. This makes it possible to design control systems as

circuits of interconnected blocks, each of which performs one or other simple task. A block diagram for the program **exrun** is shown in figure 4.19. The functions of the important parts of the system are as follows.

- The message-passing process commences with **root** which is a block of type **msg_main**. During operation, **clock** starts new cycles at a frequency determined by the user, and passes control back to **root** when the experiment is over, at which point the process terminates.

- Key presses are read and stored by the **msg_readkey** block **read**. This allows other blocks to check for keyboard input.

- Timing of events is governed by the three **msg_delay** delay generators **init**, **start** and **stop**. **init** resets the position counter (through the digital output **reset**) and attempts to clear any errors (through **clear**) at the start of the experiment. **start** starts signal generation and **stop** times the end of the experiment.

- A sine wave generated by the **msg_siggen** signal generator **sig** is played out to the wavemaker through the tank control block **iwt**. This block, which is of type **msg_int_wave**, sends most of the necessary digital and analogue outputs to the control hardware, including the position demand signal and the "watchdog" safety signal.

- Data storage is accomplished by **stores**, which is a compound block of type **msg_standard_stores**. This block is set up beforehand to read data from a number of analogue inputs at a preset subdivision of the **clock** frequency, and store the data in arrays.

- The camera is triggered by the blocks **ind**, **scycle** and **photo**. The first of these is of type **msg_index**, which counts cycles and outputs the current cycle number. The second, of type **msg_shot_cycle**, is preloaded with a list of cycle numbers on which photographs are to be taken. The last is a digital output which is connected to the camera via the image shifter.

- Finally, a compound block **check**, of type **msg_check_abort**, monitors the status of the tank and checks the keys read by **read**. If an error occurs, or if the **escape** key is pressed, this block terminates the process.

The whole program **exrun** allows variations on this circuit, such as to play a time series to the output instead of a sine wave, or to trigger the camera in response to particular

events such as phases of the wave. The form shown was used for all of the experiments described in this study.

Software to measure density profiles and calibrate the wave gauges was written using the same building blocks as the experiment driver program **exrun**.

## 4.6 Wave height gauges

In surface waves, the definition of "wave shape" is the vertical deflection of the free surface. For waves propagating along a discontinuity between two immiscible fluids (interfacial waves), the wave shape can be defined as the deflection of the surface of discontinuity. A similar definition of wave shape for true internal waves, where there is no discontinuity but rather the density varies continuously with depth, might be the shape of that isopycnal which is most deflected by the passage of the wave.

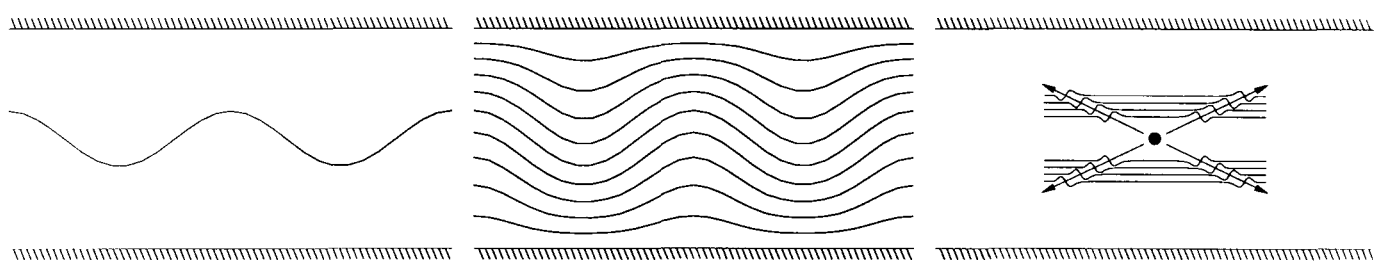


Figure 4.20: *Forms of internal wave shape*

The appropriateness of this definition depends on the particular stratification and excitation conditions, as shown in figure 4.20. In case (a), the variation in density is confined to a thin pycnocline. Here the wave behaves in a manner similar to interfacial waves, and this definition of wave shape is a useful one. In case (b), the stratification is linear, but motions associated with the wave are present throughout the fluid domain (Turner's (1973) "modes" case). Here again the definition appears to be useful. In case (c) waves are generated from a point source in a linearly stratified fluid (Turner's "rays" case). Here the "wave shape" as defined above is ambiguous.

### 4.6.1 Options for a wave height gauge

All of the experiments conducted fall (approximately) into categories (a) or (b), the majority being of the near-two-layer type (a). Hence it was thought that a useful

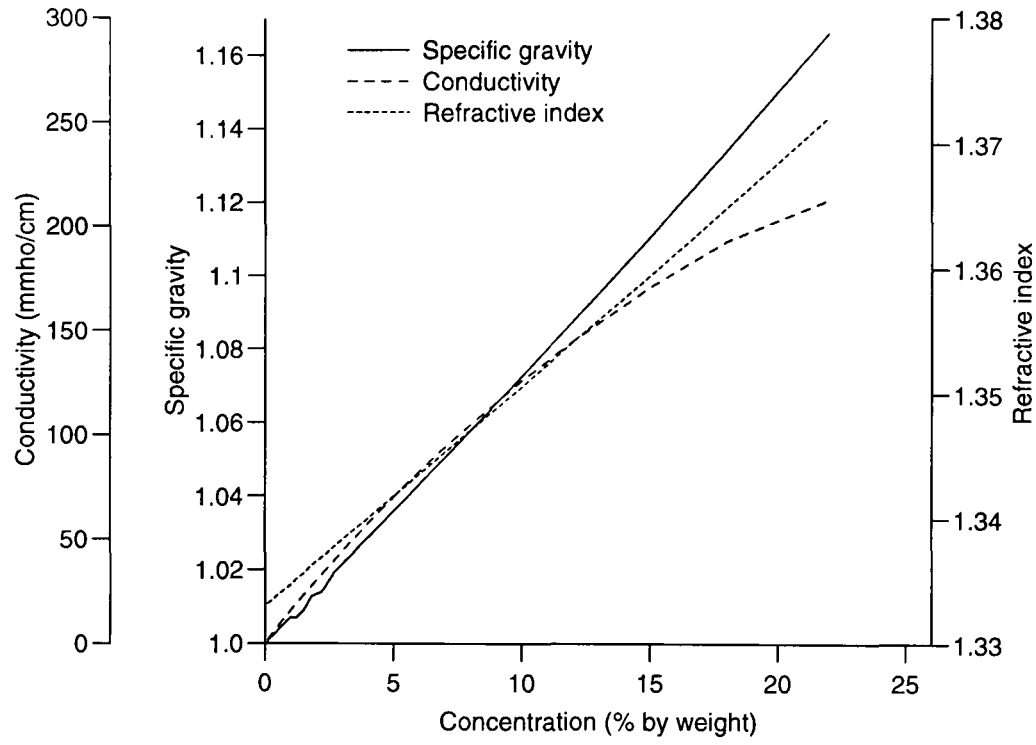


Figure 4.21: *Characteristics of aqueous sodium chloride solution (Lide, 1993)*

measure of the wave shape would be the elevation of the lower (saline) layer as the wave passed. Three properties of the saline solution appeared to offer possible means of measuring its elevation:

1. The electrical conductivity of aqueous sodium chloride solution with a density of $1100 kgm^{-3}$ is many orders of magnitude greater than that of notionally "fresh" water (filtered but not deionised tap water). Changes in the electrical impedance of a fixed section of the fluid would provide a measure of the internal wave shape.

2. The refractive index of saline solution is a known function of salt concentration (with a similar form to its density and conductivity, as shown in figure 4.21). The difference in refractive index between the fresh and salty water could be used to

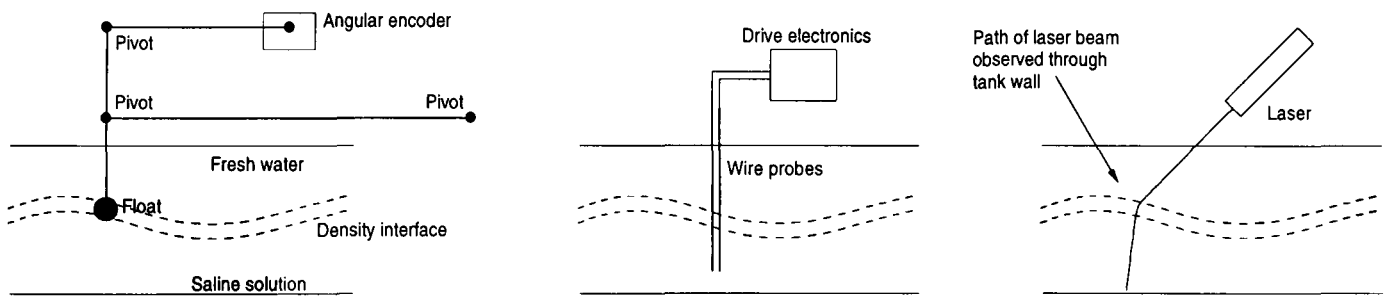


Figure 4.22: *Sketches of some possible wave height gauges*

deflect a laser beam. Some optical detection of the path of the laser beam could allow back-calculation of the form of the stratification at an instant in time.

3. The buoyancy forces exerted on an object placed in the flow would change as the saline solution rose and fell. If the object were neutrally buoyant and allowed to rise and fall with the wave, its motion would be a measure of the wave shape.

The first option is analogous to the wire wave gauges commonly used in surface wave measurements (e.g., Skyner, 1992), and it might appear that a simple adaptation of surface wave gauges would suffice. The second option is rather more complex, since it would require some form of integration to derive a wave shape from the path of a refracted beam. The third option is similar to the "float" wave gauge used by the Edinburgh Wave Power Project (1987). Sketches of internal wave height gauges based on these methods are shown in figure 4.22.

Concerns about the influence an object in the centre of the flow would have on the internal waves themselves ruled out the float gauge. It seemed that wire gauges offered a much simpler solution than optical methods, and so a wire wave gauge was developed.

### 4.6.2 Wire wave height gauges

Some of the points of importance in the design of wire wave gauges for use in internal waves are listed below.

1. In the two-layer approximation, a wire wave gauge will see motion in both the fresh and saline layers. As the saline layer rises to cover more of the gauge, the amount of fresh water "seen" by the gauge falls. However, as the conductivity of the saline solution is orders of magnitude greater than that of the fresh water, it can be argued that the wave gauge does not "see" the fresh water at all. Rather, it measures only the elevation of the saline layer.

2. True two-layer stratification was not obtained in any of the experiments. Therefore, the wave gauges were exposed to the motion of the interface as well as the body of the lower layer. It was necessary to establish that the output of the wave gauge was representative of the elevation of the interface. This is essentially a "sensor linearity" consideration, and was resolved by experiment.

3. The much lower resistance seen by an internal wave gauge, when compared with that seen by a surface wave gauge, means that a simple adaptation of the electron-

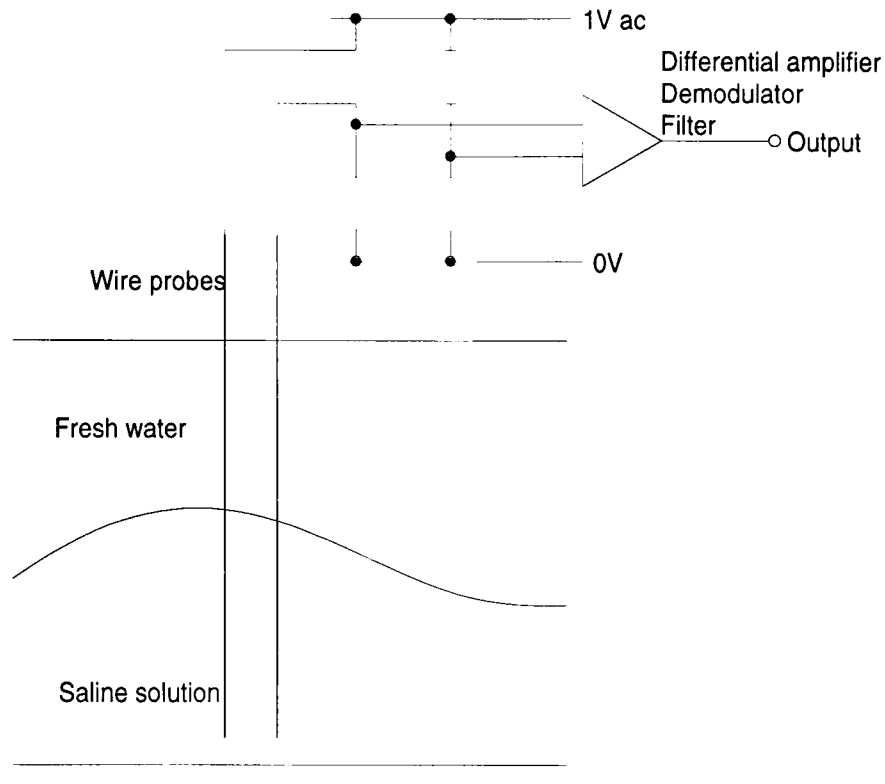


Figure 4.23: *Block diagram of a Wheatstone Bridge wire wave height gauge*

ics of a surface gauge was not appropriate. The resistance being measured was a fraction of one ohm, rather than a few hundred ohms, and so special methods were needed.

4. Alternating currents and voltages were required at the probes, because a DC voltage across two conductors in water forms an electrolysis cell.

### Wire gauge design

The first attempt was a simple Wheatstone Bridge circuit, shown in figure 4.23. The circuit measured the resistance between two stainless steel rods immersed in the fluid. Unfortunately, the very small resistance being measured made this method unworkable.

Several ideas were considered in an attempt to improve this system, including capacitance measurement, and platinum resistance wires. In the end the successful solution was to switch from measuring voltage across a low resistance to measuring current through it, using a circuit suggested by Mr Douglas Rogers[3]. A block diagram of the circuit used is shown in figure 4.24, while the full schematic is shown in figure A.1.

At heart of the circuit are two operational amplifiers which together control a very small differential (a.c.) voltage across the two probes. The outputs of the operational

[3]Edinburgh Designs Ltd.

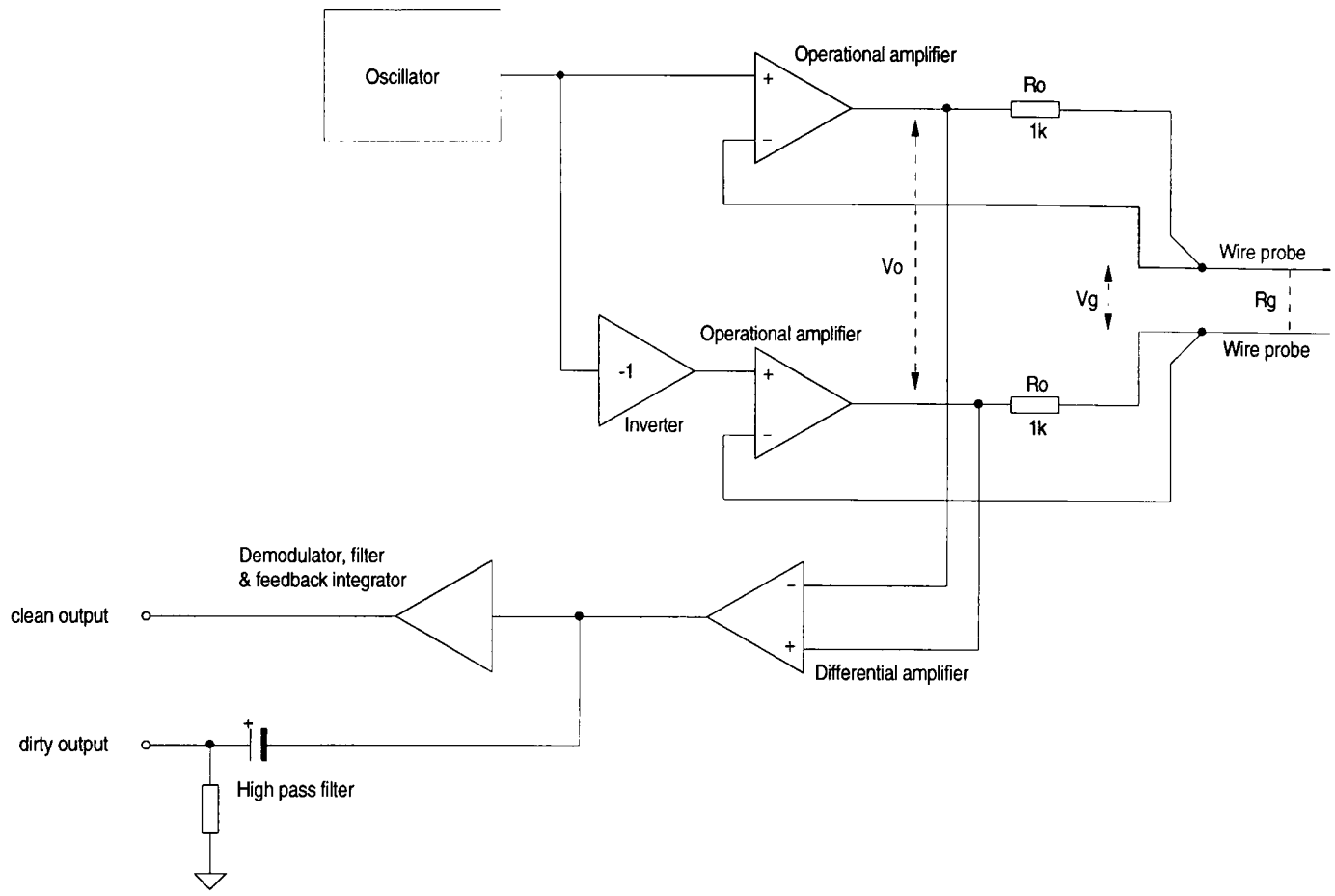


Figure 4.24: *Block diagram of the wire wave height gauges*

amplifiers (op-amps) are connected to the probes via a high value ($1k\Omega$) resistor. The negative feedback connection to each op-amp is made after the resistor, so that the op-amps attempt to fix the a.c. voltage $v_g$ across the probes themselves. In order to do this the a.c. output voltage of the op-amps $v_o$ must be defined by the ratio of the resistances.

$$\frac{v_o}{v_g} = \frac{R_o}{R_g} \tag{4.6}$$

If the water resistance is of the order of $1\Omega$, the $1000\Omega$ output resistor gives a gain of 1000 between the voltage measured at the wires and that measured at the op-amp outputs. This overcomes the difficulty of measuring the tiny resistance of the saline solution.

A differential mode drive was used (two op-amps operating in a push-pull configuration) because of the much greater common mode rejection ratio.

Two alternative outputs were offered from the gauge: a "clean" (filtered) output from which the high frequency carrier wave had been removed, and a "dirty" (untreated)

output, containing the modulated carrier. The clean output contained a feedback integrator which automatically zeroed the signal slowly over time, as well as a second order low pass Bessel filter with a cut-off of 7.2Hz. The dirty output contained only a high-pass filter to remove common-mode oscillations in the d.c. level of the signal.

The purpose of the "clean" output was to provide a stable, easy to use output which required no extra treatment. The "dirty" output was intended for situations where adjustment of the zeroing and filtering of the gauge output was required. In practise, the dirty output proved more useful.

### Wire gauge linearity and calibration

The linearity of the wire wave height gauge was tested by using the wavemaker (without the paddle) to move the gauge vertically in a near two-layer stratification. This test did not perfectly imitate the situation of the gauge measuring real waves, since the depth of fresh water above the interface stayed constant. This difference is not expected to be significant.

The results of the linearity test are shown in figure 4.25. This test was conducted with the gauge interfacing circuit shown in figure A.2. It is seen that the gauge output is linear with position. The coefficient of linear correlation for the data shown was evaluated as 0.999. The results shown are for both upwards and downwards movement of the gauge.

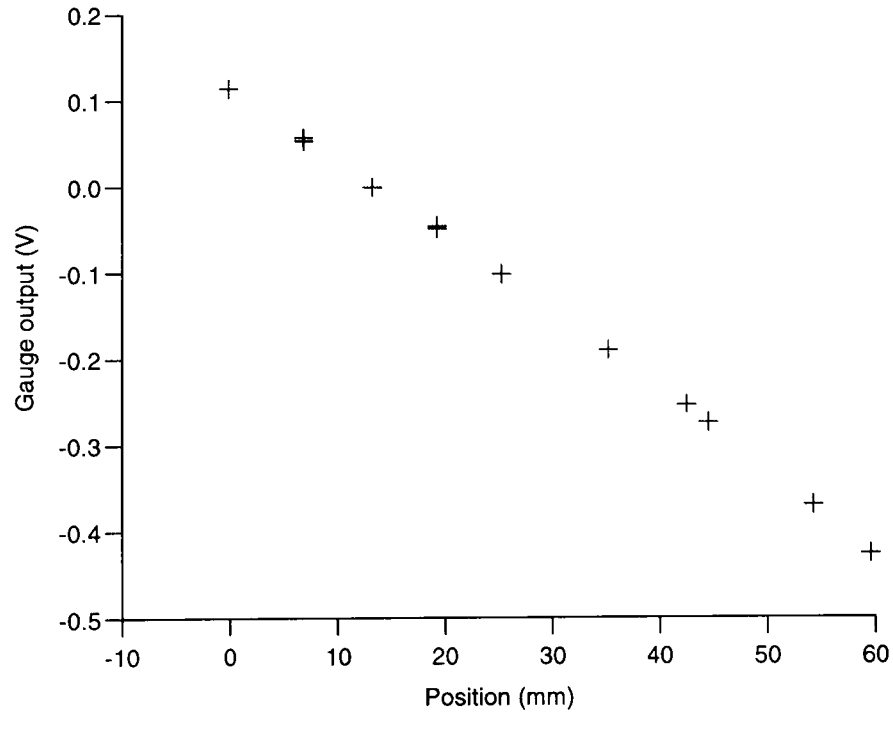


Figure 4.25: *Linearity test of the wire wave height gauge*

The wave gauges had to be calibrated before each experiment. This was done by recording the average output of each gauge, then raising the gauges by a fixed distance (10mm) and measuring the new average output.

### 4.6.3 Other means of measuring the wave motions

In the parallel experiments conducted by Mrs Nadine Thompson at the University of Dundee, the use of a density probe to measure the wave shape was investigated. Density probes are discussed in section 4.7. With a density probe in a fixed position near the centre of the interface, the density fluctuations at a fixed point produced by the internal wave could be recorded. This measures the wave shape according to an Eulerian definition.

In the experiments on internal waves with non-uniform stratification in the upper layer, the wire wave gauges performed poorly. The variation in the overall resistance of the water column as the wave passed was much smaller in this case than in the near-two-layer case. A fixed density probe situated in the region of greatest density gradient proved more valuable in these cases.

An optical scheme developed by Hammack (1980), which was not known about at the time, could potentially have been used. Hammack's system, which is applicable to waves in an approximately two-layer stratification, is shown figure 4.26. The saline lower layer is dyed in this system. An expanded laser beam passes horizontally through the tank. The laser beam is then focused onto a photodiode, which records the variation in intensity as the dyed lower layer rises and falls, absorbing greater or lesser amounts of light. The gauge is inherently nonlinear, but a calibration curve is easily obtained before each experiment by moving the whole assembly up and down. Although the variation in intensity is brought about by dye in the lower layer, it might be possible to dispense with the dye and rely on the variation brought about by the change in refractive index. This would make the gauge usable in a particle image velocimetry experiment.

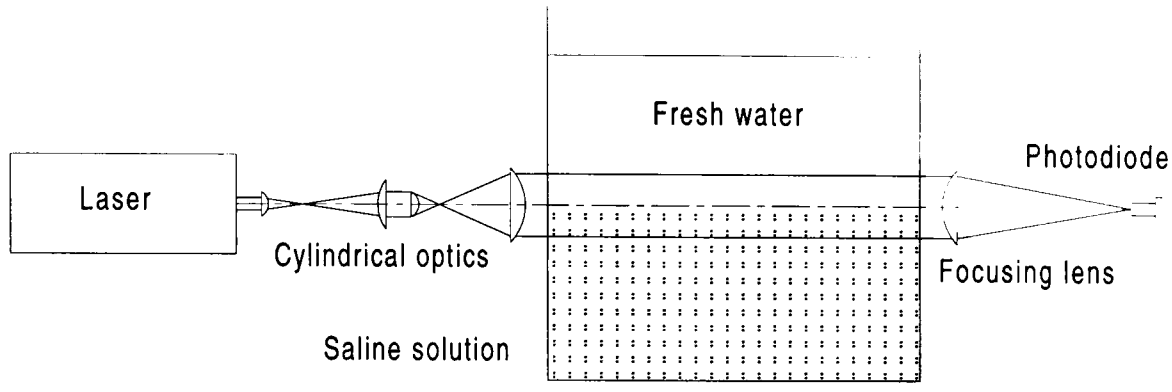


Figure 4.26: *Hammack's (1980) optical wave gauge*

## 4.7 Density probes

In order to gain accurate knowledge of the form of the stratification in the tank, it was decided to use a traversing conductivity probe to measure static density profiles before and after each experiment. Two alternative technologies were available:

1. Commercial micro-scale conductivity probe (figure 4.27);
2. Aspirating conductivity probe (figure 4.28).

The micro-scale conductivity probe works by driving a constant a.c. current through the fluid between the two inner current electrodes, and measuring the a.c. voltage that develops across the outer electrodes. The electrodes are platinum coated. The sensor spatial resolution is approximately 4 cycles/cm (3dB point), which would be more than adequate for this experiment. The time response is also far greater than required, with a 3dB bandwidth of 800Hz.

Rather than relying on very small electrodes permanently in a volume of fluid, aspirating probes work by constantly drawing a small amount of fluid past one or two somewhat larger electrodes, and measuring its conductivity as it passes the electrode. The fluid drawn past the electrodes is then discarded. The electrodes are doughnut-shaped, and the fluid flows through the very fine central hole. The size of the central hole is such that the fluid flows quickly past the electrode, and this is supposed to improve the time response.

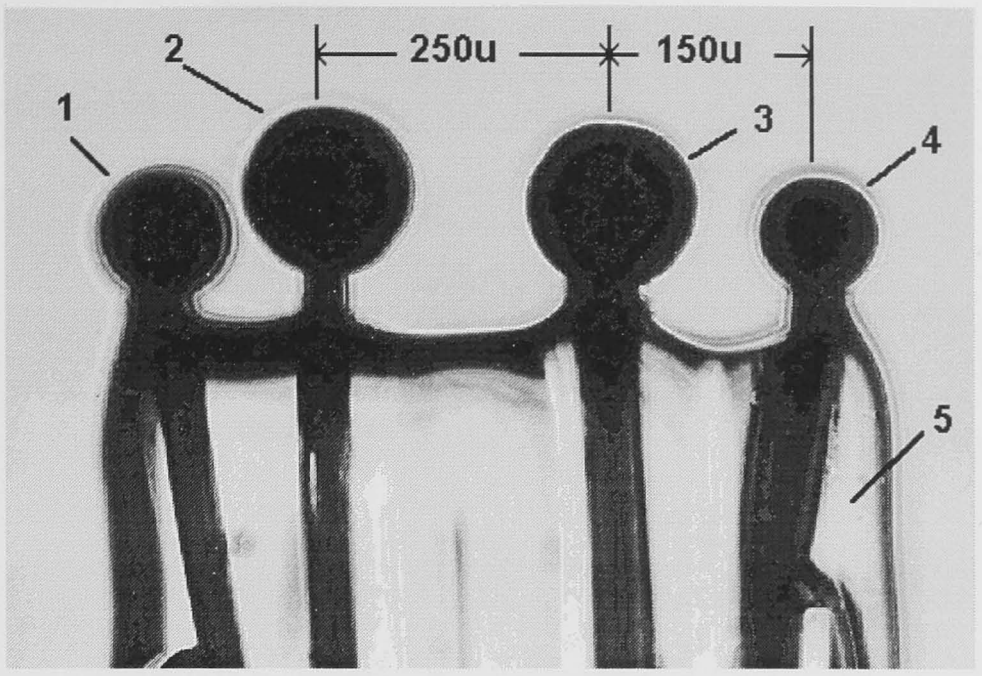


Figure 4.27: *Precision Measurement Engineering fast micro-scale conductivity sensor. 1 & 4: voltage sensor electrodes; 2 & 3: current drive electrodes; 5: glass support. Source: PME website (http://www.pme.com/pmeinfo); used by permission*

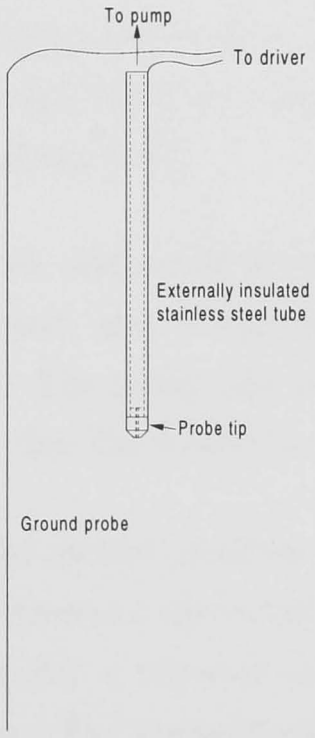


Figure 4.28: *Aspirating density probe*

The cost of the micro-scale probe is around £2,000. An aspirating conductivity probe was available on loan from the collaborators in the project[4] for the duration of the experiments.

[4]Professor Peter Davies, University of Dundee

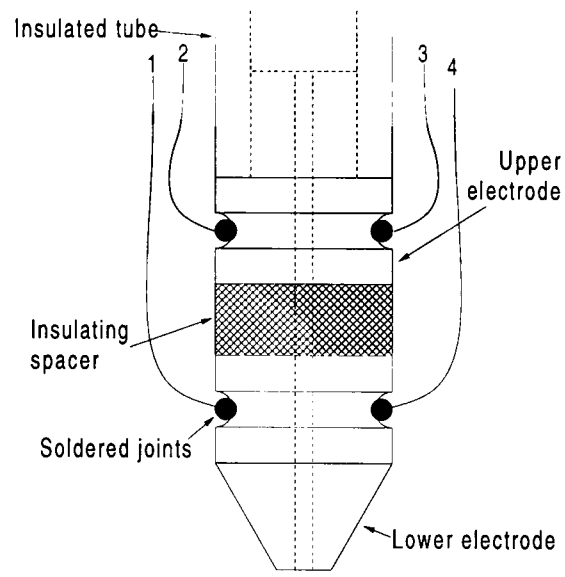


Figure 4.29: *Redesigned aspirating density probe. 1 & 2: upper and lower electrode current drive connectors; 3 & 4: upper and lower electrode current sense connectors.*

### 4.7.1 Density probe redesign

It was discovered that the aspirating probe suffered from two problems: firstly, the output at times appeared to be strongly cyclic, and secondly, output drift was observed while the probe was stationary in dense fluid.

The first problem was traced to the method of drawing fluid through the probe. A perystaltic pump had been employed, and it was found that it did not draw fluid evenly through the pumping cycle. The pump was discarded and siphoning was used instead. The conditions were such that the fluid flowed more quickly with the siphon.

An attempt was made to solve the second problem by redesigning the probe. The original probe had one annular electrode at the end of an externally insulated stainless steel tube. The ground electrode was a stainless steel rod placed directly into the tank, reasonably close to the probe. The probe functioned by directly measuring the voltage required to pass a certain current from the probe tip electrode to ground. It was thought that the unknown current path between the probe and ground might be responsible for the behaviour.

The redesign, shown in figure 4.29, involved substituting the ground electrode for a second annular electrode in the probe tip, and insulating both of these electrodes from the support tube. The wave height gauge driver (figure A.1) was used in place of the

original probe electronics. It is noted that the wave gauge driver was in principal a double ended version of the original probe driver. However, by driving the current between symmetrical halves of the same circuit rather than to ground, it was hoped that the probe would be insensitive to common mode interference picked up by the highly conductive saline solution.

The fluid flowed past the two electrodes which were insulated from the external fluid by epoxy resin, and from each other by a water-resistant Tuffnol spacer. Aluminium bronze, a common marine alloy, was used for the electrodes to inhibit corrosion. A thin, stable film of oxide on the electrodes could be tolerated since the current was driven in a.c., whereas the formation of a unstable oxide might result in flaking and blockage of the flow path.

Considerable difficulty was experienced in manufacturing this probe. It proved impossible to drill the hole in both electrodes and the spacers in one pass until the tip was encased in a thick coat of epoxy resin. Uniformity of the hole was found to be essential, as deviations in the flow path caused small quantities of fluid to become trapped behind sharp corners in the flow path, giving rise to anomalies in the output. After strengthening the tip assembly with epoxy, the central hole had to be redrilled at a larger diameter to remove the corners. This appeared to improve performance, but resulted in a bulky probe tip. Soldering of the wires onto the electrodes was also difficult.

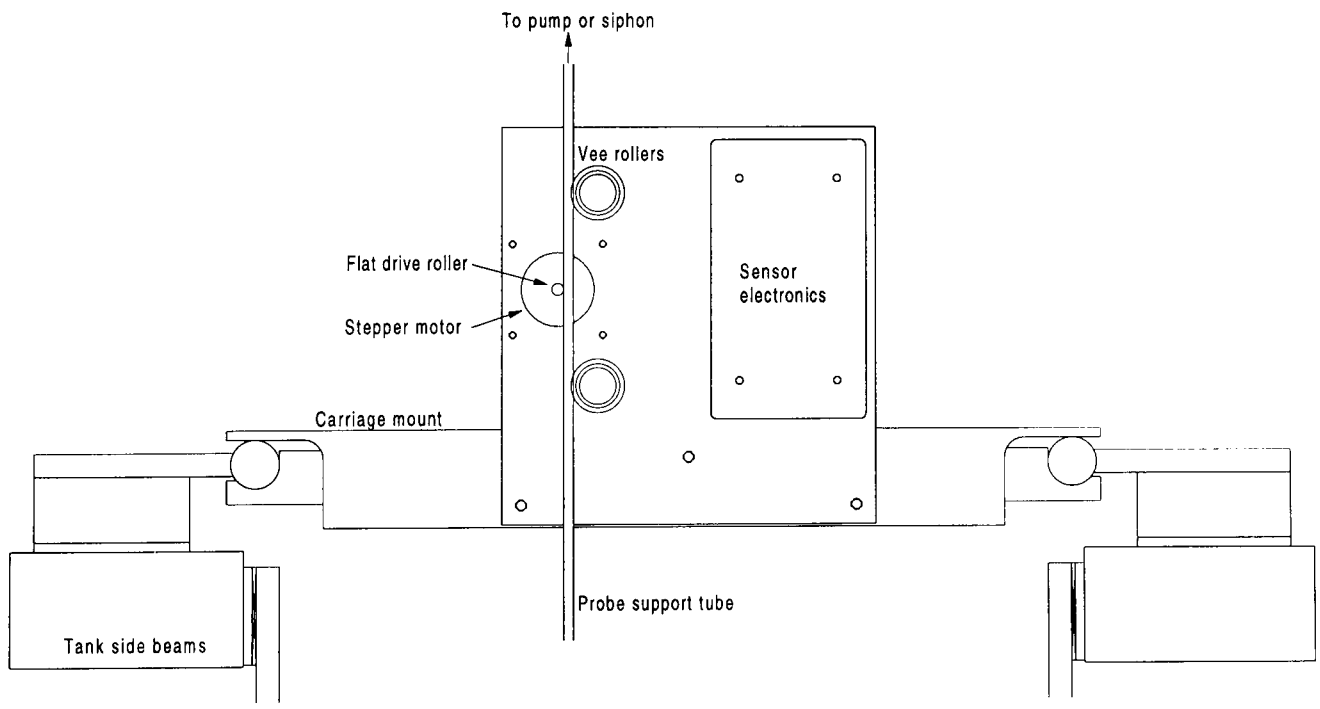


Figure 4.30: *Carriage for density probe*

### 4.7.2 Probe performance and parameterisation

The modifications described did not solve the apparent long time constant. Since neither time nor money were available to improve the probe, it was decided to make the best of the existing equipment.

The effect of the long time constant on the density profile measurements was minimised by driving the probe extremely slowly through the fluid. For this purpose a stepper motor driven probe carriage was designed (figure 4.30). The stepper motor was driven by a commercial drive board (RS) which included an on-board variable frequency oscillator to generate the stepping pulses. A counter recorded the number of steps taken, and this information was passed back to the control computer. The computer simultaneously recorded the probe output. A fuller description of the density probe drive system is given in section 4.5.1.

As did the wave height gauges, the probe suffered from interference picked up from the highly conductive saline solution. Some of the profiles contained clearly unphysical glitches, which made them unusable. Others contained an element of noise which was exaggerated by the post-processing differentiation. Nevertheless, reasonably clean density profiles were obtained for most of the experiments.

There remained a danger that the long time constant would exaggerate the thickness of the density interface, or give an incorrect idea of its shape. It was not clear that the form of this problem was slow response, drift or some kind of hysteresis. After the experimental programme had been completed, money became available to purchase the micro-scale conductivity probe described above. This was used to aid in the interpretation of the existing density profiles.

The micro-scale probe was checked by placing it in solutions of known conductivity. It was then mounted in "piggy-back" fashion onto the existing probe, so that it could be driven through the fluid and measure the fluid density simultaneously with the aspirating probe. The probe tips were placed on the same horizontal level but they were separated by about 100mm to reduce crosstalk between them.

Simultaneous profiles were taken under a variety of stratification conditions. The result of one such profile is shown in figure 4.31. It is clear that the micro-scale probe records a thinner interface at a higher level than does the aspirating probe. Visual observations of the density interface also favoured the micro-scale probe.

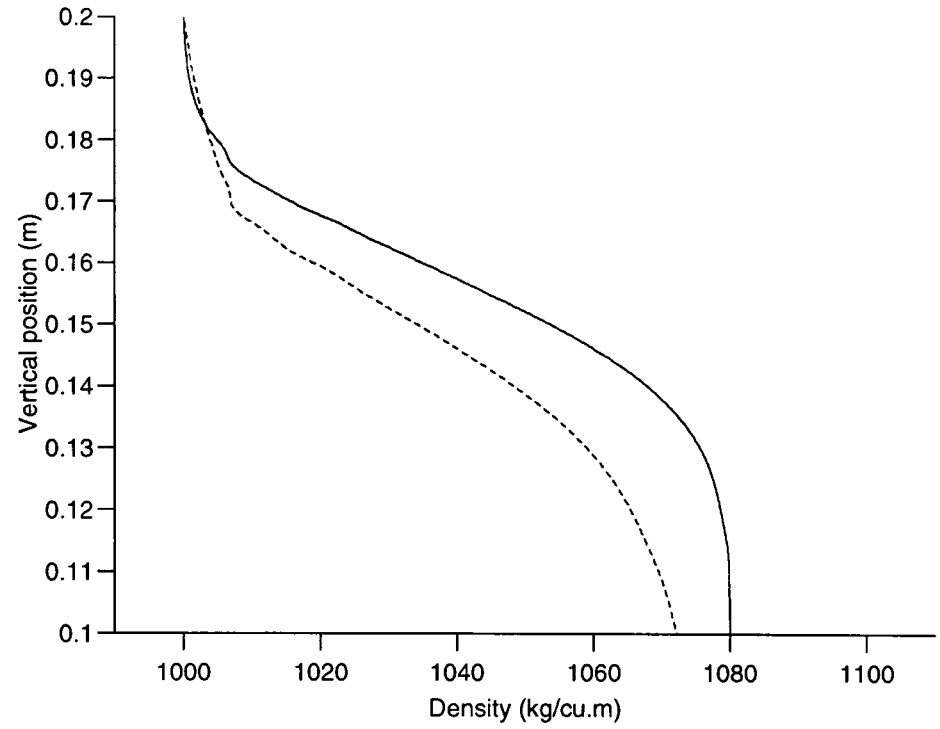


Figure 4.31: *Close-up of density interface as measured simultaneously by the two probes. Microscale probe: ——; aspirating probe: – – –*

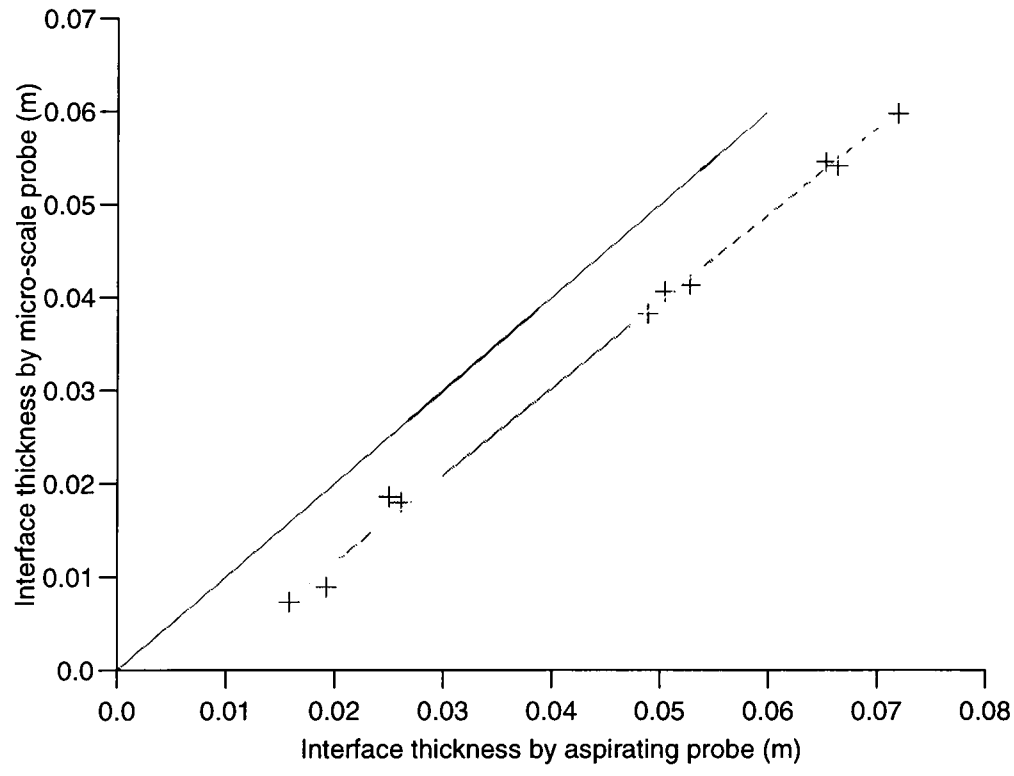


Figure 4.32: *Comparison of estimates of interface thickness using the two probes. Best fit: – – –; exact correspondence: ——.*

It was concluded that the aspirating probe had been exaggerating the interface thicknesses and depth because of some form of hysteresis. This was most probably due to interaction between the probe and the fluid. It was noted that both of the aspirating density probes relied on the assumption that fluid was drawn from the density surface

at the same level as the probe tip. It was not clear that this would always be the case, especially if the probe was in motion.

It was also noted that in drawing the probe up through the fluid, there was a danger that dense fluid would adhere to the probe as it rose and drop back gradually, contaminating the reading. All of the profiles were recorded with the probe moving downwards.

A parameterisation was used to correct the aspirating probe measurements based on the assumption that the micro-scale probe gave the correct measurements. This assumption was justified because of the consistency and lack of drift in the preliminary measurements using that probe, and the fact that the probe was in use worldwide for similar work (e.g. Stevens & Imberger, 1996; Head, 1983).

The parameterisation is that of equation 3.21, repeated below:

$$\overline{\rho} = \rho_0 \left(1 - \alpha \tanh\left(\frac{z - z_0}{\delta}\right)\right)$$

where $\delta$ is the thickness parameter (equal to half of the thickness of a linear interface whose maximum density gradient was equal to that of the tanh profile); $\alpha$ is one half of the density change; $z_0$ is the height of the co-ordinate origin above the interface; and $\rho_0$ is the median density. Knowledge of the unknowns $\delta$ and $z_0$ would allow density profiles to be fed into the numerical simulation programs.

The interface thicknesses were obtained by measuring graphically the maximum density gradient. A comparison of the thicknesses obtained by these two methods is shown in figure 4.32. A linear regression was performed, and the best fit line is plotted. This line had the equation

$$y = 0.934x + 0.007 \tag{4.7}$$

which had a correlation coefficient $r^2 = 0.996$. This fit was remarkably good and so the formula above was used to correct the aspirating probe measurements of the interface thicknesses in the experiments.

The height of the interface $z_0$ was also underestimated by the aspirating probe. This was corrected by estimating graphically the heights of the median density points from both probe traces. The median density point is essentially the centre of the interface,

which is assumed to be symmetrical. The mean difference between the two methods of measurement was 6.3mm, while the standard deviation was 1.9mm. Given that these estimates were graphical, this is also a remarkably good fit. Therefore it was used to correct the layer depths $H_{1,2}$, where

$$H_1 = \text{Surface elevation} - \text{Median density point elevation}$$
$$H_2 = \text{Median density point elevation} - \text{Bottom elevation}$$

It is noted that this definition of layer depths and density profile parameterisation also allowed for cases where the upper layer was linearly stratified (section 6.5). In such cases the median density height was in the centre of the inhomogeneous upper layer. Accordingly, the depths $H_{1,2}$ marked the centre of this layer and the interface thickness $\delta$ marked its extent.

## 4.8 Evaluation of the experimental equipment

Retrospectively, several comments can be made about the equipment described in this chapter. Some design choices have been shown to be justified, while in other cases better ways of achieving the desired results can be seen.

1. **Wave tank**

   The design of the wave tank was on the whole a success. The tank has proved relatively easy to maintain, owing largely to the ease of sealing and the absence of any metal in contact with the fluid. The long wave studies might have benefited from some extra length; however, neither funds nor space were available to add an extra bay.

2. **Wavemaker**

   The friction drive design performed well, once initial problems had been ironed out. The choice of contact material for the drive roller may not have been the best. The stress calculations showing that the perspex would survive in contact with the carbon fibre drive rods have been seen to be correct in normal operation, however, as soon as slippage occurs, both perspex and carbon fibre suffer damage.

   The drive mechanism is nevertheless extremely positive, and (with a smooth drive roller and smooth drive rods) free of lost motion and non-linearities. This makes it very easy to control.

The two wavemaker paddles performed adequately for small to moderate wavelengths. Longer waves might have been better generated with a different paddle shape.

3. **Control and data acquisition hardware**

   The electronic hardware which controls the wavemaker and gathers data is complex, and consumed more time and money than was envisaged in its construction. It could however be argued that time was saved at a later stage in more efficient running of the experiments. The self-protection features of the wavemaker prevented any damage due to slippage or other problems during the whole course of the experiments. Given the effort required to set up the experiments, any problems with the wavemaker would be highly undesirable.

   The analogue side of the control system possessed some features which did not make a great impact on the success of this project; notably the ability to set gain and damping factors from software. One of the reasons for building this feature was the desire to make the system easily extensible to different types of paddle and completely different wavemaker mechanisms. Without the ability to set control parameters in software, interchanging paddles or mechanisms would necessitate manually resetting all of the parameters and rechecking the frequency response of the system.

   Although the two paddle sizes used in the present study did not require different gain and damping factors, new work currently in progress uses the same controller to control a different drive. The ability to switch between this device and the original wavemaker without rechecking the frequency response of the system is now a clear advantage.

   The data collection electronics could be improved. It was found that setting of the gain and offset for the wave gauges was difficult since the gain had often to be set very high. This aspect is discussed below.

4. **Control and data acquisition software**

   The software kernel written by Mr Peter Woodhead has proved to be very useful, and like the electronic control system, it is easily extensible. No amendments were required to the fundamental message-passing system, and extensions to the kernel were easy to write. The software kernel is sufficiently general for it to be usable in a variety of other circumstances. The block-diagram based program design method which it encourages might prove useful in circumstances other than real-time control or data acquisition. In this study, the flexibility of the

software made it easy to create auxiliary programs, such as the density probe driver program and the wave gauge calibration program.

A slight disadvantage was the fact that the program was run on MS-DOS on a IBM-compatible PC. This environment is rather unstable, and program crashes did occur. More advanced operating systems are now available, although the difficulty in creating real-time programs might be greater on these. The software kernel could be ported to a different system with only minor modifications, but the extensions to the kernel would not be easy to port.

The complexity of the loop in the program `exrun` meant that care had to be taken in ensuring that all of the control paths were connected. Disconnected control paths caused crashes. A graphical program design system would be an advantage.

5. **Wave height gauges**

Individually, the wave height gauges functioned very well. Problems arose when several gauges were used together. Several improvements to the gauges and the gauge interface board would be useful:

- The on-board oscillator in the gauges converts the sine wave generated to a square wave, in order to smooth out variations in amplitude. It is possible that the harmonics created by this increased the tendency of the gauges to interfere with one another. A better system would use a pure sine wave.
- A further improvement would be to drive all of the wave gauges from the same signal source, ensuring that "beats" could not occur. If the gauges were driven alternately in a multiplexed arrangement, interference would be eliminated entirely, since only one gauge would be active at any time.
- The gauge interface board reads single-ended inputs. Double-ended (differential) inputs might help to reduce noise.
- The offset and gain adjustments on the box should be redesigned to make them easier to set.

On the whole, however, the gauges performed adequately in near two-layer stratification. A completely different gauge might be required for waves with a continuously stratified upper layer, or density probes could be used to infer wave height.

6. **Density probe**

Problems with the aspirating density probes are described in detail in section 4.7. The poor performance of the aspirating probes made it necessary to take repeated

density profiles, and still (as has been shown) gave an incorrect impression of the form of the interface.

The microscale probe which was purchased after the end of the project has been shown to be much more reliable. It may even be possible to correct PIV measurements for refractive index effects using density profiles read using this probe.

# Chapter 5

# Velocity measuring equipment

The selection of Particle Image Velocimetry (PIV) as the flow measurement technique is discussed followed by a summary of the main features of PIV. The particular PIV implementation used in these experiments is then described, including consideration of the means of light delivery and the choice of seeding particle. The errors in PIV are reviewed first in general terms and then with reference to stratified flows. Using techniques such as ray tracing, the errors are quantified. A brief retrospective review of the performance of the PIV system concludes the chapter.

## 5.1 Introduction

A large number of fluid velocity diagnostic technologies are used at present in laboratories. They may be categorised in a variety of ways.

- *Qualitative/quantitative*—Often the intention is to build up a qualitative picture of the characteristics of the flow, and identify first-order features such as streamlines, vortices and shocks. *Flow visualisation*, including smoke visualisation, streak photography, Schlieren photography and others (Prandtl, 1952; Van Dyke, 1982) provides such information. Where second order information such as velocity is required, a quantitative technique is employed.

- *Invasive/non-invasive*—Invasive techniques such as hot wire anemometry rely on the insertion of a probe into the flow. Non-invasive techniques usually rely on

optical methods to separate the measurement device from the fluid. Usually, however, the fluid must be "seeded" with some form of tracer particle, which may itself interact with the flow.

- *Dimensions*—Velocity measuring devices are typically restricted in the dimensions in which information can be obtained. Their "measurement zones" can be classified as bulk, point, profile, full field or three-dimensional.

  Orifice plates, venturis and weirs allow measurement of a *bulk* quantity such as volume flow rate. A *point* measurement technique, such as Laser Doppler Anemometry (LDA) or hot wire anemometry, measures velocity at an isolated point in space over time. Acoustic Doppler Current Profilers (ADCP) used in the ocean (e.g. Bole et al., 1994), and the related Sound Detection and Ranging (SODAR) devices used in the atmosphere (Helmis et al. 1996) use the Doppler effect to measure velocity at several points along an axial *profile*.

  A *full-field* method, such as Particle Image Velocimetry (PIV), allows the capture of velocities over a large, generally two-dimensional area, usually at an instant in time. PIV has also been developed to measure velocities in a *three-dimensional* volume using holography. The volumes which can practically be treated in this way are typically very small.

- *Velocity components*—All velocity measurement techniques are limited in their ability to resolve individual velocity components. LDA and SODAR can be adapted to use intersecting light and acoustic beams respectively to measure two velocity components. Most full-field velocimeters, including conventional PIV, measure the two velocity components in the plane of view. Holographic and stereographic PIV measure three components.

For measurements of the kinematics of internal waves, a measurement technique with the following characteristics was required:

1. A non-invasive technique was considered essential, since the driving buoyancy forces in internal waves are small, and the effect of any probe in the flow would be large.

2. Exact repetition of experiments in stratified flows is very difficult, and so repeated point measurements were not considered practical. Consequently, either a full-field technique yielding time-instant velocity maps, or a profiling technique, yielding a time series of depth profiles, was required.

3. Since the flow in the tank was two-dimensional, a two-dimensional measurement technique was sought. A high vector resolution (number of velocity vectors extracted from a single two-dimensional image) method was desired, which recommended PIV over particle tracking.

4. As many experiments were planned, a method capable of automated analysis was necessary.

5. Accurate velocity information was required; specifically, errors in the region of 2–5% were desired wherever possible.

These criteria were largely met by a PIV system which was already in use at the University of Edinburgh, and which is described in section 5.3.

## 5.2 Summary of Particle Image Velocimetry

Particle Image Velocimetry (PIV) was developed from Laser Speckle Velocimetry in the early 1980s, and has now reached an advanced state. The technology required to implement PIV is well documented in the literature (e.g., Adrian, 1991), and only a brief summary will be given here.

The process of velocity measurement by PIV can be divided into the following stages:

1. *Seeding* of the flow with small, passive tracer particles which follow the motion of the fluid;

2. *Illumination* of the measurement zone with a two-dimensional pulsing light sheet;

3. *Image capture*, using either a photographic camera, a video camera or a CCD camera, to a resolution which allows individual particles to be distinguished;

4. *Analysis* of the image by dividing it up into a number of small "interrogation areas" and calculating one velocity vector for each interrogation area; and

5. *Post-processing* of the resulting vector map to remove systematic errors, noise and erroneous vectors.

The following sections describe these stages, concentrating on auto-correlation PIV as this was the method employed.

### 5.2.1 Seeding and illumination

Figure 5.1 shows the characteristics which are sought in capturing PIV images. This figure is a small region of a much larger image, which might resemble figure 5.2.

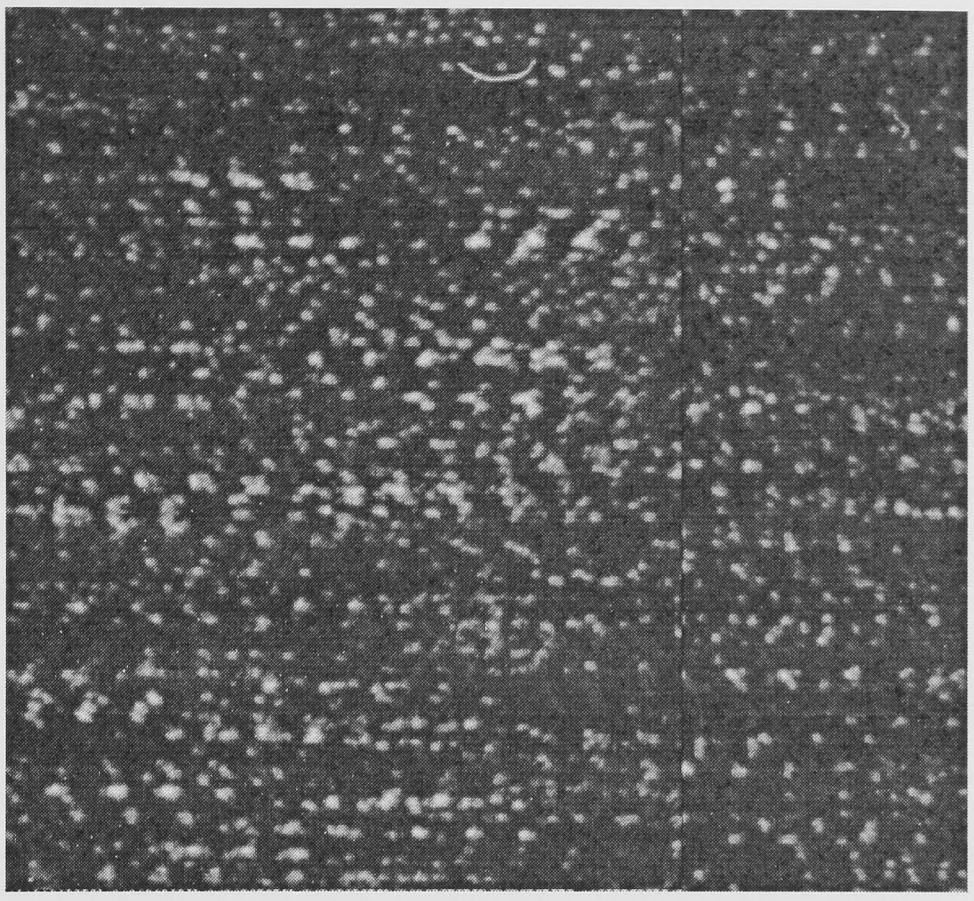

Figure 5.1: *A small section from one of the PIV images.*

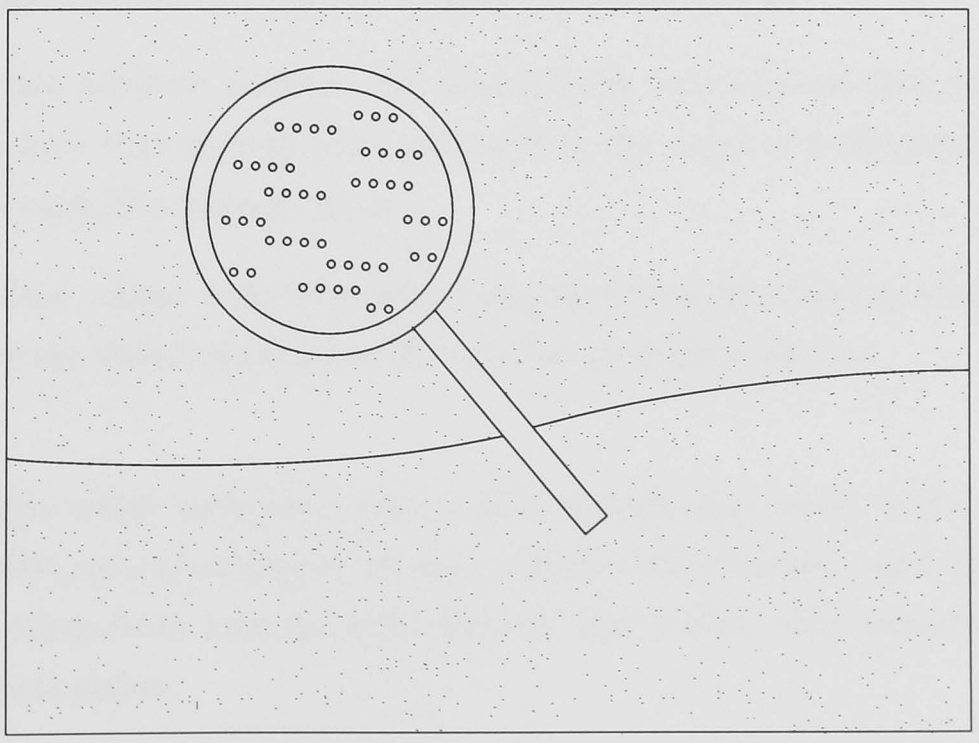

Figure 5.2: *Sketch of a typical PIV negative (adapted from Skyner, 1992; used by permission)*

On this figure, images of individual seeding particles can be seen. These particles behave as tracers, following the motion of the fluid both passively and faithfully. Several distinct images of each particle can be seen, showing that pulsing illumination has been used to illuminate the particles.

PIV obtains velocity information by estimating the distance travelled by seeding particles between illumination pulses, according to the approximate formula:

$$\tilde{\mathbf{u}}(\mathbf{x}, t) = \frac{\widetilde{\Delta \mathbf{x}}(\mathbf{x}, t)}{\Delta t} \tag{5.1}$$

Here $\widetilde{\Delta \mathbf{x}}(\mathbf{x}, t)$ is the local mean displacement vector of particles in a small region around $(\mathbf{x}, t)$, over the small time interval $\Delta t$. This interval is known as the illumination interval, and is the time between successive illumination pulses. $\tilde{\mathbf{u}}(\mathbf{x}, t)$ is the resulting local mean velocity.

The requirements that this imposes on the seeding and illumination are listed below.

- The seeding particles must follow the flow faithfully without influencing it. Thus they must be small in size and of a similar density to the fluid.
- Under the illumination power available, the seeding particles must scatter sufficient light that distinct particle images can be detected.
- Due to the analysis method, the illumination interval and flow velocity range must be such that seeding particles travel in the range of 2–20 particle diameters between each illumination pulse.
- Illumination pulses must be short compared to the illumination interval, and the length of the illumination interval must be accurately known.

Seeding particles which have been used in PIV include aluminium oxide, helium bubbles, oil droplets, glass/polymeric/ceramic spheres and bubbles, and conifer pollen. Typical sizes range from $1\mu$m for glass bubbles and metal oxide particles, to around $70\mu$m for natural pollen.

PIV usually requires a high power laser to generate a pulsing light sheet of sufficient intensity that individual particles can be detected. The choice is between solid state (e.g. Nd:YAG) lasers, which deliver intense pulses of light, and continuous wave lasers

(e.g. Argon Ion), whose output must be modulated to create a pulsing illumination. The latter are cheaper but are more limited in their applicability.

The output beam of a continuous wave laser may be modulated by periodically closing and opening ("chopping") the beam path, or by periodically scanning the beam through the measurement zone. As the illumination pulse duration must be small compared to the illumination interval, the chopping method makes poor use of the available light in comparison with the scanning method.

### 5.2.2 Image recording and image shifting

#### Recording devices

PIV images may be captured by conventional photography or using a charge-coupled device (CCD) sensor, such as those used in video cameras. For auto-correlation PIV, resolution is a governing parameter in the dynamic range of the system, and is therefore very important in the choice of image capture method.

CCD cameras are available with resolutions up to $4096 \times 4096$ pixels, though these are extremely expensive. Video cameras have resolutions around $768 \times 484$ pixels (which is further halved by the field separation employed in standard video signals). In contrast, a moderately fast photographic film such as Kodak TMax 400 has a resolution of about 125 lines/mm, giving an equivalent resolution of $6250 \times 6250$ on a 120-format (50mm square) negative.

Photographic cameras, despite their high resolution and low cost, are limited by the attainable repeat time (about 2 seconds, in comparison with 40ms for low resolution CCD cameras), and also by the inconvenience of wet-film processing. Most users of PIV are now moving from photographic to CCD cameras for these reasons.

CCD cameras yield digitised images of the flow, normally monochrome using an 8-bit grey scale. Photographic images can be digitised in the same way, with the partial loss of the advantage of higher resolution. Alternatively, photographic negatives can be analysed optically.

### Dynamic range and image shifting

As was mentioned in section 5.2.1, in auto-correlation PIV, the flow and illumination parameters must be such that each particle moves between 2 and 20 particle diameters between each illumination pulse. The lower limit is imposed by the fact that, in order to estimate displacement, successive images of each particle must be distinct. Therefore low and zero velocities cannot be resolved by this method. Additionally, since individual images of any one particle are not marked with order of illumination, there is no means of determining the sign of the motion.

The most common solution is image shifting, which means viewing the measurement zone from a moving frame of reference. A standard method is to place a rotating mirror in the optical path from the measurement zone to the camera. Other methods involve rotating or translating the camera itself, or (in CCD cameras) electronically shifting the image on the CCD sensor array between pulses. The result of image shifting is that a mean velocity is imposed on the flow. With freedom to select both the shift velocity and the illumination interval, the dynamic range of the system can be fine-tuned to match the characteristics of the flow and eliminate the directional ambiguity.

## 5.2.3 Analysis and post-processing

PIV is distinguished from particle tracking by its analysis method. PIV analysis does not follow the fate of individual particles, whereas each particle is treated separately by particle tracking. The seeding concentration is higher in PIV and following the motion of individual particles is not possible. Instead, PIV performs a point-by-point statistical analysis of small regions of the flow field, building up a grid of velocity information. Each of the small regions is termed an "interrogation area", and for each interrogation area, one velocity vector is computed. Figure 5.1 shows a typical interrogation area.

Typically, interrogation areas for auto-correlation PIV might measure $64 \times 64$ pixels on a digitised image of $1024 \times 1024$ pixels, yielding a $16 \times 16$ vector map (if the interrogation areas do not overlap). A photographic negative can be analysed optically with an interrogation area size of roughly $1\text{mm}^2$, yielding a $50 \times 50$ vector map on a 120-format negative. Interrogation areas are often overlapped by up to 50%.

Analysis of a digitised PIV image is basically the evaluation of the auto-correlation function of each interrogation area. The location of symmetrical peaks in the two-dimensional auto-correlation plane gives the local mean particle displacement between

successive illumination pulses. The auto-correlation function is evaluated using Fourier transforms.

The fact that low or zero velocities cannot be resolved is due to the strong central "self-correlation" peak which is always found in the autocorrelation function. In order for a signal peak to be detected, it must be distinct from the central peak. The symmetry of the auto-correlation function reflects the directional ambiguity.

Optical analysis of a PIV negative proceeds by probing each interrogation area using a coherent laser beam. The evenly spaced particle images in the interrogation area form a diffraction grating, which creates a Young's fringe interference pattern in the far field. The orientation of the fringes gives the direction of motion of the particles, and the spacing of the fringes is related to the displacement (figure 5.3).

Equivalently, the formation of the Young's fringe pattern may be seen as an optical Fourier transform. The auto-correlation function is obtained simply by reverse-transforming an image of the fringes (this time captured on a CCD array).

**Post-processing**

PIV analysis is a statistical process relying on parameters which are not always fully under control, most notably local seeding concentration, but also variations in illumination and visibility. Hence for each interrogation, there is a finite probability of an erroneous vector being returned.

These vectors can be detected using estimates of the signal-to-noise ratio in the correlation plane, prior knowledge of poorly resolved areas in the flow, or prior knowledge of the likely velocity field. True "bad vectors", where the relevant peak(s) in the correlation plane were missed entirely, can be easily removed manually or by filtering, since they almost always show a velocity very different from that of the surrounding vectors. Vectors with a less pronounced variation from the expected flow pattern are less easy to validate. These can be regarded as true signal contaminated by noise, which might arise from (for example) inappropriate illumination timing, excessive seeding concentration or vibration.

## 5.3 The PIV implementation

The equipment which was available for use, or could be easily purchased, at the outset for use in this project was as follows:

1. *Illumination*

   - Spectra-Physics 171 Argon Ion continuous wave laser (15W output);
   - Optical Flow Systems scanning beam system (0.5m light sheet length);

2. *Recording*

   - Hasselblad 120-format photographic camera;
   - Nikon 35mm photographic camera;
   - S-VHS video camera;
   - Developing and printing facilities;
   - Nikon 35mm negative scanner and various flat-bed A4 scanners;

3. *Analysis and post processing*

   - Optical Flow Systems/University of Edinburgh PIV analysis rig, for Young's fringe analysis of 120 format or 35mm negatives, with driver software;
   - Optical Flow Systems VidPIV analysis software for digitised PIV images.

The equipment available offered some flexibility in the choice of implementation. The options selected are listed below.

- The required illumination was achieved using the continuous wave laser and the scanning beam system. The laser was sited with the experimental tank in a new laboratory, where it was to be made available to various low-to-medium speed flow experiments. The scanning system, described in this section, was also shared between experiments. This choice combined the correct speed range with the required power. The 0.5m light sheet length was also ideal, since it allowed capture of the whole water depth in a roughly square frame.

  As the laser was to be shared, a flexible means of delivering the laser beam to experiments was required. This is discussed below.

- At the time of the experiments, the highest resolution CCD camera available was the S-VHS video camera. This was not considered adequate for the large flow area. A 35mm photographic camera could have been used, and the negatives digitised using the scanner, but the detail would have been inferior to that obtained using the 120 format camera. Since no 120 format scanner was available, direct analysis of digitised images was not practical. This led to the choice of the Hasselblad 120 format camera and the Young's fringe analysis method.

  Recent developments in CCD cameras have meant that, if the experiments were to be repeated, the choice of image capture system would be different (section 5.5).

The system described above is essentially the same as that used by Skyner (1992) and Whale (1996). An overview of the whole system is given in figure 5.3.

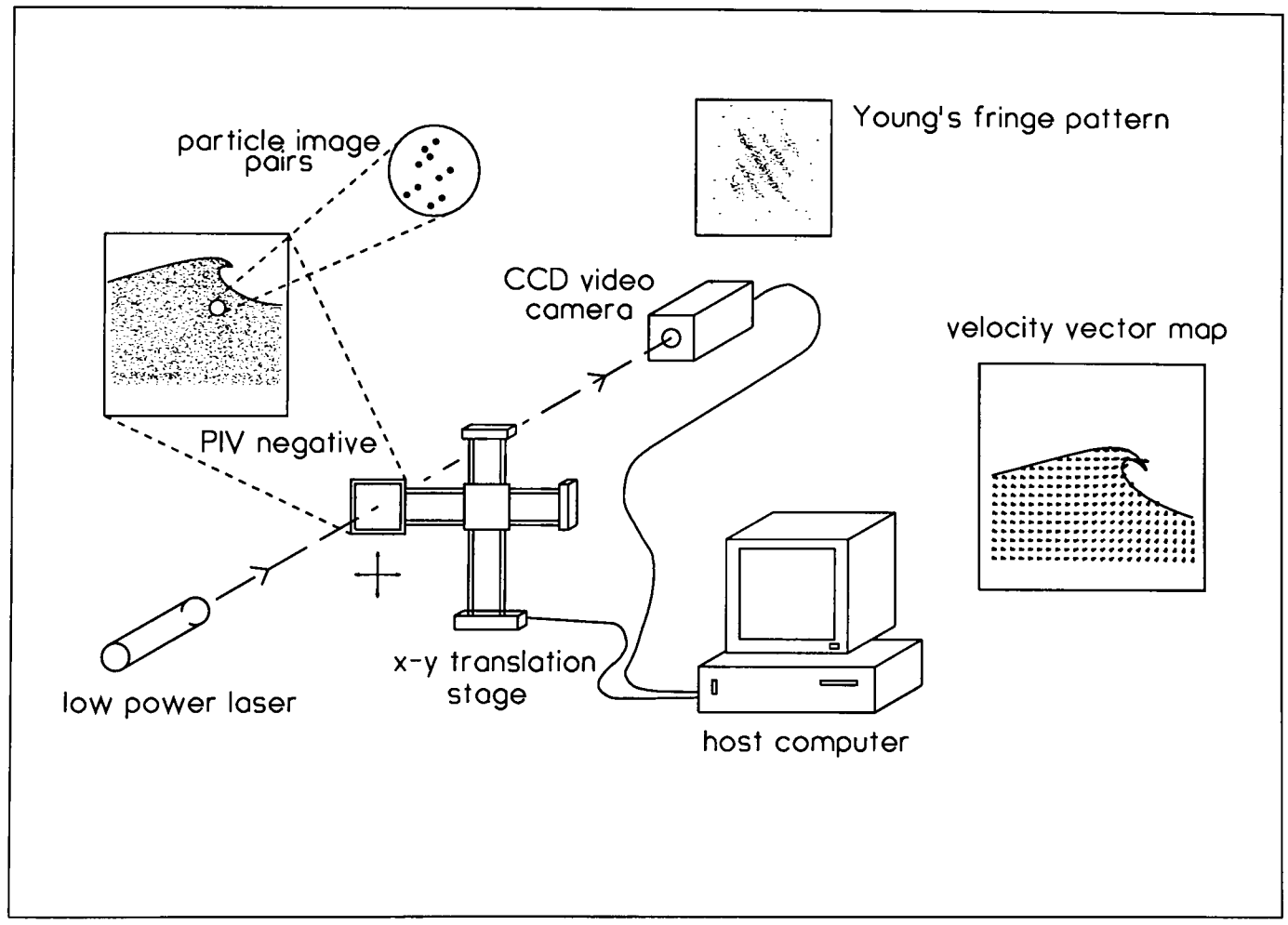


Figure 5.3: *Overview of the PIV system (courtesy of Tom Bruce)*

Selection of the best method for delivering the laser beam to the scanning beam system, and of the best seeding material, was less straightforward and involved some experimentation.

### Laser beam delivery

Traditionally, high power laser beams have been routed between a succession of beam steering mirrors. A typical laboratory beam steering mirror arrangement (about 6 mirrors with a 95% reflection coefficient) would have an overall efficiency of 74%. The optical components for such a system might cost around £200–300 per mirror. In addition, the beam path of such a high power laser (class IV) would have to be enclosed for safety reasons, but the enclosure would have to be made adjustable to allow the scanning beam system to be positioned anywhere in the lab.

Optical fibres were available which were able to transmit high power continuous wave laser beams. A Schott 12W multimode optical light guide (comprising fibre, launch and delivery optics, and fibre protection) was obtained for test. Experiments were performed on the fibre in conjunction with Dr Duncan Anderson[1], Dr Heather Earnshaw[2] and Mr Jean-Baptiste Richon[3]. The cost of the fibre was around £2,000. The saving in effort and cost was expected to be significant if the fibre was deemed suitable.

The characteristics of interest were:

- Maximum deliverable power from the fibre to the measurement zone (12W was the maximum power which could be safely launched into the fibre by the laser);
- Minimum attainable light sheet thickness, since a thinner light sheet concentrates the light and increases the brightness of the particle images;
- Stability of light launch from the laser into the fibre, since any wandering of the laser beam over time in the fibre launch could lead to poor coupling efficiency, hotspots and finally the destruction of the fibre.

The important characteristics of an optical fibre light guide are shown in figure 5.4. This figure is based on the supposed construction of the Schott fibre (firm details were not available from the manufacturer). The basic components and related parameters are as follows:

1. *Fibre and cladding*—the fibre itself is generally glass, while the cladding is made from a material of lower refractive index. The ratio of the refractive indices of the

[1] Formerly of the Department of Physics and Astronomy, The University of Edinburgh; now at Sharp Electronics Ltd.

[2] Department of Mechanical and Aerospace Engineering, Arizona State University

[3] Optical Flow Systems Ltd.

cladding and the fibre fixes the numerical aperture ($NA$) or acceptance angle of the fibre. A low numerical aperture means that launch alignment is more critical but that the output beam is easier to focus.

2. *Launch lens*—with a fibre diameter around 50$\mu$m, the input laser beam (diameter around 1mm) must be focused onto the end of the fibre. This was accomplished using a graded index (GRIN) lens bonded directly onto the fibre end.

3. *Launch adjuster*—The fibre must be sufficiently well aligned to the output beam of the laser that (i) the launch lens focuses the beam onto the fibre end rather than onto the cladding or sheath, and (ii) the light arrives at the fibre end within the acceptance angle of the fibre. If these two considerations are poorly met, the result can be low coupling efficiency or damage to the fibre.

4. *Delivery lens*—The output of a fibre with no lens is a cone of light with an angle to the fibre axis equal to the acceptance angle. The Schott light guide was terminated with a lens which delivered a beam with a diameter of about 6mm and a divergence of about 0.06°. It was necessary to add a second recollimating lens to provide a more collimated beam for the experiments.

It is not possible to converge a laser beam to a point. Most laser beams have a Gaussian intensity profile across a finite diameter. Such a beam will converge to a minimum diameter $d_w$ for a given convergence angle $\theta$ given by

$$d_w\theta = \text{constant} \tag{5.2}$$

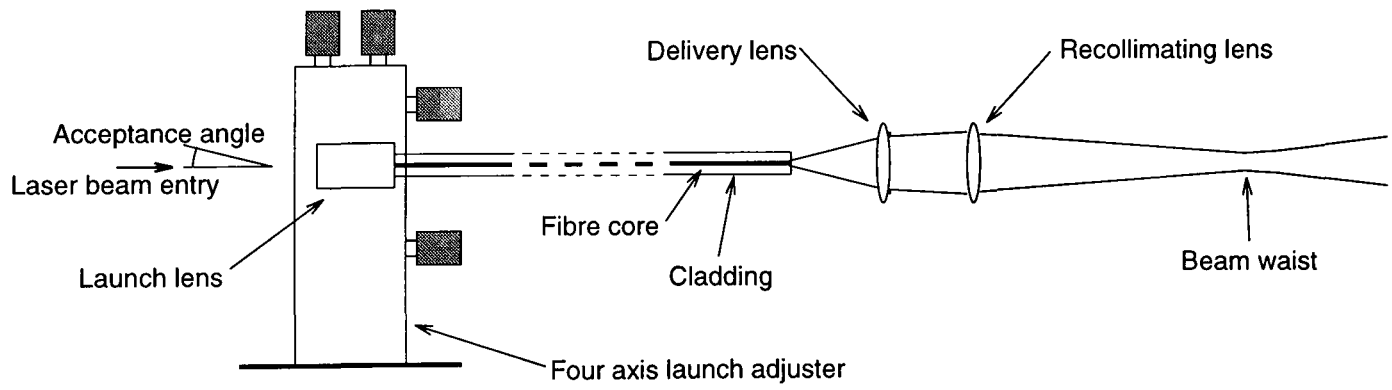


Figure 5.4: *Characteristics of an optical fibre laser beam delivery system, based on the Schott light guide*

where the constant may be thought of as a property of the particular beam, and in practical terms this may be considered as an indicator of the "beam quality".

The Schott fibre was of the multi-mode type, which means that it transmits light of various wavelengths in a variety of transverse modes. The coherence of the beam delivered by the fibre is poorer than that of the laser output beam. A single mode fibre would have required modification of the laser to produce monochromatic light in one mode only, with a large decrease in output power. The output of a multi-mode fibre does not follow a Gaussian intensity distribution; instead, constructive and destructive interference result in a speckle pattern[4]. Practically, this may be viewed as a decrease in the "beam quality" (an increase in the constant in equation 5.2), although Gaussian optics cannot strictly be used here. Therefore, the beam delivered by the fibre optic light guide is much harder to collimate than the beam produced by the laser.

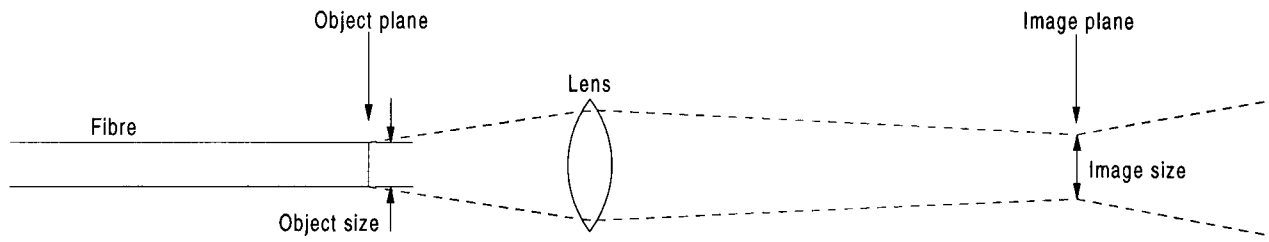


Figure 5.5: *Focusing the laser beam using a lens system*

An alternative way to present the problem is shown in figure 5.5. The fibre end is regarded as an object of dimension 50$\mu$m, which is to be imaged at a distant point (in conventional terms, the image plane) using a lens system. The magnification of the lens system gives the image dimension, which corresponds to the collimated beam diameter.

The second lens had to be selected so that the output beam would converge gradually to a diameter of about 2–3mm at a distance of 1–2m from the fibre (this being the optical path length through the scanning beam system to the measurement zone). Unfortunately the characteristics of the Schott lens (focal length and distance from the fibre end) were not known and could only be calculated approximately, and so the choice of second lens had to be made by experiment.

Figure 5.4 shows the dimensions relevant to the experiment which was conducted on the delivery optics. The experiment was conducted by Jean-Baptiste Richon and the author. Several different lenses of focal length were placed at varying distances from the fibre end. The beam diameter was estimated at varying distances from the converging lens by observing it on paper on which circles of known diameter had been printed.

[4]The speckle pattern is also referred to as Gaussian for a different reason

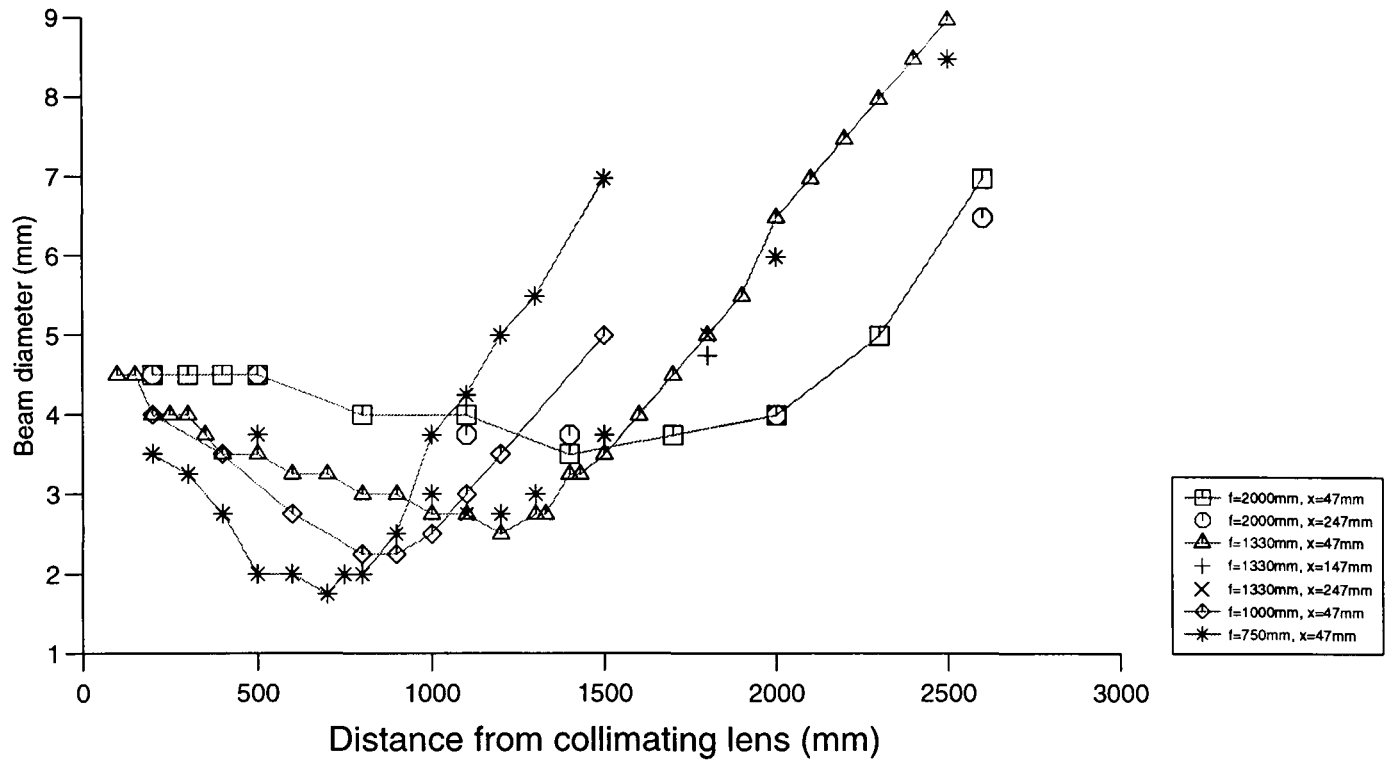


Figure 5.6: *Characteristics of the fibre output beam with various collimating lens configurations*

The circle which appeared to be closest in diameter to the beam was chosen, and its diameter recorded.

This procedure was easy close to the lens, but as the distance was increased it became increasingly difficult to distinguish a clear boundary amongst the speckle pattern and the various transverse mode shapes which were observed.

The results of the experiment are shown in figure 5.6. As expected, the distance $x$ between the fibre and the lens was not important, which lessened the practical problem of choosing the location of the lens in the scanning beam system. The best lens for the range of distances anticipated had a focal length of $f = 1.33$m.

A final point of concern was the pointing stability of the laser, that is, whether the direction of the laser beam would change over time (e.g. during warm-up) to such an extent that correct fibre alignment would be lost. It was found that the beam direction was sufficiently stable to ensure good coupling efficiency even after a long period.

### Choice of seeding

As mentioned in section 5.2.1, the seeding material is required to follow the flow both passively and faithfully, and scatter light efficiently.

The most important parameter in determining whether the particle follows the flow is the difference in density between it and the fluid. This is due to both dynamic and buoyancy considerations. In a continuously stratified fluid, a continuum of densities is present in the flow, and so either a compromise must be reached, or a substance in which the density of the particles varies must be found. One substance with a distributed density is Sphericel 110 P8, a glass filler for injection moulded plastics. Its density and size were ideal for the experiments but unfortunately it was not sufficiently visible in the flow.

Conifer pollen had been in use at the University of Edinburgh for some time in water studies. Its density was known to be of the order of 10% less than that of water (Bruce, private communication), which gave it good dynamic properties in fresh water. The scattering properties of conifer pollen, which is yellow, under green (Argon-Ion wavelength) light, are excellent.

The densities in the experiment were 1000–1100kg/m$^3$. The performance of the pollen in the lighter fluid was noticeably superior to its performance in the denser. The errors which arose from this are discussed in section 5.4.2.

Introduction of the pollen into the denser fluid was done by first soaking the pollen for several minutes in a small amount of water of density greater than the highest density present in the tank. Then a small amount of fluid was bled into the bottom of the tank around the measurement zone using a funnel and perforated tube. This fluid spread out and slowly released the pollen into the body of the denser fluid.

The denser fluid had to be reseeded occasionally due to the slow upward rise of the particles. This was seldom necessary in the fresh layer. Particles rising from the lower layer tended to collect in the interface, resulting in excessive seeding concentration there (which led to some signal loss).

## 5.4 Errors in particle image velocimetry

### 5.4.1 Errors common to most PIV applications

#### Illumination errors

Errors which arise in the illumination phase of PIV are related to timing and to the form of the light sheet.

1. *Illumination interval*—From equation 5.1, an error in the illumination interval $\Delta t$ will translate directly into an error in the measured velocity. In the system used here, $\Delta t$ was fixed by a quartz crystal oscillator. The user was able to select intervals from a fixed set of possible values, each subharmonics of the crystal frequency. The unit locked the rotation rate of the synchronous motor on to the selected subharmonic, and once the controller had been allowed to settle the error in $\Delta t$ could be assumed to be zero.

2. *Systematic scan time error*—Gray et al. (1991) point out that the time interval between successive illuminations of one particular particle is not constant if the particle has moved along the light sheet between illuminations. The systematic error in the velocity which results is the ratio of the maximum displacement of a particle in the measurement zone between illuminations, to the length of the light sheet. For the low velocities in the present study, this was $< 0.1\%$.

3. *Light sheet form*—As noted by Skyner (1992), if the light sheet is not perfectly straight, an error in the magnification arises which is in direct proportion to the magnitude of the variation divided by the optical distance from the centre of the camera lens. Similarly, random errors in the magnification result from the finite thickness of the light sheet. Where the deviations from straightness and the sheet thickness are of the order of a few millimetres, and the zone is viewed from a distance of about a metre, the total error is $< 1\%$.

#### Seeding motion

An important assumption in PIV is that the seeding particles follow the flow both passively and faithfully. The first requirement can be checked as follows. Using the

approximate formula given by Gray (1989), successful PIV can be achieved if the seeding concentration $C$ is approximately

$$C \simeq \frac{24M^2}{\Delta z \pi d_i^2} \tag{5.3}$$

where $M$ is the magnification, $\Delta z$ is the thickness of the light sheet, and $d_i$ is the diameter of the interrogation area. This gives a seeding concentration of around $10^7$particles/m$^3$. For natural pollen, this suggests that approximately $10^{-6}$ of the flow volume is taken up by seeding material. It is concluded that this proportion will not be sufficient to influence the flow.

With the aim of evaluating the degree to which seeding particles faithfully follow the flow, Bruce (private communication) has discussed the forces on a small particle in a fluid in the context of PIV. He points out that, for a small particle such as natural pollen (mean size $\sim 70\mu$m) in fresh water, the motion is governed by Stokes drag (which is linear) provided the slip velocity (the difference between particle and fluid velocities) is less than 15mm/s, a condition which is readily met in the present study.

Since the drag force is linear, a frequency response of the particle to the fluid motion may be evaluated. Bruce found that for a deviation of 1% between fluid velocity and particle velocity, the frequency of fluctuations in velocity must be less than 200Hz. Such fluctuations would not be recorded by the PIV system used, nor are they present in the flow of interest.

Buoyancy effects are discussed in section 5.4.2.

### Image shift errors

The most common means of removing the directional ambiguity and increasing the dynamic range of auto-correlation PIV is the rotating mirror image shifting system (section 5.2.2). This method is described in detail by Raffel and Kompenhans (1995), and is illustrated in figure 5.7. The principal is to interpose a rotating mirror between the measurement zone and the camera, so that the measurement zone is viewed from a moving frame of reference.

The largest source of error is in the assumption that the optical reference frame is effectively moving linearly, while it is in fact rotating about a point. Equivalently, one

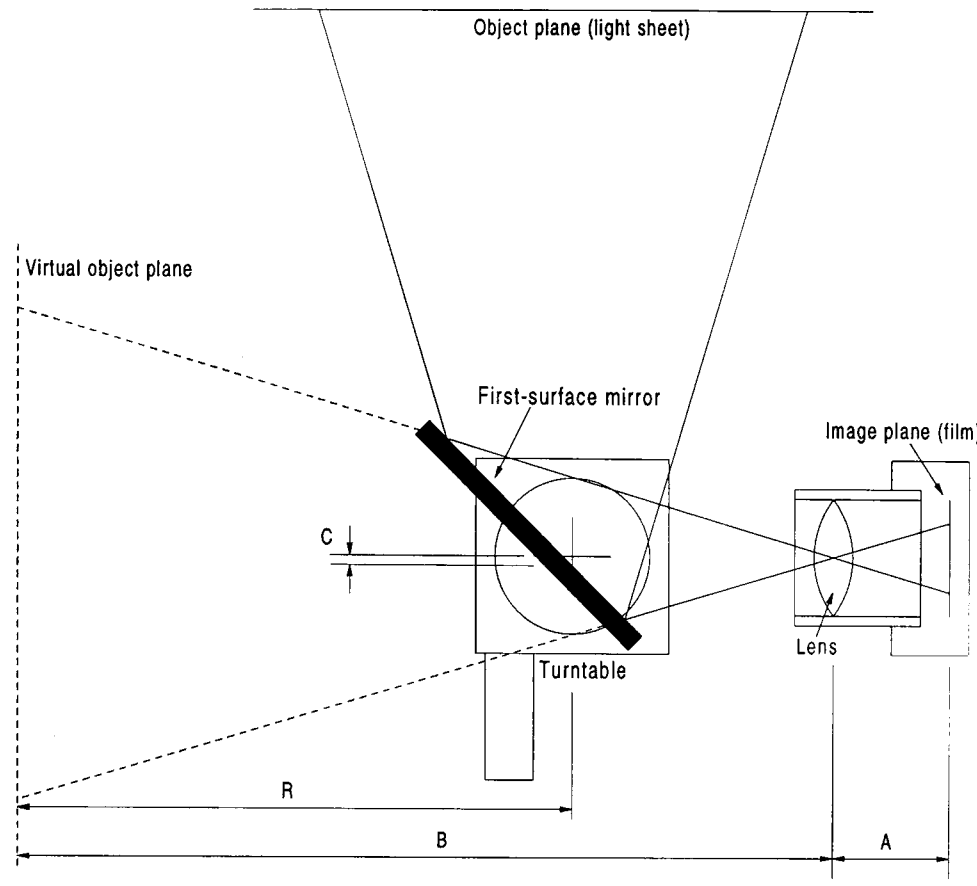


Figure 5.7: *Image shifting using a rotating mirror*

may state that the mirror distorts the apparent measurement zone as it rotates. This is illustrated in figure 5.8, which is due to Morrison (1995). The error which results from this distortion is not dependent on the shift velocity but only on the optical geometry.

An analytic result for the shift distortion is possible using methods of ray tracing by e.g. transformation matrices. This was carried out by Raffel and Kompenhans (1995) and also by Morrison. Raffel and Kompenhans' equations for the displacement in the image plane are given below.

$$\left.\begin{aligned} \Delta X(X,Y) &= \frac{X - MR2\omega\Delta t}{(X+CM)2\omega\Delta t F^{-1}(1+M)^{-1}+1} - X \\ \Delta Y(X,Y) &= \frac{Y}{(X+CM)2\omega\Delta t F^{-1}(1+M)^{-1}+1} - X \end{aligned}\right\} \tag{5.4}$$

The distances $A$, $B$, $C$ and $R$ are defined in figure 5.7. The thin lens formula $1/F = 1/A + 1/B$ is used, and the magnification is given by $M = A/B$. The mirror rotation rate is $\omega$ and the illumination interval is $\Delta t$. The equations are exact except for the assumption of small angles ($\sin x \simeq x$) and the use of the ideal (thin) lens formula.

These equations are compared to the idealised shift:

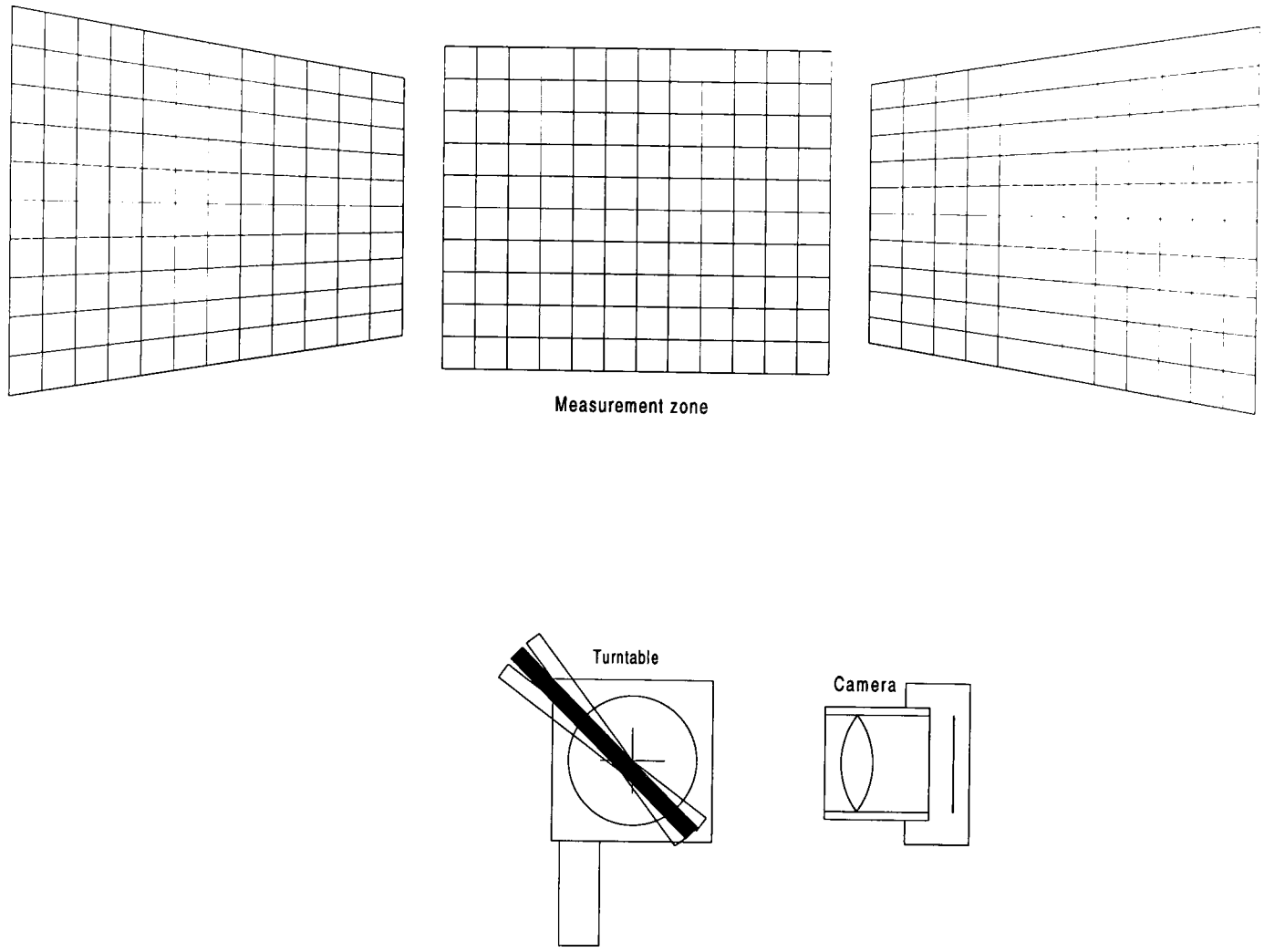


Figure 5.8: *Image shift distortion (after Morrison, 1995)*

$$\left.\begin{aligned} \Delta X(X,Y) &= 2\omega RM\Delta t \\ \Delta Y(X,Y) &= 0 \end{aligned}\right\} \tag{5.5}$$

In ideal conditions (i.e. where the geometry and shift velocity have been chosen to maximise the dynamic range of the system), Morrison (1995) has shown that the difference between equation 5.4 and equation 5.5 can lead to errors of 10% in the measured velocity. If the shift velocity is higher than necessary then the error will be correspondingly larger. Experiments by Morrison and by Raffel and Kompenhans confirm this.

The approximation of small angles leads to no significant uncertainty in the shift velocity. However, the thin lens formula is not necessarily applicable to a real camera lens, which consists of many elements occupying a distance comparable to the film-mirror separation $A$. Morrison used an empirical characterisation of a lens to get round this problem.

Of even more importance is the accuracy with which the distances $A$, $B$, $C$ and $R$ can be known in a laboratory. In the first place, these are optical distances and the refractive indices of all media in the optical path must be known. Secondly, physical measurement of these distances in the laboratory is difficult, since meaningful reference points on components such as the mirror, camera or lens are not usually available.

For the internal waves experiments, the shift error was removed approximately by taking a reference photograph in still water before every experiment. After subtracting the mean (desired) shift velocity, a third order polynomial fit was applied to the residual vectors. This polynomial was used to correct all frames which were taken in that particular experimental run. This approach had the added advantage of helping to correct for other errors which are described in section 5.4.2.

Other errors which may arise from image shifting may be identified from equation 5.5. The error in the magnification $M$ is described below. The uncertainty in the shift radius $R$ may be easily estimated for any particular configuration; in the present case it was $O(1\text{–}2\%)$. The error in $\Delta t$ affects the measured velocities, but not the calculated shift velocity, since $\Delta t$ cancels in the formula

$$u_{shift} = \frac{dX}{dt} \simeq \frac{\Delta X}{\Delta t} \tag{5.6}$$

after substitution from equation 5.5.

The use of a high gear ratio worm drive turntable for the rotating mirror, together with a shaft encoder and a closed loop control system, effectively eliminates any significant uncertainty in the rotation rate $\omega$, except for that due to vibration (section 5.4.2).

A final source of error is in the assumption that the centre of the exposure time of the camera was coincident with the mirror passing through its rest position. Uncertainty here results in a further static magnification error. This was minimised by the shift controller, which times the opening of the camera shutter along with the rotation of the mirror. The small delay between sending a trigger signal to the camera and the actual opening of the shutter was an input parameter to the shifter control program. This delay was measured for the type of camera used by Skyner (1992).

### Image capture errors

- *Lens aberrations*—Magnification errors due to pincushion/barrel distortion were minimised by the use of a Zeiss Planar $T^*$ lens. Manufacturer's data stated that the barrel distortion reached a maximum of about 1% at the outer edges of the frame.

- *Film/sensor errors*—McCluskey (1992) discusses the various errors which arise from the use of photographic film in PIV. These are: film noise (graininess and variations in emulsion thickness), adjacency effects (related to the developing process) and shrinkage. The first two errors can be virtually eliminated by the use of high resolution film and following proper darkroom procedures. The latter is irrelevant if magnification calibrations are performed, and all films for a particular calibration are handled in the same way.

  Where CCD sensors are used (in this study, one was used in the *analysis* phase), similar errors arise from uncertainty about the pixel dimensions. Again, calibration reduces these errors to the uncertainty in the calibration itself.

### Analysis errors

1. *Magnification errors*—Many of the errors mentioned above are best understood as affecting the magnification of the image, which allows translation from image plane co-ordinates to physical co-ordinates. In almost all cases the basic magnification is fixed by placing an object of known dimensions into the plane of the light sheet, and measuring its size in the image plane. Determination of the magnification by estimating optical distances can be done only after cross-checking against a calibration.

2. *Analysis calibration*—Where a Young's fringe analysis method is used, the separation of the fringes (which gives the particle displacement) is related to the distance from the film to the plane in which the fringes are observed. This is accounted for by calibrating the analysis rig against a simulated PIV negative where the image displacements are known *a priori*. When direct analysis of a digitised image is used, this error does not arise. The analysis rig used for the study was used concurrently by Quinn (1995), who estimated the analysis rig calibration error to be 0.1%.

3. *Velocity gradient biasing*—In extracting a single velocity vector from an interrogation area, the assumption is made that the local fluid velocity does not change

significantly over that area. In regions of strong velocity gradient, two problems arise. Firstly, the variation in image separation tends to lower and broaden the correlation peaks, increasing the probability of the peak being obscured by noise. Secondly, if the peak is successfully detected, the peak centroid does not simply correspond to the local velocity averaged over the interrogation area. Rather, as faster particles have a higher probability of moving out of the interrogation area between illuminations, and thus contributing nothing to the auto-correlation, a statistical bias in favour of the lower velocities is introduced.

From an equation presented by McCluskey (1992), due to Keane and Adrian (1990), it can be estimated that for the flow of interest, if a worst case variation of velocity across the interfacial shear layer is 50%, the error introduced there is less than 1.5%.

4. *Out-of-plane motion*—If the fluid motion has a velocity component normal to the plane of the light sheet, an enhancement to the observed velocity at the extremities of the light sheet results. This is caused by parallax effects. In order to estimate the error which results, it is necessary to know the magnitude of the out-of-plane motion. In the internal wave experiments, it seemed reasonable to regard this component as zero, since there was no exitation for out-of-plane motions.

   Where an out-of-plane component is present, the error can be minimised by the use of a telephoto lens at a greater distance from the flow, or, if this is not possible, a telecentric lens may be used.

5. *Quantisation errors*—In the Young's Fringe analysis method used, the resolution of the CCD camera restricts the accuracy which may be attained by the analysis system. Fortunately, the fringes always span a large number of pixels. This fact combined with the image depth (8-bit gray levels) allows estimation of the fringe separation to much greater accuracy than the $256 \times 256$ array size might seem to allow.

   The reverse Fourier transform was performed on a $64 \times 64$ grid. Here, however, the "depth" was that of the floating point type `double` in the C language (64 bits on a PC running MS-DOS).

   The significance of quantisation is far greater in direct analysis of digitised images, where the chance of a particle not covering at least two pixels in each direction is much higher. Should this happen, the velocity resolution is immediately cut to the spatial resolution of the interrogation area (normally about $64 \times 64$ pixels), and image depth does not help. This is a particular problem with video cameras,

which normally employ field separation, cutting the vertical resolution down to 240–290 pixels over the whole field. This is the main reason why traditional photographic methods were employed in the study.

### 5.4.2 Errors specific to stratified flows

Two main classes of problems arise when flow measurement techniques are applied to stratified flows. The first is that the velocities of interest are typically an order of magnitude smaller than those in unstratified flows (e.g., surface waves against internal waves; forced circulation against natural convection). These very low velocities stretch the dynamic range of most flow measurement methods. The second class of problem relates to the density variation itself. Optical methods (PIV, LDA, LIF, etc.) are affected by the differences in refractive index which are found in stratified flows. Further, density differences make the choice of seeding material difficult (as discussed in section 5.3), and the necessity of preserving stratification means that introducing seeding is difficult. Both classes of problem are discussed below.

#### Measurement of low velocities

- *Image shifter*

In theory, PIV can be optimised for low velocity ranges simply by increasing the illumination interval $\Delta t$. However, where image shifting is used, the shift velocity must also be reduced.

The scanning beam controller used in this experiment had a maximum illumination interval of $12.7ms$. The image shifter had a minimum shift velocity of $5°/s$, increasing in increments of $5°/s$. The shift velocity range proved the major constraint.

When the shifter was programmed to rotate at $5°/s$, poor correlation was observed. Close examination of the images showed that the particle tracks were not always straight, but toward the edges of the frames, considerable waviness in the tracks was found (figure 5.9). This waviness was attributed to vibrations being set up in the rotating mirror by the motor or the control system, presumably by the excitation of a natural frequency of the mirror. This was confirmed by measurements using an accelerometer on the mirror as it rotated. Therefore it was necessary to use the shifter at $10°/s$.

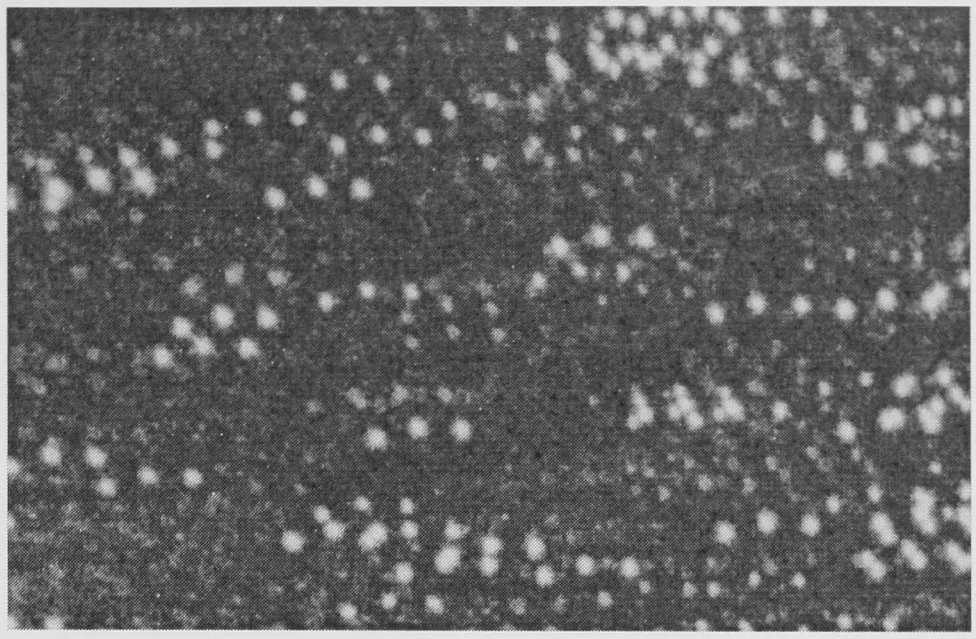

Figure 5.9: *Close-up of a PIV image affected by shifter vibration. Successive images of a particle do not show a constant displacement (compare figure 5.1).*

The ideal shift velocity for a flow field containing reversing velocities is slightly greater than the maximum negative velocity present. This makes all of the velocities positive. As shown by Morrison (1995; section 5.4.1), in this case shift distortion creates errors of approximately 10% of the maximum velocity present. In this study, typical maximum velocities were $50mm/s$, and typical shift velocities were $300mm/s$. A simple calculation shows that in this case, the shift errors can be expected to be of the same order of magnitude as the velocities in the flow.

It was therefore impossible to leave the vector maps uncorrected, and the method of still-water calibrations described in section 5.4.1 was essential.

- *Residual motion*

  If the phenomenon of interest is created in a fluid initially at rest, it is important that the fluid be genuinely at rest before starting the experiment. If this is not achieved, residual motions will be prominent in the measurements and may obscure the motions of interest.

  The introduction of the seeding was the main source of residual motion. By introducing seeding into the bottom of the tank and allowing it to slowly rise until a good distribution was obtained, there was also time for the vorticity generated to dissipate.

  Motion due to waves from a previous experiment was minimised by the wave absorber at the far end of the tank. Wave motions were observed on an oscilloscope,

and another experiment was not commenced until the previous waves had died away to about 1% of their initial amplitude.

### Density effects: seeding motion

Differences in density affect the errors related to the seeding in two ways. Firstly, the particles will rise faster under gravity in the denser fluid than in fresh water. Secondly, calculations of the degree to which the particles follow the fluid motion will have to be revised, since they depend on the difference in density between the particle and the fluid.

1. *Rise time*

   The density of conifer pollen was estimated empirically by Bruce (private communication) to be about 10% lower than that of fresh water. Stokes' law thus gives a rise velocity of $\sim 0.3mm/s$. The maximum density of fluid used in the experiments reported here was $\sim 10\%$ greater than that of fresh water. As Stokes' law is linear, the rise velocity in the denser fluid will be approximately $0.6mm/s$.

   Pollen is a natural material whose properties vary from season to season. Also, pre-soaking of the pollen is likely to increase its density to that of the water (though whether the pollen takes up saline solution or not is not known). Observations in the experiments suggested that the rise velocities given above were reasonable for the denser layer, but that the stability of the pollen in the fresh layer was greater than anticipated.

2. *Frequency response*

   The frequency response of a particle of density $\rho_p$ in a fluid of density $\rho_f$ is predominantly linear in $\rho_f$. This is shown by figure 5.10, which is an empirical plot of the particle response at different fluid densities from the equation given by Hinze (1975). In this plot, the frequency is 16Hz, while the particle density has been fixed at $\rho_p = 900\,\mathrm{kg/m^3}$. The particle diameter is $70\mu$m and the viscosity is that of fresh water. Even at this relatively high frequency it is seen that the particle follows the flow very closely.

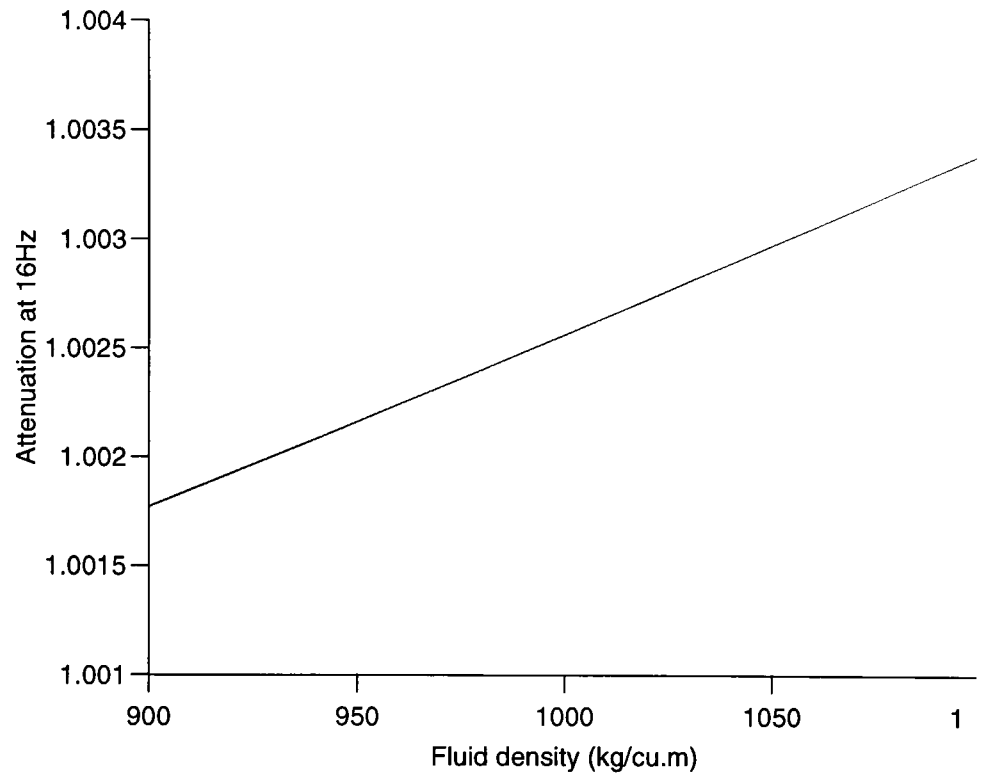


Figure 5.10: *Attenuation ratio of particle motion against fluid density*

### Density effects: optical distortion

The difference in refractive indices between fresh water and saline solution affects both incoming light and light scattered by the particles. The motion of the density interface will modify the path of an incoming laser beam, but since the timescale over which the density interface moves is long compared to the illumination interval $\Delta t$, it can be assumed that the effect on $\Delta t$ will be very small.

Of much greater concern is the effect of the stratification on the path of the scattered light. Observation of a stratified flow clearly shows that optical paths are distorted (figure 5.11), and in fact this distortion is of sufficient magnitude for it to be useful in visualising the motion of isopycnals. This is the principle of the shadowgraph and Schlieren photography.

Refractive index changes affect all optical techniques, including LDA and LIF. Consequently, efforts have been made to get around the distortion problem. For use with LDA, McDougall (1979) created a flow in which the refractive index was constant but the density was not. He did this by mixing Epsom salts into one layer and sugar into the other. This choice of solutes, for the density ranges of interest, made it possible to eliminate the possibility of double-diffusive convection which can occur in a flow with more than one stratifying quantity (Turner, 1973). McDougall's tank held a volume of about 50 litres, and the experiments were conducted with a density difference of 1.5%.

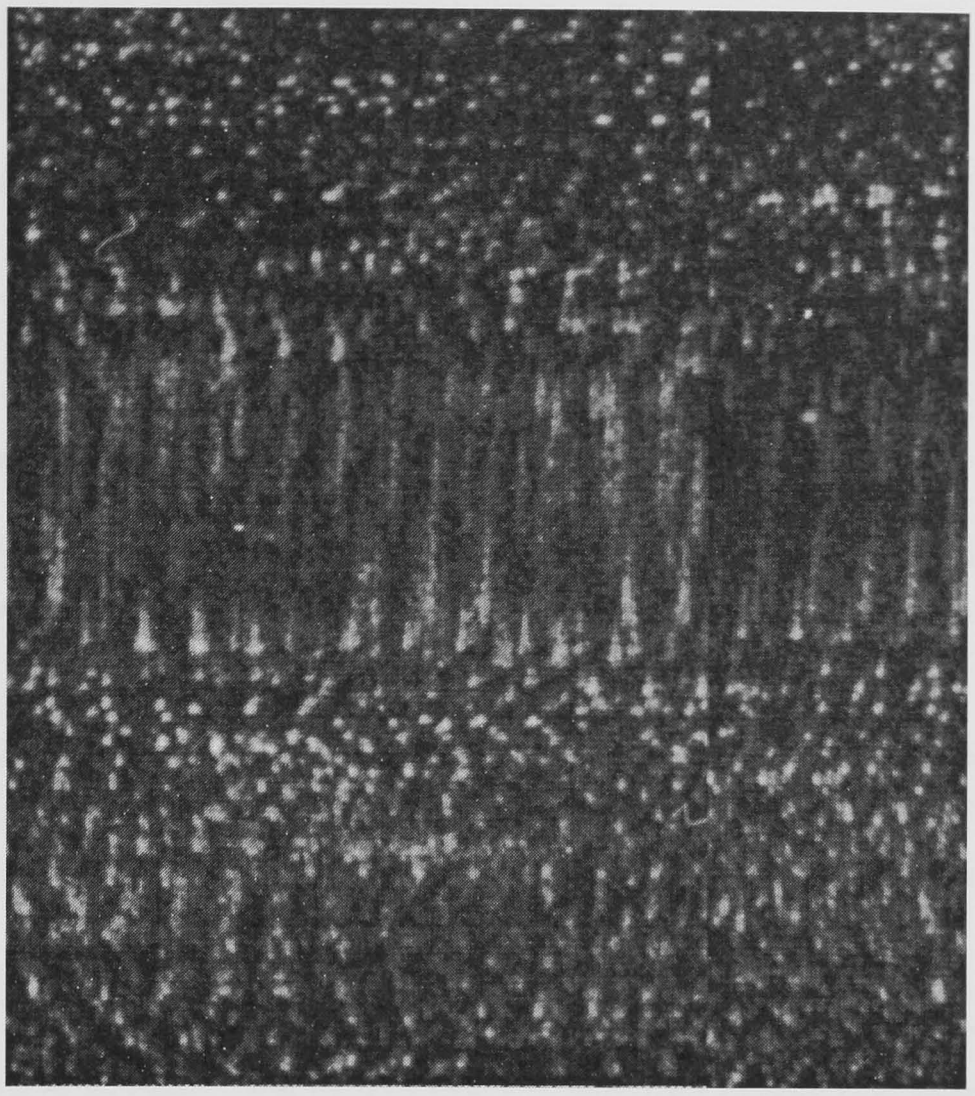

Figure 5.11: *Close-up view of the refractive index distortion of a PIV image*

For LDA experiments in a larger tank (approximately $4.5m^3$) with a density difference of up to 2%, Hannoun et al. (1988) found it necessary to use ethyl alcohol and common salt as the stratifying solutes. Epsom salts were eliminated because of cost.

The effort in matching refractive indices made by these experimenters was considerable. In LDA work these efforts are especially important since the refractive index variations create severe signal drop-out. Further, as the two LDA laser beams are also in motion as a result of the refractive index gradient, a random velocity shift is superimposed on the results.

The PIV experiments differed from the LDA ones on this matter in several ways:

1. For the velocities to be measurable, a density difference of the order of 5–10% was required. This took the desired performance of any compensation scheme well outside the range achieved by either Hannoun et al. or McDougall.

2. Signal drop-out due to the refractive index variations was expected to be small and confined to the density interface.

3. The error induced by the motion of the laser beam was expected to be similar to the systematic error in the scanning beam system (up to 0.5%).

4. Errors due to deviation of scattered light were expected to be confined to measurements made through the interface (the error in the upper and lower layers being small).

5. Equipment for matching refractive indices (a refractometer), as well as storage and mixing equipment for the large volume of water (up to $1.5\text{m}^3$) was not available.

For these reasons, it was decided that no attempt would be made to eliminate the refractive index variation in the flow, but that the magnitude of the error induced would be calculated by ray tracing. The ray tracing method[5] is as follows:

1. Properties of the camera lens and film format, together with knowledge of the geometry of the flow, allow calculation of the path of light through the system. A thin lens formula is used. A ray, assumed to start *on the film*, is traced back through the centre of the lens to the tank wall.

2. The transformation of the ray as it is refracted by the glass wall of the tank is calculated.

3. The following equation governs the propagation of the ray through the stratified fluid to the measurement zone (Born & Wolf, 1959):

$$\frac{d^2\mathbf{r}}{ds^2} = \frac{\nabla n}{n} \tag{5.7}$$

where $\mathbf{r}$ is a point a distance $s$ along a ray path in a fluid whose refractive index $n$ varies continuously. For ray tracing, this equation can be integrated twice to give the following:

$$\mathbf{r}_{k+1} = \frac{\nabla n}{n} s^2 + \hat{\mathbf{a}} s + \mathbf{r}_k \tag{5.8}$$

In this equation, $s$ is a small step along a ray path from a point $\mathbf{r}_k$ to a point $\mathbf{r}_{k+1}$. Here $\hat{\mathbf{a}}$ is the unit vector which gives the direction of the ray at point $\mathbf{r}_k$.

[5]Suggested by Dr Michael Jackobsen, Department of Physics, Heriot-Watt University

This equation is used to step along the ray path through the fluid to the measurement zone. The refractive index $n$ may vary in all co-ordinates, but in this implementation it varies only in $z$ (vertical co-ordinate) and, when a wave passes, in $x$ (co-ordinate in direction of wave propagation). The density, and hence the refractive index, is assumed constant along the optical axis $y$.

4. The refractive index field is derived from the density field using known characteristics of aqueous sodium chloride (Lide, 1993). Typical stratification and wave parameters are used to create the density field.

5. The distortion due to the refractive index variation is expressed as a variable magnification (ratio of image size to object size) across the field of view. The magnification is calculated in both $x$- and $z$-components.

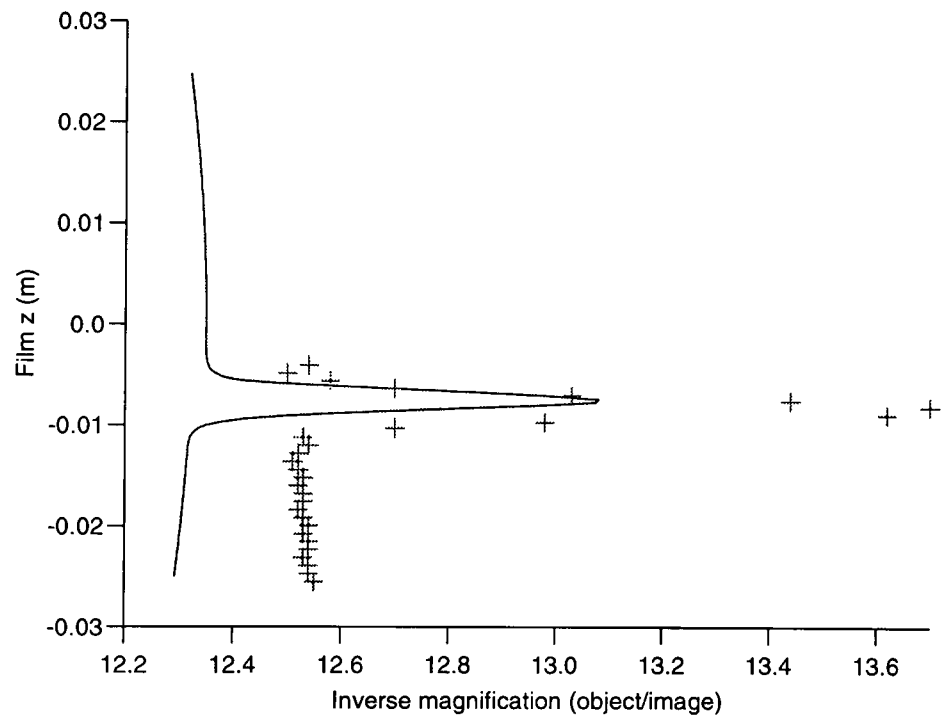


Figure 5.12: *Predicted (—) and measured (+) inverse vertical magnification*

The calculated $z$-component of magnification was checked against a static magnification calibration image. A vertical length scale was placed in the measurement zone and photographed prior to many of the experiments. Figure 5.12 shows the reciprocal of the magnification calculated using the ray tracing method against that measured with the vertical scale. It can be seen that the ray tracing method underestimates the distortion in the interface in this case, but that it predicts its extent and location well.

The disparity between the prediction and the measurements is not surprising considering the uncertainty in the measurements of the interface characteristics and the optical system geometry, as mentioned in connection with image shifting (section 5.4.1). It

is noted that through most of the flow the magnification is predicted to within 2.5%, while in the interface the deficit is less than 5%.

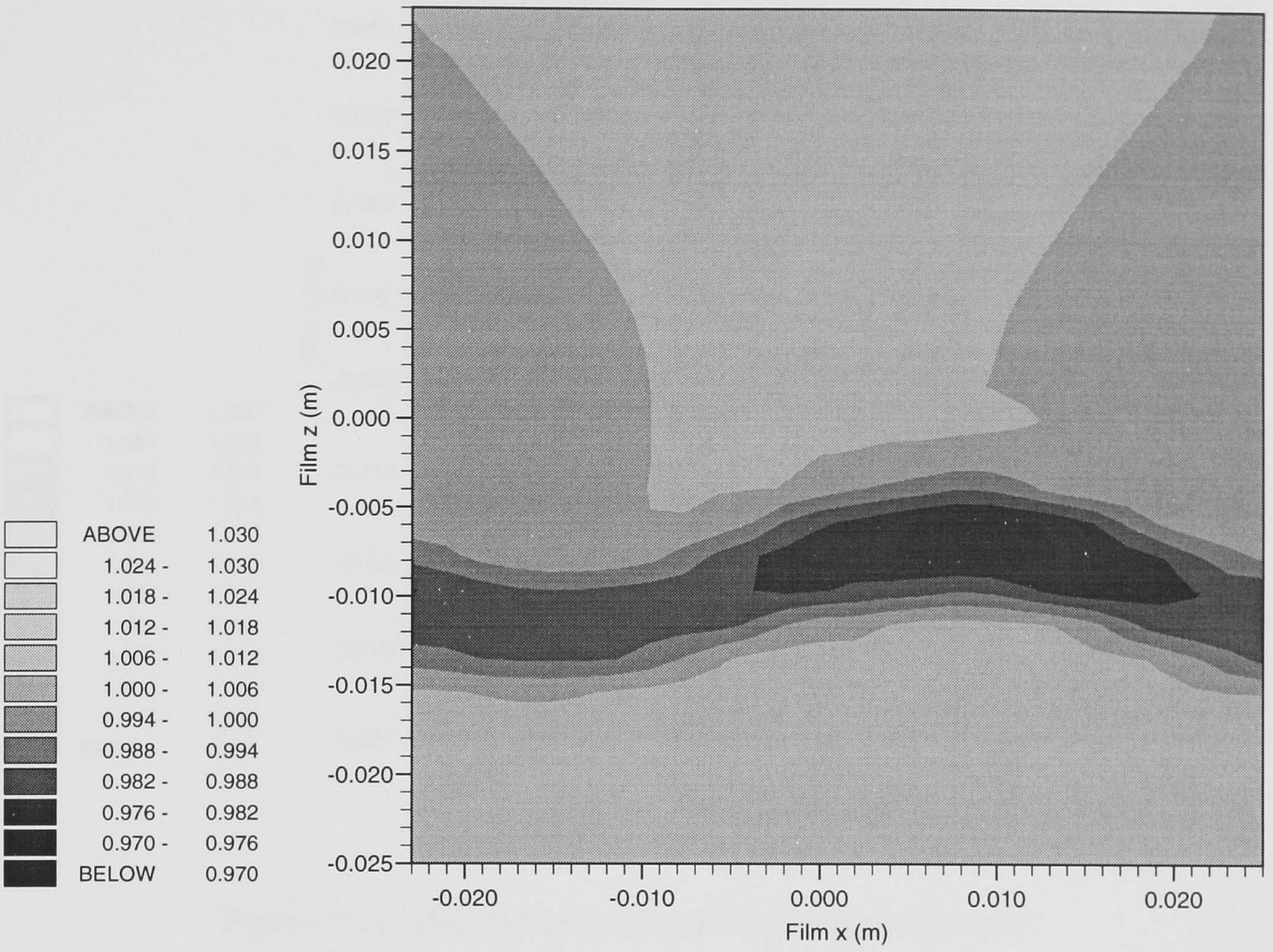


Figure 5.13: *Relative error in vertical magnification*

For all of the experiments, a value for the magnification was obtained using a simple optical calculation based on fresh water. This was found to be consistent with the measured value in several experiments, and so this method was used for all subsequent experiments. An error of less than 2.5% is therefore assumed away from the interface, but in the interface it rises to 11%.

To test the effect on the distortion of the movement of the interface, magnification maps were simulated for the $x$- and $z$-magnifications over a 120-format negative ($50 \times 50$mm) during the passage of a typical wave. These maps are shown in figures 5.13 and 5.14 respectively. The maps show the ratio of the distorted magnification to the magnification which would occur in fresh water. The wave has a wavelength of 0.5m and an amplitude of 0.03m (a large wave of frequency $\sim 0.4$Hz), and the density changes by 8.8% over about 24mm.

It can be seen that only a small distortion occurs away from the interface. It is also seen that the $x$-distortion is very small. This is to be expected, given that the slope

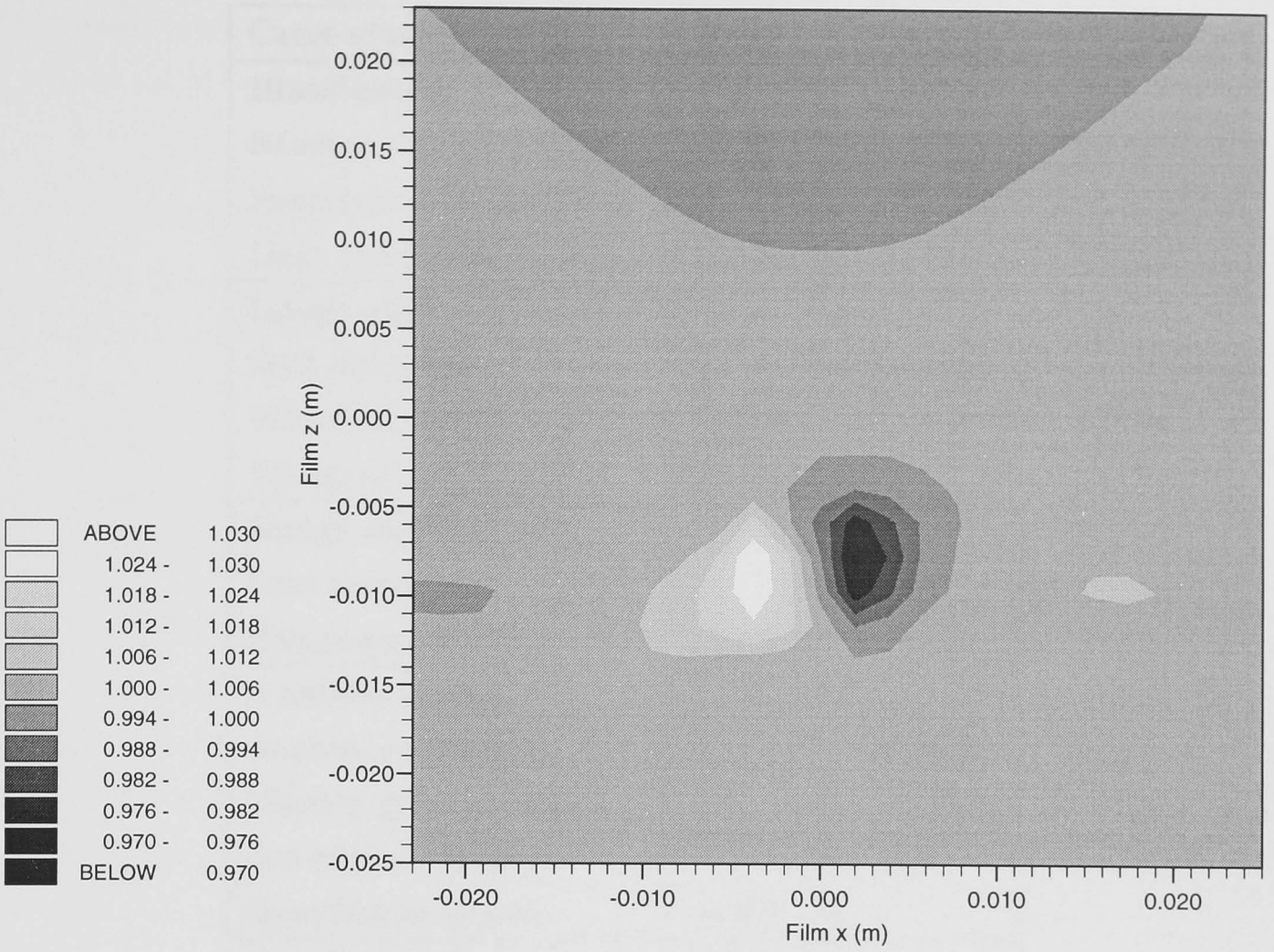


Figure 5.14: *Relative error in horizontal magnification*

of the interface is never great even in large, short waves. The strong distortion near the horizontal origin is believed to be a numerical instability which occurs near $x = 0$ (which is a singularity in this scheme).

### 5.4.3 Summary of errors

Table 5.1 is a summary of the magnitudes of the various random and systematic errors present in the velocity measurements. Each of the systematic errors acts differently. A rough upper bound for the combined errors away from the interface is about 9%, while in the interface the total error is about 17%.

## 5.5 Retrospective on this PIV implementation

The PIV implementation used for these tests was adequate for measuring velocities in the medium to high end of the flow range. It was not capable of accurately measuring

| Cause of error | Random | Systematic |
|---|---|---|
| **Illumination** | | |
| Random scan time error | $\sim 0\%$ | |
| Systematic scan time error | | $< 0.1\%$ |
| Light sheet form | $< 1\%$ | |
| **Image shift** | | |
| Shift distortion | | Removed |
| Vibration: $10°/s$ | Small | |
| Vibration: $5°/s$ | Large | |
| **Image capture** | | |
| Lens aberrations | | 1% |
| Film/sensor errors | $\sim 0\%$ | |
| **Analysis errors** | | |
| Analysis calibration | | 0.1% |
| Velocity gradient biasing | | $< 1.5\%$ |
| Out-of-plane motion | | 0% |
| Quantisation errors | $\sim 0\%$ | |
| **Seeding motion** | | |
| Residual motion | $\sim 1\%$ | |
| Buoyancy | | 1.5% |
| Frequency response | | $\sim 0\%$ |
| **Refractive index effects** | | |
| Away from interface | | $< 2.5\%$ |
| Within interface | | 11% |

Table 5.1: *Summary of the errors in the velocity measurements*

the lower velocities present in the smaller waves. Several areas where improvements could be made in the future were identified. These are:

1. **Image shifting**

   The image shifting system introduced the most significant errors into the measurements, and made it impossible to measure the velocities in small waves. Vibrations in the mirror were the largest problem, preventing the use of the lowest shift speed. A more rigid mirror mount might help to alleviate the problem.

   Shift distortion, being a systematic rather than a random error, was less of a problem. Still water calibration pictures were used to remove this error. A

more neutrally buoyant seeding material would have increased the accuracy of the calibrations, since it would have been possible to leave the tank to settle for a much longer period after introducing the seeding.

2. **Analysis method**

   The Young's Fringe auto-correlation analysis system was rather slow and inflexible, though it did make good use of the resolution of the photographic film. If a cross-correlation CCD camera had been available, direct analysis of digitised images would have been performed using cross-correlation, dispensing with the need for the image shifter. The effect of this would have been to dramatically increase the accuracy of the measurements.

3. **Refractive index correction**

   Had a more accurate density probe been available, it might have been possible to correct for the refractive index distortion explicitly. However, accurate knowledge of the wave shape would be required for this to be effective. The use of different solutions to match the refractive indices might be possible, but additional liquid storage would be required, and handling difficulty would be increased.

4. **Seeding material**

   A variety of seeding materials were tried in order to find the best for the flow. Some alternative seeding materials which were not tried might perform slightly better. These were not known about at the time of the measurements. They are:

   - Ceramic microbubbles are manufactured for similar purposes to the glass microbubbles (Sphericel) described in section 5.3. The distribution of density in the ceramic bubbles is not known; however, if it is similar to that of the Sphericel, then the ceramic bubbles would probably perform very well. This is because the main drawback of the Sphericel was the lack of side-scattered light, while the opaque ceramic bubbles would probably scatter much more efficiently.
   - It was suggested by Mr Tully Peackocke that the glass Sphericel could be coated with a very thin layer of silver. The coat would not need to be particularly stable as the particles would not suffer much abrasion in use. The cost of silvering would also not be particularly high. The effect of the silver on the particle density would not be relevant, since a large fraction of the Sphericel is lighter than the fluid.
   - Fluorescent polymer microspheres are manufactured for flow measurement applications. Unfortunately these particles are rather expensive, and do not have a distributed density.

# Chapter 6

# Results

The parameter space of the experiments is presented and subdivided into short waves, intermediate length waves, long waves, and waves with a continuously stratified upper layer. For each of these categories wave gauge traces are discussed followed by qualitative assessment of the velocity measurements. Where possible, quantitative assessments of the measurements against theoretical predictions (linear, second order and KdV) are made, and it is shown that while theory compares reasonably well in the short waves, the kinematics are not adequately predicted in the longer waves. Using numerical experiments, features of the theory are identified, and an example ocean-scale comparison is made.

## 6.1 Summary of experiments selected

A total of 63 films of 12 frames each were exposed for this study. About 1/3 of these were spent adjusting the PIV technique to the particular situation of internal waves. A further 1/3 gave poor results, mainly due to two problems: (i) shifter vibration, and (ii) limited dynamic range at the lower end of the velocity scale. Consequently small-amplitude waves could not be reliably measured, and so the results which will be presented here are all for moderate to large amplitudes.

The sample space of the experiments can be divided as follows:

- Short waves in a nearly two-layer stratification, where the wavelength $\lambda < H_{1,2}/3$ and $H_{1,2}$ refers to the upper and lower layers respectively:
- Intermediate length waves in a nearly two-layer stratification (for which only a few cases are available);
- Long waves in a nearly two-layer stratification, where $\lambda > 10H_{1,2}$ at least (in most cases $\lambda > 16H_{1,2}$);
- Waves where the upper layer is linearly stratified (with both intermediate and long wavelengths).

The long wave cases can be subdivided into those where the layers were of equal depth, and those where one layer (the upper layer) was considerably shallower than the other. These last cases simulate the ocean thermocline more closely than the others. In the cases where one layer was linearly stratified, that layer was always shallower than the homogeneous (lower) layer.

A summary of the parameters of the experiments which were selected for further analysis is given in table 6.1. Experiments are numbered first by a film number (e.g. f019), and then by an experiment number within that film (1, 2, etc). In most cases only one or two experiments were run for each film.

## 6.2 Short waves

### 6.2.1 Arrangement

The measurement zone for the short wave tests was close to the centre of the tank (centred around 2.6m from the wavemaker). This was done to maximise the time available before reflected waves returned to the measurement zone, yet still allowing the waves to evolve for a few wavelengths. Typically, the water was stratified in two equal layers, each of depth around 0.25m. This allowed the generation of a reasonable range of wavelengths which would fall into the category of short waves.

| Film, experiment | frames | f | $\Delta\rho/\overline{\rho}$ | $\delta$ | $H_1$ | $H_2$ | $H_{1/3}$ | Regime | Figures |
|---|---|---|---|---|---|---|---|---|---|
| f019, 01 | 4 | 0.3 | 9.4% | 0.012 | 0.222 | 0.271 | 0.031 | Short | 6.1, 6.7 |
| f019, 02 | 2 | 0.3 | 9.4% | 0.012 | 0.222 | 0.271 | 0.038 | Short | 6.1 |
| f023, 01 | 4 | 0.4 | 10.4% | 0.016 | 0.236 | 0.254 | 0.037 | Short | 6.3 |
| f023, 02 | 3 | 0.4 | 10.4% | 0.016 | 0.236 | 0.254 | 0.036 | Short | 6.3, 6.8 |
| f023, 03 | 4 | 0.4 | 10.4% | 0.016 | 0.236 | 0.254 | 0.033 | Short | |
| f029, 01 | 5 | 0.2 | 8.8% | 0.019 | 0.245 | 0.254 | 0.032 | Short | 6.4 |
| f029, 02 | 5 | 0.3 | 8.8% | 0.019 | 0.245 | 0.254 | 0.030 | Short | 6.9 |
| f038, 01 | 4 | 0.2 | 4.9% | 0.016 | 0.249 | 0.251 | 0.030 | Short | 6.10 |
| f038, 02 | 4 | 0.2 | 4.9% | 0.016 | 0.249 | 0.251 | 0.056 | Short | 6.5, 6.11 |
| f039, 01 | 4 | 0.2 | 4.9% | 0.022 | 0.244 | 0.256 | 0.024 | Short | 6.10 |
| f039, 02 | 5 | 0.2 | 4.9% | 0.022 | 0.244 | 0.256 | 0.033 | Short | 6.5, 6.11 |
| f048, 01 | 11 | 0.2 | 8.8% | 0.012 | 0.146 | 0.155 | 0.040 | Intermediate | 6.16, 6.18 |
| f052, 01 | 10 | 0.2 | 8.8% | 0.015 | 0.119 | 0.180 | 0.082 | Intermediate | 6.16, 6.19 |
| f028, 01 | 10 | 0.1 | 8.8% | 0.012 | 0.248 | 0.251 | 0.020 | Long, equal layers | 6.21, 6.26 |
| f031, 01 | 10 | 0.1 | 9.7% | 0.014 | 0.146 | 0.154 | 0.022 | Long, equal layers | 6.21, 6.27 |
| f035, 01 | 10 | 0.1 | 9.7% | 0.005 | 0.065 | 0.186 | 0.071 | Long, unequal layers | 6.23, 6.28, 6.29, 6.30 |
| f036, 01 | 10 | 0.1 | 9.7% | 0.035 | 0.079 | 0.164 | 0.022 | Long, unequal layers | 6.23 |
| f040, 01 | 9 | 0.2 | 8.8% | 0.045 | 0.058 | 0.168 | – | Stratified upper layer | 6.33, 6.38 |
| f043, 01 | 10 | 0.1 | 8.9% | 0.031 | 0.042 | 0.261 | – | Stratified upper layer | 6.34 |
| f044, 01 | 10 | 0.1 | 8.9% | 0.040 | 0.051 | 0.252 | – | Stratified upper layer | 6.35, 6.39 |

Table 6.1: *Experiments selected; here $f$ is the paddle oscillation frequency (Hz), $\Delta\rho/rhobar$ is the percentage difference in density from the fresh water to the saline solution, $2\delta$ is the interface thickness (m), $H_{1/3}$ is the significant wave height (m, see section 6.2.5) and $H_1$ and $H_2$ are the upper and lower layer depths respectively (m).*

### 6.2.2 Wave height gauge traces

Two wave gauges were used for these tests, one just upwave from the measurement zone (1.8m from the wavemaker), and another just downwave (3.6m from the wavemaker). Two gauges were used to enable the calculation of phase velocities and hence wavelengths from the gauge traces. The intention was to use this information to infer the shape of the wave in the measurement zone at the measurement time. In practise, instabilities in the wave shapes made this inference difficult. At the time it was considered too awkward to place a wave gauge in the measurement zone, because of optical considerations and laser safety. In retrospect this would have been worth some extra effort, although in fact transformation of the temporal wave gauge signal into a spatial wave shape would still have been subject to error.

Some typical wave gauge traces for the short waves (with corresponding film and experiment numbers) are shown in figures 6.1–6.5. In these figures the measured significant wave height ($H_{1/3}$) is used (this is discussed in section 6.2.5).

#### Wave group formation

All of the example traces clearly show a tendency for the waves to form wave "groups" as they propagate down the tank. This may be due to an instability akin to the Benjamin–Fier instability of short surface waves (Lighthill, 1978). This should be expected, for, as Lighthill points out, "To every property of surface gravity waves noted...there are corresponding properties of internal waves." (p.468). Benjamin–Fier instability, a consequence of non-linearity in short, steep waves, causes progressive waves to concentrate their energy into distinct wave "groups" or "packets".

In most of the experiments, the wavemaker amplitude was constant throughout the experiment, rather than being ramped gradually from zero to the working level at the start. This would have tended to make the "grouping" behaviour more obvious at the start of the wave train. Later experiments (from films f045 onwards) were performed with a gradual ramping of the paddle amplitude.

An alternative explanation for the apparent "groupiness" of the waves is the possibility that free harmonics were generated by the wavemaker. Mismatch of the paddle motion kinematics with the kinematics of the generated wave could have caused such behaviour, and this would be seen as an irregularity in the wave shape.

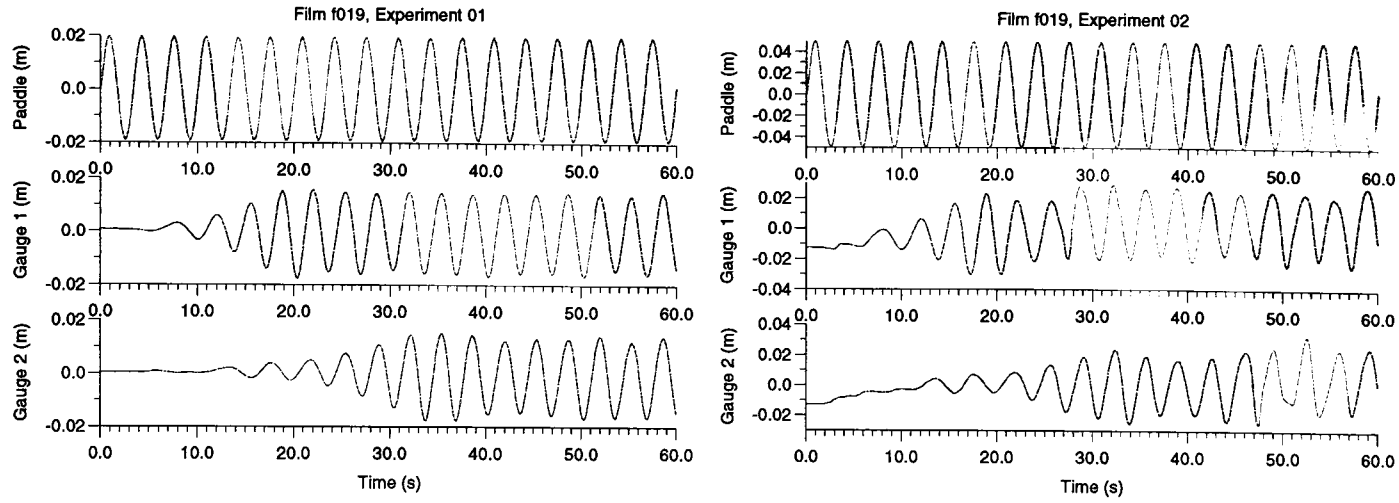


Figure 6.1: *Wave gauge traces with* $f = 0.3Hz$, $\Delta\rho/\overline{\rho} = 9.4\%$. *Left picture:* $H_{1/3} = 0.031m$; *right picture:* $H_{1/3} = 0.038m$

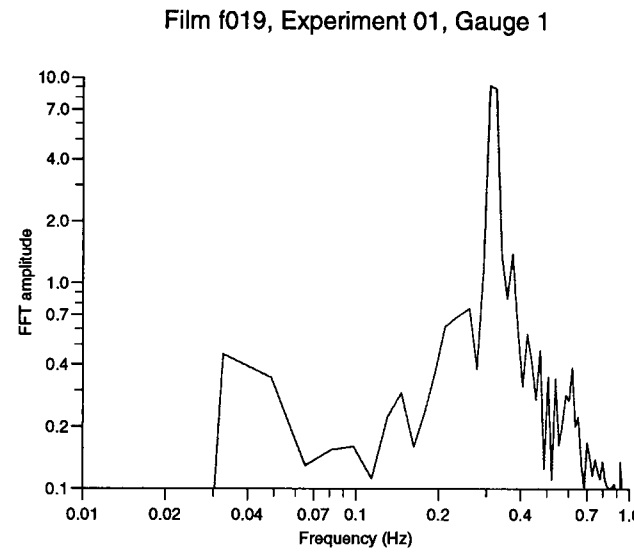


Figure 6.2: *Fourier transform of gauge 1, experiment 01 in figure 6.1*

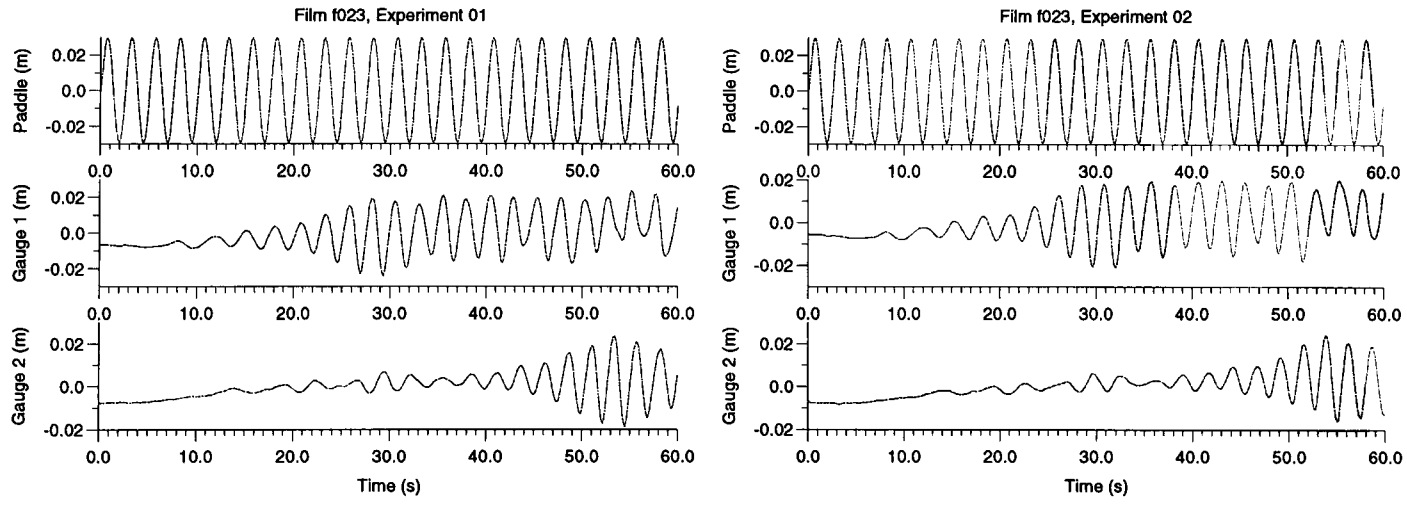


Figure 6.3: *Wave gauge traces with* $f = 0.4Hz$, $\Delta\rho/\overline{\rho} = 10.4\%$, $H_{1/3} \simeq 0.036m$; *consecutive experiments*

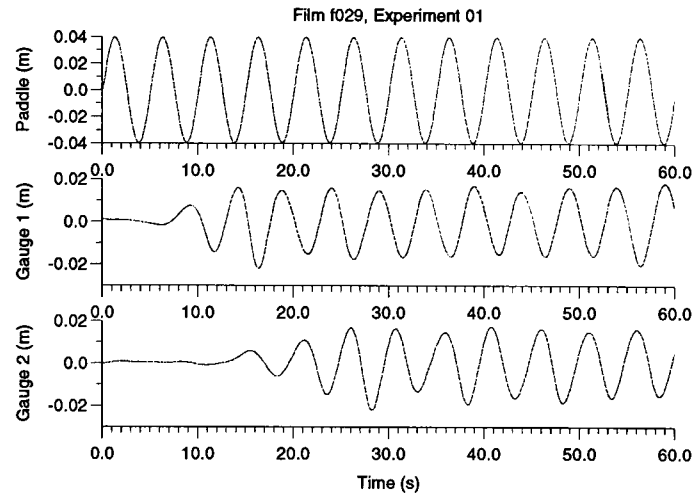


Figure 6.4: *Wave gauge traces with* $f = 0.2Hz$, $\Delta\rho/\overline{\rho} = 8.8\%$, $H_{1/3} = 0.032m$

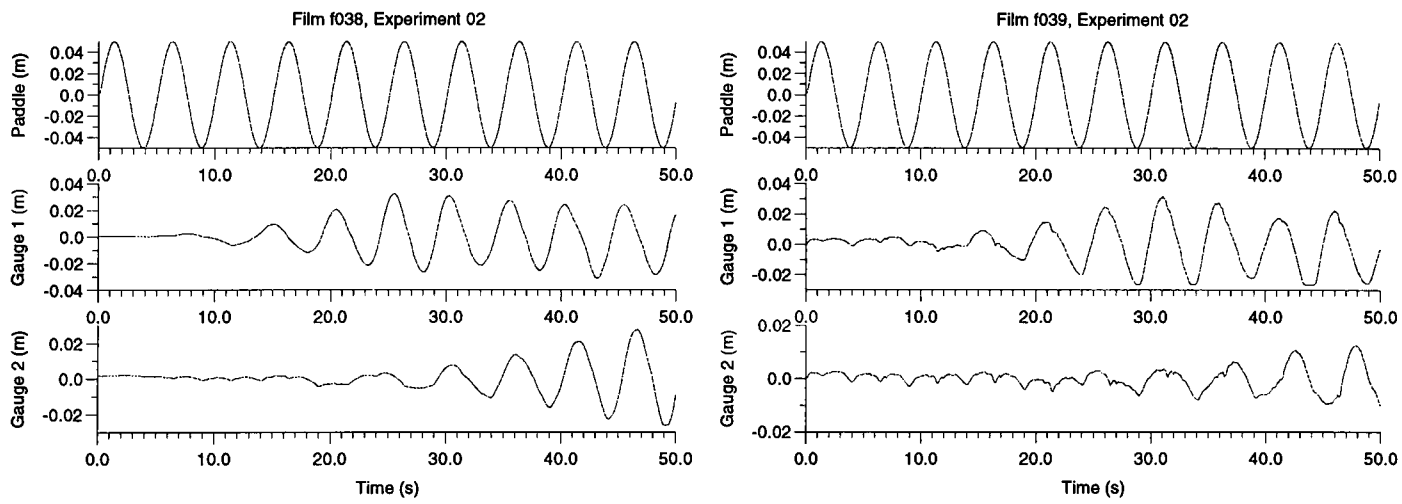


Figure 6.5: *Wave gauge traces with* $f = 0.2Hz$, $\Delta\rho/\overline{\rho} = 4.8\%$. *The right hand picture* ($H_{1/3} = 0.033m$) *shows a rerun of the experiment depicted in the left hand picture* ($H_{1/3} = 0.056m$) *after the interface had diffused overnight.*

A sample Fourier transform is shown in figure 6.2. While there is some energy in low frequencies as a consequence of the modulation, there is no particularly strong harmonic or subharmonic. Note that the second-order peak (at $0.6Hz$) is small (about 3% of the main peak height). There are small side-lobes around the main peak; however, these are expected when the main generating frequency does not fall directly onto one of the bins in the discrete Fourier transform (as in this case).

The modulation was observed to increase as the wave propagated down the tank, as seen in figure 6.3. Also, shorter waves suffered more modulation than longer ones in this set (compare section 6.3). Therefore, it is concluded that some form of instability of the Benjamin-Fier type is the most likely cause of the modulation.

In the derivation of the theory of Stokes waves (section 3.4), it was hypothesised that, due to the boundary conditions in the confined tank, there would be no relationship between wave height and phase speed to third order. The apparent Benjamin-Fier instability suggests that in fact some variation of the wave velocity with wave height was present. It would be advantageous to investigate this further by attempting to evaluate the unknown density fluctuations $f_2$ and $f_3$ in the tank; however, this was not possible with the equipment available.

The direct consequence of this instability was the transformation of the wave group as it propagated. Two problems which resulted from this were: a difficulty in calculating the phase velocity from the gauge traces, and inaccuracy in the estimation of the wave shape in the measurement zone.

### 6.2.3 Other features of wave gauge traces

Figure 6.1 shows two consecutive experiments run at different paddle amplitudes, but with the same frequency of oscillation. The instability in the wave group appears to be worse in the higher amplitude case, as might be expected if it is due to Benjamin-Fier instability. Figure 6.3 is significant in that it shows two consecutive experiments performed with virtually the same parameters. The consistency between the two traces is remarkable.

Comparing figures 6.4 and 6.5 one sees the effect of differences in the stratification on the group velocity of the waves. The latter figure shows experiments conducted with half the density difference of the former, and the group velocity is correspondingly smaller, as expected. Within figure 6.5, the effect of the thickness of the interface is

also seen, reducing the group velocity but also reducing the efficiency with which the paddle generates waves.

The increase in electrical noise in the right hand half of figure 6.5 is believed to be due to the increase in the thickness of the interface. With the thicker interface, saline solution was more inclined to periodically spill over onto the top of the paddle as it moved down. Since the paddle drive rods were made of conductive carbon fibre, they were able to transmit noise from the motor drive to the saline solution, causing the unevenness in the wave gauge trace.

### 6.2.4 Phase speed measurement for short and long waves

Estimation of the phase velocity of the waves from the wave gauge traces was achieved by the following method.

1. The time shift between corresponding peaks in the two wave gauge traces was calculated by imposing a shift time on the first trace, and then subtracting the shifted first trace from the second. The sum of the errors $s_e(t)$ at all points along the time axis, suitably normalised to remove end effects, was calculated repetitively for all possible shift times.

2. Prior knowledge of the expected wavelength allowed calculation of the number of whole wavelengths $n_w$ separating the gauges in the tank.

3. Each minimum of the error $s_e(t)$ corresponded to a particular shift time $t_s(i)$ between the gauge traces. A "residual time" $t_r(i)$ was calculated for each of these by subtracting whole wave periods $T$ from the shift times until the remainder was found. The mean residual time $\tilde{t}_r$ was then calculated.

4. The phase velocity was then calculated from the formula

$$c_p = \frac{d}{\tilde{t}_r + T n_w} \tag{6.1}$$

where $d$ is the distance between the wave gauges.

This method is clearly related to cross-correlation. Formal cross-correlation (by Fourier methods) was used at first, but the method was found to be highly sensitive to small errors in the matching of the two traces. This method is less sensitive to such errors.

Figure 6.6 is a comparison between the phase velocity calculated from the wave gauge traces and that predicted using the model described in chapter 3. This graph includes both short wave and long wave data. Intermediate length waves were not included, since only two cases were available. Cases with a linearly-stratified upper layer were omitted because the phase speed calculation could not be performed (section 6.5). It can be seen that the correspondence between theoretical and predicted phase velocities is strong.

Two outliers (data points marked $\times$ in figure 6.6; corresponding to figures 6.4 and the right hand trace in figure 6.23) were removed from the data. It is believed that incorrect phase speed calculations resulted from local minima in the error function $s_e(t)$. The potential for this is clearly seen at least in the latter case.

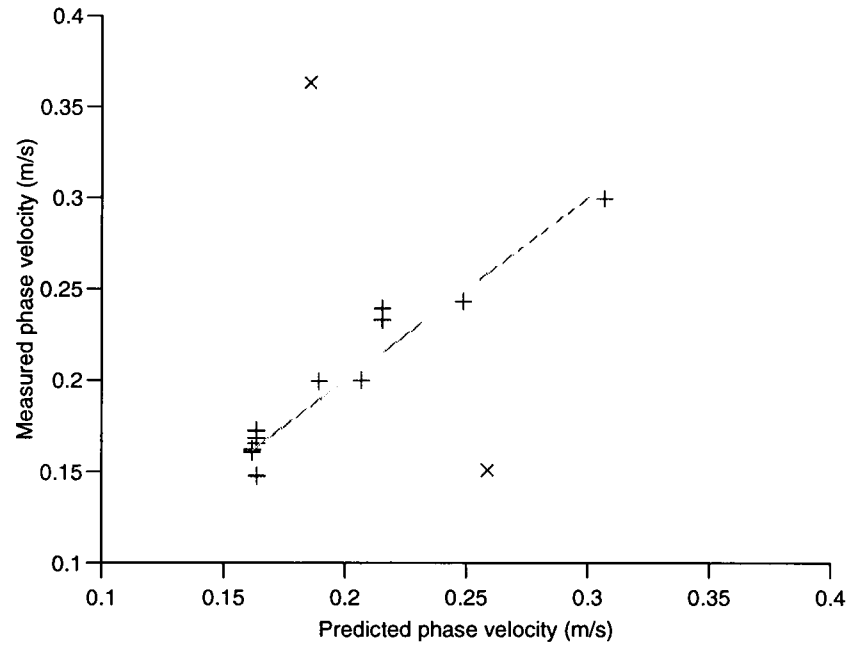


Figure 6.6: *Comparison of measured and predicted phase velocities for waves in two-layer stratification. The line shows exact correspondence.*

Performing a linear regression on this data, a coefficient of 1.007 is found, with a negligible offset. The correlation coefficient $r = 0.97$. This lends support to the assertion in chapter 3 that the phase velocity in the confined tank is not significantly modified by moderate non-linearities. The comments above regarding wave grouping must be borne in mind, however, and it would be useful to have a more accurate means of measuring the phase velocity.

### 6.2.5 Velocity measurements

#### Procedure for experimental and numerical results

The arrangement for velocity measurement by PIV is described in chapter 5, along with the various limitations of the technique in the present context. The most significant error was the shift distortion (section 5.4.1), with residual seeding motion and refractive index variation also significant. The magnitudes of these errors were controlled by the methods described in section 5.4.1, including subtraction of a fit to the still-water calibration image, which removed the shift distortion error.

A large number of velocity maps were obtained for short waves, so that they cannot all be presented here. For each map, a corresponding theoretical map was created by running either the first or second order Stokes simulation (section 3.4) based on the input parameters relating to the stratification and generating frequency, and the measured wave heights.

As discussed in section 6.2.2, calculation of the wave shape in the measurement zone, from which the wave height could be derived, was unfortunately prone to error. Consequently, the significant wave height $H_{1/3}$, defined as the mean height of the highest 1/3 of the waves in a record, was used.

From these parameters, numerical predictions were made as follows. Firstly, the first-order equation was solved to give the phase velocity. The second order equation (if required) was then solved. Finally, the phase of the wave in the measurement zone was found. This was done by repeatedly recalculating the theoretical velocity map at different phases, and evaluating the fit between it and the measured map. The fit parameter was defined as the sum of the absolute values of the difference between measured and predicted velocities, for both components. This fit parameter, with the phase shift as the only degree of freedom, was used in a minimisation algorithm using Brent's method of parabolic interpolation (Press et al., 1994).

#### Qualitative results for short waves

The full data record for all cases contains some 100,000 data points, all of which are to some degree subject to experimental error and noise. Approximately half of these points relate to short wave experiments. It is not possible to present all of these results

here, nor would it be particularly informative. However, it is worth using a selection of the short wave data record to present some of the features of short internal waves.

Although the waves travelled from right to left in the tank, all of the velocity maps are presented mirrored so that the waves are travelling from left to right. The measured velocity maps are presented alongside second order numerical predictions. The second order corrections, for reasons described in section 6.6, are relatively small for these cases.

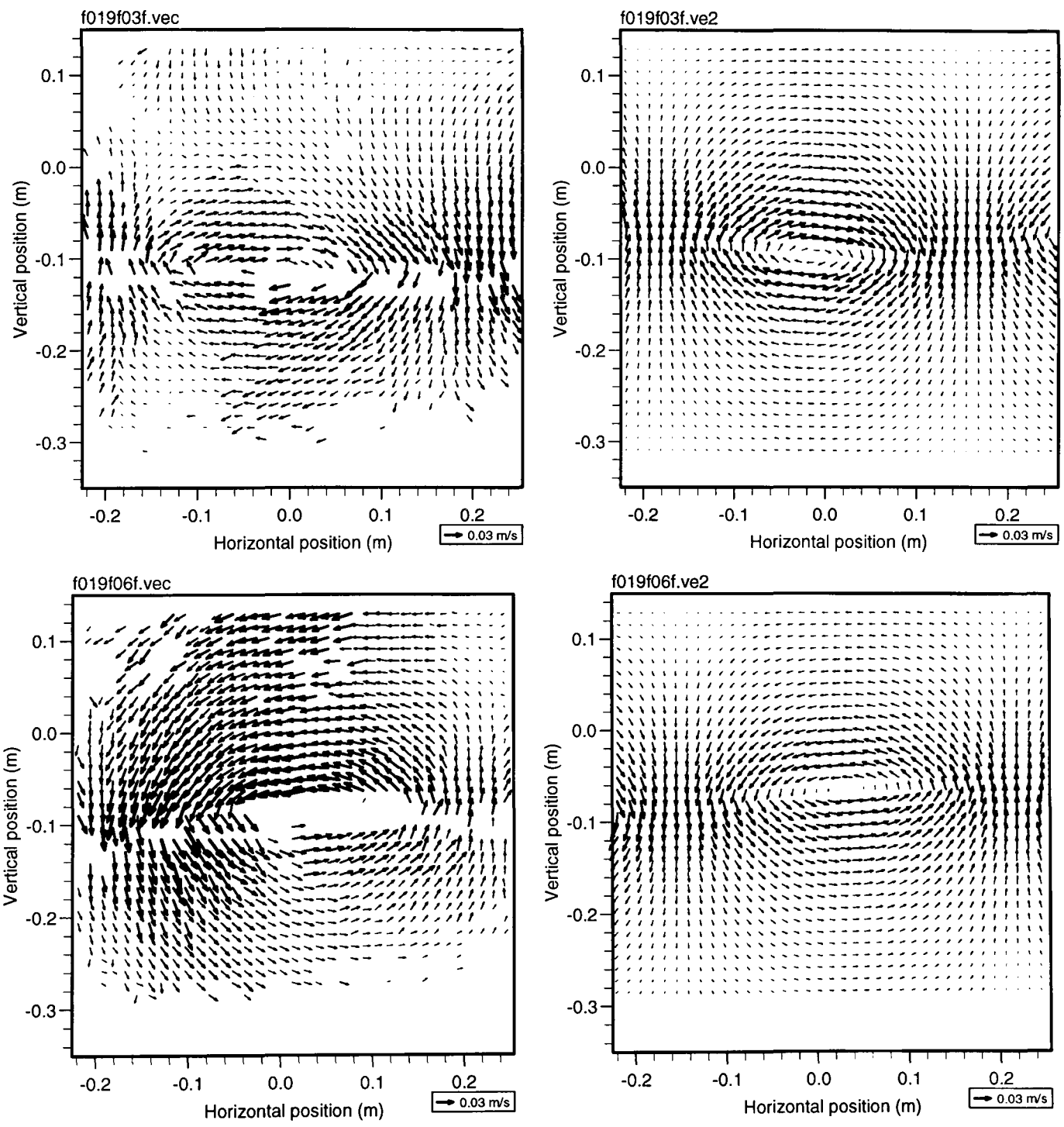


Figure 6.7: *Short wave trough (top) and crest with* $f = 0.3Hz$, $\Delta\rho/\overline{\rho} = 9.4\%$, $H_{1/3} = 0.031m$; *experimental (left) and numerical velocities*

Figure 6.7 shows typical experimental and numerical results for a typical short internal wave. The layer depths in this case (and for most of the short waves) were both

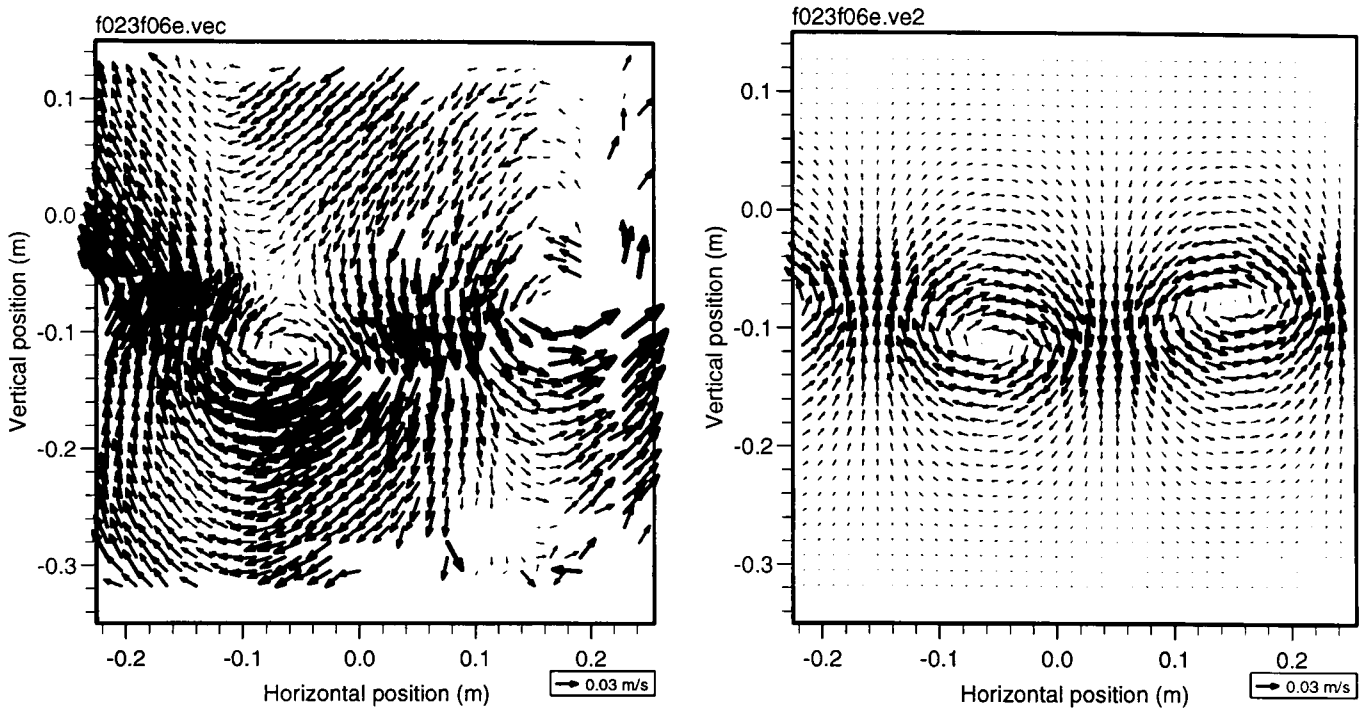


Figure 6.8: *Short wave trough and crest with* $f = 0.4Hz$, $\Delta\rho/\overline{\rho} = 10.4\%$, $H_{1/3} = 0.036m$; *experimental and numerical velocities*

approximately 0.25m, while the wave shown had $\lambda = 0.72$m. The image of the wave crest was taken 15 seconds after the wave trough (4.5 wave periods).

The blank areas in the experimental maps correspond to areas were valid velocity vectors were not obtained. Within the shear layer, few vectors were obtained. This is because optical distortion in this area (section 5.4.2) stretches the particle images and broadens the auto-correlation peak in the vertical direction, resulting in spurious results.

The wave-driven shear at the crest and trough is clearly seen, as is the strong upwelling and downwelling associated with the zero crossing points. Despite appearances, the shear layers are not sloping. Since the roots of the vectors mark the measurement points, the vectors themselves present a slightly illusory view of the shape of the flow, especially in the shear layer.

The match between numerical and experimental results is reasonably good, although there are some significant differences. Assessment of the degree of agreement is presented later in this section. There is clearly some random noise in the experimental results. Because no strong instabilities were observed in the tank, this noise is thought to be due to the factors discussed in chapter 5 rather than to turbulence.

The more systematic differences between the predictions and measurements might be ascribed to non-linearity. For reasons described in section 6.6, the second order correc-

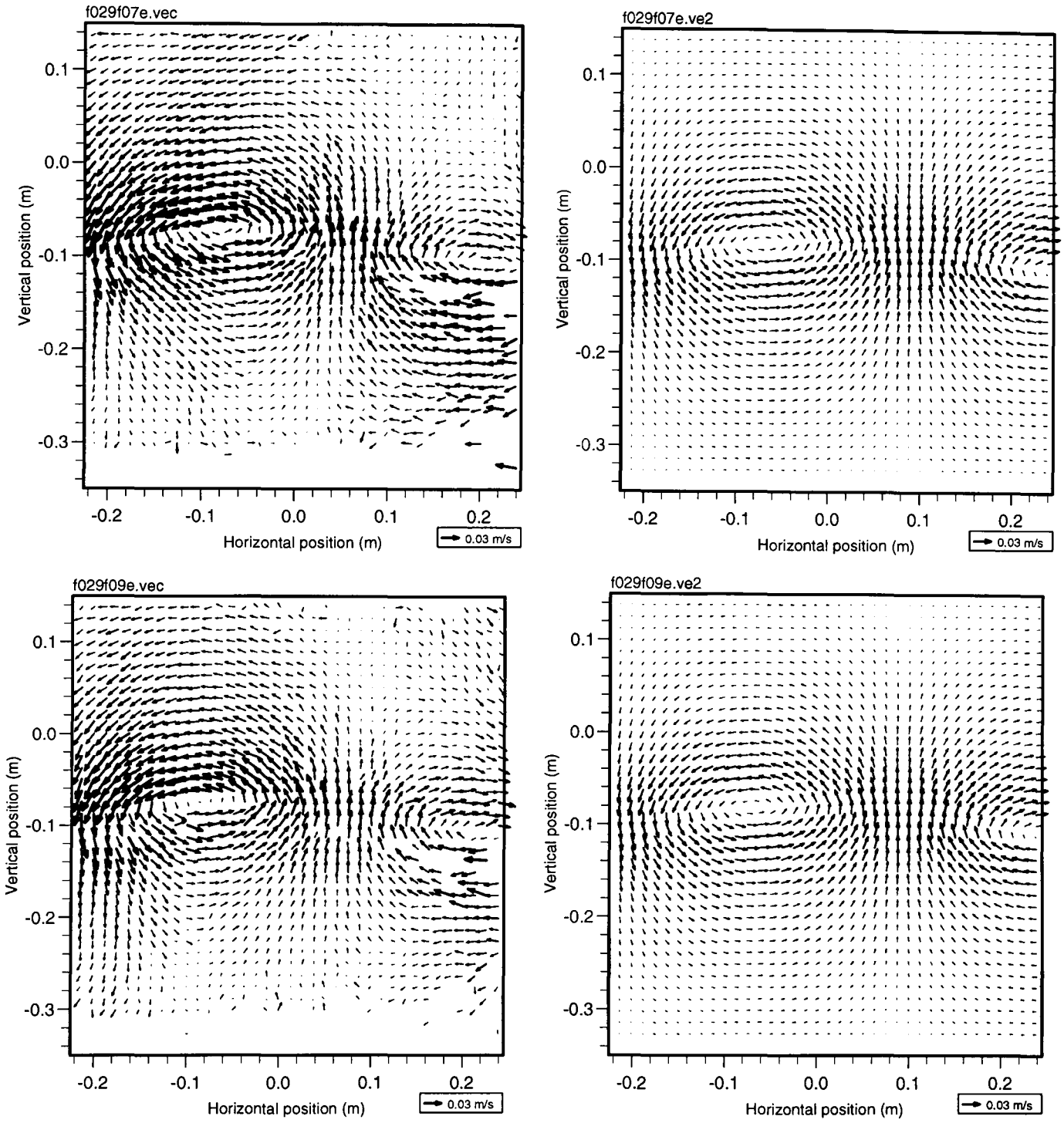


Figure 6.9: *Two successive views of a short wave crest and trough with* $f = 0.3Hz$, $\Delta\rho/\overline{\rho} = 8.8\%$, $H_{1/3} = 0.030m$; *experimental (left) and numerical velocities. The lower images were taken three wave periods after the upper ones*

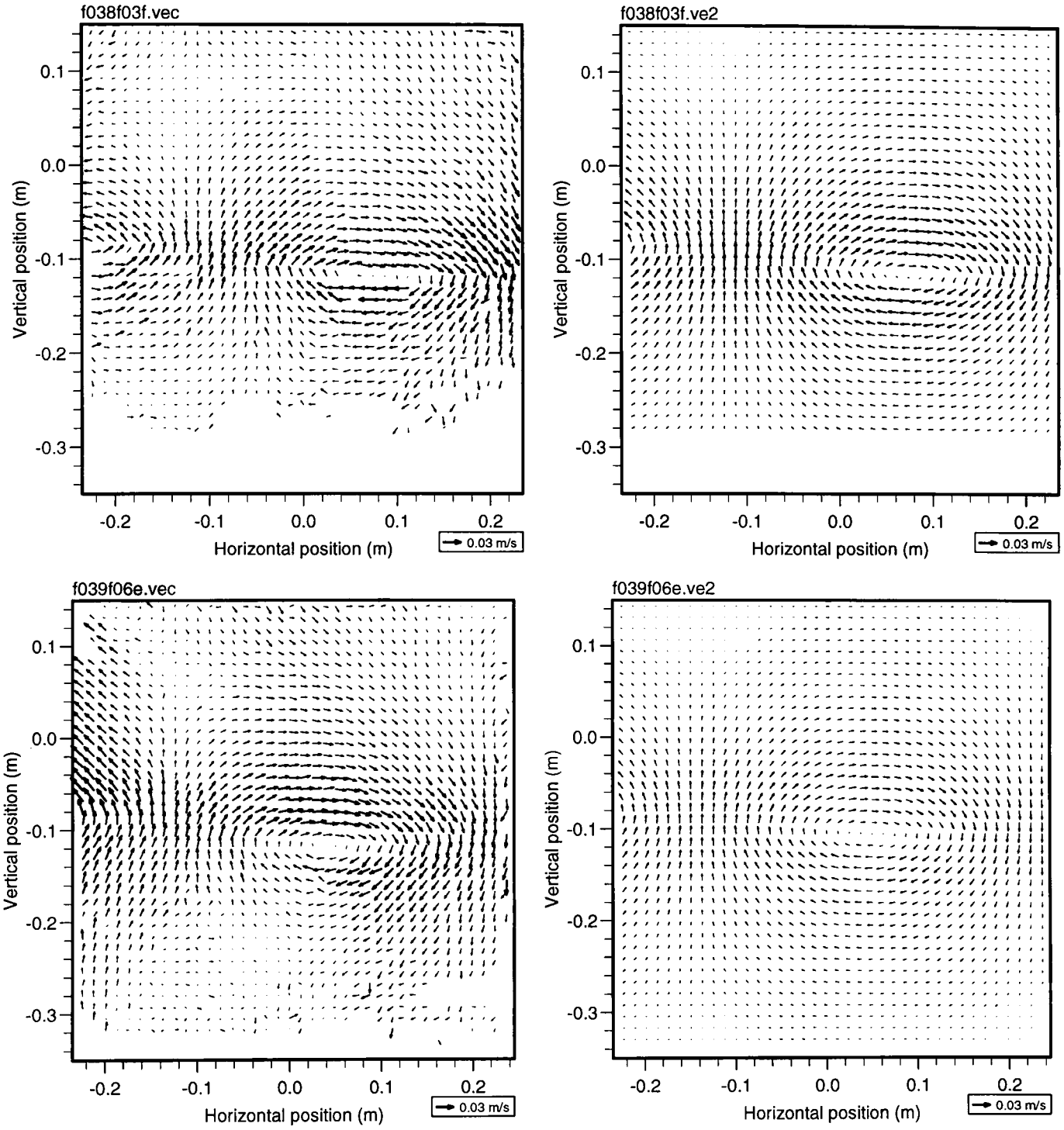


Figure 6.10: *Similar short wave troughs from two different experiments with* $f = 0.2Hz$, $\Delta\rho/\overline{\rho} = 4.8\%$; *experimental (left) and numerical velocities. The upper images had* $H_{1/3} = 0.031m$ *while the lower ones had* $H_{1/3} = 0.024m$. *The interface was slightly thicker in the lower images.*

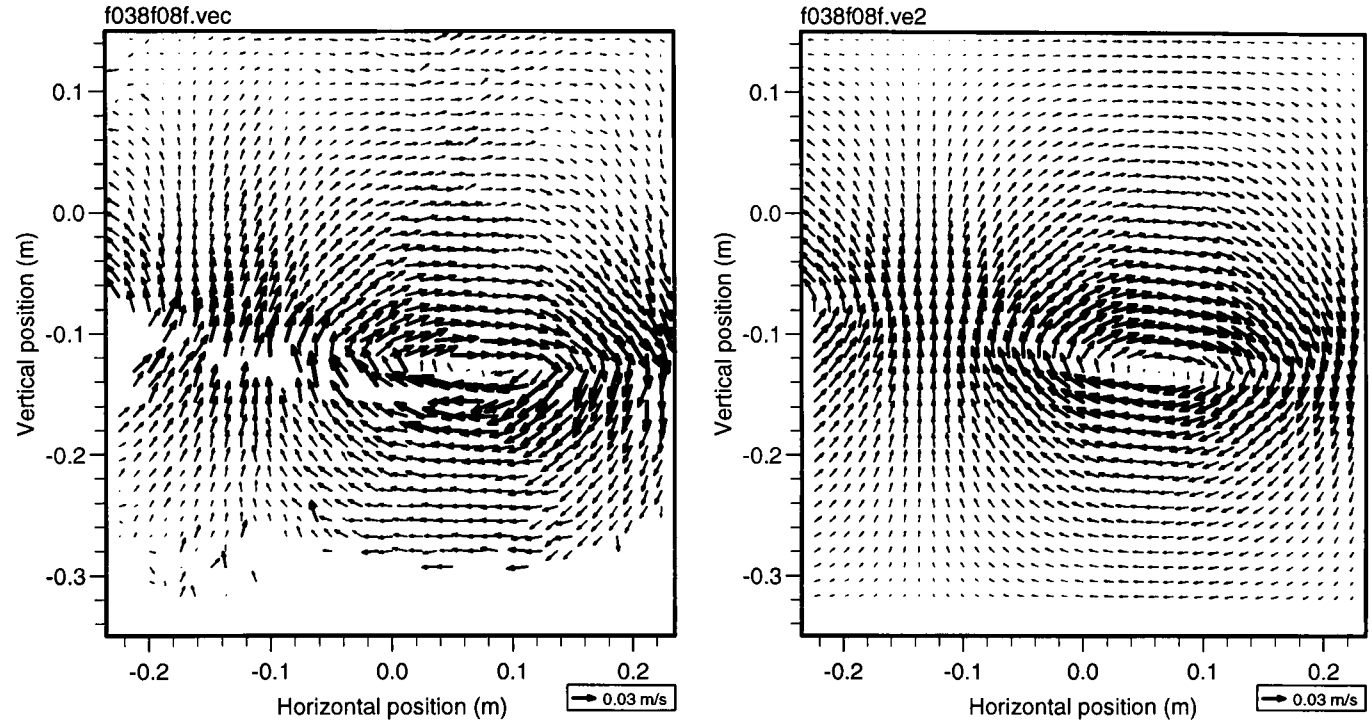


Figure 6.11: *Similar short wave troughs from two different experiments with* $f = 0.2Hz$, $\Delta\rho/\overline{\rho} = 4.8\%$; *experimental (left) and numerical velocities. The upper images had* $H_{1/3} = 0.056m$ *while the lower ones had* $H_{1/3} = 0.033m$. *The interface was slightly thicker in the lower images. These two experiments were repeat runs of those shown in the previous figure, but with higher generation amplitudes.*

tion to the velocity field is fairly small, and the third order part could not be used. A third order viscous comparison might give better results.

Figure 6.8 is a much shorter wave ($\lambda = 0.41$m, $f = 0.4Hz$) at a similar amplitude. This was one of the steepest waves generated ($ak = 0.29$). Given the wavelength, it is surprising that motions were produced not just near the interface but also near the tank bottom and water surface. This may be due to non-linearity, or possibly to mismatch of the boundary condition at the paddle.

There were also some deviations from the actual flow pattern predicted (such as above the wave trough). This may be related to non-linearity, but turbulence seems a more plausible explanation, given that resonance instabilities were observed in the wave train (section 2.2.1).

Figure 6.9 shows two successive measurements of the wave crests in one experiment. The two images are separated by three wave periods. The self-consistency of the measured flowfields is strong.

Figures 6.10 and 6.11 show similar events at two different amplitudes. In each case, the top vector maps show wave troughs in a relatively thin interface. The bottom vector maps show crests of a wave generated using the same parameters, but where the interface had been allowed to diffuse and thicken overnight. The timing of the images is the same in each of the four cases, but the crests in the lower images lag behind those of the upper images because of the retarding effect of the diffuse interface on the phase velocity.

It is notable that amplitude does not have any obvious effect on the phase speed. However, the agreement between theory and experiment appears to be greater in the small amplitude case. For example, the extension of wave-driven motions from the interface to near the bottom below the wave trough is apparent on the large amplitude images but is less obvious on the small amplitude ones.

Velocity enhancement below the wave trough, or above the wave crest, is also apparent on the other figures. This phenomenon was seen on many other vector maps, and is most likely due to non-linearity.

### Data reduction and integral quantities for short waves

In order to make practical use of the data generated by these experiments, it is necessary to extract some integral quantities from the vector maps. This will enable the measured behaviour to be characterised in terms of a small set of numbers, and will help to average out some of the measurement noise.

Such quantities could be derived from mean measures of velocity, circulation or shear, possibly making use of directional information. Use could be made of entire velocity maps or of selected parts of maps. Where entire maps were used, it would be necessary to compensate in some way for the fact that the maps each present different aspects of the waves, e.g., crests, troughs, etc.

- **Evaluation as "strengths"**

  Maintaining focus on the need to generate practical information of engineering relevance, the following quantities were evaluated.

  1. *Crest and trough "strengths"*—Crests and troughs were identified in the velocity maps from their shear maxima. The "strengths" of the crests and troughs were then evaluated as the rms horizontal velocity averaged through a vertical column around the identified crest or trough. From the maps, the column of vectors with the maximum shear, and the two columns on either side, were averaged. Crests or troughs were rejected if they lay near the edge of a velocity map. Exactly the same procedure, including independent identification of crests and troughs, was followed for the measured maps and the corresponding predicted maps.
  2. *Rising and falling "strengths"*—These strengths were defined as the rms vertical velocity averaged through a vertical column located around a maximum in vertical velocity magnitude. Maxima were identified using the same procedure as for crest and trough strengths.

An attempt was also made to characterise the crests and troughs by the strength of the shear generated. Unfortunately, since many of the vector maps had missing values around the interface, a "strength" for the shear could not be evaluated reliably.

Crest, trough, rising and falling strengths were evaluated for each vector map in the short wave data set. On each vector map, only a subset of features was identified, for example, from the vector maps in figure 6.11 only a trough and a

rising maximum would be identified, since the other apparent features occur too close to the edges of the maps. Averages of each quantity were then calculated for each individual experimental run.

The results of this evaluation are presented in figures 6.12 and 6.13. Correlations were poor, for the reasons previously described. Nevertheless, some conclusions may be drawn from these graphs. Figure 6.12 shows that measured velocities in both the crests and the troughs were usually significantly greater than those predicted by second order non-Boussinesq theory. Similarly, the velocity of upwelling or downwelling associated with the zero crossings exceeds the theoretical prediction (figure 6.13), with very few points falling below the lines.

There is no significant bias towards upward velocities, as might be expected if the calculation of the particle rise velocity were in error. There appears to be a slight bias in the horizontal velocities, but the degree of scatter is such that no firm conclusions can be made about this. Crest/trough strengths are on the whole comparable to rising/falling strengths, which should be expected in short waves.

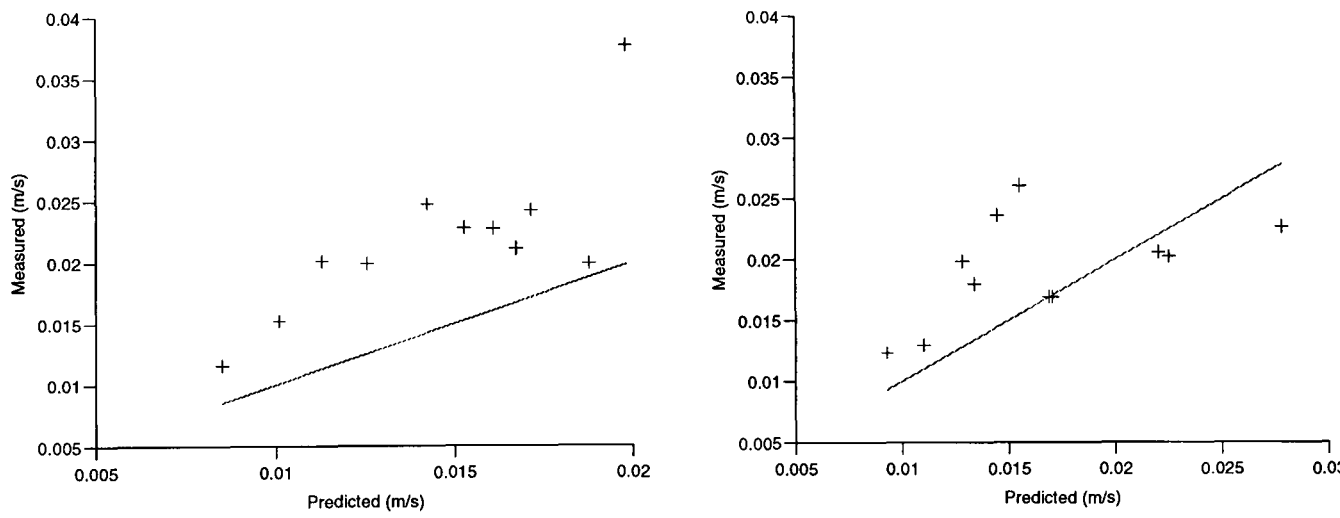


Figure 6.12: *Comparison of measured and predicted mean crest strengths (left) and trough strengths for the short wave cases. The line shows exact correspondence.*

- **Evaluation as coefficients**

  The quantities described above do not make use of all of the measured velocities, but rather focus on extremes. In order to compare theoretical and experimental results for all of the measurements, a further characterisation was used.

  Figure 6.14 shows scatter plots of the velocities presented in figure 6.10 (top), showing measured velocities against the corresponding second order predicted velocities. Scatter plots for the higher amplitude case of the same wave (figure 6.11, top) are shown in figure 6.15. These plots show that there is a linear

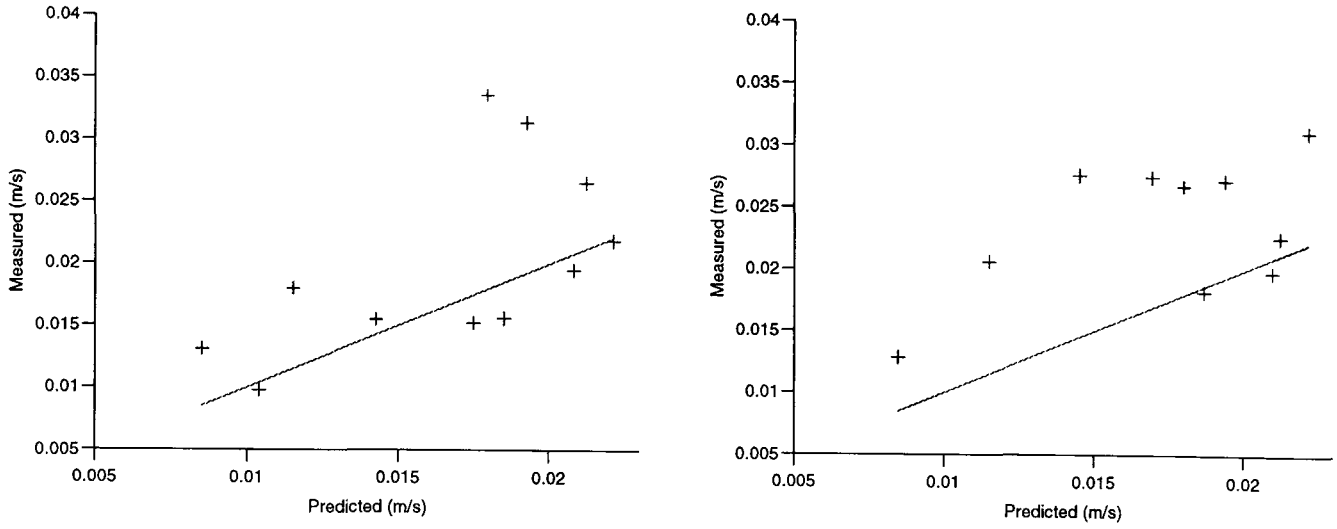


Figure 6.13: *Comparison of measured and predicted mean rising strengths (left) and falling strengths for the short wave cases. The line shows exact correspondence.*

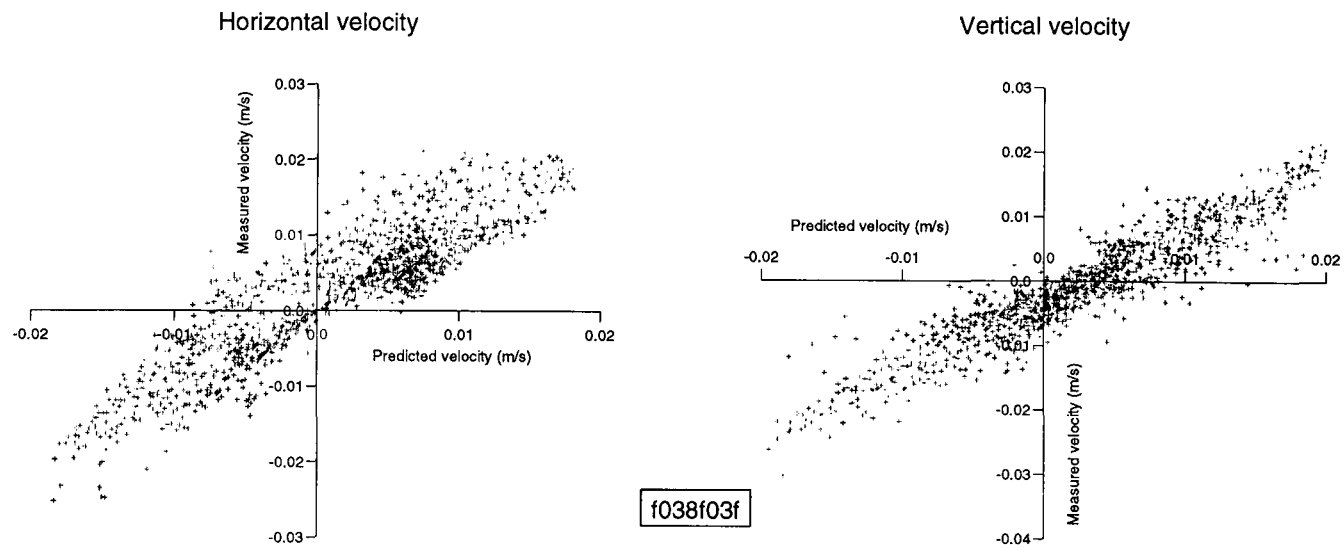


Figure 6.14: *Scatter plots of the horizontal and vertical velocities of vector map f038f03f.vec against second order predictions*

relationship between the measured and predicted velocities. Scatter plots of other vector maps show very similar behaviour.

One way of characterising these plots is to fit a straight line to the data, such as

$$\left.\begin{aligned} u_{meas} &= a_1 u_{pred} + a_0 \\ w_{meas} &= b_1 w_{pred} + b_0 \end{aligned}\right\} \tag{6.2}$$

where $u_{meas}$, $w_{meas}$ are the measured horizontal and vertical velocities, $u_{pred}$, $w_{pred}$ are the predicted velocities, and $a_i$, $b_i$ are coefficients to be evaluated by least squares.

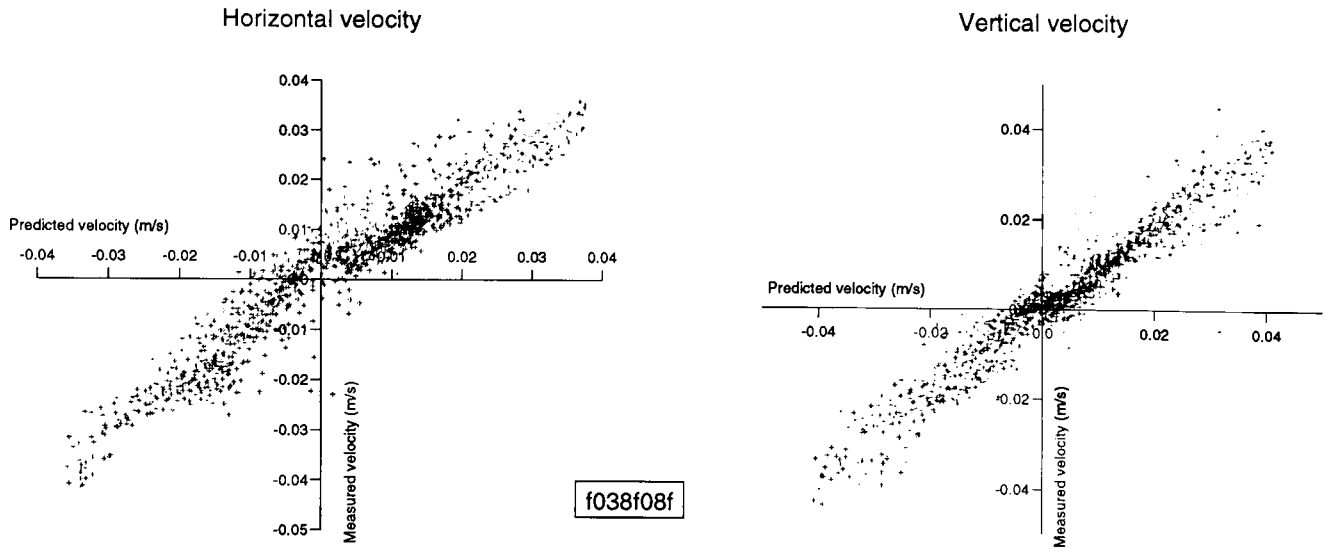


Figure 6.15: *Scatter plots of the horizontal and vertical velocities of vector map f038f08f.vec against second order predictions*

| | $a_0$ | $a_1$ | $b_0$ | $b_1$ |
|---|---|---|---|---|
| Mean | -0.003 | 1.12 | -0.002 | 1.16 |
| SD | 0.004 | 0.31 | 0.004 | 0.40 |

Table 6.2: *Means and standard deviations for the short wave velocity coefficients*

The coefficients $a_0$ and $b_0$ reveal the offset in the velocities; for example a non-zero mass transport velocity should induce an offset in the horizontal velocities. The coefficients $a_1$ and $b_1$ reveal the proportionality in the relationships.

These coefficients were evaluated for all of the vector maps in the short wave data set. Means and standard deviations for these coefficients were calculated and are given in table 6.2. This table clearly shows that no offset was observed in either the vertical or horizontal direction. Both horizontal and vertical velocities were generally in excess of the predicted values.

The standard deviations on these coefficients were high. The reason for this is most likely that the wave heights were assessed as *significant* heights (at 1/3 significance) rather than being measured on a wave by wave basis.

Another possible reason may be the quality of the density profiles, which may have caused an error in the prediction of the height of the density interface. Where the interface was not at the measured height, the shear layers would not match between predicted and measured vector maps. Due to the strong shear, vectors above the interface in one map might be matched with vectors below it in the other map, which would result in an error of sign. The result of this would be a bias towards smaller horizontal velocity coefficients.

| | 95% | | 90% | | 70% | |
|---|---|---|---|---|---|---|
| | u | w | u | w | u | w |
| mean | 1.41 | 1.26 | 1.37 | 1.23 | 1.36 | 1.26 |
| sd | 0.33 | 0.33 | 0.32 | 0.33 | 0.33 | 0.35 |

Table 6.3: *Ratios of measured to predicted velocity percentiles for the short wave cases*

- **Evaluation as percentiles**

  A final characterisation of the difference between measured and predicted velocities was to calculate percentiles. This focuses on the extremes, and is much less vulnerable to interface height errors. Percentiles at 95%, 90% and 70% were calculated for each vector map in the short wave record. The percentiles were calculated against the number of vectors present on the theoretical map. This is because the measured vector maps contained areas of missing data, which would cause the percentiles for these maps to be underestimated if they were evaluated against the number of successfully measured vectors.

  Absolute values were used for both the vertical and horizontal velocities. The ratios of measured to predicted percentiles were evaluated, and the means and standard deviations of these ratios were calculated. The results are presented in table 6.3.

  This table shows that the difference between measured and predicted horizontal velocities is slightly more pronounced in the extremes. This fact is hidden in the linear coefficients comparison above. The actual values of the percentile ratios are higher than the linear coefficients. This may be partly due to the possible bias towards lower coefficients in horizontal velocities. The difference between vertical percentile ratios and vertical linear coefficients is less pronounced.

## 6.3 Intermediate length waves

Owing to the experimental problems previously described, only a few intermediate length cases were available. These waves had wavelengths around $\lambda/H_{1,2} \simeq 7$. Unfortunately, the second-order equation in the Stokes expansion (equation 3.41) could not be solved as the algorithm would not converge. Therefore only first-order comparisons were available for these cases. The domain of convergence for the second-order theory is discussed in section 6.6.

### 6.3.1 Wave height gauge traces

Several modifications to the method were made for the intermediate wavelength cases.

- Tank control software was modified so that the wave generation signal would ramp slowly from zero to the required amplitude at the start of each experiment. This was done in an attempt to reduce the tendency of the first wave in the sequence to steepen.
- The signal from the aspirating density probe was recorded alongside the wave gauge traces. The probe was positioned in the interface, at a distance of 0.76m from the wavemaker.
- Five wave gauges instead of two were recorded. One of the gauges (gauge 4) was sited in the centre of the measurement zone. The gauges were sited as follows: gauge 1: 1.6m; gauges 2 and 3: 2.6m; gauge 4: 3.8m; and gauge 5: 5.0m; where the distances are from the wavemaker.
- Two of the gauges (2 and 3) were paired at the same distance from the wavemaker. The pair of gauges was configured with one in the centre of the tank and one near the wall. The object of this was to make sure that tank wall effects were not significant.
- The measurement zone was moved further down the tank to 3.8m from the wavemaker.

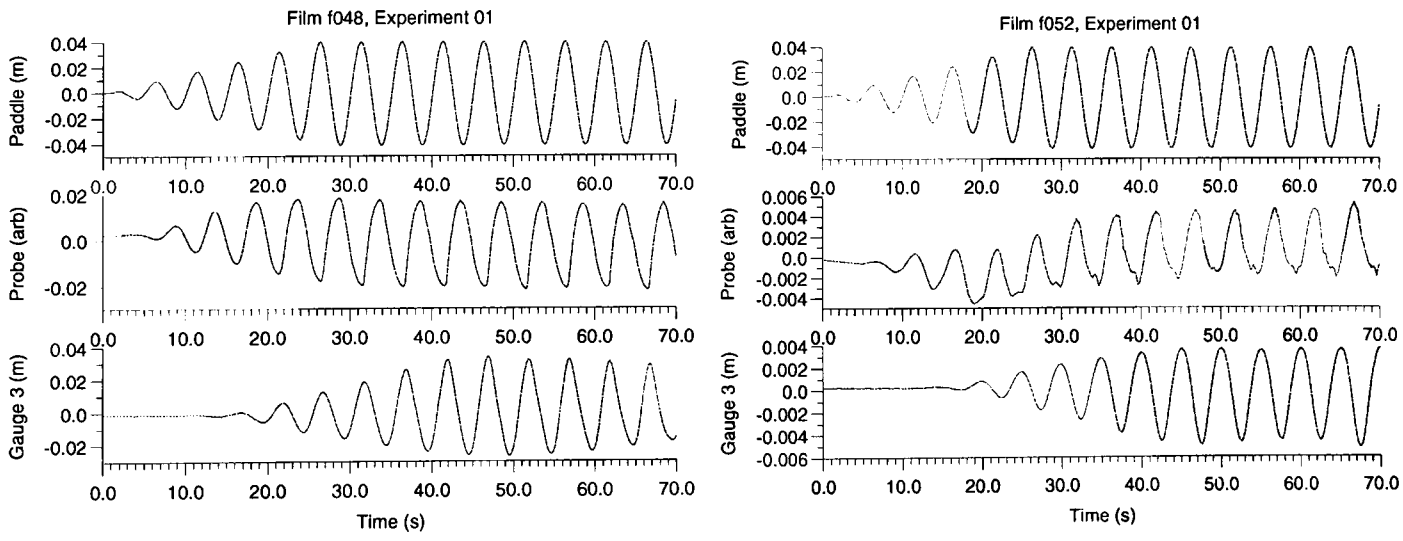


Figure 6.16: *Wave gauge traces with* $f = 0.2Hz$, $\Delta\rho/\overline{\rho} = 8.8\%$. *Left picture:* $H_{1/3} \simeq 0.040m$, *equal layer depths; right picture:* $H_{1/3} \simeq 0.079m$, *unequal layer depths*

With more gauges in the tank, cross-talk between the gauges became a serious problem. In the end, false signals upset the calibration procedure, so that some of the gauge signals were clipped, and it was not possible to use the pair (2 and 3) to evaluate wall effects. Estimation of the wave height for comparison with theory was also affected.

Gauge traces for these experiments are shown in figure 6.16, and associated FFTs are shown in figure 6.17. The time traces show the signals from the density probe alongside one gauge signal. Units for the density probe scale are arbitrary. Comparing the shapes of the waveforms in figure 6.16, especially the left figure, the limited frequency response of the aspirating density probe, discussed in section 4.7, is apparent.

Figure 6.16 shows a lessened tendency for the wave train to be lead by a steep wave. The formation of groups due to Benjamin-Fier instability is also reduced. This may be because the instability is lessened by having a gradually ramped paddle amplitude. However, Benjamin-Fier instability is a short-wave effect (Lighthill, 1978) and the waves seen in the figure are of intermediate length. Furthermore, the effect of ramping the paddle amplitude would be most apparent at the front of the wave train, but the whole wave train appears to be more stable than in the short-wave cases.

The Fourier transforms (figure 6.17) now show a significant second harmonic. The third harmonic is still absent.

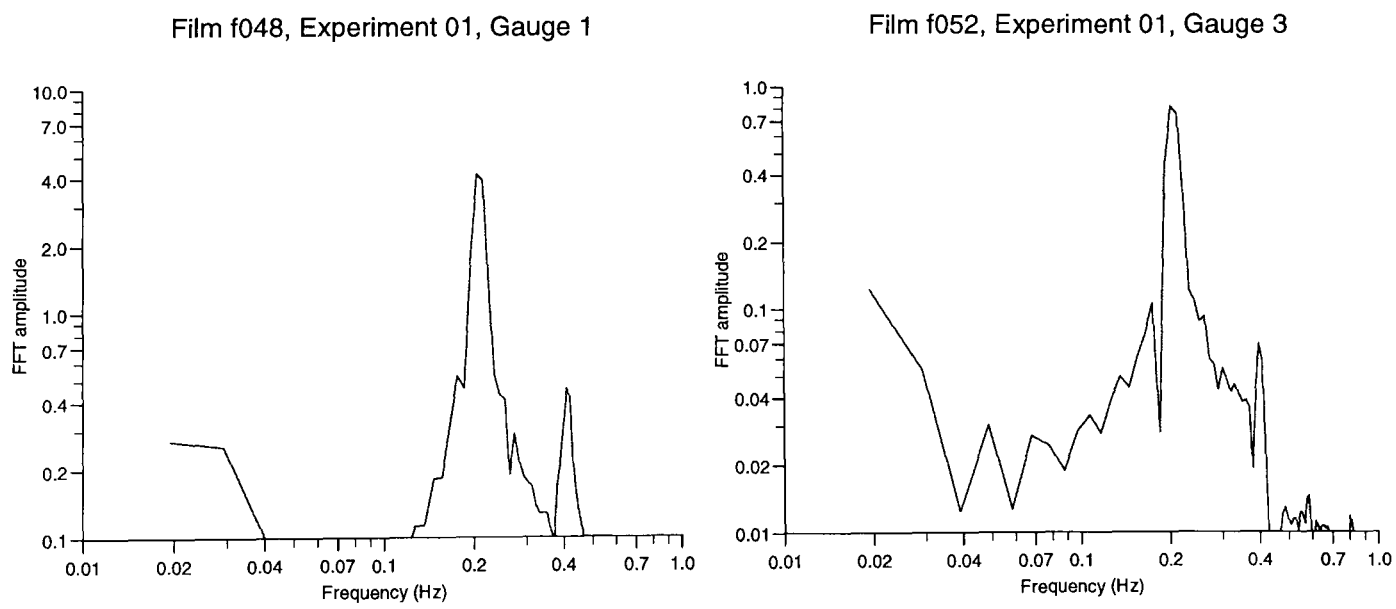


Figure 6.17: *Fourier transforms for the previous figure*

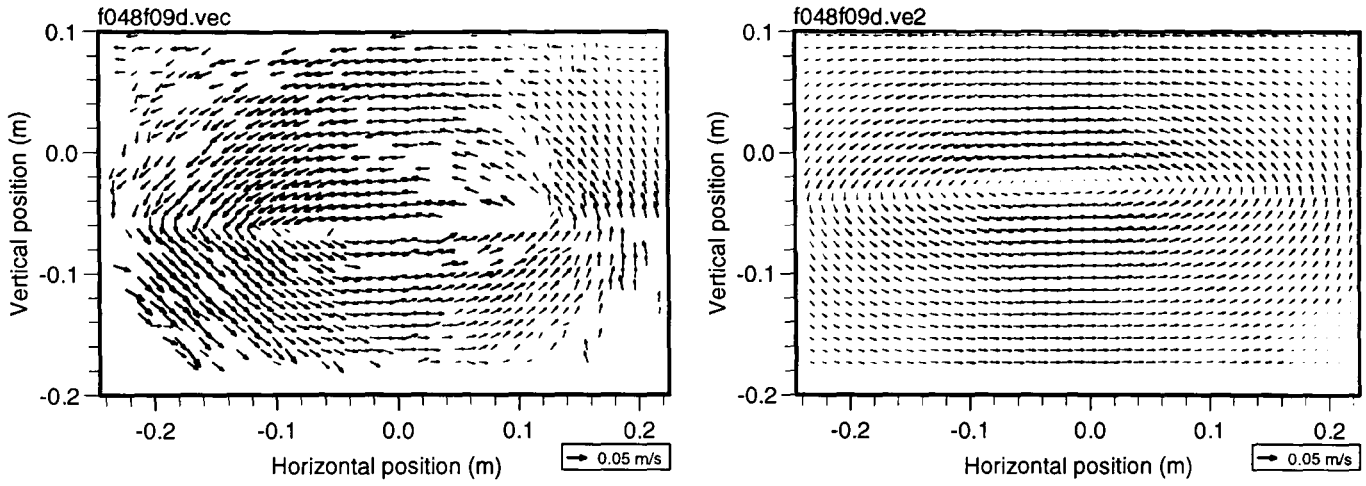


Figure 6.18: *Intermediate-length wave crest with* $f = 0.2Hz$, $\Delta\rho/\overline{\rho} = 8.8\%$, $H_{1/3} \simeq 0.04m$; *experimental (left) and numerical velocities*

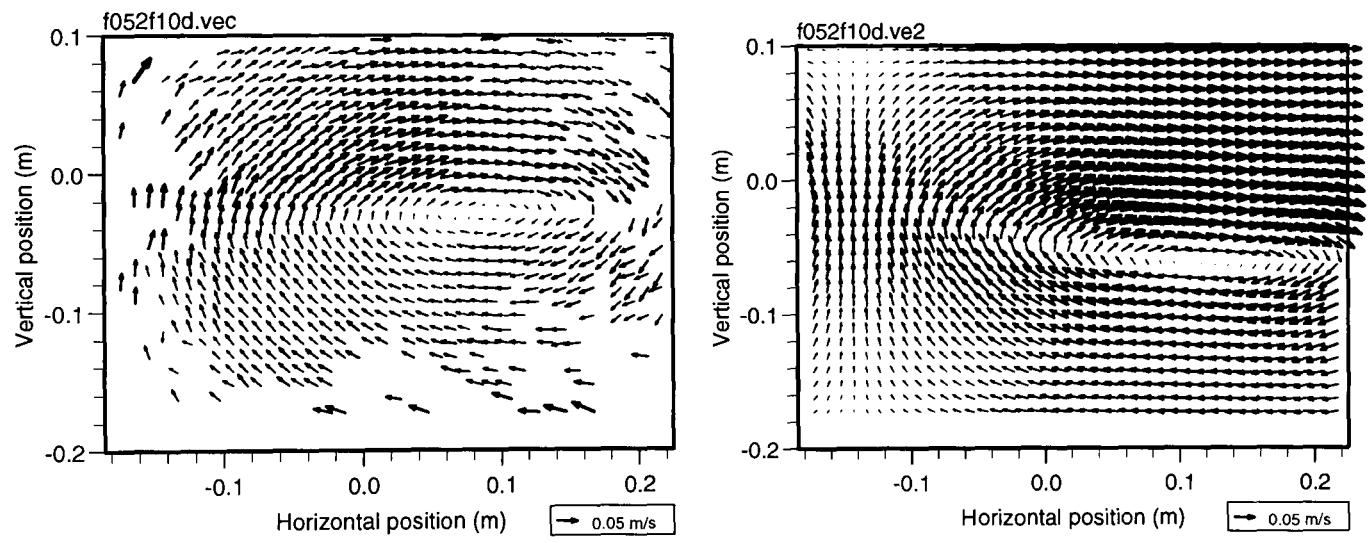


Figure 6.19: *Intermediate-length wave crest with* $f = 0.2Hz$, $\Delta\rho/\overline{\rho} = 8.8\%$, $H_{1/3} \simeq 0.08m$; *experimental (left) and numerical velocities*

### 6.3.2 Velocity measurements

The method of mounting the rotating mirror onto the turntable of the image shifter was improved before these experiments were run. It was hoped that this would reduce the problem of resonant vibrations (section 5.4.2) and allow the use of the lowest mirror rotation rate. Unfortunately, it was found that the vibrations were not reduced, and so vibration noise was a serious problem in these cases. It was concluded that the vibrations were related to the turntable itself and not to the mirror mounting,

Problems with the calibration of the wave height gauges, discussed above, also contributed to the lack of good measurements for the intermediate wavelength cases. Quantitative conclusions cannot therefore be drawn.

Figures 6.18 and 6.19 show that the wave-induced motions now extend to the top and bottom boundaries of the domain, as anticipated. There also appears to be asymmetry in both the horizontal and vertical velocities. The lack of cases makes it impossible to postulate a cause for this.

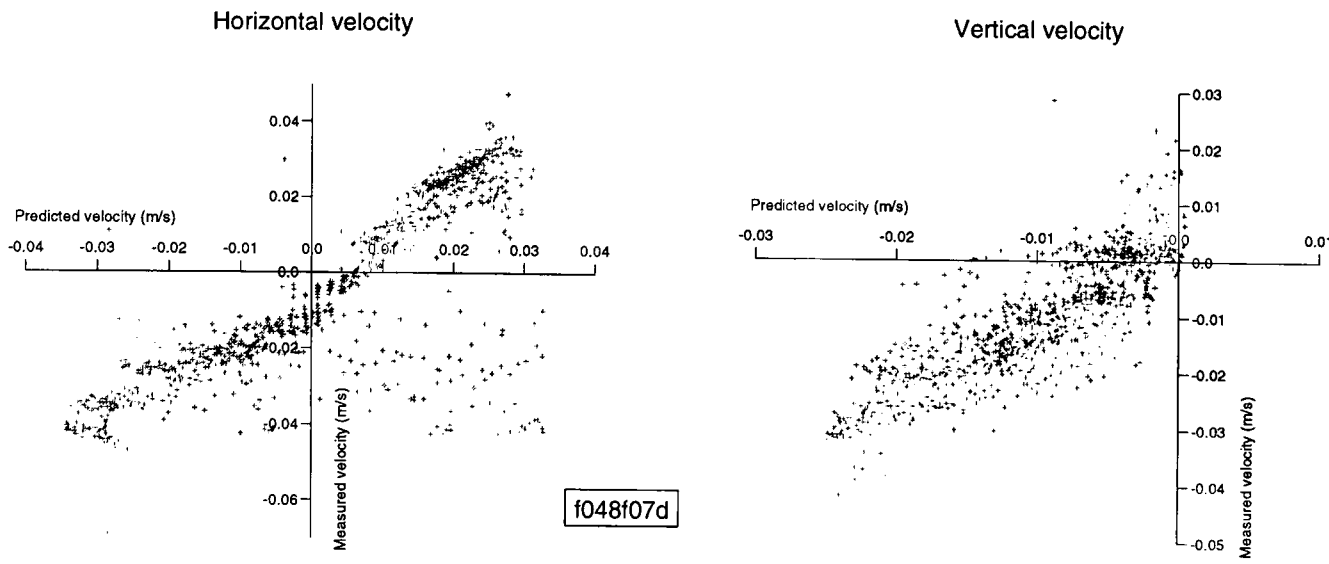


Figure 6.20: *Scatter plots of the horizontal and vertical velocities of vector map f048f07d.vec against first order predictions*

## 6.4 Long waves

The long wave experiments were conducted with the same arrangement as the short wave cases. Two wave height gauges were used for each case. The generating frequency was selected so as to produce a wave which was long compared to the depth of either layer. The experiments were conducted in two sets: the first set had equal layer depths and the second set had unequal layer depths.

Unfortunately, as for the intermediate depth waves, the second and third order stream-function profiles in the Stokes expansion could not be made to converge. Accordingly, linear theory is used along with KdV theory to represent these waves.

### 6.4.1 Wave height gauge traces

#### Equal layer depths

The equal layer depth wave gauge traces are shown in figure 6.21, with figure 6.22 being the corresponding Fourier transform.

It can be seen from these traces that the form of the wave is altered by the proximity of the horizontal boundaries, being clearly distorted from the near-sinusoidal shape of (e.g.) figure 6.1. One might suspect that this distortion is due to a small number of bound or free harmonics. The former could be caused by non-linearity (in the Stokes sense), while the latter could result from a mis-match between the paddle motion and the wave kinematics. However, the Fourier transform reveals that the wave energy is not confined to a small number of harmonics, but is in fact spread over a range of frequencies above the generating frequency.

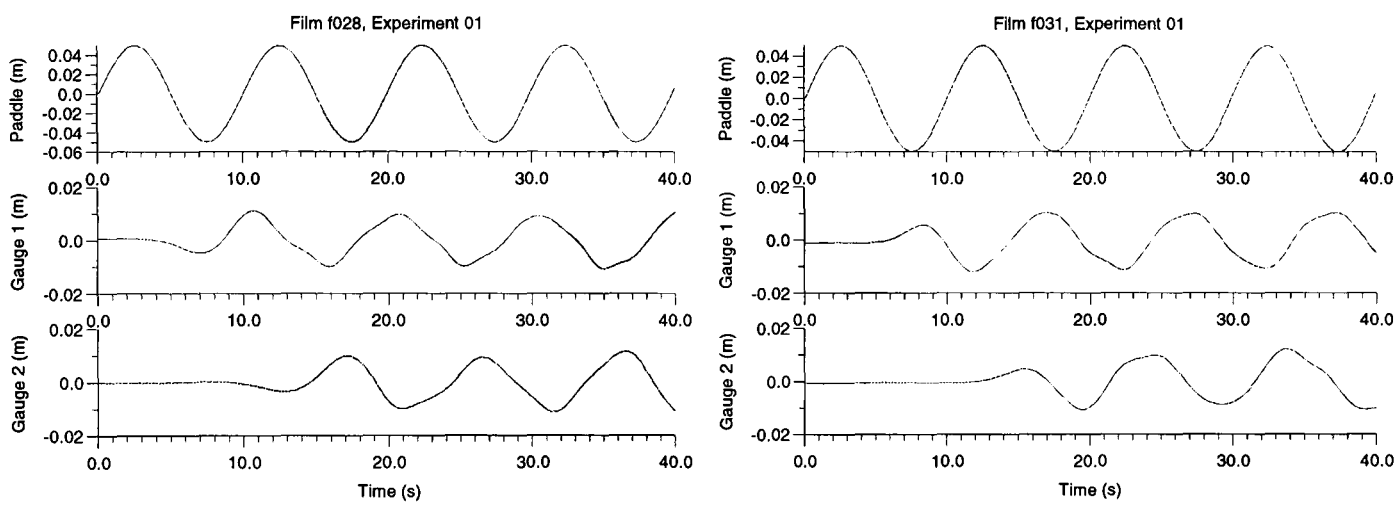


Figure 6.21: *Long waves with equal layer depths,* $f = 0.1Hz$, $H_{1/3} \simeq 0.020m$. *Left figure:* $H_{1,2} \simeq 0.25m$, $\Delta\rho/\rho = 8.8\%$; *right figure:* $H_{1,2} \simeq 0.15m$, $\Delta\rho/\rho = 9.7\%$.

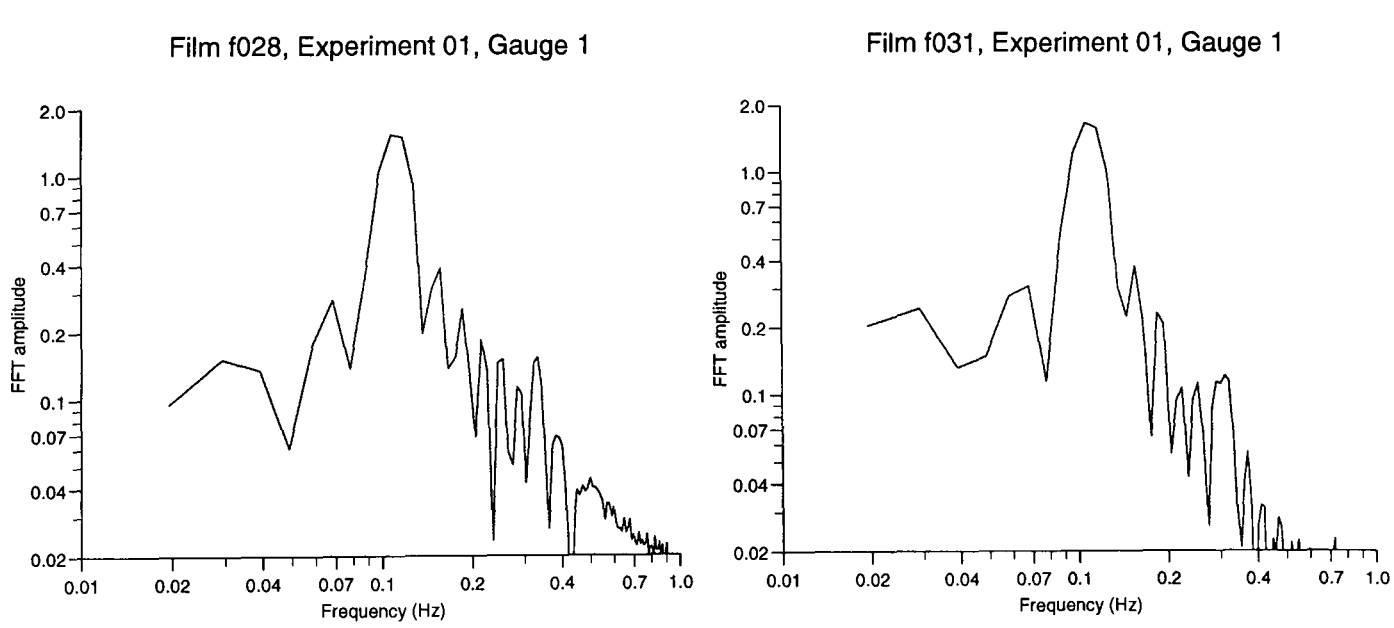


Figure 6.22: *Fourier transforms for the previous figure*

### Unequal layer depths

Figures 6.23 and 6.24 show the form and spectrum of a wave in which the lower layer is considerably deeper than the upper layer, but is still shallow compared to the expected wavelength. This case was intended to more closely resemble the field measurements of Bole et al. (1994), Osborne and Burch (1980) and Apel et al. (1985), where waves occurred in shallow thermoclines. Although most of these writers observed waves where the lower layer was in fact fairly deep, they all used Korteweg-de Vries theory (where the lower layer is also relatively shallow) to describe the behaviour.

The solitary waves discovered by these writers were, as required by KdV theory, waves of depression, possessing a single sharp trough with no true wave crest. In these experiments, the wave was generated by a smooth sinusoidal paddle motion. This motion, as can be seen on figure 6.23, produced sharp-troughed waves which resemble cnoidal waves. Additionally, the paddle motion appears to have produced harmonics of a higher frequency. This is to be expected since the kinematics of a cnoidal wave are significantly different to those of a sinusoidal wave, therefore a paddle which produces the latter reasonably well may do less well in producing the former.

The Fourier transform (figure 6.24) shows that a far larger proportion of the wave energy ended up in harmonics than in any of the other cases. The frequencies at which the second and third order (Stokes) contributions to the wave shape should be found are $0.2Hz$ and $0.3Hz$. Strong peaks are seen at these frequencies, and weaker ones at the higher orders ($0.4Hz$ and so on). Further significant peaks are seen at other frequencies not connected with the generating frequency.

Consideration of these points and the time series leads to the conclusion that non-linearity is very significant in these waves, but that the true form of the non-linearity is not observable due to the additional free harmonics. Further, the strength of the harmonics suggests that the perturbation series Stokes expansion would be slow to converge, and high orders would be required.

The strength of the third order component is surprising, since it is at this order that the effects of viscosity should become significant. These low frequency waves, according to the scaling argument of section 3.3.5, should be, if anything, more affected by viscosity than the higher frequency ones. It is possible that the third order peak coincides with the frequency of a strong free harmonic, which would be less affected by viscosity (as it must be regarded as the first order component of a different wave).

Figure 6.25 shows the shapes of KdV solitary waves which would be found in the experiments described above. Only the background stratification, layer depths and wave height are needed to compute the characteristics of this wave. The computed solitary waves appear to have similar slopes to the measured waves, which suggests that at least for the vertical motions they might provide a good comparison. However, the obvious presence of harmonics, and the clear periodicity of the waves, must be borne in mind.

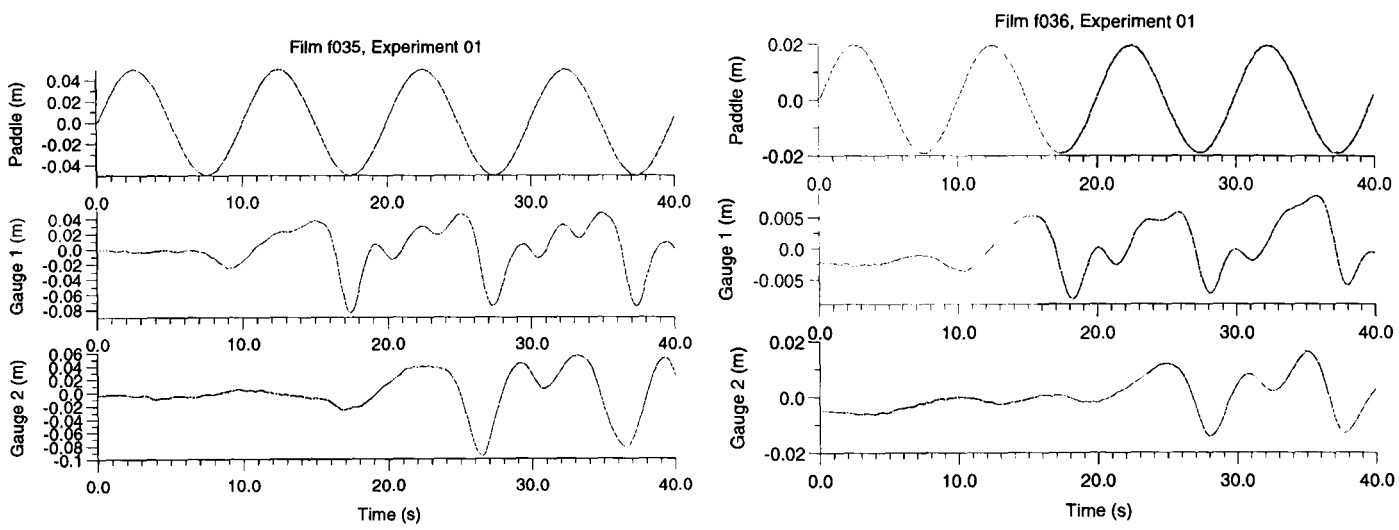


Figure 6.23: *Long waves with unequal layer depths,* $f = 0.1Hz$, $\Delta\rho/\rho = 9.7\%$. *Left figure:* $H_1 = 0.065m$, $H_2 = 0.186m$, $H_{1/3} = 0.071m$, *fresh interface; right figure:* $H_1 = 0.079m$, $H_2 = 0.164m$, $H_{1/3} = 0.022m$, *diffuse interface.*

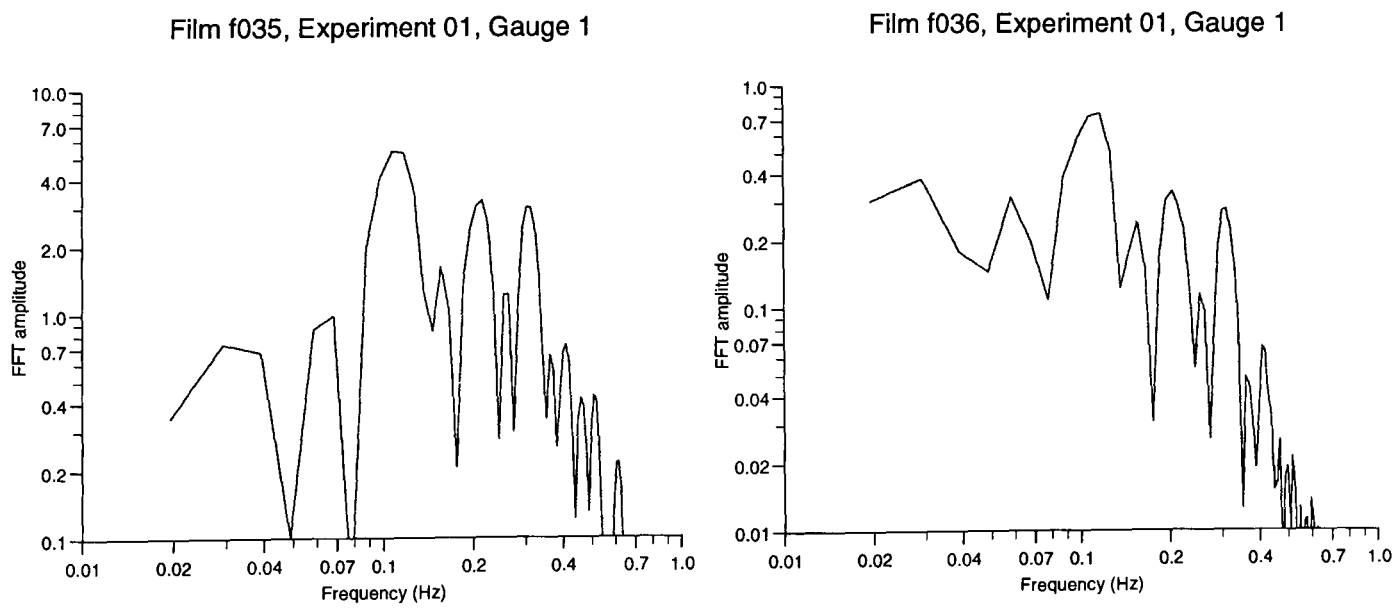


Figure 6.24: *Fourier transforms for the previous figure*

### 6.4.2 Velocity measurements

#### Qualitative results

Figures 6.26 and 6.27 show measurements of the kinematics of long wave troughs where the layer depths are approximately equal. Alongside are shown linear predictions of the velocity map. Linear theory appears to predict a far broader wave trough than is actually encountered. This is seen in the shear layer, which in the numerical wave remains roughly constant across the vector map. In the measured wave the shear changes in form, with much larger gradients in the vertical velocity component.

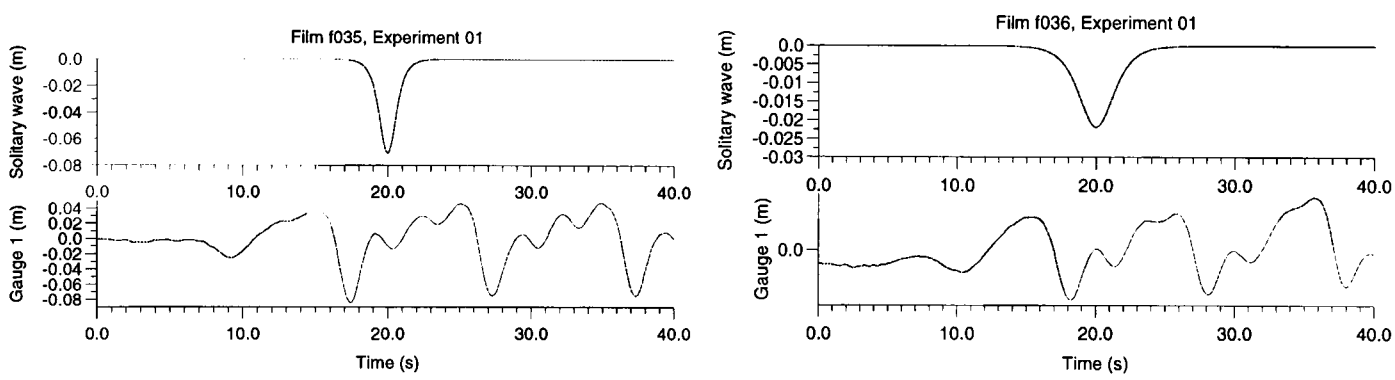


Figure 6.25: *KdV solitary waves matched to the conditions of the long waves which were generated in layers of unequal depth*

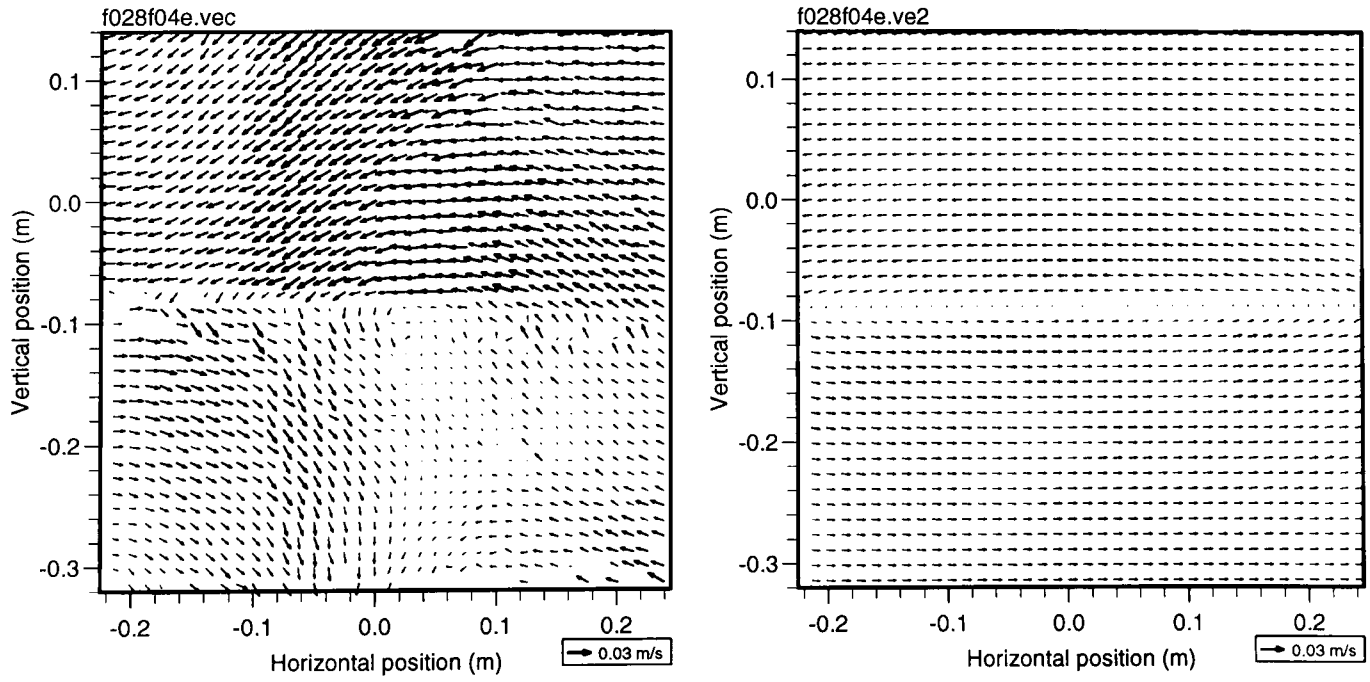


Figure 6.26: *Long wave trough with* $f = 0.1Hz$, $\Delta\rho/\overline{\rho} = 8.8\%$, $H_{1/3} = 0.020m$, $H_{1,2} \simeq 0.25m$; *experimental (left) and linear velocities*

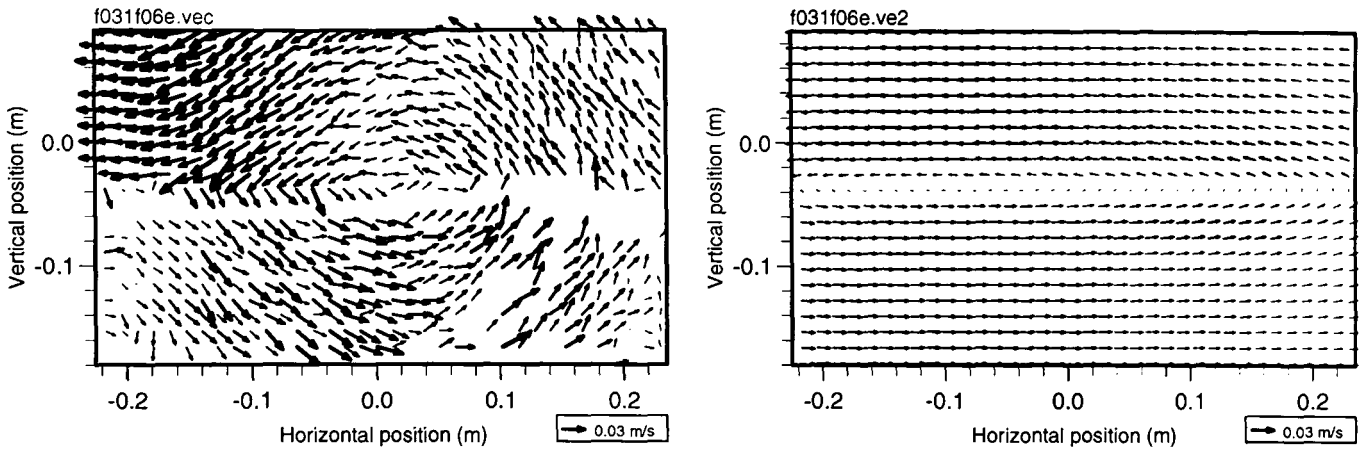


Figure 6.27: *Long wave trough with* $f = 0.1Hz$, $\Delta\rho/\overline{\rho} = 9.7\%$, $H_{1/3} = 0.022m$, $H_{1,2} \simeq 0.15m$; *experimental (left) and linear velocities*

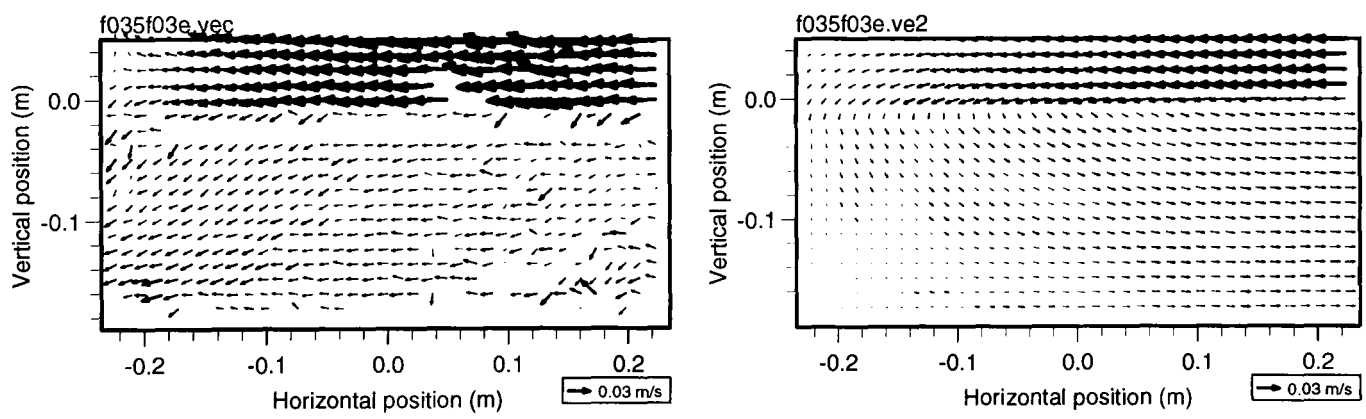


Figure 6.28: *Long wave crest with* $f = 0.1Hz$, $\Delta\rho/\overline{\rho} = 9.7\%$, $H_{1/3} = 0.071m$, $H_1 = 0.065m$, $H_2 = 0.186m$; *experimental (left) and numerical velocities*

Figures 6.28 to 6.30 show the behaviour of long internal waves where the upper layer is much shallower than the lower.

Figure 6.28 shows the broad crest of such a wave. A notable feature is the high negative horizontal velocity above the interface, which the linear theory succeeds qualitatively in predicting. The solitary wave prediction is not shown here because a solitary wave of depression possesses no crest, and the velocities tend to zero in the outskirts.

Figures 6.29 and 6.30 show the flow around the troughs of these waves. The intensity of the negative velocity below the trough is a surprise, and neither the linear nor the KdV theory predict this. The strong vertical motions, which are a result of the non-linearity, would not be predicted by linear theory. The KdV predictions also fall short because of the length of the KdV solitary wave which would propagate under these parameters.

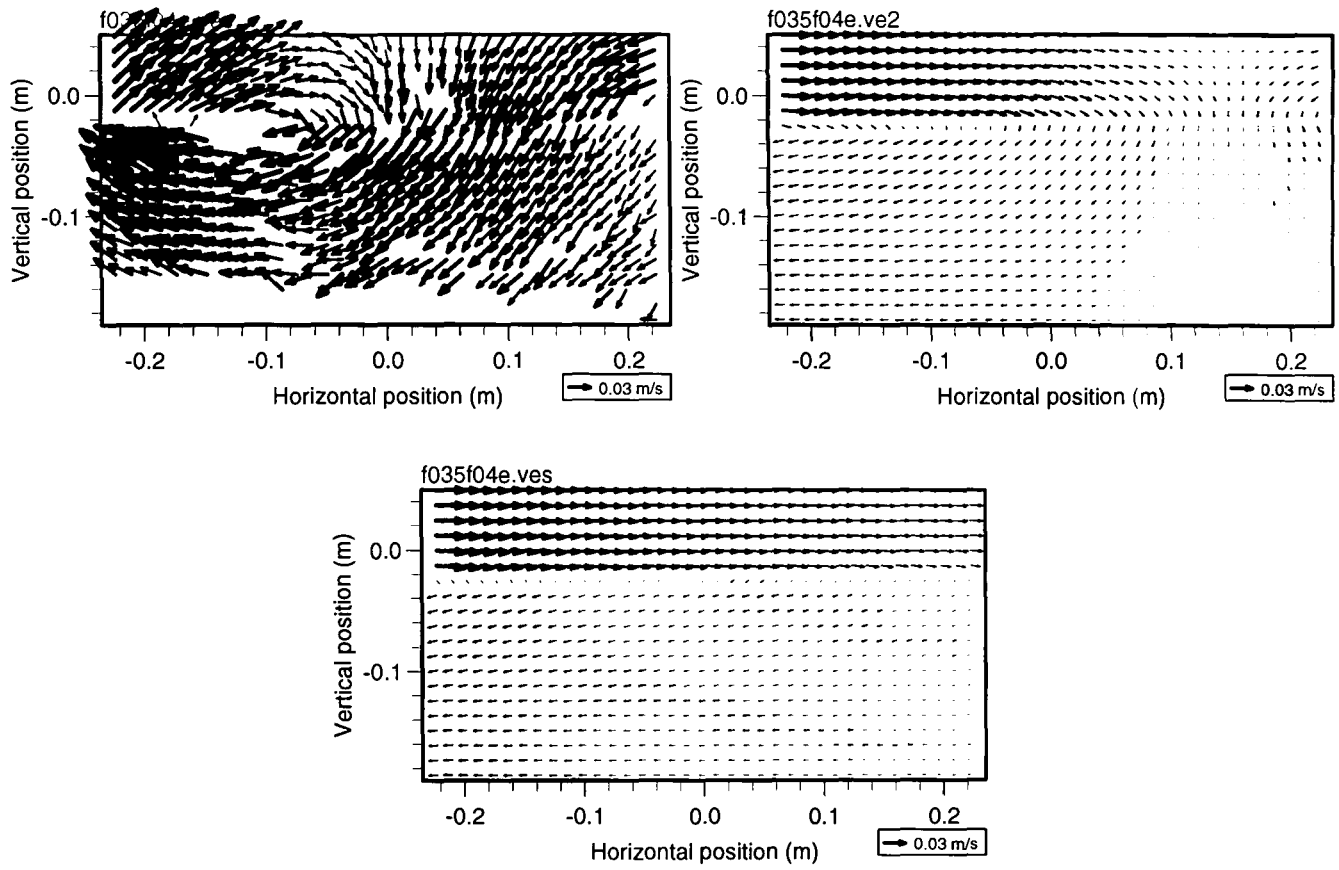


Figure 6.29: *Long wave trough with* $f = 0.1Hz$, $\Delta\rho/\overline{\rho} = 9.7\%$, $H_{1/3} = 0.071m$, $H_1 = 0.065m$, $H_2 = 0.186m$; *experimental velocities (left), linear theory (right) and KdV theory (bottom).*

## Integral quantities for long waves

The long wave cases were assessed in terms of crest/trough and rising/falling strengths, linear coefficients, and velocity percentiles as was done for the short wave cases. The crest/trough and rising/falling strengths calculations did not prove useful, mainly due to the lack of cases.

Velocity coefficients for the long waves are given in table 6.4. As for the short wave cases, very little offset can be seen in either direction. The horizontal coefficients are close to unity, although once again the standard deviations are high. However, the vertical velocity coefficients are subject to an extremely high standard deviation, such as to make the value of the actual coefficient irrelevant.

The reason for this is revealed by consideration of the vector maps above. As mentioned previously, the vector maps and wave gauge traces for both equal and unequal layer depths show that linear theory fails to predict the wave shape, with a marked deviation from sinusoidal motion in both. Where the layer depths are equal, both crests and troughs are sharper than a corresponding sinusoid. Where the upper layer is thinner, the crests become very broad and the troughs very narrow. Therefore, in matching predicted to measured velocity maps, maxima in vertical velocities may be found to

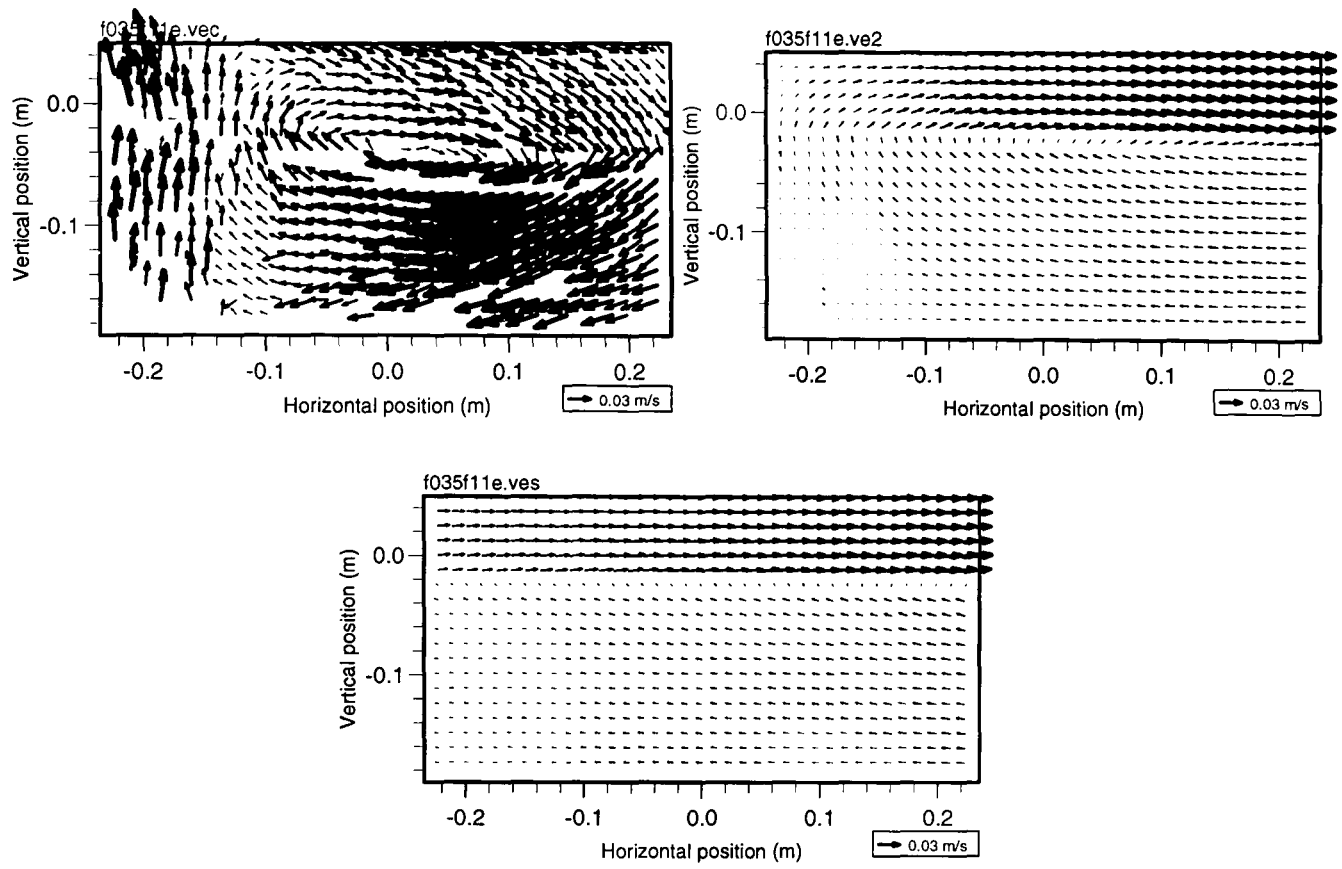


Figure 6.30: *Long wave trough with* $f = 0.1Hz$, $\Delta\rho/\overline{\rho} = 9.7\%$, $H_{1/3} = 0.071m$, $H_1 = 0.065m$, $H_2 = 0.186m$; *experimental velocities (left), linear theory (right) and KdV theory (bottom)*

| | All cases | | | |
|---|---|---|---|---|
| | $a_0$ | $a_1$ | $b_0$ | $b_1$ |
| Mean | -0.009 | 1.08 | -0.005 | 1.24 |
| SD | 0.005 | 0.49 | 0.006 | 3.08 |
| | Equal layer depths | | | |
| | $a_0$ | $a_1$ | $b_0$ | $b_1$ |
| Mean | -0.006 | 1.08 | -0.004 | 1.47 |
| SD | 0.003 | 0.56 | 0.005 | 3.20 |
| | Unequal layer depths | | | |
| | $a_0$ | $a_1$ | $b_0$ | $b_1$ |
| Mean | -0.012 | 1.07 | -0.006 | 0.89 |
| SD | 0.006 | 0.39 | 0.008 | 3.02 |

Table 6.4: *Means and standard deviations for the long wave velocity coefficients*

occur in different locations. Additionally, horizontal velocities may appear to have the wrong sign as the position of the interface has been wrongly estimated.

Both of these features are seen on figure 6.31, which is typical of the velocity scatter plots in the unequal-depth long wave cases. Some of the horizontal velocity values

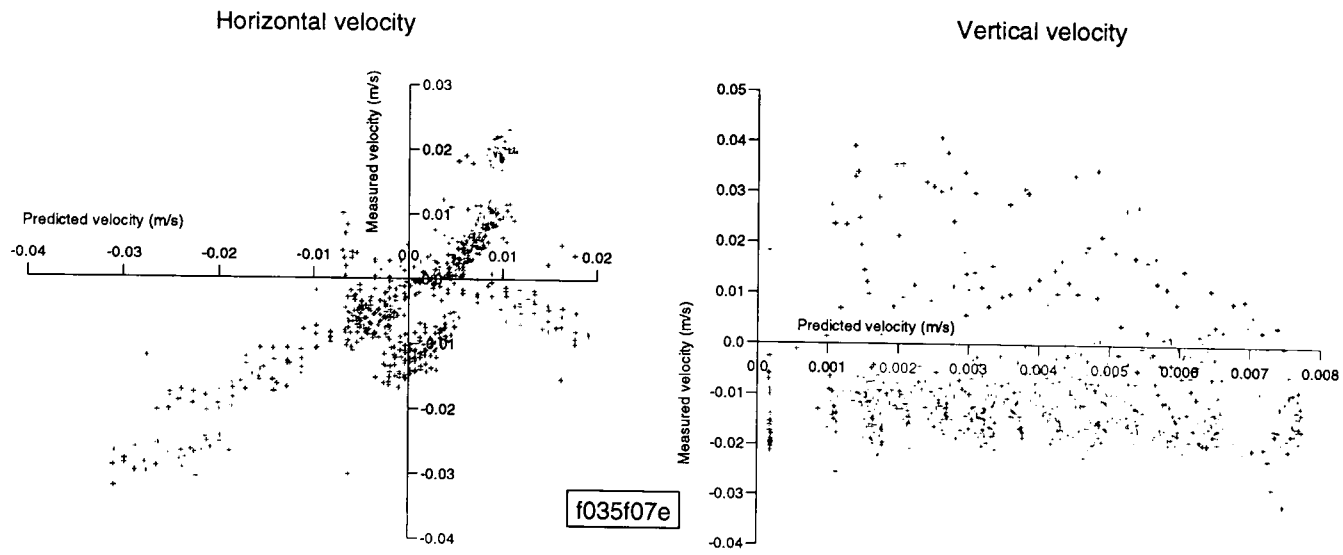


Figure 6.31: *Scatter plots of the horizontal and vertical velocities of vector map f035f07e.vec against linear predictions*

appear to be in the wrong quadrant, as would be the case if the sign of one quantity were wrong. It can also be clearly seen that the vertical velocities have been wrongly estimated. This figure corresponds to figure 6.29, and from that map it can be seen that the sharpness of the trough has created high rise velocities behind the trough, which are completely missing on the sinusoidal theoretical prediction.

The standard deviations were as high in the equal layer depth cases as in the unequal depth cases. The same considerations of wave shape apply, as can be seen from figure 6.27. It must be noted that the presence of free harmonics in the tank will also be a significant contributor to any difference between measured and predicted velocities.

| | 95% | | 90% | | 70% | |
|---|---|---|---|---|---|---|
| All cases | u | w | u | w | u | w |
| Mean | 1.72 | 3.99 | 1.67 | 3.82 | 1.62 | 3.73 |
| SD | 0.53 | 1.68 | 0.49 | 1.69 | 0.42 | 1.84 |
| Equal layer depths | u | w | u | w | u | w |
| Mean | 2.07 | 4.12 | 1.97 | 4.05 | 1.78 | 4.09 |
| SD | 0.38 | 1.83 | 0.37 | 1.87 | 0.39 | 2.05 |
| Unequal layer depths | u | w | u | w | u | w |
| Mean | 1.20 | 3.80 | 1.22 | 3.48 | 1.38 | 3.21 |
| SD | 0.21 | 1.49 | 0.22 | 1.41 | 0.35 | 1.41 |

Table 6.5: *Ratios of measured to predicted velocity percentiles for the long wave cases*

The final method of characterising the velocities is by percentiles. This method is largely immune to mismatches between wave shapes, as it merely selects the highest velocities from anywhere in the flow. The results are presented in table 6.5.

In this table a clear difference between equal depth and unequal depth cases is seen. There is also a difference between the behaviour of the two velocity components.

For the horizontal velocity components, it is seen that the measured extreme velocities tend to be up to double the predicted ones. For the equal layer depths, this disparity is reduced by moving from the most extreme values (95th percentile) to the less extreme ones (70th percentile). Surprisingly, the cases of unequal layer depths show the opposite trend, although the standard deviation also increases. It is notable that the disparity between measurement and linear theory never rises above 40% for these cases.

The vertical velocity components are poorly predicted by the theory. Percentiles for "all cases" suggest that the measured vertical velocity extremes are of the order of 4 times the predicted velocity extremes. When this result is decomposed into equal depth and unequal depth cases, it is seen that the greater disparity is found in the former, although the difference is not great. For unequal layer depths, the disagreement decreases from the 95th percentile to the 70th.

These figures are significant because they show that linear theory is not able to predict the vertical velocity components of long waves with sufficient accuracy for engineering purposes. The disparity between measured and predicted percentiles is too great for it to be attributed to errors in the wave height or velocity measurements.

The performance of solitary wave theory could not be measured using statistics because the solitary wave possesses no crest, and so there would be no match except in the trough. There were insufficient cases of wave troughs to allow meaningful statistics to be calculated.

## 6.5 Waves with a stratified upper layer

### 6.5.1 Wave height gauge traces

The first tests using an inhomogeneous upper layer were conducted with three wire wave height gauges in the tank. It was noted that the signal from these gauges was

very low. Consideration of the method of calibration led to the conclusion that these gauges could not be relied upon to give reliable quantitative measurements. However, information about the wave shape could be discerned.

Later experiments in this set were conducted with the aspirating probe in the tank, close to the level of maximum gradient. The poor time constant of the probe, discussed in section 4.7, meant that the wave shape could not be regarded as accurate. Calibration of the probe was done by inference from approximate knowledge of the background stratification, hence estimates of the wave height were only approximate.

The tank was stratified using the rotameters described in section 4.3.3. First, the lower layer was created by filling direct from the saline reservoir. The stratified upper layer was created by pumping through the sponge float. The thickness of the upper layer was set to be a nominal 100mm, and was created by adjusting the rotameters from the fresh water and saline reservoirs differentially after every 10mm of additional tank depth (25 litres). The fine layers which were created by this method quickly (over one or two hours) diffused into a smooth profile. This profile was represented mathematically using the same parameters as before; however, the thickness parameter $h$ was larger than in the other experiments, and the mathematical layer depths $H_{1,2}$ were set so that the centre of the stratified portion (median density position) was the "boundary" between the layers. A typical density profile (calculated from a measured profile as described in section 4.7) is shown in figure 6.32.

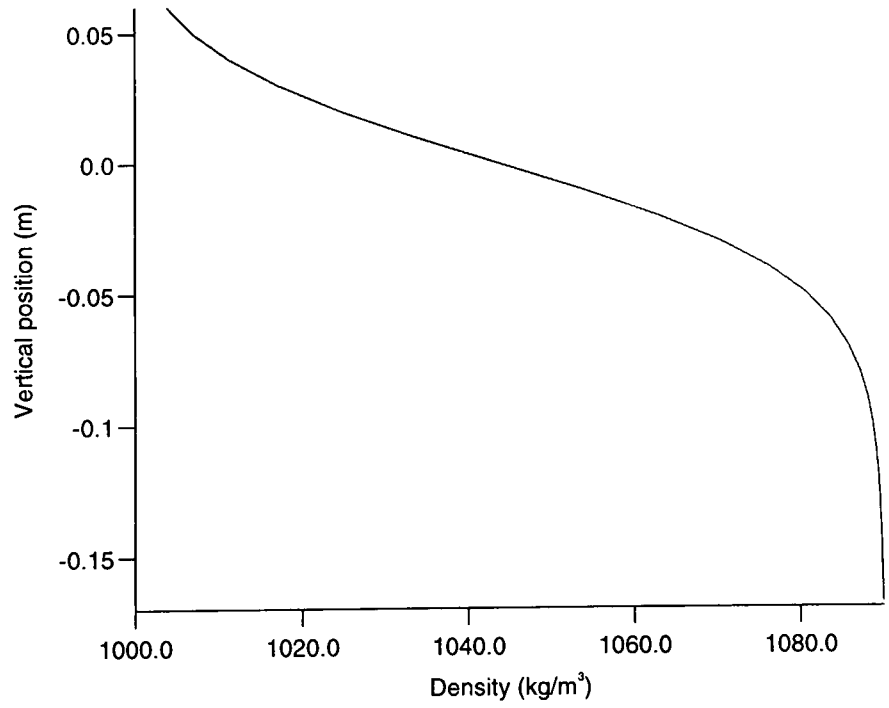


Figure 6.32: *Typical stratification used for the linearly stratified upper layer cases (modelled from a measured profile)*

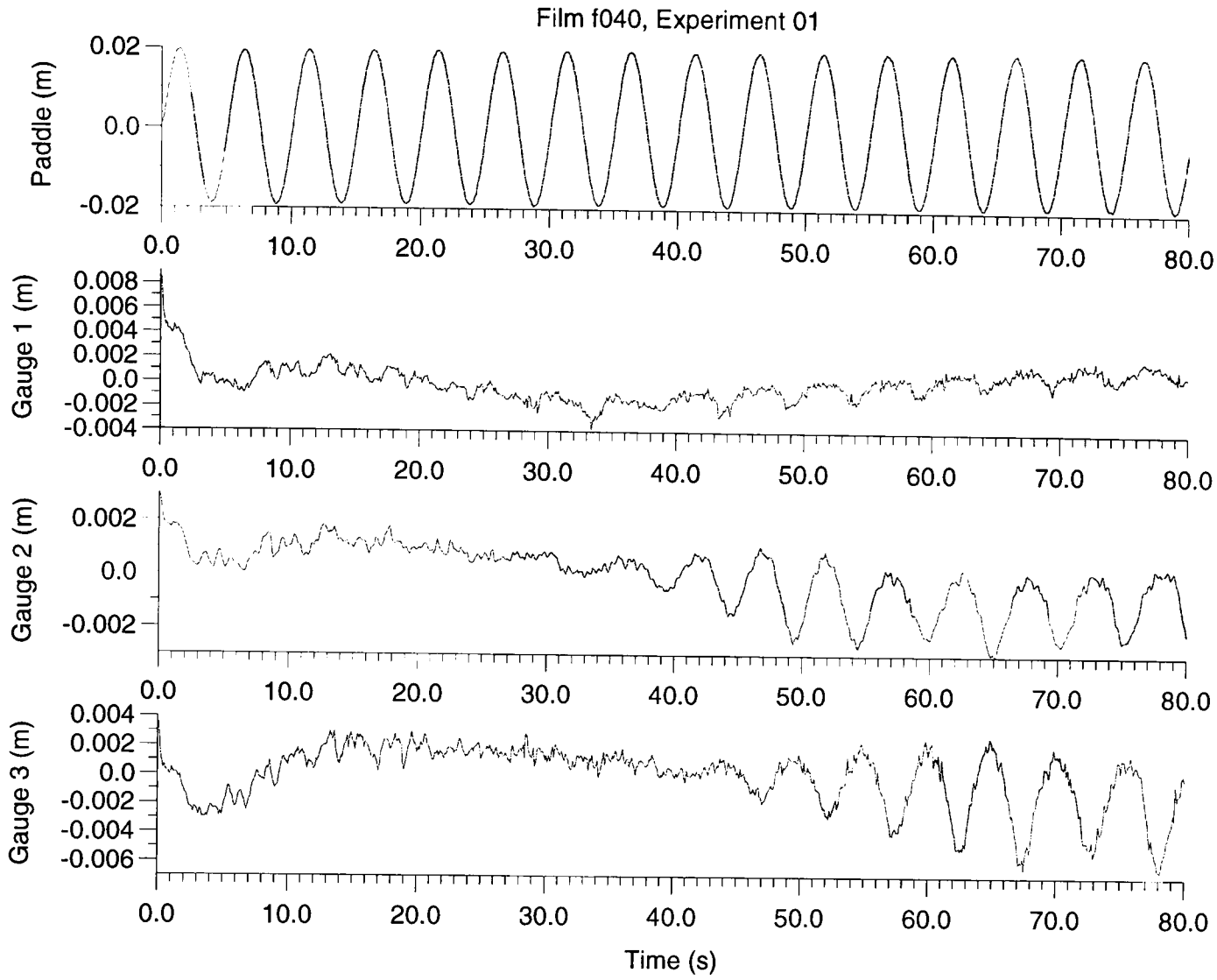


Figure 6.33: *Wave gauge traces in a linearly stratified upper layer with* $f = 0.2Hz$ *and* $\Delta\rho/\overline{\rho} = 8.8\%$

Figures 6.33–6.35 show the wave gauge and probe records from three experiments. The gauge locations are described in table 6.6.

| Item | Distance from wavemaker end of tank |
|---|---|
| Probe | 0.75m |
| Gauge 1 | 2.4m |
| Gauge 2 | 3.8m |
| Measurement zone | 3.8m |
| Gauge 3 | 4.8m |

Table 6.6: *Locations of the wave gauges in the inhomogeneous upper layer experiments*

In all of the figures shown, the first wave gauge suffered from significant drift during the experiment. This may be due to its relative proximity to the wavemaker, i.e., if

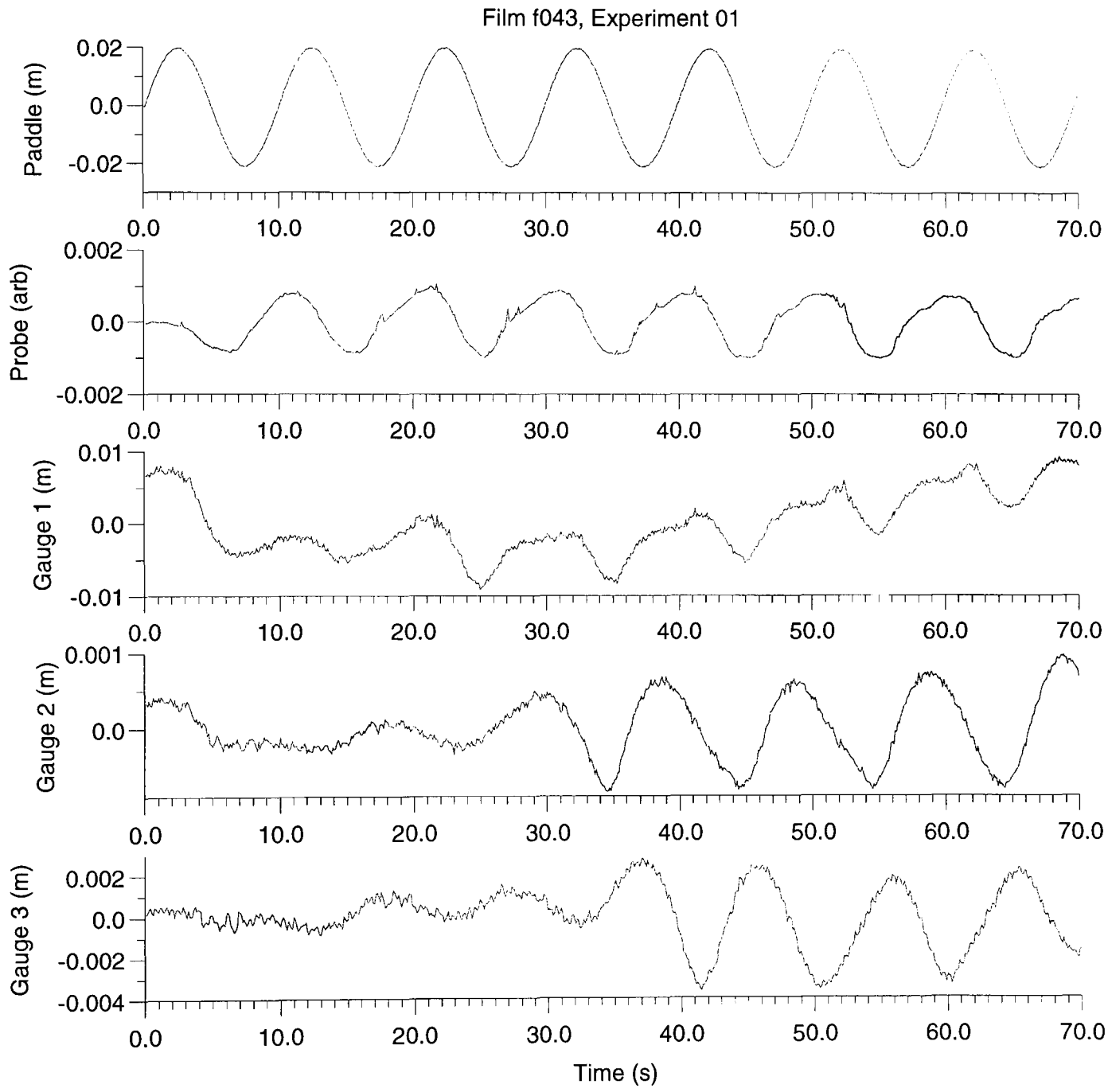


Figure 6.34: *Wave gauge traces in a linearly stratified upper layer with* $f = 0.1Hz$ *and* $\Delta\rho/\overline{\rho} = 8.9\%$

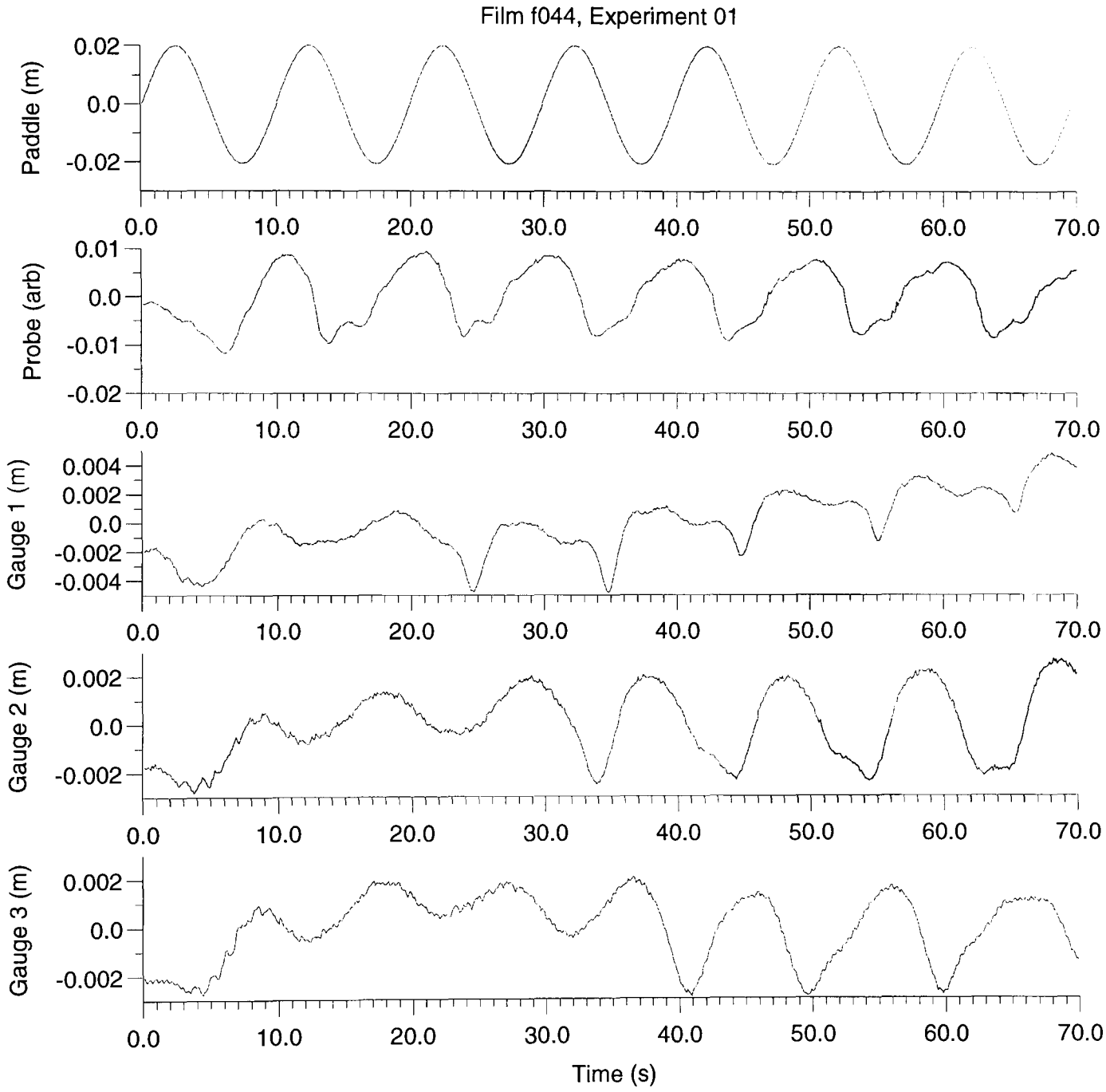


Figure 6.35: *Wave gauge traces in a linearly stratified upper layer with* $f = 0.1Hz$ *and* $\Delta\rho/\overline{\rho} = 8.9\%$ *(more diffuse stratification than the previous figure)*

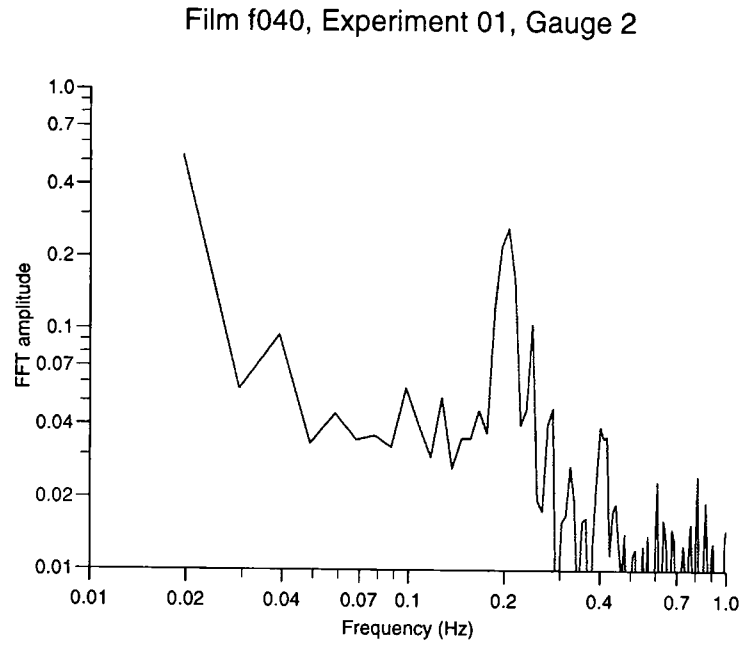


Figure 6.36: *Fourier transform of gauge 2 in figure 6.33*

mixing were generated at the wavemaker, gauge 1 would show an offset before the other gauges. Depending on the form of the mixing, the probe might or might not show an offset. In figure 6.33, this gauge also suffers from considerable noise, which also affects the other gauges. It is possible that the signal earth in the tank was faulty during this experiment, and gauge 1 was most affected as it was closest to the main noise source (the wavemaker).

Figure 6.33 shows waves of intermediate length relative to the layer depths, while figure 6.34 and 6.35 shows waves which are long relative to the layer depths. The layer depths are unequal, so asymmetry in the wave profile is to be expected.

Fourier transforms of the previous gauge traces are shown in figures 6.36 and 6.37. The strong low frequency component shows that some signal drift is present on this gauge. The fundamental component (at 0.2Hz) dominates the higher frequencies, but other harmonics are also present. Not all of these harmonics fall on the frequency bins which would be expected from non-linearity. It is not possible to say from the Fourier Transform what proportions of the harmonics are bound or free.

The gauge traces of the long wave cases (e.g. figure 6.34), together with the Fourier transforms, show an interesting transformation of the wave as it propagates up the tank. The first gauge trace shows a strong non-linearity in the wave shape, resulting in a strongly sharpened trough and a strong second harmonic. However, whereas in the two-layer cases this shape persisted as the wave propagated, in this case the second harmonic, and the distorted shape, have all but disappeared by the time the wave reaches gauge 3.

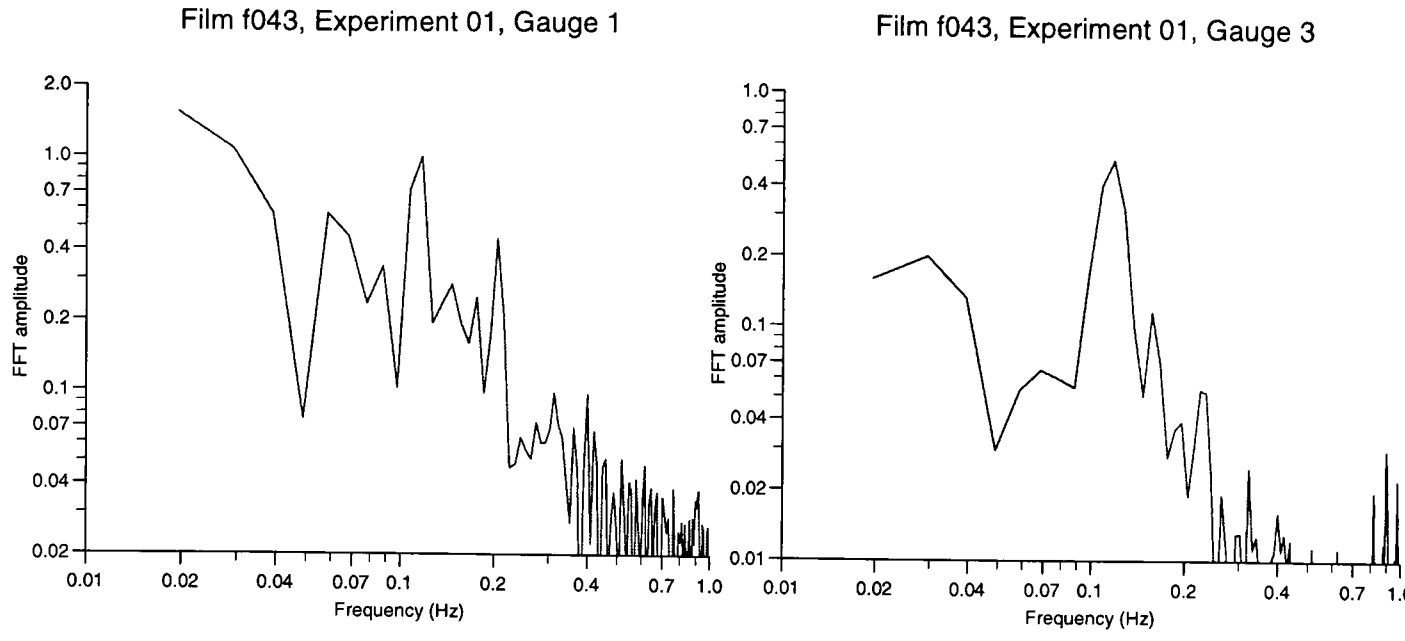


Figure 6.37: *Fourier transforms of gauges 1 and 3 in figure 6.34*

It was thought that this might be due to the lower buoyancy frequency in these tests, which should act to limit the highest frequency which could propagate. However, it was found that the buoyancy frequency was approximately 0.5Hz; not low enough to explain the disappearance of the second harmonic at 0.2Hz.

One possible explanation is the "resonant" effect which is possible when the interface is thick. Wave energy may be able to transfer into higher modes, which, despite having the same frequency as the first mode, travel at a lower phase speed, possess more than one velocity reversal in their kinematic profile, and are more affected by viscosity (section 3.3.5).

### 6.5.2 Velocity measurements

Owing to the difficulties experienced in measuring the heights of the waves in this set of experiments, theoretical comparisons are not available. Some qualitative conclusions can be drawn from the vector maps in figures 6.38 and 6.39.

The most noticeable feature of these waves is the persistence of a strong velocity gradient right up to the surface, for both intermediate and long waves. Thus the maximum horizontal velocity associated with an internal wave crest in such a situation occurs at the water surface. The project was originally focused on the effects of internal waves on the risers and tethers associated with floating production systems. However, this finding suggests that internal waves in broad thermoclines may pose a problem for surface operations.

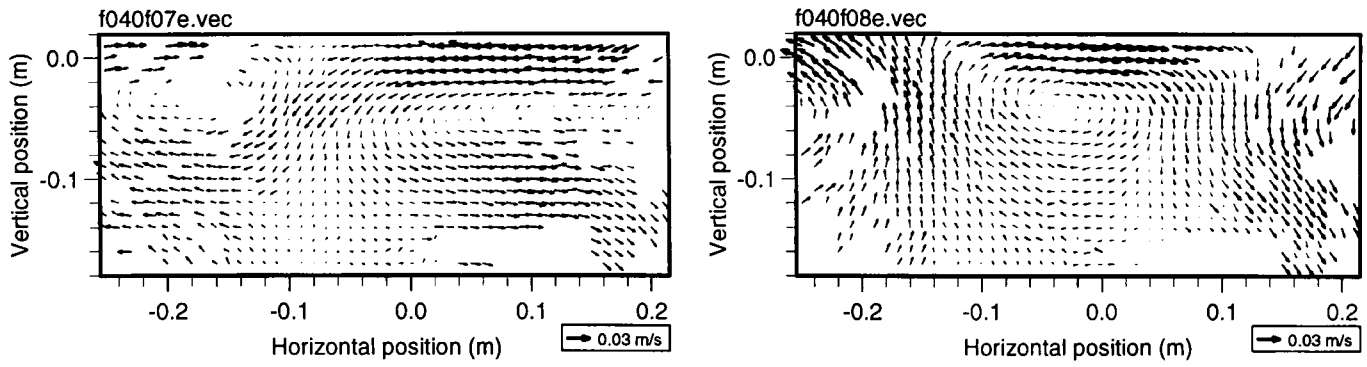


Figure 6.38: *Intermediate length waves with an inhomogeneous upper layer*

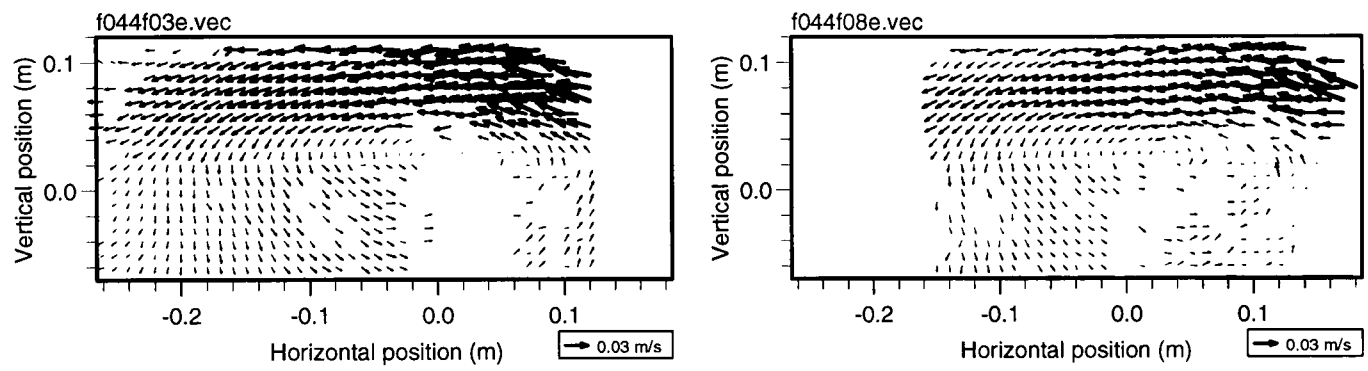


Figure 6.39: *Long waves with an inhomogeneous upper layer*

## 6.6 Numerical experiments

### 6.6.1 Convergence of the numerical scheme

In this section "convergence" refers mainly to the ability of the numerical scheme to provide solutions for given input parameters. An alternative meaning in the context of a series expansion is the convergence of the series itself. In this section the performance of the series itself is referred to in terms of "validity".

Section 3.4.6 describes how the first, second and third order equations were solved to obtain particle velocities and wave shapes. Solutions for the first order equation were obtained successfully for all of the cases of interest. The second order solution converged only for a subset of these, unfortunately failing to provide comparisons for any of the long and intermediate length waves.

Figure 6.40 shows the approximate domain of convergence over a range of parameters. Both graphs show lines of marginal convergence against the Froude number $Fr = c^2k/g'$. The left hand graph shows convergence over a range of values of the non-

dimensional interface thicknesses $k\delta$, while the right hand graph shows the behaviour over a range of non-dimensional layer depths $kH_1$, where $H_1$, the upper layer depth, is less than the lower layer depth $H_2$.

These graphs were produced by running the simulation to second order for a variety of cases, and adjusting the input parameters until convergence was only just achieved. The curves shown were fitted to the results; both are cubic in $Fr$. The number of steps was set at 200 after experimentation showed that there was no gain in working with smaller steps.

It can be seen that the system converges more readily when the interface is thick. This is presumably because the thinner interfaces produce high derivatives in the streamfunction, which would be more inclined to upset the system. In the limit of two immiscible fluids, the streamfunction would be discontinuous, and no solution could be found by the present method.

It is clear from the right hand graph that long waves converge less well than short. This is consistent with the Dean and Dalrymple's (1991) criteria for the validity of the Stokes series expansion, discussed in section 3.3.3. However, convergence of the second order solution does not necessarily guarantee validity of the expansion. Validity was tested using the criteria of Dean and Dalrymple (equations 3.24 and 3.25). The first criterion enforces convergence of the series, while the latter, stricter criterion prevents anomalies in the theoretical wave shape at small orders of expansion.

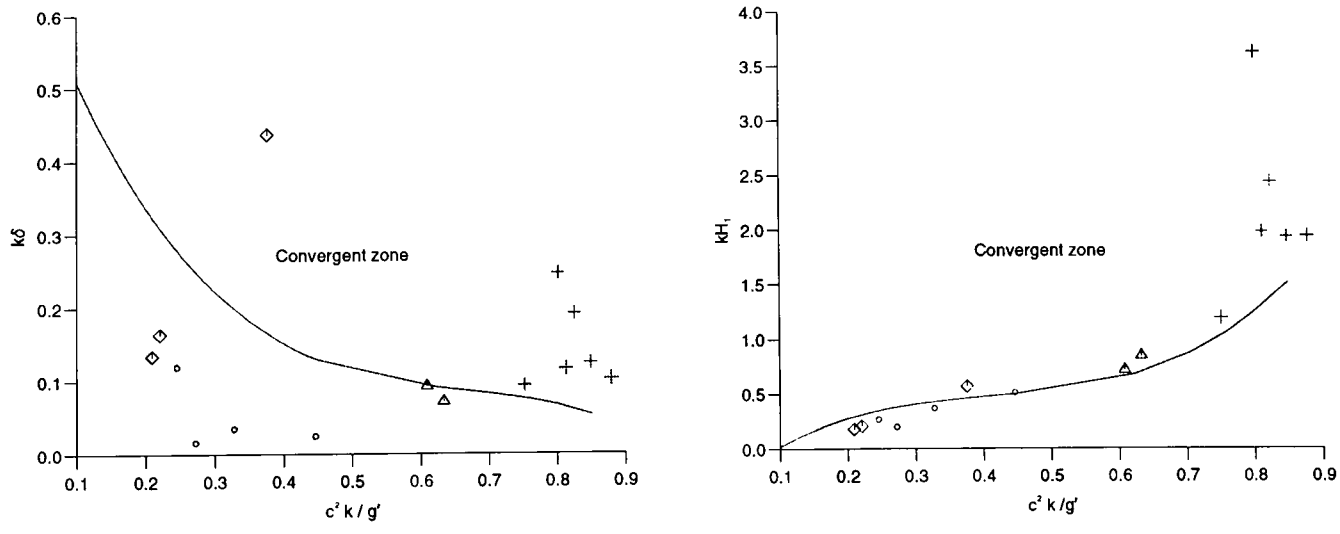


Figure 6.40: *Approximate domains of convergence for the second order Stokes solution for ranges of non-dimensional interface thickness, non-dimensional depth and Froude number. Short wave cases: +; intermediate wavelength cases: △; long wave cases: ○; linearly stratified upper layer: ◇*

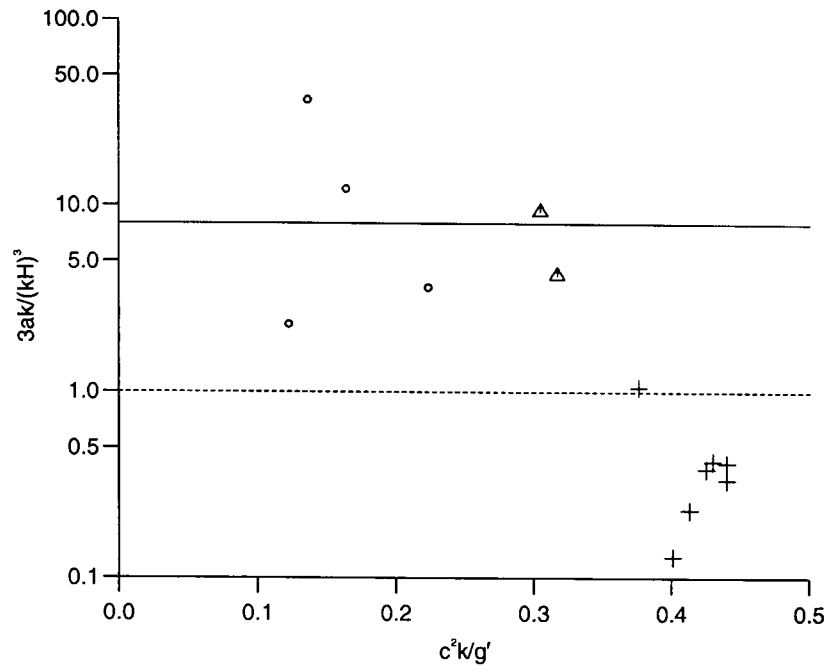


Figure 6.41: *Domain of validity of the Stokes solution based on wave shape criterion. Short wave cases:* +*; intermediate wavelength cases:* △*; long wave cases:* ○*. Above the dashed line anomalies in the wave shape may occur, while above the solid line the series may not converge.*

The status of the experiments in regard to these criteria is shown in figure 6.41. It is seen that all of the short wave results, although they occupy the steep extreme of the graph (high Froude number), can be treated using the second-order Stokes expansion. Of the long and intermediate-length waves, all would show anomalous wave shapes if the second order solution were to be used, and for a few, the series would not be expected to converge. It is not true that the failure to find a valid second-order solution for these cases means that it can be ignored; rather, this finding indicates that a non-linear long wave theory would be more appropriate than a Stokes theory.

A final point about the use of the smoothness of the wave shape to predict the performance of the expansion is that the shape anomalies should disappear with higher orders of expansion. That is, the presence of bumps in the wave trough indicates that the expansion has not been carried far enough. From an engineering perspective, it may be the case that the kinematics in the extreme regions might still be reasonably well predicted by the expansion. One would not wish to proceed to design on this assumption, however, and it would only be possible to test it by calculating the higher order terms.

### 6.6.2 Interpretation of the numerical results

#### The third order term

Having extended the expansion to third order, it is important to test the behaviour of the expansion under different conditions. Figures 6.42 and 6.43 show velocity profiles for a short wave of moderate amplitude. The second order part is discussed below. The third order part acts in both cases to sharpen the peaks in the velocity profile.

As with the second order component, the addition of the third order component may generate an unphysical wave shape if the wave is large. The shapes of the waves in figures 6.42 and 6.43 were calculated and are shown in figure 6.46. The first wave, with a sharper interface, has a distorted shape, from which it is concluded that more terms in the expansion would be needed to provide a realistic wave shape. The smoother shape of the wave in the broader interface reflects the less extreme kinematics of that type of stratification.

These effects may be seen more clearly in figures 6.44, 6.45 and 6.47, which show waves of larger amplitude in the same configuration. It is clear that the third order expansion does not provide a realistic wave shape, especially in the case of the sharper interface.

In considering the third order term it must be remembered that, at tank scale, the effect of viscosity should not be neglected (section 3.3.5). The effect of viscosity will be greatest where the interface is sharp. If viscosity were included in the calculations the wave shape would appear to remain smooth at greater degrees of non-linearity.

#### Asymmetry and the Boussinesq approximation

An important point about the second order component of the wave is that where the flow is perfectly symmetrical its magnitude is zero. This occurs in deep water under the Boussinesq approximation and was observed by Thorpe (1968b). The reason is that the second order component (and higher even orders) acts to sharpen crests and flatten troughs, or to sharpen troughs and flatten crests. Clearly there must be some asymmetry for this to occur.

In surface waves, the asymmetry is always present since the dynamical effect of upper layer (the atmosphere) is negligible in comparison with that of the lower layer (the water). Likewise, in an otherwise symmetrical stratified flow, the differing densities of

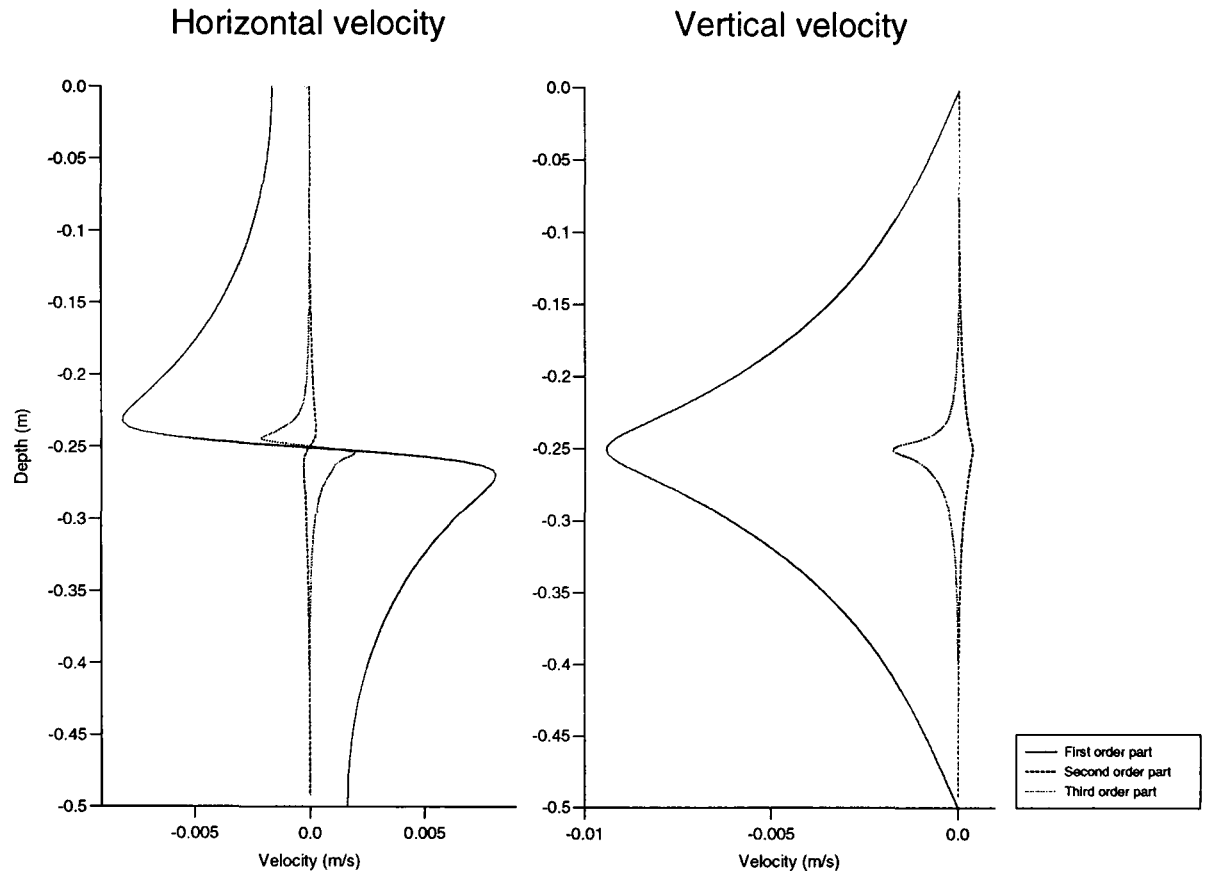


Figure 6.42: *First and second order velocity profiles for a short wave with* $\delta = 0.01m$, $H_w = 0.01m$, $\alpha = 0.04$

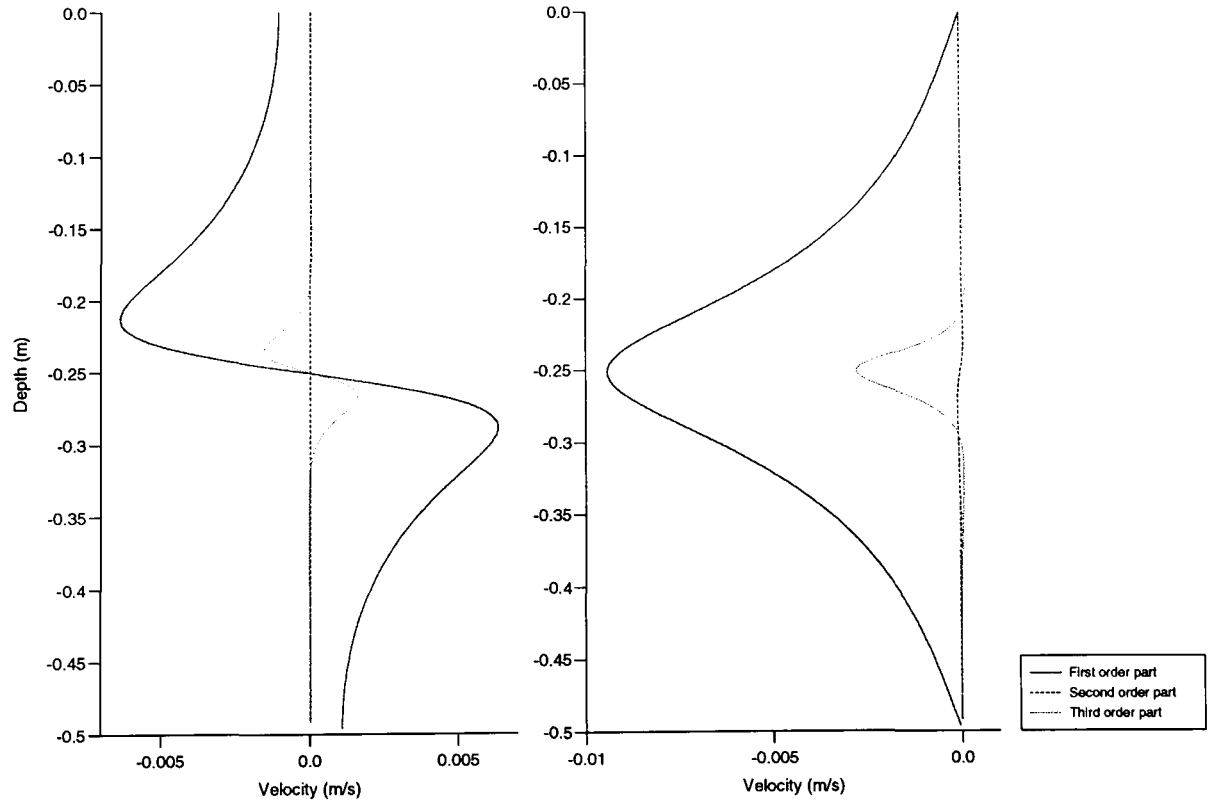


Figure 6.43: *First, second and third order velocity profiles for a short wave with* $\delta = 0.03m$, $H_w = 0.01m$, $\alpha = 0.04$

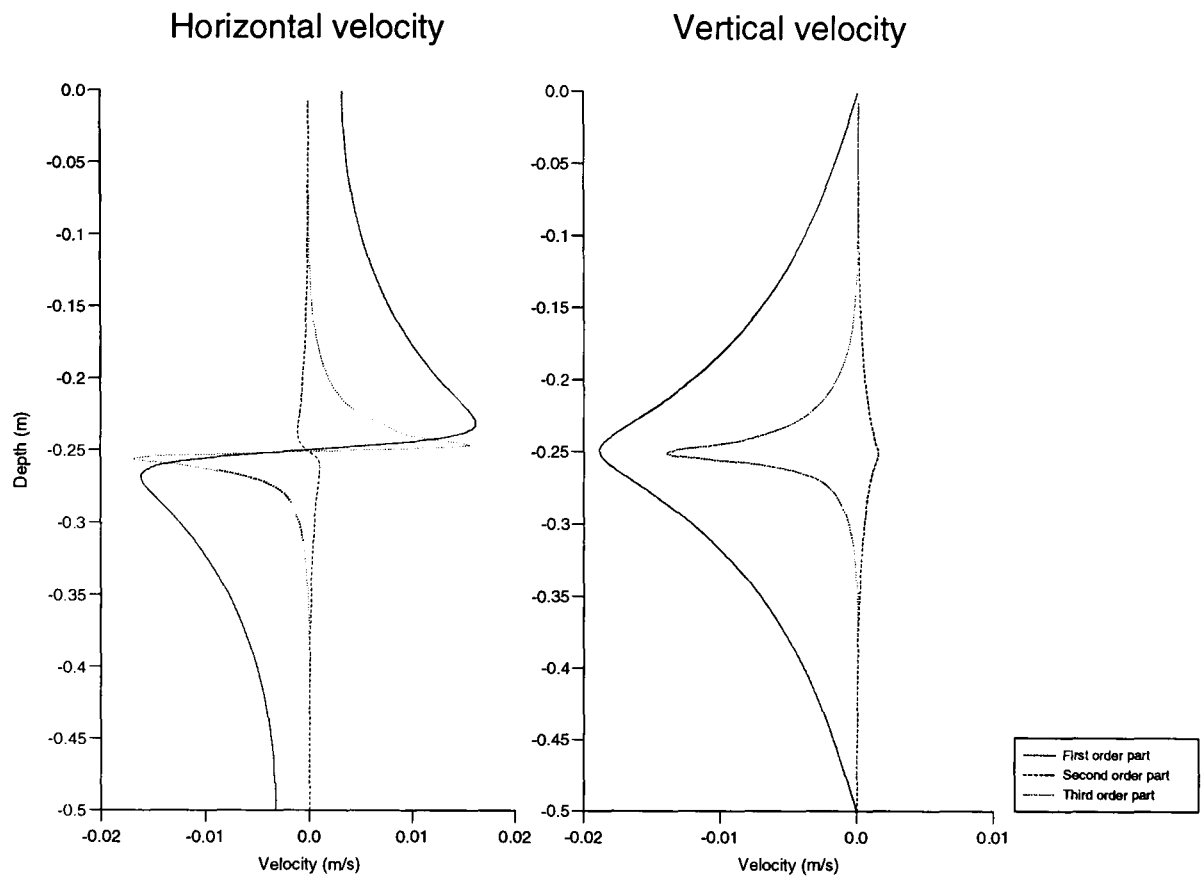


Figure 6.44: *First, second and third order velocity profiles for a short wave with* $\delta = 0.01m$, $H_w = 0.02m$, $\alpha = 0.04$

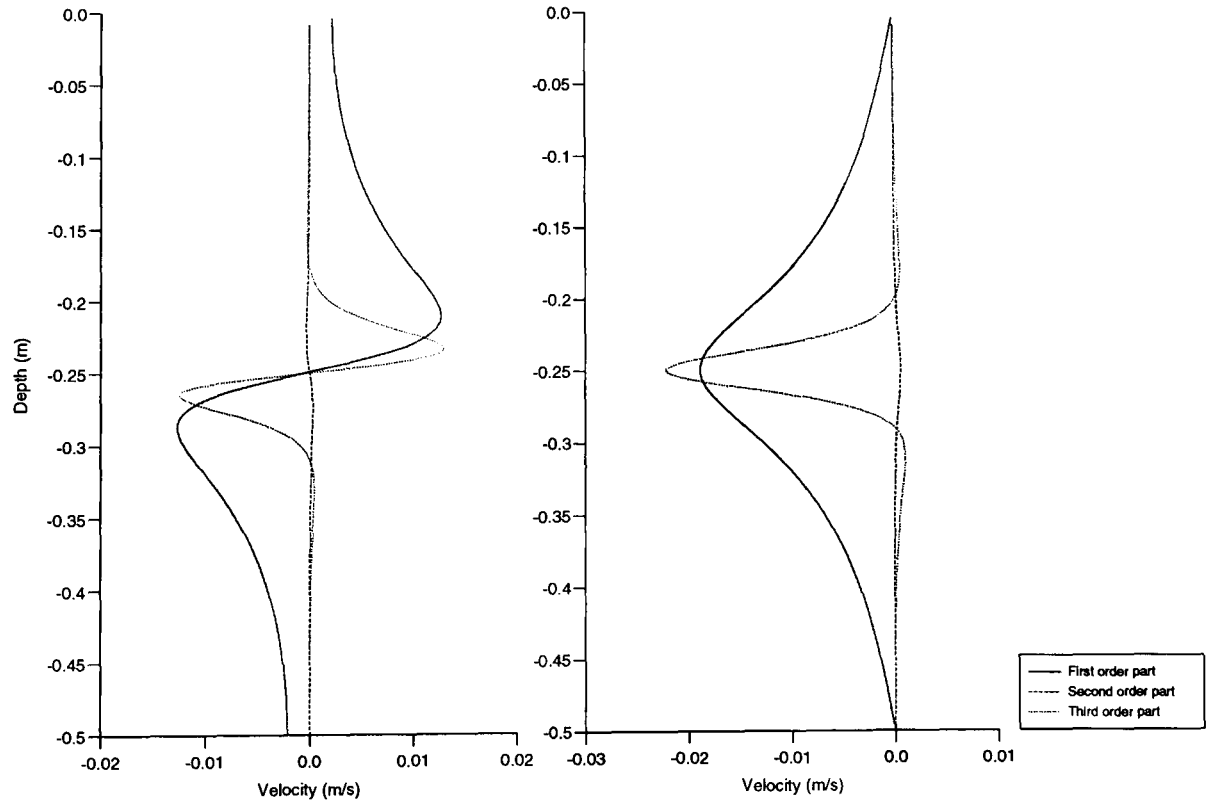


Figure 6.45: *First, second and third order velocity profiles for a short wave with* $\delta = 0.03m$, $H_w = 0.02m$, $\alpha = 0.04$

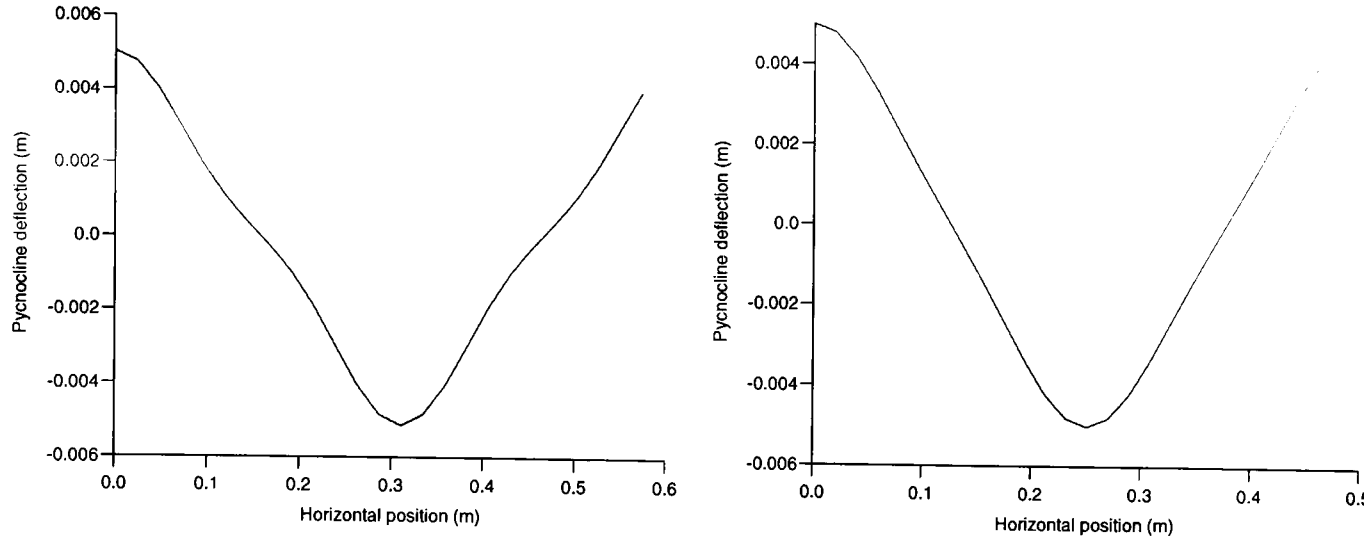


Figure 6.46: *Wave shapes for short waves calculated to third order with* $H_w = 0.01m$*; left:* $\delta = 0.01m$*, right:* $\delta = 0.03m$

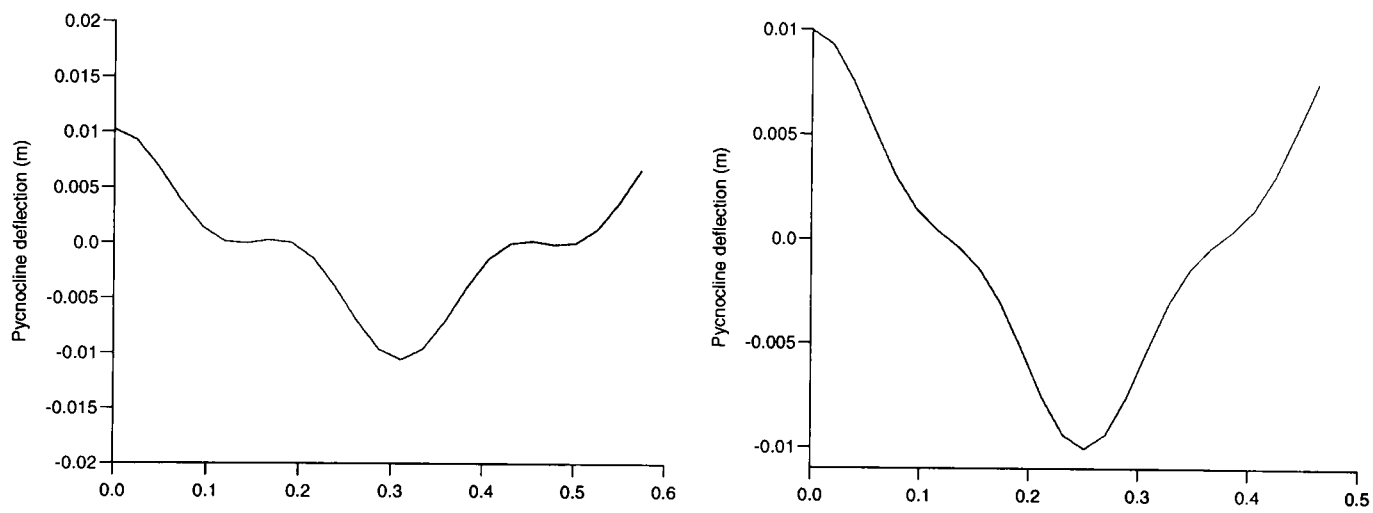


Figure 6.47: *Wave shapes for short waves calculated to third order with* $H_w = 0.02m$*; left:* $\delta = 0.01m$*, right:* $\delta = 0.03m$

the fluids will provide the asymmetry. Therefore one would expect deep water waves in a non-Boussinesq fluid to have a non-zero second order component, while in a Boussinesq fluid the second-order component would be zero.

Figure 6.43 shows velocity components in a deep water wave with $\alpha = 0.04$, a density difference of 8%. Velocity components for a wave with the same parameters but with $\alpha = 0.15$, a density difference of 30%, are shown in figure 6.48. The relative significance of the second order components is clearly greater in the latter case. This is because the Boussinesq approximation is essential for even orders to exist in deep water.

By contrast, the impact of the Boussinesq approximation at first order is small, as shown in figure 6.49. The first order horizontal velocity is not significantly modified by the Boussinesq approximation under these conditions.

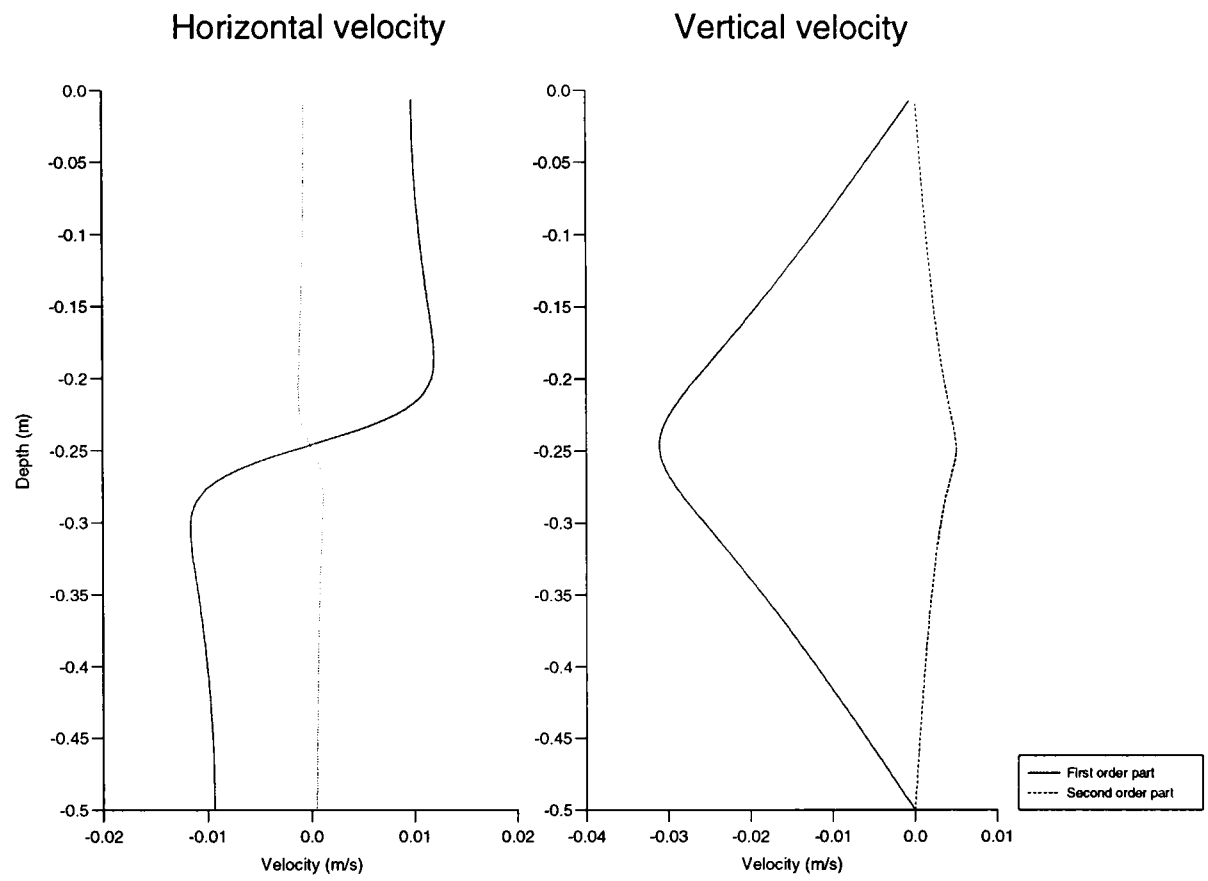


Figure 6.48: *First and second order velocity profiles for a short wave with* $\delta = 0.03m$, $H_w = 0.01m$, $\alpha = 0.15$

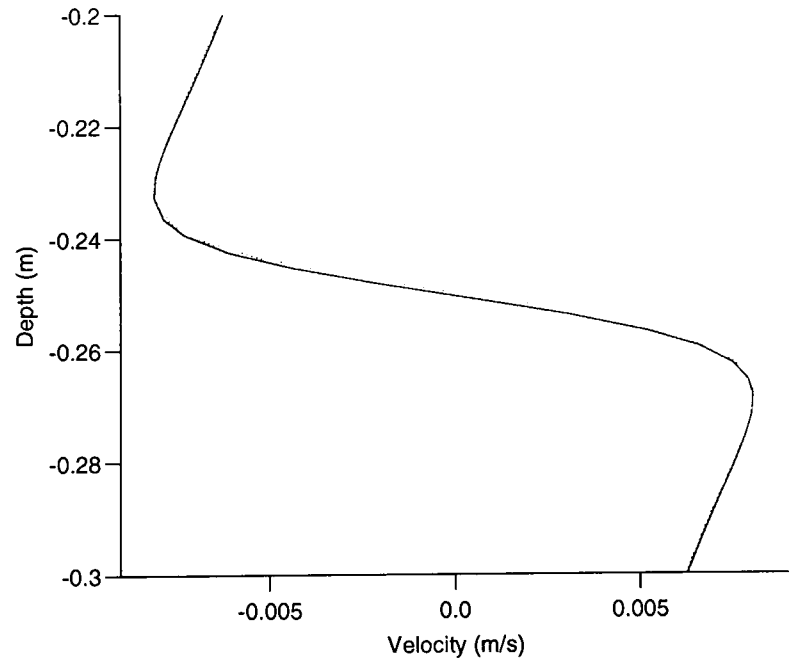


Figure 6.49: *First order horizontal velocities computed with (broken line) and without (solid line) the Boussinesq approximation;* $\delta = 0.01m$, $H_w = 0.01m$, $\alpha = 0.04$

### 6.6.3 An ocean-scale comparison

Curtin and Mooers (1975) observed an internal wave packet in a shallow pycnocline near Oregon, using a profiling current meter, shipboard sonar, temperature and salinity instruments, water sampling and aircraft visual observations. The observation point was at a water depth of about 80m, while the broad pycnocline was centred at around 12m depth. The density change across the pycnocline was about 0.3%. A dense layer of plankton just below the pycnocline was detected in water samples; this layer strongly reflected the sonar signal. Oscillations of the plankton layer were used to gauge the heights and periods of the internal waves, which were estimated at 11m and 9 minutes respectively.

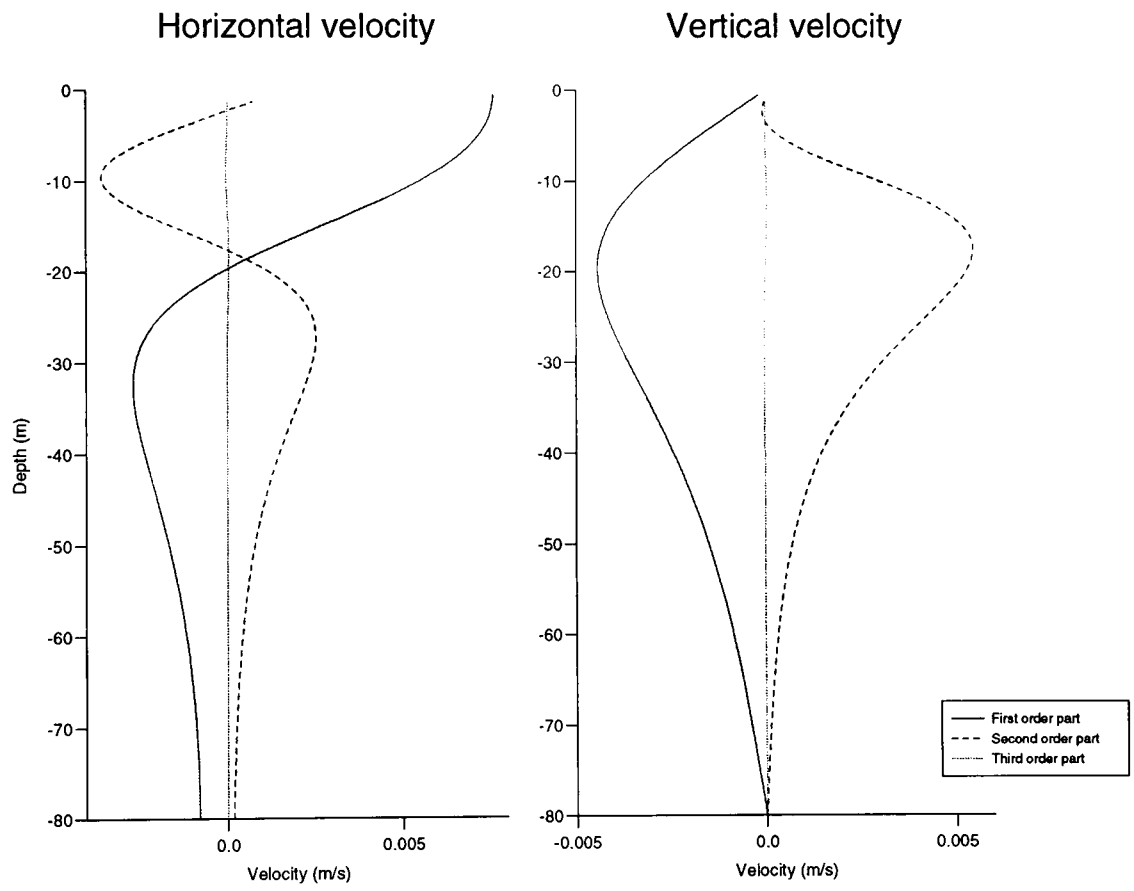


Figure 6.50: *First, second and third order velocity profiles for a wave of reduced amplitude, with other parameters taken from Curtin and Mooers' data*

Using Curtin and Mooers mean density profile and the observed period as starting points, the first order equation was solved to yield a prediction for the wavelength of about 140m, roughly consistent with Curtin and Mooers observations. The same linear modal analysis was performed by Curtin and Mooers. Unfortunately, the current profiling instrument took approximately 10 minutes to take one current/depth profile, and so their velocity measurements did not have sufficient temporal resolution to allow comparison with the numerical model. In any case, given the wavelength to depth and

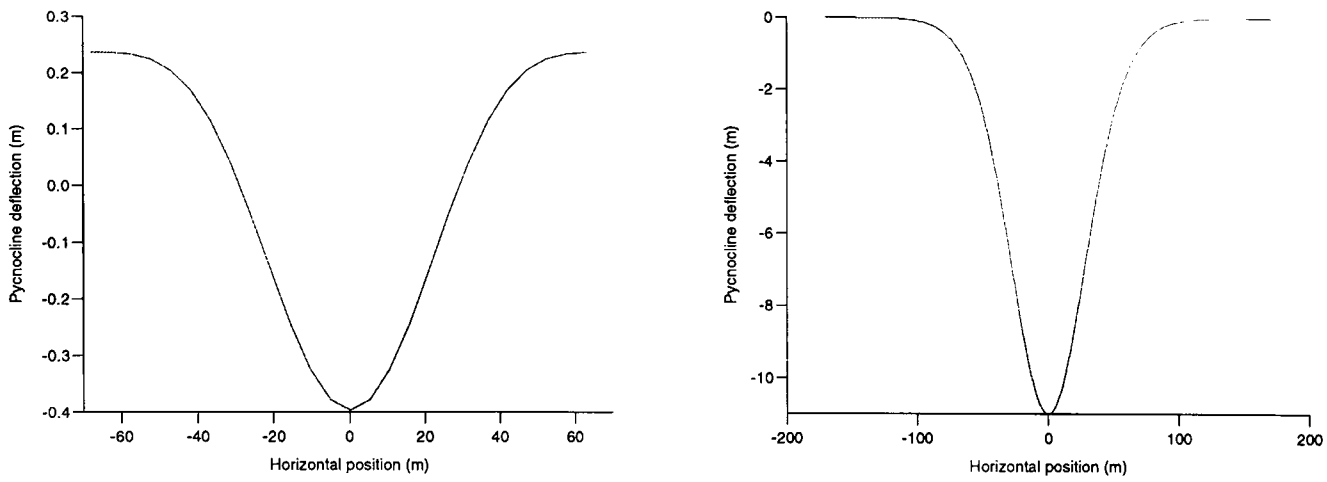


Figure 6.51: *Left: shape of the reduced amplitude wave with other parameters taken from Curtin and Mooers' data; right: KdV solitary wave with the same height as Curtin and Mooers' observations*

amplitude to depth ratios, the linear model would not be expected to yield accurate results.

To investigate this further, the ratios described in section 3.3.3 which express the validity of the Stokes expansion were evaluated. These are, from equation 3.24

$$\frac{3}{8}\frac{ak}{k^3H^3} \simeq 0.56 < 1 \tag{6.3}$$

indicating that the series should converge, and from equation 3.25

$$3\frac{ak}{k^3H^3} \simeq 4.5 > 1 \tag{6.4}$$

indicating that the solution will not provide a realistic wave shape at small orders of expansion.

An estimate of the amplitude at which the Stokes expansion would be valid can be obtained from the above equation. A wave height of 0.76m is close to the upper limit. For this case, the equations were solved to third order. Velocity profiles for the first, second and third order parts are shown in figure 6.50, while the resultant wave shape is shown in figure 6.51. The shape of a KdV solitary wave propagating under similar circumstances is also shown.

The second order component is seen to have the opposite sign to the first order. Since the periodicity of the second order part is twice that of the first order part, this indicates

that the velocities will be enhanced by non-linearity in the wave trough, and reduced in the wave crest. The wave shape shown has a sharpened trough and a flattened crest, as must be the case for long waves in a shallow pycnocline. The third order component is insignificant.

Having only one point from which measurements could be taken, Curtin and Mooers were not able to measure the phase speed of the disturbance. The waves observed on the sonar trace had periods which in the linear approximation corresponded to phase speeds of around 0.26m/s. An infinitesimal long wave would have a phase speed of about 0.34m/s. A KdV solitary wave of equivalent height to the heights observed on the sonar trace would have a phase speed of 0.43m/s, with a correspondingly greater lengthscale. Evaluation of the actual phase speed could thus be used to help ascertain the type of the observed disturbance.

Knowledge of the phase speed would clarify what form of disturbance was being measured. Nevertheless, it seems most likely that the waves observed by Curtin and Mooers were packets of waves which may have been evolving into solitary or cnoidal waves. The height of the disturbances is great, however, and even weakly non-linear theory might not be adequate.

# Chapter 7

# Discussion

The major findings of the experiments are discussed and the quality of the data is considered. Basic marine loading theory is reviewed and some ocean-scale loading calculations are performed. It is shown that non-linearity may be important factor in loading. The significance of the findings to offshore engineering is discussed, including the vulnerability of offshore structures to internal waves, the significance of the experimental results, and the special case of the North-West Approaches.

## 7.1 Comparison of measurements and numerical predictions

### 7.1.1 Quality of the raw data

The program of experiments suffered from some equipment problems, which are described in detail in sections 4.8 and 5.5. The largest problems were the performance of the density probe and the dynamic range of the PIV system. It is felt that the adjustments which were made to the density probe data to compensate for its performance gave estimates of the interface thicknesses of adequate quality for use in the numerical schemes. The dynamic range of the PIV system was rather more limiting.

As was seen in section 6.6, most of the *long* and *intermediate length* waves which were successfully measured were of rather large amplitude. It would have been desirable to measure a range of amplitudes which included smaller waves, in order to perhaps

observe a gradual increase in the deviation from predicted velocities. The *short* waves could also have been treated in this way, although the predictions correlated much better with the measurements in these cases.

The PIV implementation which was used for these experiments was, in terms of accuracy and dynamic range, not inferior to other systems in use at the time. The advent of, for example, digital CCD cameras in PIV at first affected only the convenience and cycle time, in some cases with a loss of performance. The only way of extending the dynamic range down to lower velocities and eliminating the image shifter would be to use cross-correlation techniques. Specialised cameras for cross-correlation PIV are only now becoming available on the market and are still very expensive.

Despite these problems, a wide sample space of experimental results was obtained and was sufficient for demonstrating many of the features of internal waves. The magnitude of the experimental errors was controlled. The repeatability of the data, where this can be assessed, is impressive, as can be seen on figure 6.9.

It is also worth mentioning the lack of good kinematic measurements of internal waves in the literature. The only other application of PIV to internal waves appears to be that of Stevens and Imberger (1996), who also reported problems in dynamic range, and in the end recorded only velocity profiles at a point. Friis et al. (1997) report the use of particle tracking velocimetry, again to measure velocity profiles. The only other attempt to measure full field velocities appears to be that of McEwan (1983b), who used streak photography to estimate the Richardson number in breaking waves.

### 7.1.2 Short waves

Three methods for reducing the data were used for the short wave cases. The purpose of data reduction was to extract a small number of parameters which would express aspects of the performance of the theory. The three methods were: crest, trough, rising and falling "strengths", linear coefficients and percentiles. All three of these methods showed that measured velocities tended to be higher than the predicted velocities. In all cases, predictions were made to second order using the Stokes expansion.

The "strengths" evaluation focused on regions of the flow where extremes are likely to be found (figures 6.12 and 6.13). Given the fact that measurements could often not be made in the interface, the scatter in these estimations is not surprising, and it seems

clear that second order theory does underpredict the magnitudes of the extremes in these waves.

The use of linear coefficients (table 6.2) to compare measured and predicted velocities is an assessment of the degree of agreement over the whole field of the measurement. The standard deviations, which are significant, express the fact that significant wave heights were used as input parameters into the numerical scheme. The variations which occurred in the wave heights as the wave trains propagated would have created equivalent variations in the coefficients.

The percentile evaluation (table 6.3) showed that extreme horizontal velocities could exceed predicted values by up to 40%, while vertical velocities would exceed predictions by around 25%. Comparing this to the linear coefficients (which predicted exceedances of 12% and 16% respectively) suggests that the second order predictions perform least well in the most active region of the flow, i.e., near the interface.

The Stokes expansion, if carried to third order, clearly applies its largest corrections to the interface region. Without a means of accounting for the effects of viscosity, it does not seem reasonable to attempt to apply the third order correction. However, it must be remembered that viscous effects will be very much smaller at ocean scale, and so the third order correction could reasonably be used.

### 7.1.3 Long and intermediate length waves

Longer waves differed from shorter ones firstly in their shape, which tended to be rather different from sinusoidal (e.g. figures 6.21 and 6.23). Second and third order predictions for these waves could not be obtained, and the parameters indicated that the series expansion would not be very successful in any case. For the case of long waves propagating in unequal layer depths, the similarity between the shapes of the largest waves and equivalent KdV solitary waves is of great interest (figure 6.25).

Only the longer waves were assessed quantitatively. The assessment was divided into cases with equal layer depths and cases with one layer shallower than the other. The linear coefficients (table 6.4) tend to show little divergence between the predictions and the measurements; however, the standard deviations show that this conclusion is misleading. For the vertical velocities there was no correlation between measurements and predictions, while for the horizontal velocities the correspondence was better though still poor.

These figures express the fact that the shapes of the measured waves were not sinusoidal. Waves in unequal layer depths tended to show the characteristic sharpened trough of cnoidal waves, solitary waves or waves with strong even harmonics, while the waves in equal layer depths showed a tendency to a more triangular waveform which might result from the addition of odd harmonics.

Percentiles were used for further comparison (table 6.5). Extreme horizontal velocities were underpredicted by a factor of up to 2, being worse for the case of equal layer depths. Measured vertical velocities exceeded the predictions by a factor of about 4, again being worse for the equal layer depth case. This is again a reflection of the divergence of the waveform from sinusoidal.

### 7.1.4 Waves with a linearly stratified upper layer

Both long and intermediate length waves were generated in cases where a relatively thin upper layer was linearly stratified. As explained in section 6.5, accurate measurements of the wave heights were not available and so only qualitative conclusions may be drawn.

The most important conclusion is that under these circumstances, the maximum horizontal velocities are found at or near the water surface. This configuration can be important in warm oceans where the main thermocline is seasonal (e.g. Apel, et al., 1985). Another interesting observation was the transformation of the wave group as it propagated, appearing to show a decrease in non-linearity with distance from the wavemaker. This latter observation would require confirmation in further experiments.

## 7.2 Internal wave loading

### 7.2.1 Basic theory of loading

Morison et al. (1950) derived the formula for the force exerted by a moving fluid on a submerged cylinder. The so-called Morison equation, in the form given by Dean and Dalrymple (1991), is as follows:

$$F = \frac{1}{2} C_D \rho A u |u| + C_M \rho V \frac{Du}{Dt} \tag{7.1}$$

where $F$ is the force per unit length on the cylinder, $A$ is the projected area (per unit length) of the cylinder, $u$ is the fluid velocity and $V$ is the volume of the cylinder per unit length. The two coefficients $C_D$ and $C_M$ are termed the drag coefficient and the added mass coefficient respectively.

The first term determines the force on the cylinder in steady flow. The drag coefficient on which it depends is itself a well known function of the Reynolds number (e.g., Massey 1989), and for most practical hydrodynamic flows falls in the range 1–2. The second term relates to the acceleration of the fluid around the structure. Hallam et al. (1978) recommend $C_D = 1.2$ and $C_M = 2$ for design purposes in the velocity range of interest. However, Efthymiou and Graham (1990) note that current North Sea practise uses $C_D = 0.7$ and $C_M = 2$, while in the Gulf of Mexico $C_D = 0.6$ is widely used. They explain:

> ...these values of $C_d$ do *not* represent the best estimate of this parameter for the relevant flow regimes. Within the context of the design recipe, it is best to view $C_d$ as an artificial parameter, whose value has evolved historically...

Here the larger value ($C_D = 1.2$) is used, since if in design a smaller value is chosen then that will be reflected in other stages of the design process, such as in safety factors, fatigue calculations and joint probability estimates. Here the purpose is merely to evaluate likely forces.

Morison's equation assumes that the diameter of the cylinder with respect to the wavelength is small; this condition is satisfied in this case. Skin friction is also assumed to be small. The total force on the cylinder is found by integrating the force along its length; this approach neglects the presence of differing regimes of vortex shedding. Finally, a rigid cylinder is assumed.

Keulegan and Carpenter (1958) discovered that the values of the coefficients $C_D$ and $C_M$ vary in oscillatory flow, due to the different vortex shedding regimes. The Keulegan-Carpenter number $KC$ is defined as

$$KC = \frac{UT}{D} \tag{7.2}$$

where $U$ is the maximum current, $T$ is the period and $D$ is (for circular cylinders) the cylinder diameter. For small $KC$ the inertia part of the Morison equation dominates,

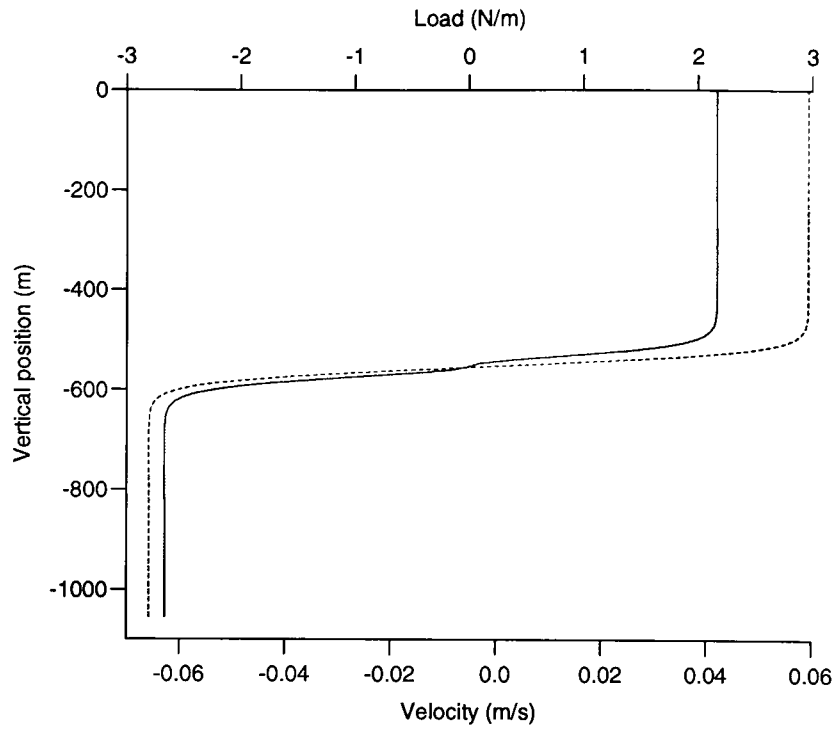


Figure 7.1: *Load per unit length on a 1m diameter circular cylinder (solid line) which would be imposed by a first mode internal tide of amplitude 25m. The maximum horizontal current is shown by the broken line.*

while for large $KC$ the drag term dominates. For high $KC$ the variation in $C_D$ and $C_M$ is not great.

### 7.2.2 Loading in internal waves

In the deep Færoe-Shetland Channel (section 7.3.3), a strong though linear internal tide exists, with energy spread across several modes (Sherwin, 1991). The amplitude of the first mode is about 25m, giving a first-mode horizontal current of about 0.06m/s in the top 500m, and the same in the bottom 500m (though in the opposite direction). If this wave applies a load to a vertical circular cylinder of diameter 1m, the tidal period ($T = 12.42$ hours) gives a value of $KC = O(10^3)$, well into the drag dominated regime.

Ignoring the inertia term, the load per unit length which would be imposed on a representative 1m diameter circular cylinder by the peak first mode tide are shown in figure 7.1. The support reactions, assuming simple supports at the surface and bottom, are around 500N, a small figure in this context.

A point of concern to the designer would be the inflection point at the interface, where the rise and fall of the point of load reversal could set up a dynamic response in the

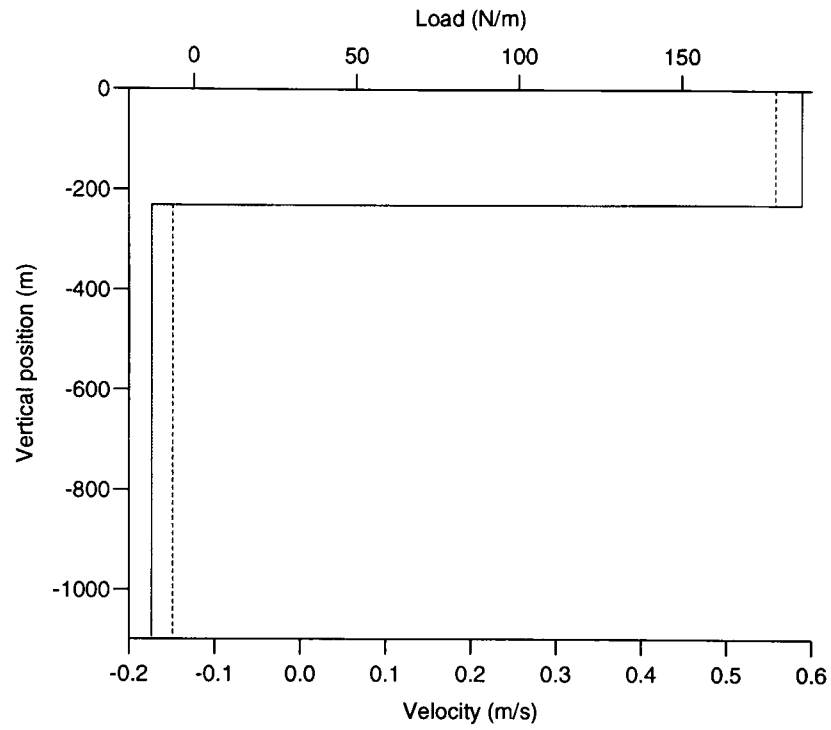


Figure 7.2: *Load per unit length on a 1m diameter circular cylinder (solid line) which would be imposed by the solitary waves observed by Osborne and Burch (two layer model). The maximum horizontal current is shown by the broken line.*

cylinder. This is outside the scope of this study, but it is noted that the modal structure of the tide would be important since several velocity reversals exist in the real tide.

Vertical motions in the internal tide drop off linearly away from the interface to the surface. The peak vertical velocity, near the interface, would be merely 3.5mm/s.

The above optimism depends on the linear nature of the internal tide. In the Færoe-Shetland Channel, the wave is likely to become non-linear as it is refracted up the side of the channel. Field data giving wave heights on the shelf are unfortunately not available. However, some data for non-linear long internal waves are given by Osborne and Burch (1980), though not enough to solve the continuous stratification model. Some comparisons can be made using the two-layer KdV model which they present.

For a 1m circular cylinder $KC = 370$, so once again the drag term dominates. The timescale of the solitary waves observed was about 10 minutes. The depth regime was shown by Osborne and Burch to be Korteweg-de Vries rather than Benjamin-Ono, and so horizontal currents are present throughout the depth. Drag calculations are shown in figure 7.2.

For a simply supported cylinder, the support forces are 2.2kN at the sea bed and 34kN at the surface. These loads are significant, although the effect on any riser or tether depends on the configuration. A flexible riser would take up some of this load in tension. On the other hand, a flexible riser would be bent by the passage of the wave and would suffer additional loads from the vertical velocity component. Further, the estimates of current speeds from the KdV model ignores the findings of the experiments that in large amplitude long internal waves, the velocities can be seriously underpredicted by both linear and KdV theory (discussed in section 7.3.2).

Although the wave parameters are not very different from those in the internal tide discussed above, the concentration of the wave energy into a short intense trough clearly raises the importance of the wave to the engineer. It seems sensible to assume that, if cnoidal or solitary waves are produced from the internal tide in the Færoe-Shetland Channel, these waves could impose significant loads on the portions of risers and tethers near the sea bed.

## 7.3 Significance of the findings to offshore engineering

### 7.3.1 Vulnerability of offshore structures to internal waves

Some general points about internal waves in the context of offshore engineering were made in section 2.4. It was noted that internal waves of various forms are likely to be present in many sea areas, especially in deep water. While in most cases surface wave, current and wind loading will govern platform design, internal waves may be very significant in the design of risers and mooring lines.

At present the most common choice for a deep water installation is a floating production system (FPS), the main component of which would be a drillship or a semi-submersible. These are usually the most flexible and cheapest options. Less commonly, tension-leg platforms (TLPs) and compliant towers may be used.

A typical mooring/riser arrangement is shown on figure 7.3. This is roughly that used at the Foinaven field, operated by BP in about 500m of water west of Shetland[1]. This figure shows the catenary arrangement of the mooring lines and the curved shape of the risers. Risers may flexible, i.e. in some form of catenary configuration (Nergaard, 1993), or rigid (i.e. tensioned) such as on the Snorre field TLP (Lim and Nielsen, 1993).

[1] Dr Colin Grant, BP Exploration, personal communication

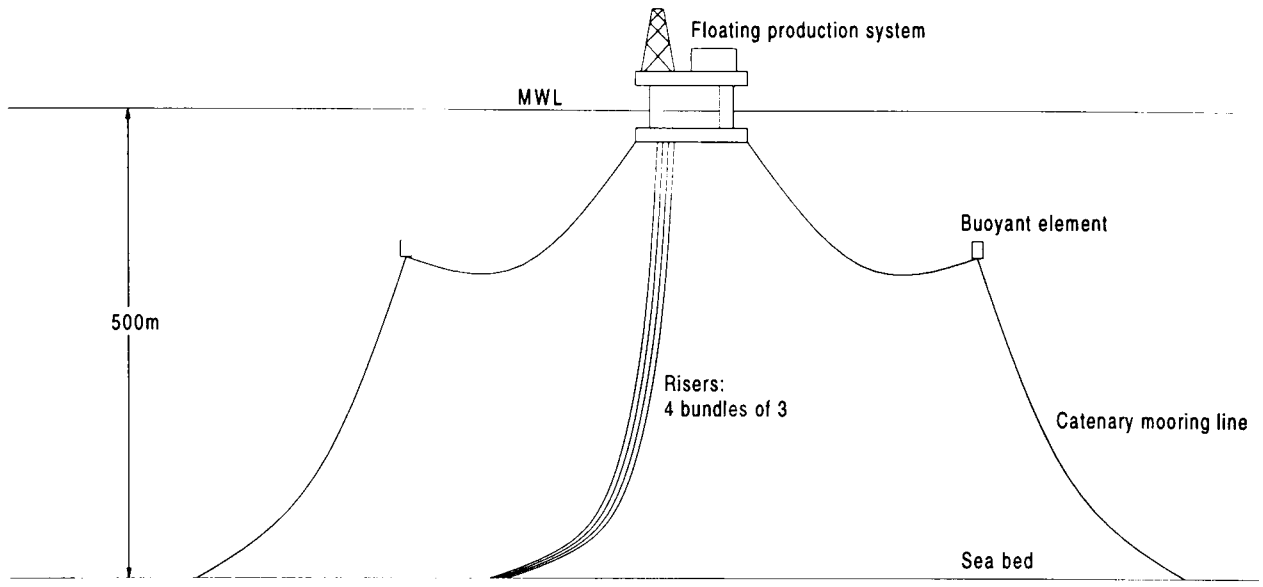


Figure 7.3: *Sketch of the mooring and riser configuration of the Foinaven platform*

TLPs have by definition a vertical arrangement of moorings (the so-called tension legs). The catenary mooring which would be used on an FPS may be multi-point (moorings are attached to several points around the vessel) or turret (moorings are attached to a central rotating turret). The former scheme is in use in the Foinaven semi-submersible while the latter is used on the drillship Discoverer 534 used by Osborne et al. (1978).

Motions distant from the surface would obviously affect only risers and mooring lines. In both cases issues of safety and ability to operate are raised. For example, riser installation is usually done by assembling and dropping the riser piece by piece from the platform. Risers are at their most vulnerable while being installed. Internal solitary waves usually concentrate their energy into packets which arrive roughly twice per day. The dangers which would arise if a packet were to arrive during such an operation would be the possible loss or damage to the riser, and the safety implications of high loads being suddenly imposed on a long riser string while work was in progress on it. For mooring lines, the extra tensions which would be imposed would have to be accounted for at the design stage.

Horizontal motions near the surface apply loads directly to the platform itself. If a platform is unable to keep station, the economic and safety implications can be severe. The necessary safety measure would ultimately be to disconnect and probably lose the risers, at great cost.

The vertical motions induced by internal waves would cause three additional problems: a catenary mooring line or riser is exposed by its shape to vertical as well as horizontal

drag forces, which would be increased; buoyant elements which are sometimes used to reduce the tension on risers would find the local buoyancy changing, resulting in fluctuations in the riser tension; and divers could be subject to dangerous upwelling and downwelling.

This last point was first noted by Evans and Ford (1996) who note that a neutrally-buoyant diver might be drawn down some distance by an internal solitary wave, and be subject to greatly increased pressure. A diver working in a shallow thermocline would regulate his buoyancy so as to make it neutral at the required depth. If the thermocline were to move with the passage of a solitary wave of height $\sim$ 80m, the diver would undergo extreme changes in pressure over a timescale of a few minutes, which could prove extremely dangerous. To work safely in such conditions a diver would require to be anchored to some fixed point, which might not be available below a catenary moored platform with flexible risers.

### 7.3.2 Implications of the measurements

Morison's equation (7.1) shows that, in the drag-dominated loading regime which is relevant here, load per unit length is a square function of the velocity. As discussed in section 7.1, the programme of experiments showed that while linear and second-order Stokes theories predict the kinematics of short internal waves reasonably well, the magnitudes of the velocity extremes is underpredicted by as much as 40%. In the case of long internal waves, horizontal velocities are underestimated by a factor of roughly 2, while vertical velocities can be many times greater than linear theory predicts. The biggest problem with the linear theory is that the sinusoidal shape is a very poor match to the observed shape. However, even weakly non-linear KdV theory fails to show the observed pattern of vertical velocities.

Engineers making calculations similar to those described in section 7.2.2 will need to consider the implications of these results. The square relationship between velocity and load means that, if the factors of 2 and 4 quoted above were to be used in design, the cost might prove prohibitive. The only safe solution is to pursue greater understanding of these non-linear waves.

It has been shown above that deep water floating production systems are vulnerable to vertical motions as well as to horizontal ones. In those few cases where engineers have assessed the risk posed by internal waves (Bole et al., 1994; Osborne and Burch, 1980), weakly non-linear KdV theory has been used to match the observed waves. In

the case of Bole et al., vertical velocities which were presented for one particular wave did show some exceedance of measurements over predictions. The exceedance (about 30%) was not as great as that found in this study, but the wave was also less steep. Osborne and Burch were not able to measure vertical velocities, but their waves were slightly steeper.

The amplitude of Bole's wave was about $a/H_1 \sim 0.4$, while Osborne and Burch had $a/H_1 > 0.5$ in some cases. Bole et al. used a Richardson number shear stability criterion to predict the maximum wave amplitude. The Richardson number was defined in section 2.3.5 as

$$Ri = \frac{N^2}{(\partial u/\partial z)^2} \tag{7.3}$$

where $Ri > 1/4$ is a *sufficient* condition for stability of the shear layer. Waves which break this condition could have currents up to twice those measured, which would require a wave of much greater amplitude. The extrapolated return time for such a wave fell into the 1–10 year range.

Evans and Ford (1996), considering a two-layer fluid case, discover a limiting amplitude where $a/H_1 = 1$ almost exactly. They show that the limiting wave profile in such conditions is one of infinite length. Shear stability cannot be evaluated in a two-layer flow because the Richardson number is undefined at the interface (but as the interface *tends* to a discontinuity the Richardson number tends to zero).

In the experiments with unequal layer depths, waves were generated with $a/H_1 > 1$, though they were not solitary and may not have fully evolved. The field studies mentioned did not discover waves of that amplitude, but Evans and Ford and Bole et al. showed by different means that it is possible for large amplitude waves to exist given sufficient forcing.

While the experimental results for long waves apply to larger waves than those so far discovered in the field, it is perfectly possible that such large waves do exist, and further investigation of the effects of large amplitude long waves would be of great interest.

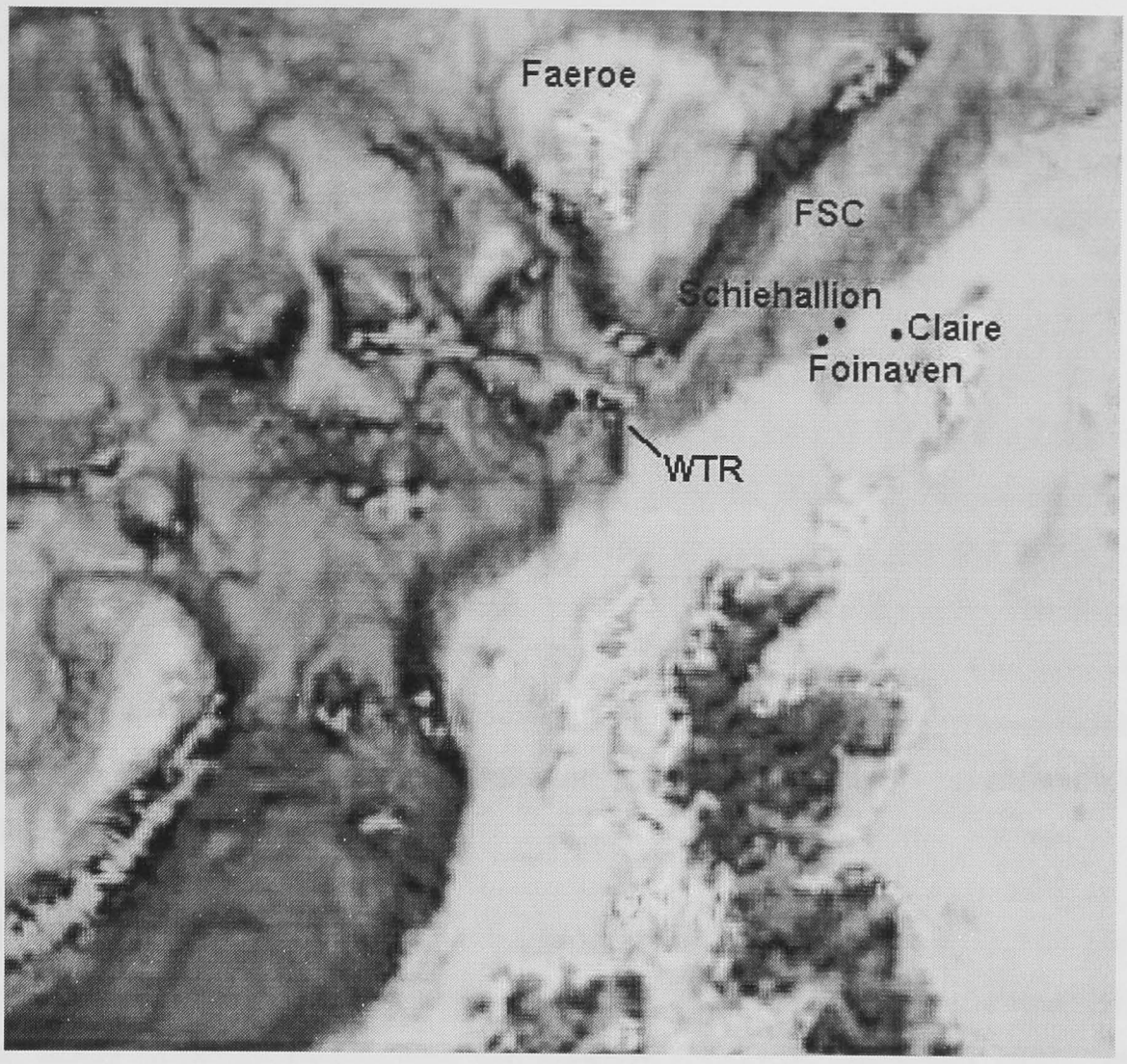


Figure 7.4: *Bathymetry of the North-West Approaches region. Foinaven, Schiehallion and Claire are major oil fields (approximate locations) on the Færoe-Shetland Channel (FSC), which is bounded to the south by the Wyville-Thomson Ridge (WTR). (Adapted from a map supplied by Dr Colin Grant, BP Exploration)*

### 7.3.3 The North-West Approaches

The United Kingdom North-West Approaches is a region of continental shelf and deep water channels roughly between Shetland, the Færoe Islands and the north of mainland Scotland. Figure 7.4 is a bathymetry map of the region. Features of particular interest are the Færoe-Shetland Channel, the Wyville-Thomson Ridge, and three oil fields (Foinaven, Schiehallion and Claire). The first two of these are in approximately 500m of water on the edge of the Færoe-Shetland Channel.

The Færoe-Shetland Channel is a particularly active area, and rather unusual oceanographically. The 500m contour is close to the top of the channel, which is closed off to the south by the Wyville-Thomson Ridge. Below that depth, a body of relatively cold

water known as the Norwegian Sea Deep Water is trapped. The warmer North Atlantic Water of the top 500m is subject to strong currents, notably the North Atlantic Drift, which due to the Earth's rotation is forced against the south-east side of the channel. For this reason it is known in that region as the slope current. The channel is 1000m deep at the south end and more than 1500m deep at the north end.

Spontaneous variations in currents have been observed at various locations in the region, including the "Nolter Maelstrom" (Sherwin, 1991), an intense deep disturbance with a return time equal to the tidal period, which affected mini-sub operations near the ridge. Three important factors in the energetics of the region are the slope current, which is known to be unstable, the tides, and the thermocline between the Norwegian Sea Deep Water and the North Atlantic Water. Sherwin notes that the tide over the Wyville-Thomson Ridge strongly forces the internal mode. The internal tidal range near the ridge appears to be about 75m, and significant energy is present in the first six modes.

Internal tides are able to force other internal wave motions (section 2.3.2) including rays and possibly solitary waves. For the complex bathymetry of the Færoe-Shetland Channel, many different phenomena are possible (Sherwin, 1989 and 1991) and it is difficult to conclude, on the available data, which type of wave is being generated. For example, it is possible that free waves generated at the ridge propagate along the channel, and as they are refracted up the slopes, turn into non-linear solitary waves (of elevation rather than depression) which eventually break on the shelf. As discussed in section 7.2, this would be particularly significant from the point of view of the Foinaven and Schiehallion fields. Additionally, the slope current itself may be a cause of the spontaneous current variations, or might even force internal waves itself.

In addition to the deep thermocline at about 500m depth, there exists a shallow seasonal thermocline at about 25m depth, on which long waves with heights of up to 10m have been inferred from satellite images[2]. The waves propagate north-east up the Færoe-Shetland Channel in packets, and appear to suffer partial refraction onto the shelf edge. They show correlation with tidal forcing. Despite its depth, it may still be the case that the Wyville-Thomson Ridge is the generating site, for as Kleuser (1996) has shown, internal waves may be generated on an interface which is well above the disturbing topography. Unfortunately Kleuser was not able to parameterise the range of the effect.

[2]Personal communication from Dr Colin Grant, BP Exploration

The inferred currents associated with the waves in the seasonal thermocline are not great ($\sim 0.1$m/s), and the inferred wave heights are such that weakly non-linear theory might account for their kinematics.

# Chapter 8

# Conclusions

This study examined oceanic internal waves from several viewpoints:

- The broad literature on the subject, including field observations;
- The design of a laboratory experiment for measuring wave kinematics;
- Assessment of the performance of linear and non-linear wave theories in predicting these kinematics;
- The significance of internal waves and the implications of the findings of the experiments for offshore engineering.

The literature review clearly showed that internal waves, though they have much in common with surface waves, are complex phenomena which exist in many forms in most deep ocean areas and many shallow seas. The conclusions of the other sections are summarised below.

1. **Experimental equipment and results**

   The experimental phase of the project was the major part, and was subdivided into the following tasks:

   (a) **Tank and wavemaker design**

   The wave tank, wavemaker and controller were the most successful parts of the experiment design. The control system and software proved robust and flexible, while the wavemaker itself exceeded specifications.

(b) **Design of new instrumentation**

The wave gauges and the data collection system were adequate for all of the experiments except for those with a stratified upper layer. The density probe was deficient and remedial post-processing was required. A commercial density probe would have been useful, but it was nevertheless possible to obtain the necessary information from the probe.

(c) **Adaptation of Particle Image Velocimetry to internal waves**

A PIV system which compared favourably to the state of the art at the time was adapted to the study of internal waves. It turned out that the velocities of interest were on the lower end of the dynamic range of the system. The PIV implementation was nevertheless capable of measuring the kinematics of large waves reasonably accurately. Techniques such as ray tracing were used to show that the errors were small in most of the flow.

(d) **Programme of experiments**

The problem of noise limited the range of waves which could be studied. Nevertheless, sufficient good results were obtained to allow comparison with the numerical models over a range of wave parameters.

The behaviour of the waves in the tank was largely as hoped. Waves propagated freely with little viscous attenuation, and in the case of the short waves, little serious harmonic distortion. As mentioned above, the dynamic range of the velocity measuring equipment was such that relatively large waves had to be studied, resulting in some modulation of the wave group as it propagated.

2. **Comparison with theory**

(a) **Short waves**

First and second order Stokes theory was applied to short internal waves. It was found that the waves which were measured possessed horizontal velocity components which exceeded predictions by up to 40%. Vertical velocities around 25% greater than predicted were also found. This was most apparent in the velocity extremes. In the bulk of the flow, the agreement was much better, with exceedances of around 12% and 16% for horizontal and vertical velocity components respectively.

Third order Stokes theory would have predicted greater velocity extremes, but in the absence of a viscous correction its use did not seem to be justifiable.

(b) **Long waves**

Linear (first order Stokes) theory and weakly non-linear Korteweg-de Vries theory were used to predict the velocities in long waves. For all of the cases it is clear that linear theory falls down because of its prediction of a sinusoidal wave shape. This results in poor correlation between measured and predicted velocities, especially for the vertical component. KdV theory appears to predict the wave shape better although it still underestimates the magnitudes of the vertical velocities.

Using linear theory, horizontal velocity extremes were underpredicted by a factor of about 2. Vertical velocity extremes were underpredicted by about 4 times. The waves in unequal layer depths represent cases where a fully non-linear solitary or cnoidal wave theory would be appropriate.

Finally, as shown by the experiments with one layer linearly stratified, the velocity maxima are always near the positions of maximum density gradient.

## 3. Engineering implications of internal waves

Internal solitary waves at present appear to pose the greatest threat to offshore engineering. It has been seen that the concentration of the energy of an internal tide into a small number of solitary waves produces transitory currents capable of imposing high loads on a riser or mooring line, or of creating dangerous conditions for diving. The findings have shown that traditional KdV theory may not be sufficient to allow accurate prediction of the kinematics of the largest of these waves, especially the vertical velocity components.

The great range of internal wave phenomena mean that full understanding of the internal wave field in a particular site can only be gained from comprehensive oceanographic studies. Density profiles combined with a knowledge of the bottom topography may indicate whether or not a site is vulnerable to internal tides, rays or solitary waves. Deployment of current profilers and thermistor chains in at least two sites would allow the tracking of the waves themselves. For solitary waves near the surface, many field studies have shown the usefulness of satellite photographs or airborne/satellite synthetic aperture radar images in tracking waves.

For the North West Approaches, it is not yet clear whether the slope current will prove to be the dominant loading factor or whether internal waves will have a significant contribution. Certainly the "Nolter Maelstrom" suggests that internal waves are significant near the Wyville-Thomson Ridge. On the south-east side of the Færoe-Shetland Channel, deep internal solitary waves may exist, and may in fact be approaching a breaking regime in the vicinity of the Foinaven and Schiehallion oil fields. This has yet to be confirmed.

## 4. Suggestions for future work

### (a) Laboratory experiments

Technological advances have made it possible to measure a much wider range of velocities with particle image velocimetry than was possible at the time of the experiments. The application of a cross-correlation camera to internal waves would allow the measurement of much smaller wave amplitudes, making it possible to observe the domain of validity of the various theories.

This study focused on periodic waves, but long waves in unequal layer depths had obvious solitary wave properties. Another study is currently being undertaken to generate and measure solitary waves directly.

### (b) Theory

Small order Stokes theory has been shown to be adequate only for relatively short waves. Expansion to high order is extremely difficult given the complexity of the equations. Long wave theories of greater accuracy than KdV are available, but they make use of a two-layer approximation. An interesting proposition would be the development of a Dean's streamfunction theory, by which coefficients could be evaluated numerically to any prescribed order. Such a theory would be applicable to a wide range of wavelengths and amplitudes. However, to be valid in the laboratory, such a theory would need to include the effects of viscosity.

There is probably scope for the development of Benjamin's (1966) KdV analysis to higher order. Higher approximations to KdV theory have been calculated for two-layer theory and used with some success.

The interaction of internal waves with steady mean flow has been studied, but in the case of the North-West Approaches, the internal tide may be interacting with the very unsteady slope current. The effect of this on the waves, and even of the waves on the current, would be of some interest.

### (c) Field studies

The study of internal waves will always depend on the availability of detailed field data. Unfortunately this is rather expensive. However, deployment of ADCPs as part of metocean site studies is now fairly common.

Current and density profiles near the south-east edge of the Færoe-Shetland Channel would be of great interest, since that is one area where large amplitude internal solitary waves may be found. The time and space detail would have to be considerable if internal wave effects were to be distinguished from instabilities in the slope current.

# Appendix A

# Control and data collection electronics

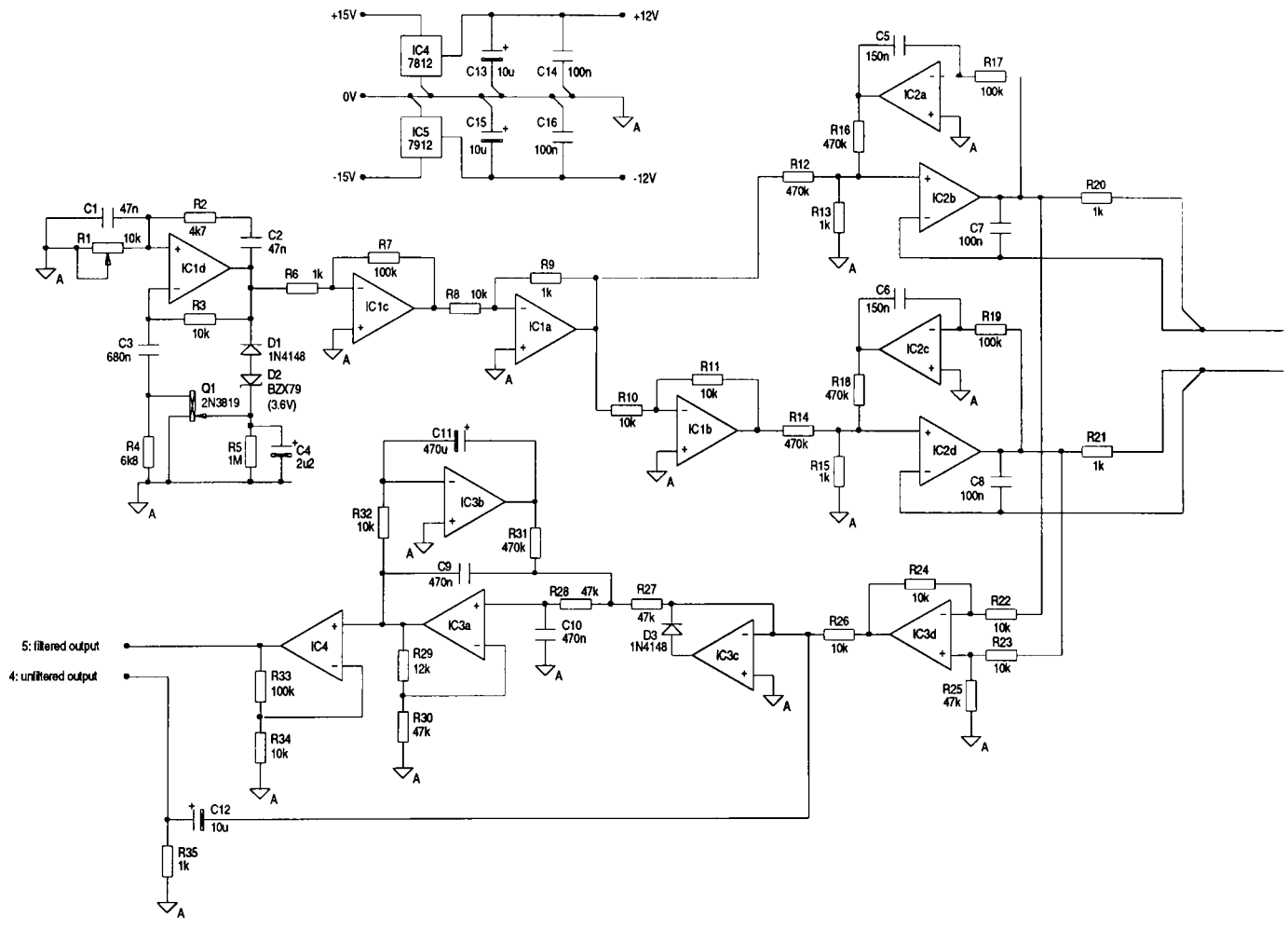


Figure A.1: *Schematic of the wire wave height gauges*

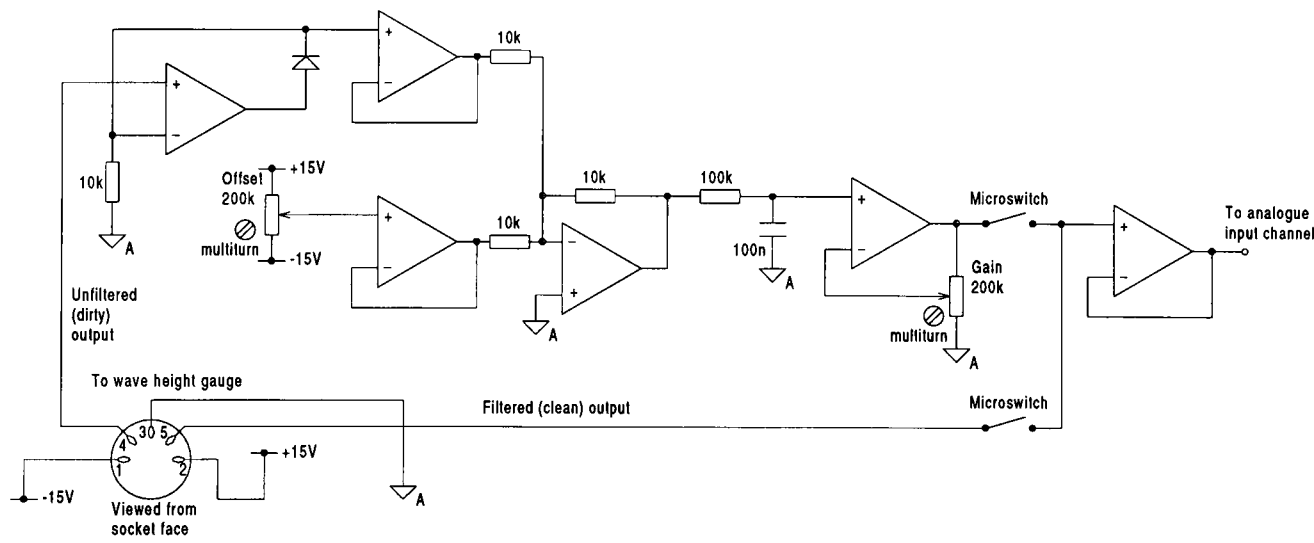


Figure A.2: *Schematic of one channel of the wave height gauge interface board*

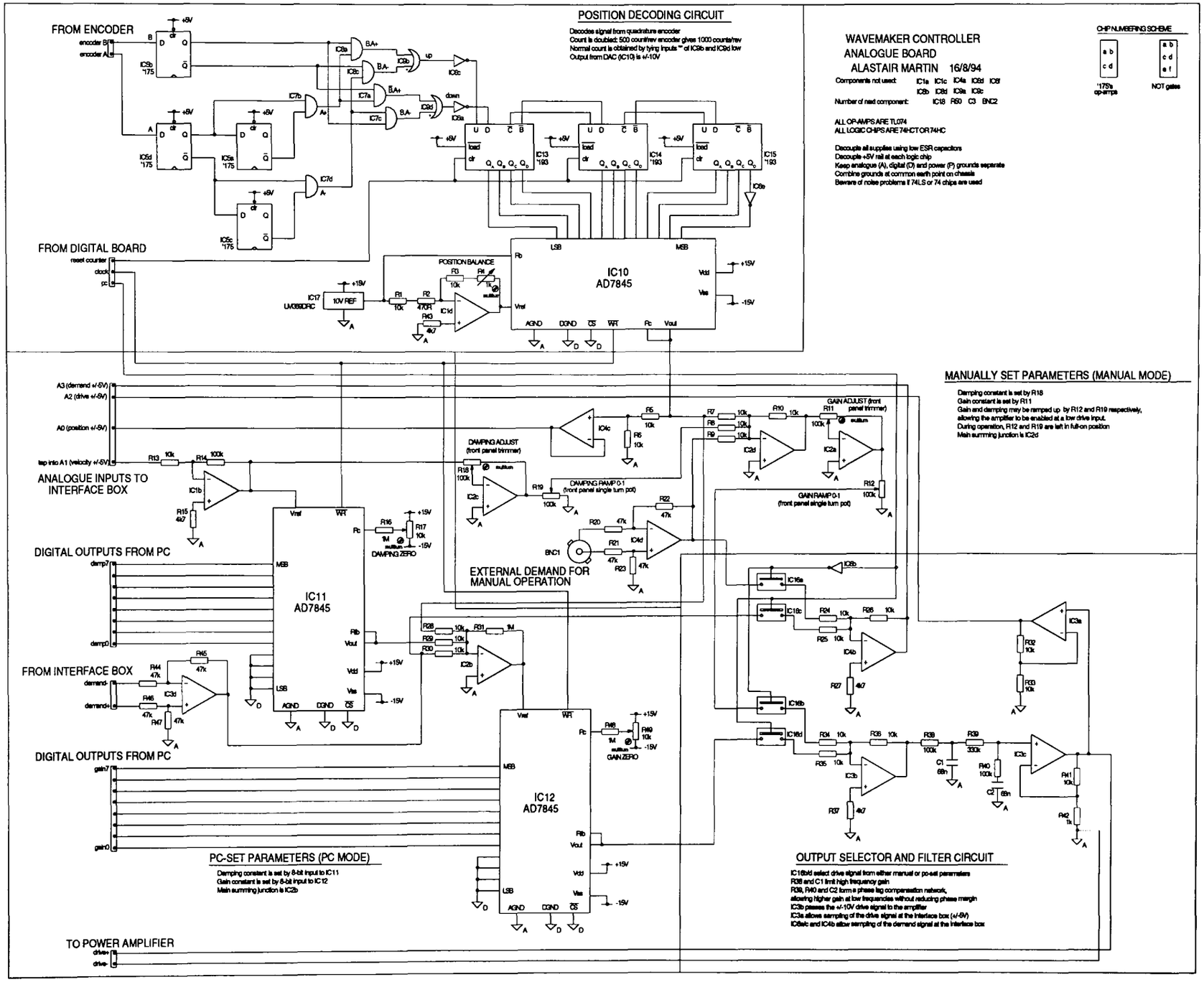


Figure A.3: *Schematic of the analogue control board*

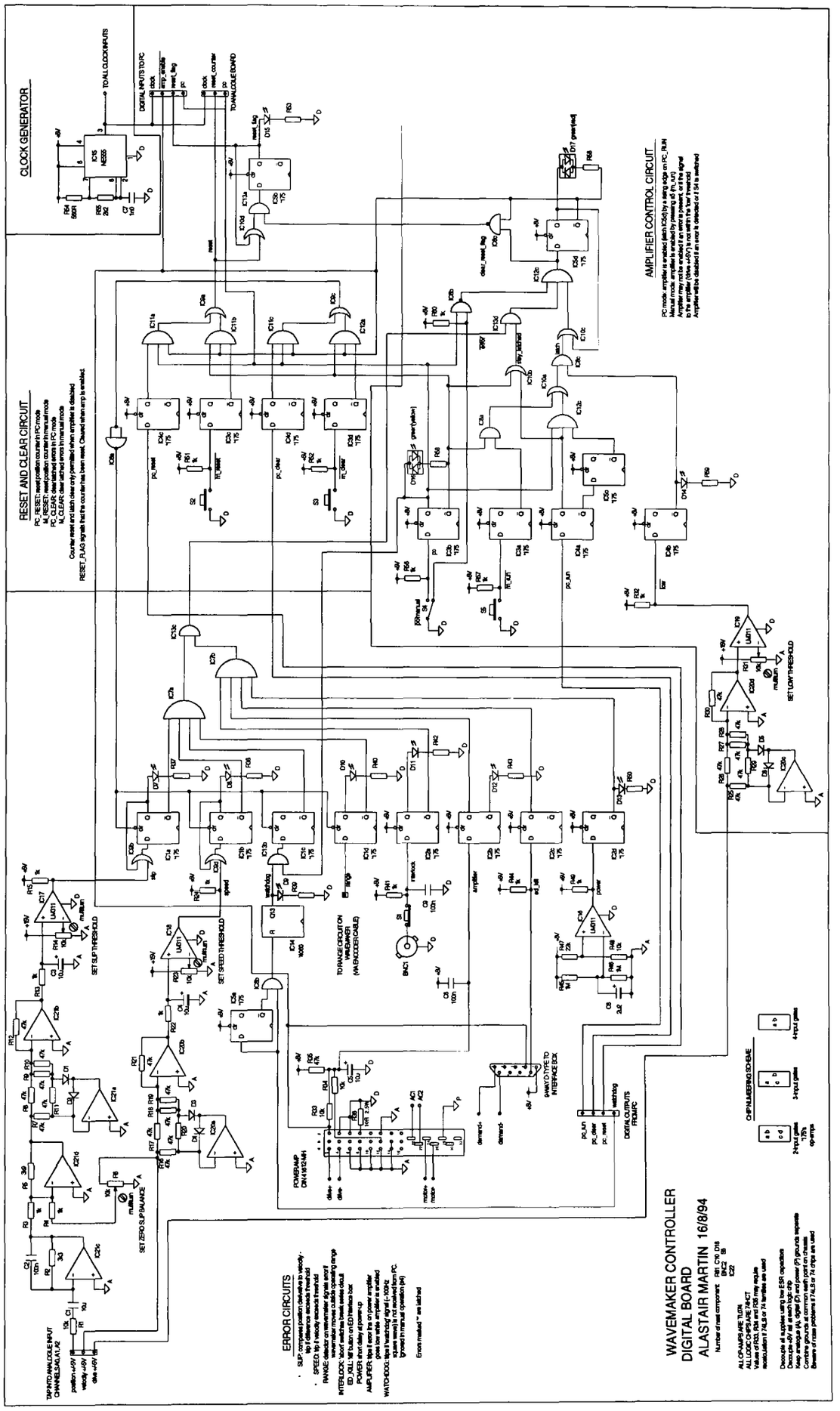


Figure A.4: *Schematic of the digital protection board*

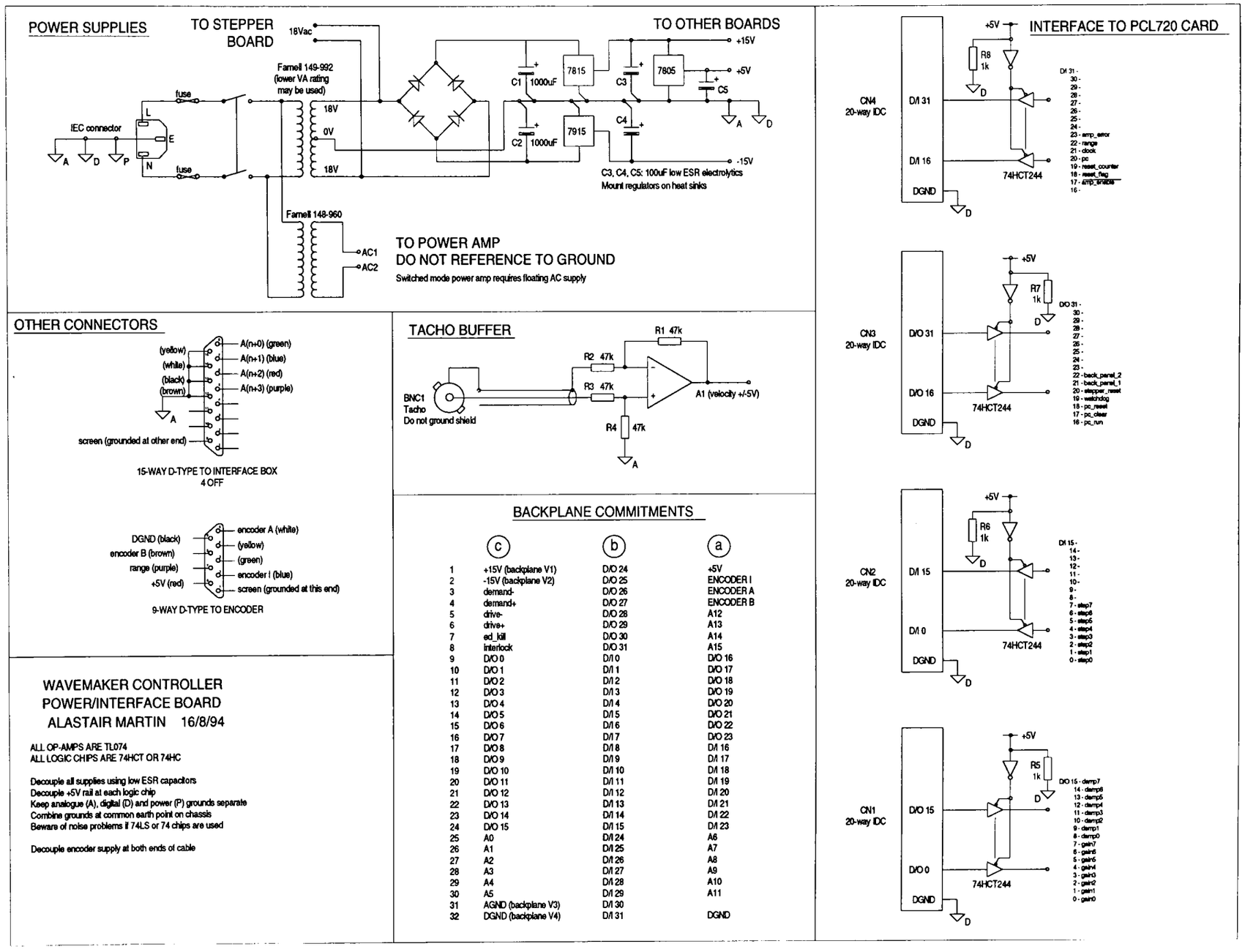


Figure A.5: *Schematic of the general power/interface board*

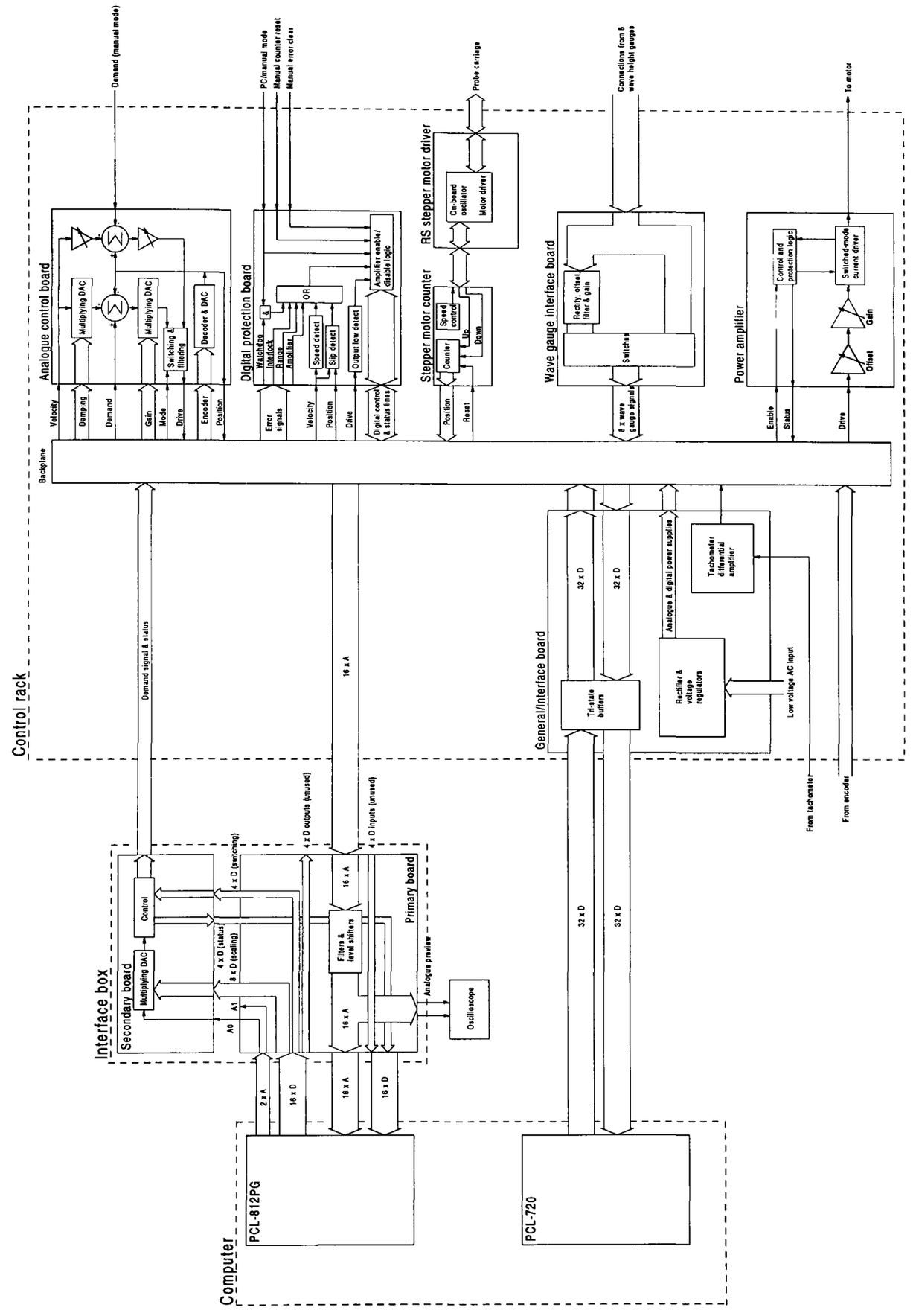


Figure A.6: *Block diagram of the complete system*

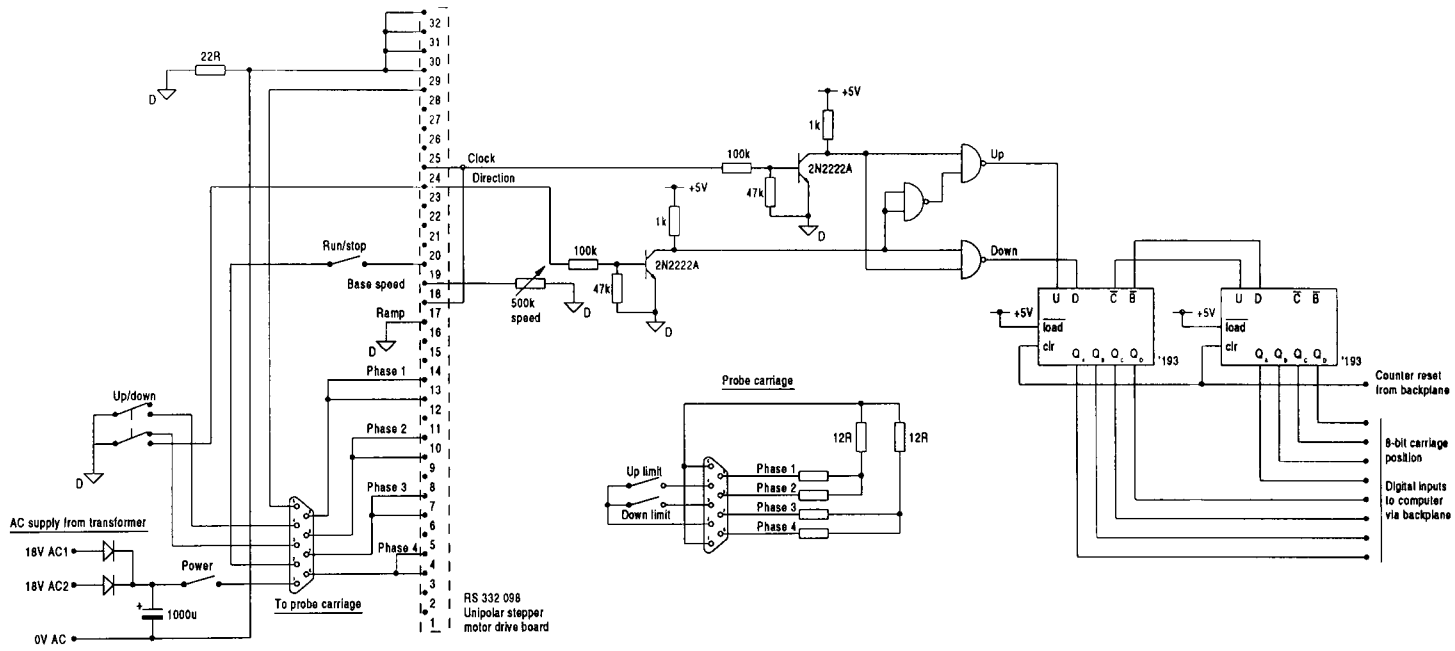


Figure A.7: *Schematic of the stepper motor driver and position counter*

# Appendix B

# Control and data collection software

This section contains truncated versions of the C++ header files related to the message-passing software library, extensions to the library, and header and source files for the experiment control program. Familiarity with C++ syntax is essential to understanding of the following sections.

The truncated header files are included as they provide synopses of the functionality of the components of the software. The full header files contain a large number of function definitions as well as declarations, which is not the usual practise. The reason for placing function definitions in the header file was to cause the compiler to generate inline code rather than function calls wherever possible, for the most time-critical parts of the library. Inline function code is generally faster than function calls, although it makes the program bulkier. The inline function definitions have been omitted in the preparation of this appendix.

## B.1 Header files for the software kernel

All of the header files (an associated source files) in this section were written by Mr Peter Woodhead. Subsequent modifications are marked.

---

The following file contains declarations and definitions for the base functions of the message passing system.

```
/* msg.h message passing header file */

#ifndef _MSG
#define _MSG

extern void msg_nop(void *pad, void *msg);

typedef void *msg_pad;

typedef void (*msg_proc)(msg_pad, void*);

typedef double m_val;

const m_false = 0.0;
const m_true = 1.0;

inline int is_m_false(double x){ return (x == m_false); };
inline int is_m_true(double x){ return (x != m_false); };

class msg_input{

  msg_pad pad;
  msg_proc proc;

public:

  inline msg_input();
  inline msg_input(msg_pad, msg_proc);
  inline int null();
  inline void call(void *);
  friend msg_input msg_in_fn(msg_pad, msg_proc);

};

class msg_path{

  msg_input input;
  msg_path *link;

public:

  inline msg_path();
  ~msg_path();
  void connect(msg_input);
  inline void call_s(void *);
  inline msg_path *next();
  inline void call(void *);
  inline int null();

};

class msg_output{

  msg_path path;
  msg_output *link;
  void *message;

public:

  msg_output();
  ~msg_output();
  inline void connect(msg_input);
  inline void insert(msg_output *);
  inline msg_output *next();
  inline void out(void*);
  void output(void*);
  inline void call();
  inline int null();

};

class msg_queue{

  msg_output *head;
  msg_output *end;

public:

  inline msg_queue();
  inline void insert(msg_output *);
  inline void remove();
```

```
  inline msg_output *next();
  inline void reset();

};

class msg_main{

  msg_main *nxt;
  msg_output rst;
  msg_output dst;
  int active;
  static msg_main *head;
  static msg_main *end;
  static int count;
  void insert();

public:

  friend void msg_main_stop(msg_main *, void *);
  msg_main();
  ~msg_main();
  void process();
  inline void reset(msg_input);
  inline void start(msg_input);
  inline msg_input stop();

};

extern msg_queue message_queue;



#define msg_in(pad, proc) msg_in_fn((msg_pad)(pad), (msg_proc)(proc))



extern msg_main message_main;

extern void message_process();

#endif
```

---

This file contains declarations and definitions for message-passing blocks to handle mathematical and Boolean logical functions.

```
/* msgmath.h message passing math header file
 *
 * Peter Woodhead 30/9/94
 * Modifications:
 * "class/public" substituted for "struct" in msg_m_....._pad (6 locations)
 * (Alastair Martin 14/9/95)
 */

#ifndef _MSGMATH
#define _MSGMATH

#include <msg.h>

class msg_m_u_op{

  msg_output dest;
  double res;

public:

  inline void connect(msg_input);
  inline void set(double);
  inline void out();
  inline void out(double);
```

```
  void output();
  void output(double);
  inline double result();

};



class msg_m_const{

  msg_m_u_op op;

public:

  friend void msg_m_const_trigger(msg_m_const *, void *);
  inline msg_m_const();
  inline msg_m_const(double);
  inline void set(double);
  inline void output(msg_input);
  inline msg_input trigger();
  inline double result();

};



class msg_m_neg{

  msg_m_u_op op;

public:

  friend void msg_m_neg_input(msg_m_neg *, double *);
  inline void output(msg_input);
  inline msg_input input();
  inline double result();

};



class msg_m_not{

  msg_m_u_op op;

  public:

  friend void msg_m_not_input(msg_m_not *, double *);
  inline void output(msg_input);
  inline msg_input input();
  inline double result();

};



class msg_m_buf{

  msg_m_u_op op;

  public:

  friend void msg_m_buf_input(msg_m_buf *, double *);
  inline void output(msg_input);
  inline msg_input input();
  inline double result();

};



class msg_m_b_op{

  msg_output dest;
  double res;
  double *val_a;
  double *val_b;
  inline void clear();

public:
```

```
  inline msg_m_b_op();
  inline void connect(msg_input);
  inline void set(double);
  inline void out();
  inline void out(double);
  void output();
  void output(double);
  inline double result();
  inline void set_a(double *);
  inline void set_b(double *);
  inline double value_a();
  inline double value_b();
  inline int ready();

};



class msg_m_add{

  msg_m_b_op op;
  inline void operate();

public:

  friend void msg_m_add_input_a(msg_m_add *, double *);
  friend void msg_m_add_input_b(msg_m_add *, double *);
  inline void output(msg_input);
  inline msg_input input_a();
  inline msg_input input_b();
  inline double result();

};



class msg_m_sub{

  msg_m_b_op op;
  inline void operate();

public:

  friend void msg_m_sub_input_a(msg_m_sub *, double *);
  friend void msg_m_sub_input_b(msg_m_sub *, double *);
  inline void output(msg_input);
  inline msg_input input_a();
  inline msg_input input_b();
  inline double result();

};



class msg_m_mul{

  msg_m_b_op op;
  inline void operate();

public:

  friend void msg_m_mul_input_a(msg_m_mul *, double *);
  friend void msg_m_mul_input_b(msg_m_mul *, double *);
  inline void output(msg_input);
  inline msg_input input_a();
  inline msg_input input_b();
  inline double result();

};



class msg_m_div{

  msg_m_b_op op;
  inline void operate();

public:

  friend void msg_m_div_input_a(msg_m_div *, double *);
  friend void msg_m_div_input_b(msg_m_div *, double *);
```

```
  inline void output(msg_input);
  inline msg_input input_a();
  inline msg_input input_b();
  inline double result();

};



class msg_m_and{

  msg_m_b_op op;
  inline void operate();

public:

  friend void msg_m_and_input_a(msg_m_and *, double *);
  friend void msg_m_and_input_b(msg_m_and *, double *);
  inline void output(msg_input);
  inline msg_input input_a();
  inline msg_input input_b();
  inline double result();

};



class msg_m_or{

  msg_m_b_op op;
  inline void operate();

public:

  friend void msg_m_or_input_a(msg_m_or *, double *);
  friend void msg_m_or_input_b(msg_m_or *, double *);
  inline void output(msg_input);
  inline msg_input input_a();
  inline msg_input input_b();
  inline double result();

};
```

```
class msg_m_min{

  msg_m_b_op op;
  inline void operate();

public:

  friend void msg_m_min_input_a(msg_m_min *, double *);
  friend void msg_m_min_input_b(msg_m_min *, double *);
  inline void output(msg_input);
  inline msg_input input_a();
  inline msg_input input_b();
  inline double result();

};



class msg_m_max{

  msg_m_b_op op;
  inline void operate();

public:

  friend void msg_m_max_input_a(msg_m_max *, double *);
  friend void msg_m_max_input_b(msg_m_max *, double *);
  inline void output(msg_input);
  inline msg_input input_a();
  inline msg_input input_b();
  inline double result();

};



class msg_m_adds;
```

```
class msg_m_adds_pad{
public:
  msg_m_adds *op;
  double *val;

};

class msg_m_adds{

  int ins;
  int count;
  msg_output dest;
  double res;
  msg_m_adds_pad *pad;

public:

  int inputs(){ return ins; };
  void inputs(int);
  msg_m_adds(){ inputs(0); };
  msg_m_adds(int n){ inputs(n); };
  ~msg_m_adds();
  void output(msg_input in){ dest.connect(in); };
  friend void msg_m_adds_input(msg_m_adds_pad *, double *);
  msg_input input(int k){ return msg_in(&pad[k], msg_m_adds_input); };
  double result(){ return res; };

};

class msg_m_muls;

class msg_m_muls_pad{
public:
  msg_m_muls *op;
  double *val;

};

class msg_m_muls{

  int ins;
  int count;
  msg_output dest;
  double res;
  msg_m_muls_pad *pad;

public:

  int inputs(){ return ins; };
  void inputs(int);
  msg_m_muls(){ inputs(0); };
  msg_m_muls(int n){ inputs(n); };
  ~msg_m_muls();
  void output(msg_input in){ dest.connect(in); };
  friend void msg_m_muls_input(msg_m_muls_pad *, double *);
  msg_input input(int k){ return msg_in(&pad[k], msg_m_muls_input); };
  double result(){ return res; };

};

class msg_m_ands;

class msg_m_ands_pad{
public:
  msg_m_ands *op;
  double *val;

};

class msg_m_ands{

  int ins;
  int count;
  msg_output dest;
  double res;
  msg_m_ands_pad *pad;

public:

  int inputs(){ return ins; };
```

```
  void inputs(int);
  msg_m_ands(){ inputs(0); };
  msg_m_ands(int n){ inputs(n); };
  ~msg_m_ands();
  void output(msg_input in){ dest.connect(in); };
  friend void msg_m_ands_input(msg_m_ands_pad *, double *);
  msg_input input(int k){ return msg_in(&pad[k], msg_m_ands_input); };
  double result(){ return res; };

};

class msg_m_ors;

class msg_m_ors_pad{
public:
  msg_m_ors *op;
  double *val;

};

class msg_m_ors{

  int ins;
  int count;
  msg_output dest;
  double res;
  msg_m_ors_pad *pad;

public:

  int inputs(){ return ins; };
  void inputs(int);
  msg_m_ors(){ inputs(0); };
  msg_m_ors(int n){ inputs(n); };
  ~msg_m_ors();
  void output(msg_input in){ dest.connect(in); };
  friend void msg_m_ors_input(msg_m_ors_pad *, double *);
  msg_input input(int k){ return msg_in(&pad[k], msg_m_ors_input); };
  double result(){ return res; };

};

class msg_m_mins;

class msg_m_mins_pad{
public:
  msg_m_mins *op;
  double *val;

};

class msg_m_mins{

  int ins;
  int count;
  msg_output dest;
  double res;
  msg_m_mins_pad *pad;

public:

  int inputs(){ return ins; };
  void inputs(int);
  msg_m_mins(){ inputs(0); };
  msg_m_mins(int n){ inputs(n); };
  ~msg_m_mins();
  void output(msg_input in){ dest.connect(in); };
  friend void msg_m_mins_input(msg_m_mins_pad *, double *);
  msg_input input(int k){ return msg_in(&pad[k], msg_m_mins_input); };
  double result(){ return res; };

};

class msg_m_maxs;

class msg_m_maxs_pad{
public:
  msg_m_maxs *op;
  double *val;

};
```

```
class msg_m_maxs{

  int ins;
  int count;
  msg_output dest;
  double res;
  msg_m_maxs_pad *pad;

public:

  int inputs(){ return ins; };
  void inputs(int);
  msg_m_maxs(){ inputs(0); };
  msg_m_maxs(int n){ inputs(n); };
  ~msg_m_maxs();
  void output(msg_input in){ dest.connect(in); };
  friend void msg_m_maxs_input(msg_m_maxs_pad *, double *);
  msg_input input(int k){ return msg_in(&pad[k], msg_m_maxs_input); };
  double result(){ return res; };

};

#endif
```

---

The following file contains declarations and definitions for other message-passing blocks, such as delay generators and synchronisers.

```
/* msgodds.h message passing odds and ends

  Peter Woodhead 30/9/94
  Modifications:
   msg_delay ticks=(n-1.5) substituted for ticks=(n-0.5
  (Alastair Martin 11/94)
   msg_delay::result() function added (Alastair Martin 11/94)
*/

#ifndef _MSGODDS
#define _MSGODDS

#include <msg.h>
#include <math.h>

class msg_sync{

  msg_output dest;
  void *val;
  int trig;
  void operate(){
    if(val != (void *)0 && trig != 0){
      dest.out(val);
      val = (void *)0;
      trig = 0;
    }
  };

public:

  msg_sync(){ val = (void *)0; trig = 0; };
  void output(msg_input in){ dest.connect(in); };
  friend void msg_sync_input(msg_sync *, void *);
  msg_input input(){ return msg_in(this, msg_sync_input); };
  friend void msg_sync_trigger(msg_sync *, void *);
  msg_input trigger(){ return msg_in(this, msg_sync_trigger); };
  void *result(){ return val; };

};

class msg_false{

  msg_output dest;
```

```
  double res;

public:

  msg_false(){ res = m_false; };
  void output(msg_input in){ dest.connect(in); };
  friend void msg_false_trigger(msg_false *, void *);
  msg_input trigger(){ return msg_in(this, msg_false_trigger); };
  double result(){ return res; };

};

class msg_true{

  msg_output dest;
  double res;

public:

  msg_true(){ res = m_true; };
  void output(msg_input in){ dest.connect(in); };
  friend void msg_true_trigger(msg_true *, void *);
  msg_input trigger(){ return msg_in(this, msg_true_trigger); };
  double result(){ return res; };

};

class msg_fork{

  msg_output f_dest;
  msg_output t_dest;
  double res;

public:

  void false_output(msg_input in){ f_dest.connect(in); };
  void true_output(msg_input in){ t_dest.connect(in); };
  friend void msg_fork_input(msg_fork *, double *val);
  msg_input input(){ return msg_in(this, msg_fork_input); };
  double result(){ return res; };

};

class msg_delay{

  msg_output dest;
  double ticks;
  double count;
  double res;

public:

  void set(double n){ ticks = (n-1.5); count = ticks; };

  msg_delay(double n){ set(n); };
  msg_delay(){ msg_delay(1.0); };

  void output(msg_input in){ dest.connect(in); };

  friend void msg_delay_input(msg_delay *, double *);
  msg_input input(){ return msg_in(this, msg_delay_input); };
  double result(){ return ticks-count; };

};

#endif
```

---

This file contains the declarations and definitions for a message-passing block which generates a sine wave of given amplitude, frequency and phase.

```
/* msgsig.h signal processing
```

```
  Peter Woodhead 30/9/94
  Modifications:
   class siggen renamed msg_siggen (Alastair Martin 11/94)
*/

#ifndef _MSGSIG
#define _MSGSIG

#include <msg.h>

class msg_siggen{

  msg_output dest;
  double gain;
  unsigned short i_phase;
  unsigned short s_phase;
  unsigned short c_phase;
  int got_s;
  int got_f;
  double val_s;
  double val_f;
  double res;
  void operate();
  void op(){ if((got_s!=0) && (got_f!=0)) operate(); };

public:

  msg_siggen();
  msg_siggen(double, unsigned short, unsigned short);
  msg_siggen(double, double, double, double);

  void set(double, unsigned short, unsigned short);
  void set(double, double, double, double);

  void output(msg_input in){ dest.connect(in); };

  friend void msg_siggen_start(msg_siggen *, double *);
  msg_input start(){ return msg_in(this, msg_siggen_start); };

  friend void msg_siggen_stop(msg_siggen *, double *);
  msg_input stop(){ return msg_in(this, msg_siggen_stop); };

};

#endif
```

---

This file contains the declarations and definitions for the block which was created to control the wave generator.

```
/* msgiwt.h message passing internal wave tank */

#ifndef _MSGIWT
#define _MSGIWT

#define IWT_0 0x220
#define IWT_1 0x2A0

class msg_int_wave{

  msg_output dest;
  int port0;
  int port1;
  int init;
  int sgain;
  int dgain;
  int ogain;
  double res;
  double rst;
  double sst;
  double wm0;
```

```
  double wm1;
  int gotr;
  int gots;
  int got0;
  int got1;
  int sramp;
  int dramp;
  int oramp;
  int sinc;
  int dinc;
  int oinc;
  int inst;
  int st;
  void operate();
  void op(){ if(gotr && gots && got0 && got1) operate(); };

public:

  msg_int_wave();

  void done(msg_input in){ dest.connect(in); };

  void set_gains(int s, int d, int o){
    sgain = s;
    dgain = d;
    ogain = o;
  };

  void set_s_ramp(int inc){ sinc = inc; };
  void set_d_ramp(int inc){ dinc = inc; };
  void set_o_ramp(int inc){ oinc = inc; };

  friend void msg_int_wave_start(msg_int_wave *, double *);
  msg_input start(){ return msg_in(this, msg_int_wave_start); };

  friend void msg_int_wave_stop(msg_int_wave *, double *);
  msg_input stop(){ return msg_in(this, msg_int_wave_stop); };

  friend void msg_int_wave_wm_sig_0(msg_int_wave *, double *);
  msg_input wm_sig_0(){ return msg_in(this, msg_int_wave_wm_sig_0); };

  friend void msg_int_wave_wm_sig_1(msg_int_wave *, double *);
  msg_input wm_sig_1(){ return msg_in(this, msg_int_wave_wm_sig_1); };
};

#endif
```

---

The basic message-passing blocks used for communication via the input/output cards in the computer are declared here.

```
/* msgpcl.h pcl pc lab card msg support

  Peter Woodhead 30/9/94
  Modifications:
msg_pcl_a_in::set(int, int) function added (Alastair Martin 11/94)
msg_pcl_a_in::msg_pcl_a_in() overloaded function added (Alastair Martin 11/94)
inline int msg_pcl_a_in::which() function addded (Alastair Martin 15/3/95)
double msg_pcl_a_in::result() function declared inline
  (Alastair Martin 15/3/95)
msg_pcl_clock::set(int,int,double,int) function added
  (Alastair Martin 15/3/95)
msg_pcl_clock::msg_pcl_clock() overloaded function added
  (Alastair Martin 15/3/95)

*/

#ifndef _MSGPCL
#define _MSGPCL

#include <msg.h>
```

```
#include <pclcard.h>

class msg_pcl_clock{

  msg_output l_out;
  msg_output c_out;
  msg_output f_out;
  int port;
  int source;
  double rate;
  int div;
  int cyc;
  double res;

public:

  msg_pcl_clock(int, int, double, int);
  msg_pcl_clock();
  void set(int, int, double, int);
  void cycle(msg_input in){ c_out.connect(in); };
  void finish(msg_input in){ f_out.connect(in); };
  friend void msg_pcl_clock_start(msg_pcl_clock *, void *);
  friend void msg_pcl_clock_repeat(msg_pcl_clock *, double *);
  msg_input start(){ return msg_in(this, msg_pcl_clock_start); };
  msg_input repeat(){ return msg_in(this, msg_pcl_clock_repeat); };

};

class msg_pcl_a_out{

  msg_output dest;
  int port;
  int chan;
  double res;

public:

  msg_pcl_a_out(int, int);
  void done(msg_input in){ dest.connect(in); };
  friend void msg_pcl_a_out_channel(msg_pcl_a_out *, double *);
  msg_input channel(){ return msg_in(this, msg_pcl_a_out_channel); };
  double result(){ return res; };

};

class msg_pcl_a_in{

  msg_output dest;
  int port;
  int chan;
  double res;

public:

  msg_pcl_a_in(int, int);
  msg_pcl_a_in();
  void set(int, int);
  void channel(msg_input in){ dest.connect(in); };
  friend void msg_pcl_a_in_trigger(msg_pcl_a_in *, void *);
  msg_input trigger(){ return msg_in(this, msg_pcl_a_in_trigger); };
  inline double result(){ return res; };
  inline int which(){ return chan; };

};

#endif
```

---

The low-level functions used by the message-passing blocks declared above are declared in the following file. These functions communicate directly with the input/output cards.

```
/* pclcard.h pc lab card interface */
```

```
#ifndef _PCLCARD
#define _PCLCARD

#define PORT 0x220

#define PCL_INT_CLOCK 0
#define PCL_EXT_CLOCK 1

#define UPV 6553.6

extern int pcl_start_clock(int, int, double, int);
extern int pcl_wait_cycle();
extern int pcl_check_cycle();
extern int pcl_end_cycle();
extern int pcl_end_clock();

extern void pcl_a_out(int, int, int);
extern int  pcl_a_in(int, int);

extern void   pcl_v_out(int, int, double);
extern double pcl_v_in(int, int);

extern void   pcl_s_out(int, int, double);
extern double pcl_s_in(int, int);

extern void pcl_w_out(int, int, int);
extern int  pcl_w_in(int, int);

extern void pcl_c_out(int, int, int);
extern int  pcl_c_in(int, int);

extern void pcl_b_out(int, int, int);
extern int  pcl_b_in(int, int);

inline void pcl_b_clear(int port, int chan){
  pcl_b_out(port, chan, 0);
}

inline void pcl_b_set(int port, int chan){
  pcl_b_out(port, chan, 1);
}
#endif
```

## B.2 Header files for the extensions to the software kernel

---

The following file contains declarations and some definitions for all of the basic message-passing blocks which were added to the software kernel. These are: data collection and storage in arrays, time stamp creation, latching, time series playback (which was not used and so has not been fully tested), clock divider, real-time keyboard reading, integration and digital input/output additions; plus specialised blocks connected with camera triggering.

```
// msgajm.h message passing data storage
//
// Alastair Martin
//

#ifndef _MSGAJM
#define _MSGAJM
```

```
#include <msg.h>
#include <pclcard.h>

extern "C" {
  int __cdecl _kbhit(void);
  int __cdecl _getch(void);
  int __cdecl _ungetch(int);
  int __cdecl _cprintf(const char *, ...);
  int __cdecl _cscanf(const char *, ...);
}

// msg_store
// stores doubles in an array as they arrive
// output mirrors input
// array elements go from zero to (size-1) inclusive

class msg_store{

  msg_output dest;
  double res;
  double en;
  double s;
  short* array;
  int count;
  int size;
  char goti;
  char gote;
  inline void op(){ if(gote && goti) operate(); };
  void operate();

public:

  msg_store();
  msg_store(int);
  int set(int);
  ~msg_store();

  void output(msg_input in){ dest.connect(in); };

  friend void msg_store_input (msg_store *, double *);
  msg_input input() { return msg_in (this, msg_store_input); };

  friend void msg_store_enable (msg_store *, double *);
  msg_input enable() { return msg_in (this, msg_store_enable); };

  short* data();
  int index();
  void scale(double);
};

// msg_index
// counts up from zero while input is high

class msg_index{

  msg_output dest;
  double res;

public:

  msg_index();
  ~msg_index();
  void output(msg_input in){ dest.connect(in); };
  friend void msg_index_input (msg_index *, double *);
  msg_input input() {return msg_in (this, msg_index_input); };

};


// d_out, based on Peters a_out
// Input: double channel (zero or non-zero)
// Output: double done (mirrors channel)

class msg_pcl_d_out{

  msg_output dest;
  int port;
  int bit;
  double res;
```

```
public:

  msg_pcl_d_out();
  msg_pcl_d_out(int p, int c){set(p,c);};
  void set(int, int);
  void done(msg_input in){ dest.connect(in); };
  friend void msg_pcl_d_out_channel(msg_pcl_d_out *, double *);
  msg_input channel(){ return msg_in(this, msg_pcl_d_out_channel); };
  double result(){ return res; };

};

// d_in based on Peters a_in
// input: double trigger
// output: double contents of bit (0.0 or 1.0)

class msg_pcl_d_in{

  msg_output dest;
  int port;
  int bit;
  double res;

public:

  msg_pcl_d_in(int, int);
  msg_pcl_d_in();
  void set(int,int);
  void channel(msg_input in){ dest.connect(in); };
  friend void msg_pcl_d_in_trigger(msg_pcl_d_in *, void *);
  msg_input trigger(){ return msg_in(this, msg_pcl_d_in_trigger); };
  double result(){ return res; };

};


// msg_playback
//
// opens a file containing a single time series
// of doubles
// reads to an arrays and plays back result
// takes inputs start and stop (numerical values ignored)
// output: double signal

class msg_playback{

  msg_output sig_out;
  double res_s;
  double* sig;
  double val_s;
  double val_f;
  int got_s;
  int got_f;
  int count;
  void operate();
  void op(){ if((got_s!=0) && (got_f!=0)) operate(); };

public:

  msg_playback(){ count = 0; };
  ~msg_playback();

  void open(char *, int);

  void signal(msg_input in){ sig_out.connect(in); };

  friend void msg_playback_start(msg_playback *, double *);
  msg_input start(){ return msg_in(this, msg_playback_start); };

  friend void msg_playback_stop(msg_playback *, double *);
  msg_input stop(){ return msg_in(this, msg_playback_stop); };

};

// msg_latch
// takes two inputs - outputs 1.0 if a non-zero value
// has arrived at any time on "input"
// reset by a non-zero value on "reset"

class msg_latch{
```

```
  msg_output dest;
  char goti;
  char gotr;
  double rst;
  double res;

public:

  msg_latch(){ res=0.0; rst=0.0; goti=0; gotr=0; };
  void operate();
  void output(msg_input in){ dest.connect(in); };
  friend void msg_latch_input(msg_latch *, double *);
  msg_input input(){ return msg_in(this, msg_latch_input); };
  friend void msg_latch_reset(msg_latch *, double *);
  msg_input reset(){ return msg_in(this, msg_latch_reset); };
  double result(){ return res; };

};

// msg_divider
//
// output goes high on every nth clock pulse,
// provided input is high

class msg_divider{

  double res;
  msg_output dest;
  int div;
  int count;

public:
  msg_divider();
  msg_divider(int);
  ~msg_divider(){};
  void set(int);

  void output(msg_input in){ dest.connect(in); };

  friend void msg_divider_input( msg_divider *, double * );
  msg_input input(){ return msg_in(this, msg_divider_input);};
};

class msg_cleanup{

  msg_output dest;
  double res;

public:

  msg_cleanup(){};
  void output(msg_input in){ dest.connect(in); };
  friend void msg_cleanup_input(msg_cleanup *, double *);
  msg_input input(){ return msg_in(this, msg_cleanup_input); };

};

// msg_key
// outputs 1.0 if a certain key has been struck
// finds out which key has been struck by asking
// a msg_readkey object (ONE per loop)

class msg_readkey;

class msg_key{

  msg_output dest;
  msg_readkey *read;
  double res;
  char ch;

public:
  msg_key(){ch = 0;};
  msg_key(char c, msg_readkey *r){set(c,r);};
  void set(char, msg_readkey *);

  void output(msg_input in){ dest.connect(in); };
  friend void msg_key_input(msg_key *, double *);
  msg_input input(){ return msg_in(this, msg_key_input); };

  double result(){ return res; };
```

```
};

// msg_readkey
// polls keyboard and stores first keystroke in buffer

class msg_readkey{

  msg_output dest;
  double res;
  int ch;

public:
  msg_readkey(){ch = 0;};

  void output(msg_input in){ dest.connect(in); };
  friend void msg_readkey_input(msg_readkey *, double *);
  msg_input input(){ return msg_in(this, msg_readkey_input); };

  double result(){ return res; };
  int compare(char);
};

// msg_wait
// version of msg_delay which gives an output lasting one tick

class msg_wait{

  msg_output dest;
  double ticks;
  double count;
  double res;
  int st;

public:

  void set(double);
  msg_wait(double n){ set(n); };
  msg_wait(){ msg_wait(1.0); };

  void output(msg_input in){ dest.connect(in); };

  friend void msg_wait_input(msg_wait *, double *);
  msg_input input(){ return msg_in(this, msg_wait_input); };
  double result(){ return ticks-count; };
};

class msg_zero_crossing{

  msg_output dest;
  int port;
  int chan;
  double res;
  double dump;
  int pos;

public:

  msg_zero_crossing(int, int);
  msg_zero_crossing();
  void set(int, int);
  void output(msg_input in){ dest.connect(in); };
  friend void msg_zero_crossing_input(msg_zero_crossing *, void *);
  msg_input input(){ return msg_in(this, msg_zero_crossing_input); };
  double result(){ return res; };

};

class msg_stepper{

  msg_output trig_dest;
  msg_output data_dest;
  double trig_res;
  double data_res;
  char last;
  char now;

public:

  msg_stepper();
  void trig_output(msg_input in){ trig_dest.connect(in); };
```

```
  void data_output(msg_input in){ data_dest.connect(in); };
  friend void msg_stepper_input(msg_stepper *, void *);
  msg_input input(){ return msg_in(this, msg_stepper_input); };
  double result(){ return data_res; };

};

// class msg_integrator
//
// integrates its input; time constant is set in seconds;
// thus clock frequency must also be supplied.
// output is inverted (for use in a feedback loop)

class msg_integrator{
  double tau_s, tau_c, clk, res;
  msg_output dest;

public:
  msg_integrator();
  msg_integrator(double,double);
  void set(double,double);
  double result(){ return res; };

  void output(msg_input in){ dest.connect(in); };
  friend void msg_integrator_input(msg_integrator *, double *);
  msg_input input(){ return msg_in(this, msg_integrator_input); };

};

class msg_shot_cycle{
  int shots;
  int cycles[12];
  int next;
  double res;
  msg_output dest;

public:
  msg_shot_cycle();
  int insert(int,int);

  void output(msg_input in){ dest.connect(in); };
  friend void msg_shot_cycle_input(msg_shot_cycle *, double *);
  msg_input input(){ return msg_in(this, msg_shot_cycle_input); };
};

#endif
```

---

The following file contains declarations and definitions for compound message-passing blocks, created by combining several individual interconnected blocks into a single utility block. The compound blocks perform the functions of multi-channel data collection and storage, camera triggering by various methods, and the detection of errors in the wavemaker hardware.

```
// msggroup.h
// A.Martin 4/11/94
//
// Blocks derived from groups of other blocks

#ifndef _MSGGROUP
#define _MSGGROUP

#include <conio.h>
#include <msgsys.h>
#include <msgajm.h>
#include <stdlib.h>
#include <fstream.h>
```

```
#include <iostream.h>
#include <stdio.h>
#include <strstrea.h>
#include <wmutils.h>
#include <pclcard.h>

inline void c_newline(){_cprintf("\r\n");}

// msg_analogue_inputs
// groups k analogue inputs
// initialise by:
// msg_analogue_inputs stores(k);
// clock.cycle(stores.input());
// stores.output(nextblock.input());
// only stores when input is high

class msg_analogue_inputs {
  double res;
  int k,cyc;
  msg_store* chans;
  msg_pcl_a_in* ins;
  msg_m_adds sum;
  msg_m_buf in;
  void connect();

public:
  msg_analogue_inputs();
  msg_analogue_inputs(int, int);
  ~msg_analogue_inputs();
  int set(int, int);

  void output(msg_input in){ sum.output(in); };
  msg_input input(){ return in.input(); };

  short* data(int i);
  int index(int i);
  int assign_channel(int,int);
  int scale_channel(int,double);
  int which(int);
};

// msg_camera_trigger

class msg_camera_trigger{
  msg_key key;
  msg_latch latch;
  msg_zero_crossing zero;
  msg_wait phase;
  msg_wait cycle;
  msg_m_and and;
  msg_m_not not;
  msg_pcl_d_out out;

public:
  msg_camera_trigger();
  msg_camera_trigger(char,int,int,msg_readkey *);
  void set(char,int,int,msg_readkey *);

  void output(msg_input in){ out.done(in); };
  msg_input input(){ return key.input(); };

};

// msg_check_abort

class msg_check_abort{
  msg_key escape;
  msg_pcl_d_in error;
  msg_m_and and;
  msg_m_or or1;
  msg_m_or or2;
  msg_cleanup end;
  msg_m_buf stopbuf;
  msg_m_buf startbuf;
  msg_pcl_d_out test;

public:
  msg_check_abort();
  msg_check_abort(msg_readkey*);
  msg_check_abort(msg_readkey*,char);
  void set(msg_readkey*);
```

```
  void set(msg_readkey*,char);

  void output(msg_input in){ end.output(in); };
  msg_input start(){ return startbuf.input(); };
  msg_input stop(){ return stopbuf.input(); };

  int result();
};

class msg_standard_stores{
  msg_analogue_inputs stores;
  msg_m_and and;
  msg_sync sync;
  msg_divider div;
  msg_m_not not;
  msg_index index;
  msg_store sto;
  msg_m_buf stopbuf;
  msg_m_buf startbuf;
  void connect();

public:
  msg_standard_stores();
  int set(int,filestore*,int,int,char*);
  int set(int,ifstream,filestore*,int,int,char*);
  void output(msg_input in){ stores.output(in); };
  msg_input start(){ return startbuf.input(); };
  msg_input stop(){ return stopbuf.input(); };
  int which(int);
};

#endif
```

---

The classes defined in this file do not form part of the message-passing system, but rather are used to gather data stored during an experiment into a structured file on disk.

```
// wmutils.h
// non message passing library
// Alastair Martin

#ifndef _WMUTILS
#define _WMUTILS

#include <fstream.h>
#include <strstrea.h>

static const int MAX_PROFILE_LENGTH=4096;

class filestore;

class column{
public:
  short* array;
  char label[9];
};

class filestore{
  int cols;
  int rows;
  int index;
  int exnum;
  column* col;
  ofstream outfile;

public:
  filestore();
  filestore(char*, int, int);
  ~filestore();
```

```
  int set(char*, int, int);
  int assign_column(short*, char*, int);
  strstream header;
  void save();
};

#endif
```

## B.3 Other components of the software

The files listed in this section contain the declarations and the code for the program `exrun.exe`. This program was written using the message passing library, and was the main experiment driver.

---

The following header file contains the definition of a class `experiment` which bundles all of the blocks used in the message-passing loop of `exrun`.

```
// ex.h
// declarations for exrun

#ifndef _EX_H
#define _EX_H

#include <time.h>
#include <fstream.h>
#include <conio.h>
#include <math.h>
#include <strstrea.h>
#include <wmutils.h>
#include <msgsys.h>
#include <msgajm.h>
#include <msggroup.h>
enum {SINE='s', SERIES='t', KEYBOARD=1, INFILE=2, QUERY='?',
      ZCROSS='z', KEYTRIG='k', CYCLE='c'};

class experiment{
public:
  msg_main root;
  msg_pcl_clock clock;

  msg_delay initialise;
  msg_delay  start;
  msg_delay  stop;

  msg_siggen sig;
  msg_m_not  not1;
  msg_m_not  not2;
  msg_m_not  not3;
  msg_m_or  or;
  msg_readkey  read;
  msg_m_const  zero;
  msg_pcl_d_out clear;
  msg_pcl_d_out reset;
  msg_int_wave  iwt;
  msg_sync sync;
  msg_sync  sync2;
  msg_playback  series;
  msg_camera_trigger  camera;
  msg_check_abort  check;
  msg_standard_stores stores;
  msg_key take;
  msg_pcl_d_out  photo;
  msg_shot_cycle scycle;
```

```
  msg_index ind;
  filestore file;

  void connect();
  void run(){ message_process(); };
};

void dotime (filestore&,int,int,char*,char*);
int dohistory (char *);
int calibrate (int, experiment*);
inline int c_wait();
int c_wait (int);

#endif // _EX_H
```

---

This file declares variables which are used by **exrun**.

```
// exrun.h

#ifndef _EXRUN
#define _EXRUN

#include <fstream.h>
#include <iostream.h>
#include <stdio.h>
#include <conio.h>
#include <math.h>
#include <strstrea.h>
#include <wmutils.h>
#include <msgsys.h>
#include <msgajm.h>
#include <msggroup.h>

extern int i,j,k;
extern int sg, dg, og, cyc, phase, chan;
extern double amp, frq;
extern double ck;
extern short* ptr;
extern int divider;
extern char* datafile;
extern char* seriesfile;
extern char label[9];
extern char type;
extern int input;
enum{SINE='s', SERIES='t', KEYBOARD=1, INFILE=2, QUERY='?'};


#endif
```

---

Code for various utility functions plus elements of the class **experiment** is found in the following file.

```
// exextra.cpp
// functions to make exrun's life easier

#include <ex.h>
#include <ctype.h>

void experiment::connect(){ // connections for non-array blocks

  root.start (clock.start()); // essentials
```

```
  clock.cycle (read.input());
  read.output (initialise.input());

  initialise.output (start.input()); // experiment timer
  initialise.output (stop.input());

  initialise.output (not2.input()); // reset counter and
  not2.output (clear.channel()); // clear error flags
  not2.output (reset.channel());
  clear.done (or.input_a());
  reset.done (or.input_b());
  or.output (not1.input());
  not1.output (iwt.start());
  sync2.output (sync.input());

  sync.output (check.stop()); // end of loop
  not1.output (check.start());
  check.output (clock.repeat());
  clock.finish (root.stop());
}

void dotime(filestore& f, int num, int sw, char* pfile, char* dfile){
  tm *curr_time;
  time_t long_time;
  time(&long_time);
  curr_time = localtime(&long_time);
  f.header << "File: " << dfile << '\n';
  f.header << "Experiment number: " << num << '\n';
  f.header << asctime(curr_time);
  switch (sw) {
  case KEYBOARD:
    f.header << "No parameter file\n\n";
    break;
  case INFILE:
    f.header << "Parameter file: " << pfile << "\n\n";
    break;
  }
}

int dohistory(char *filename){
  int exnum;
  ifstream histin;
  ofstream histout;
  histin.open(filename, ios::nocreate);
  if(!histin){
    _cprintf("File %s not found - creating...", filename);
    c_newline();
    exnum = 0;
  }else if(!(histin >> exnum)){
    _cprintf("File %s corrupt - replacing...", filename);
    c_newline();
    exnum = 0;
  }
  if(histin.is_open()) histin.close();
  histout.open(filename);
  if(histout){
    histout << ++exnum;
    histout.close();
  }else{
    _cprintf("Couldn't write to file %s - ignoring...", filename);
    c_newline();
  }
  return exnum;
}

int calibrate(int k, experiment *ex){
  int i, j, c, ignore[16];
  double up[16], down[16];
  if(k>=16) return 0;
  short *data;

  msg_main  local_root;
  msg_pcl_clock  local_clock;
  msg_divider  local_div;
  msg_analogue_inputs local_stores;
  msg_delay local_delay;
  msg_sync local_sync;

  for(i=0;i<k;i++){
    c = ex->stores.which(i);
    ignore[i] = (c<4)? 1:0;
```

```
    if(!local_stores.assign_channel(i,c)) return 0;
  }

  local_clock.set (PORT, PCL_INT_CLOCK, 40, 0);
  local_div.set (4);
  local_stores.set(k,50);
  local_delay.set (200);

  local_root.start (local_clock.start());
  local_clock.cycle (local_div.input());
  local_clock.cycle (local_delay.input());
  local_div.output (local_stores.input());
  local_stores.output (local_sync.trigger());
  local_delay.output (local_sync.input());
  local_sync.output (local_clock.repeat());
  local_clock.finish (local_root.stop());

  _cprintf("Move gauges to upper position and press a key");
  c_newline();
  c_wait();
  _cprintf("Wait...");
  c_newline();
  message_process();

  for(i=0;i<k;i++){
    if(ignore[i]) continue;
    data = local_stores.data(i);
    up[i] = 0.0;
    for(j=0;j<50;j++) up[i] += data[j];
    up[i] /= 50;
  }

  _cprintf("Move gauges to lower position and press a key");
  c_newline();
  c_wait();
  _cprintf("Wait...");
  c_newline();
  message_process();

  for(i=0;i<k;i++){
    if(ignore[i]) continue;
    data = local_stores.data(i);
    down[i] = 0.0;
     for(j=0;j<50;j++) down[i] += data[j];
down[i] /= 50;
ex->file.header << "Calibration for column " << i << ": "
<< 0.01/(down[i]-up[i])
<< " counts/m" << endl;
  }

  return 1;
}

inline int c_wait()
{
  return c_wait(0);
}

int c_wait(int c)
{
  int ch;
  for(;;){
    while(!_kbhit());
    ch=_getch();
    if(!c) if(isalnum(ch) || ch==' ') break;
    if(ch==c) break;
  };
  return ch;
}
```

---

Following is the code for the program **exrun**.

```
/* exrun.cpp
```

```
  Experiment driver for internal wave tank
  Alastair Martin 12/12/94
*/

#include <ex.h>

int main(int argc, char **argv){

// parameters

  int  a,i,j,k,exnum;
  int  sg, dg, og, cyc, phase, chan;
  double  amp, frq;
  double  ck;
  int  divider;
  char  datafile[_MAX_FNAME];
  char  seriesfile[_MAX_FNAME];
  char buffer[_MAX_FNAME];
  char  type,trigger;
  int  input;
  ifstream params;
  experiment ex;

  input = argc;
  if(input==INFILE && argv[1][0]=='?') input=QUERY;
  switch (input){
  case INFILE:
    params.open(argv[1], ios::nocreate);
    if(!params.is_open()){
      _cprintf("Can't open %s", argv[1]);
      c_newline();
      exit(1);
    }
    params >> ck; if(!params){_cprintf("ck=%d", ck);exit(1);}
    params >> cyc; if(!params){_cprintf("cyc=%d", cyc); exit(1);}
    params >> type; if(!params){_cprintf("type=%c", type);exit(1);}
    switch (type) {
    case SINE:
      params >> amp; if(!params){_cprintf("amp=%lf", amp);exit(1);}
      params >> frq; if(!params){_cprintf("frq=%lf", frq);exit(1);}
      break;
    case SERIES:
      params.ignore(1,'\n');
      params.getline(seriesfile,_MAX_FNAME);
      if(!params){_cprintf("seriesfile=%s", seriesfile);exit(1);}
      break;
    default:
      _cprintf("Valid modes are: Sine wave generator (s) or time series (t)");
      c_newline();
      exit(1);
    }
    params >> sg; if(!params){_cprintf("sg=%d", sg);exit(1);}
    params >> dg; if(!params){_cprintf("dg=%d", dg);exit(1);}
    params >> og; if(!params){_cprintf("og=%d", og);exit(1);}
    params >> divider; if(!params){_cprintf("divider=%s", divider);exit(1);}
    params >> k; if(!params){_cprintf("k=%d", k);exit(1);}
    break;
  case KEYBOARD:
    _cprintf("Clock frequency (min 40Hz): ");
    _cscanf("%lf",&ck);
    c_newline();
    _cprintf("Number of cycles: ");
    _cscanf("%d", &cyc);
    c_newline();
    _cprintf("Sine wave (s) or time series (t): ");
    _cscanf("%s", buffer);
    c_newline();
    sscanf(buffer, "%c", &type);
    switch (type) {
    case SINE:
      _cprintf("Amplitude (V): ");
      _cscanf("%lf", &amp);
      c_newline();
      _cprintf("Frequency (Hz): ");
      _cscanf("%lf", &frq);
      c_newline();
      break;
    case SERIES:
      _cprintf("Time series input filename: ");
      _cscanf("%s", seriesfile);
```

```
    c_newline();
    break;
  default:
    _cprintf("Valid modes are: Sine wave generator (s) or time series (t)");
    c_newline();
  }
  _cprintf("Loop gain (0-255): ");
  _cscanf("%d", &sg);
  c_newline();
  _cprintf("Damping (0-255): ");
  _cscanf("%d", &dg);
  c_newline();
  _cprintf("Output gain (0%%-255%%): ");
  _cscanf("%d", &og);
  c_newline();
  _cprintf("Sampling interval (cycles): ");
  _cscanf("%d", &divider);
  c_newline();
  _cprintf("Number of channels to sample: ");
  _cscanf("%d", &k);
  c_newline();
  break;
case QUERY:
default:
  _cprintf("EXPERIMENT DRIVER PARAMETER INPUTS:\r\n"
   "Clock frequency (>=40Hz)\r\nNumber of cycles\r\n"
   "Sine wave (s) or time series (t)\r\n"
   "Either:\r\n\tAmplitude (V)\r\n\tFrequency (Hz)\r\n"
   "Or:\r\n\tTime series input filename\r\n"
   "Loop gain (0-255)\r\nDamping (0-255)\r\nOutput gain (0%%-255%%)\r\n"
   "Sampling interval (cycles)\r\n");
  _cprintf("Number of channels to sample\r\n"
   "Output file name\r\n"
   "Channel number for each channel\r\n"
   "Labels for each channel\r\n"
   "Zero crossing (z), keyboard (k) or cycle (c) camera triggering\r\n"
   "Either:\r\n\tCamera trigger phase (cycles)\r\n\tReference channel\r\n"
   "Or:\r\n\tNumber of frames\r\n\tCycle number for each frame\r\n\r\n");
  _cprintf("Existing output files will not be overwritten\r\n"
   "Press ESC to abort during experiment\r\n"
   "Press SPACE to trigger camera (z/k only)\r\n");
  exit(0);
}
```

```
  if(cyc%divider){
    _cprintf("Cycles/divider must be a whole number");
    c_newline();
    exit(1);
  }
  if(ck<40){
    _cprintf("Clock frequency is too low");
    c_newline();
    exit(1);
  }
  if(sg<0) sg=0;
  if(sg>255) sg=255;
  if(dg<0) dg=0;
  if(dg>255) dg=255;
  if(og<0) og=0;
  if(og>255) og=255;

// set block parameters

  ex.clock.set(PORT, PCL_INT_CLOCK, ck, 0);
  ex.zero.set(0.0);
  ex.clear.set(IWT_1, 17);
  ex.reset.set(IWT_1, 18);


  ex.initialise.set(0.5*ck);
  ex.start.set(2*ck);
  ex.stop.set(cyc+2*ck);

  ex.iwt.set_gains(sg,dg,og);
  ex.iwt.set_s_ramp(1);
  ex.check.set(&(ex.read),1);
    // suppress error polling with check.set(&read,1);

  if(type==SERIES) ex.series.open(seriesfile, cyc);
  else ex.sig.set(ck, amp, frq, -M_PI_2);
```

```
// array blocks

switch (input) {
case INFILE:
  if(!ex.stores.set(k,params,&(ex.file),cyc,divider,datafile)) return 1;
  params >> trigger;
  break;
case KEYBOARD:
  if(!ex.stores.set(k,&(ex.file),cyc,divider,datafile)) return 1;
  _cprintf("Camera trigger (zero/keyboard/cycle): ");
  _cscanf("%s", buffer);
  c_newline();
  sscanf(buffer, "%c", &trigger);
  break;
}

// camera trigger mechanism

switch(trigger){
case ZCROSS:
  switch(input){
  case INFILE:
    params >> phase; if(!params){_cprintf("phase=%d", phase);exit(1);}
    params >> chan; if(!params){_cprintf("chan=%d", chan);exit(1);}
    break;
  case KEYBOARD:
    _cprintf("Camera trigger delay (cycles): ");
    _cscanf("%d", &phase);
    c_newline();
    _cprintf("Analogue channel to trigger camera: ");
    _cscanf("%d", &chan);
    c_newline();
    break;
  }
  ex.camera.set(0x20,phase,chan,&(ex.read));
  break;
case KEYTRIG:
  ex.take.set(0x20,&(ex.read));
  break;
case CYCLE:
  switch(input){
  case INFILE:
    params >> a; if(!params){_cprintf("a=%d", a);return 1;}
    for(i=0;i<a;i++){
params >> j; if(!params){_cprintf("j=%d", j);return 1;}
ex.scycle.insert(i,j);
      }
      break;
    case KEYBOARD:
      _cprintf("Number of frames (maximum 12): ");
      _cscanf("%d", &a);
      c_newline();
      if(a>11 || a<0){_cprintf("Bad number of frames");return 1;}
      for(i=1;i<=a;i++){
_cprintf("Cycle for frame %d: ", i);
_cscanf("%d", &j);
c_newline();
ex.scycle.insert(i-1,j);
      }
      break;
    }
    ex.photo.set(IWT_1,21);
    break;
  default:
    _cprintf("Valid camera trigger modes are z,k or c");
    c_newline();
    return 1;
  }

  ex.connect(); // basics

  switch (type){
  case SINE:
    ex.start.output (ex.sig.start()); // signal generator
    ex.stop.output (ex.sig.stop()); // and iwt controller
    ex.stop.output (ex.iwt.stop());
    ex.sig.output (ex.zero.trigger());
    ex.sig.output (ex.iwt.wm_sig_1());
    ex.zero.output (ex.iwt.wm_sig_0());
    ex.iwt.done (ex.sync2.input());
    break;
```

```
  case SERIES:
    ex.start.output (ex.series.start());    // time series playback
    ex.stop.output (ex.series.stop()); // and iwt controller
    ex.stop.output (ex.iwt.stop());
    ex.series.signal(ex.zero.trigger());
    ex.series.signal(ex.iwt.wm_sig_1());
    ex.zero.output (ex.iwt.wm_sig_0());
    ex.iwt.done (ex.sync2.input());
    break;
  }

  switch(trigger){                  // camera trigger connections
  case ZCROSS:
    ex.start.output (ex.camera.input());
    ex.camera.output(ex.sync2.trigger());
    break;
  case KEYTRIG:
    ex.start.output (ex.take.input());
    ex.take.output (ex.not3.input());
    ex.not3.output (ex.photo.channel());
    ex.photo.done (ex.sync2.trigger());
    break;
  case CYCLE:
    ex.start.output (ex.ind.input());
    ex.ind.output (ex.scycle.input());
    ex.scycle.output(ex.photo.channel());
    ex.photo.done (ex.sync2.trigger());
    break;
  }

// connections for array blocks

  if(k){
    ex.start.output (ex.stores.start());
    ex.stop.output (ex.stores.stop());
    ex.stores.output(ex.sync.trigger());
  }else ex.iwt.done (ex.sync.trigger());

// number experiment & calibrate gauges (calibration doesn't work)

  exnum = dohistory("e:\\exp\\history");
  _cprintf("Experiment number: %d", exnum);
  c_newline();
  // if(calibrate(k,&ex)) _cprintf("Gauges calibrated");
  // else _cprintf("Couldn't calibrate gauges");
  // c_newline();

  // run experiment

  _cprintf("Press a key to start...");
  c_newline();
  c_wait();
  _cprintf("Running experiment...");
  c_newline();
  ex.run();

  // report

  if(ex.check.result()){
    i = (int)(ex.stop.result()-ex.start.result());
    _cprintf("Experiment aborted at end of cycle %d", i);
  } else _cprintf("Experiment completed");
  c_newline();

  // save array block data

  if(k) dotime(ex.file,exnum,input,argv[1],datafile);

  if(k){
    _cprintf("Saving data...");
    c_newline();
    ex.file.save();
  }

  return 0;
}
```

## B.4 Manual for extending the software kernel

The following is the text of a brief manual which was written by the author for future users of Peter Woodhead's software kernel. The manual was written directly around sample header and source files, including a test application (`dostest.cpp`) written by Mr Woodhead.

---

**How to program and use blocks**
(Based on Peter Woodhead's template and test program (Sept. 1994))

Creating a new block type requires the construction of a new class which will represent objects of that type. Class declarations are contained in a header (`.h`) file while the functional code is contained within a source (`.cpp`) file. The `.h` and the `.cpp` files have the same name, and the `.h` file must be `#included` in the `.cpp` file.

Every block has a number of inputs and a number of outputs. The types used for input and output (`in_type_1`, `out_type_1` etc) are generally `double`, whether binary signals (such as triggers) or numerical values are being transmitted. The inputs and outputs in the template have been named `input1` and `out1` (etc) respectively. The classes `msg_input` and `msg_output` are declared in `msg.h`; they contain member functions such as `connect()` which are used to set up links between blocks.

Message passing requires connections to be made between blocks. This is done by the `main` function which you write. If this function makes (say) a connection between the output of `block1` and the input of `block2`, then operation is as follows: `block1` performs its task and places a message in the queue. This message contains a numerical value and a destination, which will be the relevant input handler of `block2`. When the message reaches the front of the queue, the relevant input handler of `block2`, which might be called `classname_input1`, is called. What the input handler will do depends on the block. For a simple block (say, one input and one output) `classname_input1` will perform the block's operation and place a new message on the queue. For more complex blocks, `classname_input1` might set a flag saying "a message has arrived on `input1`", and then call a function `op()` which checks all the input flags. If all the input flags are set (meaning "messages have arrived on all inputs", then `op()` might call a function `operate()` to do the work of the block. Output messages are then placed on the message queue.

The user of the block never sees names like `classname_input1`; these names are passed between blocks using the setup functions provided by the `msg_input` and `msg_output` classes.

### In the header (`.h`) file

```
#ifndef _HEADERFILE
#define _HEADERFILE

class name{

        msg_output dest1;
        msg_output dest2;
        out_type_1 out1;
        out_type_2 out2;
```

This sets up the outputs from the class.

```
        int flags;
        void operate();
        void op() { if( condition ) operate(); };
```

This sets up extra variables which may be used to trigger class operation, in the case of the more complex class described above. An example is the class `msg_int_wave`, in which each input has a flag which it sets when the input handler is called. The condition would test to see whether all the flags have been set. There would be one flag for each input handler.

```
public:
        name();
        ~name();
```

The class constructor `name()` may take arguments, or there may be a function such as `set(arguments)`, also declared here. Function name overloading allows both possibilities and allows a range of ways in which the object may be constructed and set up. All the different ways must be accounted for here in a function declaration, and coded either here or in the `.cpp` file.

```
        void output1(msg_input in){ dest1.connect(in); };
        void output2(msg_input in){ dest2.connect(in); };
```

The functions `output1` and `output2` are called at initialisation time; they take as their arguments the destinations of the messages they will write. As part of a `main()` function, you would write `block1.output1(block2.input1());`.

A single output can be connected to many inputs, so that you could add another line `block1.output1(block3.input1());`. These initialisation functions pass pointers to the relevant input handlers to the output handler, so that the output handler can place the pointers to the input handlers into the message, along with the actual numerical value of the message.

```
friend void name_input1( name *, in_type1 * );
msg_input input1(){ return msg_in(this, name_input1);};

friend void name_input2( name *, in_type2 * );
msg_input input2(){ return msg_in(this, name_input2);};
```

The functions `input1` and `input2` are called at initialisation as part of the calls to `output1` and `output2`, as part of the same command. `input1`, for example, calls the function `msg_in` which returns the pointer to the relevant input handler, `name_input1`.

Included in this section will be declarations of any other functions necessary for the class.

```
};
#endif
```

### In the source (.cpp) file

All the functions declared but not coded in the header file are coded here. There may be a range of constructors and setup functions. The input and output handlers, and the `operate()` function (if there is one) will also be found here.

```
#include "headerfile.h"

name::name() {
        .
        .
}

name::~name() {
```

```
        .
        .
}

name_input1 (name *pad, in_type1 *val){
        .
        .
```

This is the input handler for `input1`. The arguments are: a pointer (`pad`) to an object of this class (the `name` class), and a pointer to the numerical value of the message being received (`val`). The `pad` pointer provides access to the individual object which is receiving an input.

In simple blocks, the input handler may create the messages to be placed in the queue. It does this by performing the calculations necessary on the private member variables `pad->out1` and `pad->out2`, and then passing them to the output handlers `pad->dest1.out` and `pad->dest2.out` via a cast:

```
        pad->dest1.out((void *) &pad->out1);
        pad->dest2.out((void *) &pad->out2);
```

In more complex blocks, the lines above will be contained within the `operate()` function. In this case the input handler may perform some simple operations such as making a local copy of the input value (buffering), setting a flag and calling the `op()` function. The `operate()` function will then be called when all the inputs have been received.

```
        pad->val1 = *val;
        pad->flag1 = 1;
        pad->op();
}

name_input2 (name *pad, in_type2 *val){
        .
        .
        pad->dest1.out((void *) &pad->out1);
        pad->dest2.out((void *) &pad->out2);
        .
        .
}

void name::operate() {
        .
```

```
}
```

### In the `main()` function

This function initialises the blocks, sets them up, sets up their connections and starts the loop. The example used is **`dostest.cpp`** (slightly altered).

```
#include <msgsys.h>
#include <iostream.h>
#include <stdio.h>
```

The header file **`msgsys.h`** includes all the relevant header files. The library which contains the functions is **`wmlib.lib`**, included in the project by the **`.mak`** file

```
#define CLOCK 100.0

int main ( int argc, char **argv ) {
        int sg, dg, og;
        double cyc, amp, frq;
        msg_main root;
        msg_pcl_clock clock (PORT, PCL_INT_CLOCK, CLOCK, 0);
        msg_int_wave iwt;
        msg_m_neg neg;
        msg_siggen sig;
        msg delay del;
        msg_sync sync;
```

The above declarations declare objects ("blocks") to be used in the program. The class definitions are contained in the library.

Every program must have a block of type **`msg_main`**, which in this program is called **`root`**. A clock is usually also necessary. Here **`clock`** is initialised in its declaration. The other blocks will be initialised once the command line arguments, which contain the parameters, have been read in.

```
if (argc != 7){
        cout << "usage: " << argv[0]
             << " cycles amp frq sgain dgain ogain\n";
```

```
}

sscanf (argv[1], "%lf", &cyc);
sscanf (argv[2], "%lf", &amp);
sscanf (argv[3], "%lf", &frq);
sscanf (argv[4], "%d", &sg);
sscanf (argv[5], "%d", &dg);
sscanf (argv[6], "%d", &og);
```

The remaining initialisations are done using the `set(...)` functions, which are each public member functions of their own class.

```
del.set(cyc);
iwt.set_gains(sg,dg,og);
sig.set(CLOCK, amp, frq, -M_PI_2);
```

The most important part is the setting up of the connections between the blocks. The syntax for connecting (say) an output called `output1` of a block called `block1`, to an input called `input2` of a block called `block3` is:

```
block1.output1(block3.input2());
```

As noted previously, a single output can be connected to several inputs. Each connection requires a separate line of code.

```
root.start(clock.start());
clock.cycle(sig.start());
clock.cycle(del.input());
del.output(sync.input());
del.output(sig.stop());
clock.cycle(iwt.start());
del.output(iwt.stop());
sig.output(iwt.wm_sig_0());
sig.output(neg.input());
neg.output(iwt.wm_sig_1());
iwt.done(sync.trigger());
sync.output(clock.repeat());
clock.finish(root.stop());
```

All of this is merely initialisation. The process is started by the function:

```
        message_process();
```

Once a message saying "I've finished" arrives at the stop input of the block of type **msg_main** (in this case **root**), the process finishes. Note that, if any of your blocks contain destructors, the destructors will not be called at this point. They will only be called when the block objects go "out of scope", which in this case is the end of the **main()** function, or when they are called explicitly. Alternatively, initialisation and process initiation can be done in a separate function, in which case the destructors will be called on return from that function.

```
        return 0;
}
```

# Bibliography


Adrian, R.J. (1991). Particle-Imaging Techniques for Experimental Fluid Mechanics. *Ann. Rev. Fluid Mech.*, **23** 261–304.

Apel, J.R., J.R. Holbrook, A.K. Liu & J.J. Tsai (1985). The Sulu Sea Internal Soliton Experiment. *J. Phys. Oceanography*, **15** 1625–1651.

Apel, J.R., M. Byrne, J.R. Proni & R.L. Charnell (1975). Observations of Oceanic Internal and Surface Waves From the Earth Resources Technology Satellite. *J. Geophys. Res.*, **80** (6) 864–881.

Arnsten, Ø. (1990). *Uniform stratified flow interaction with a submerged horizontal cylinder: a revisit of "dead-water" in Norwegian fjords.* Ph.D. Thesis, NTH (Norwegian Institute of Technology), University of Trondheim.

Baines, P.G. (1983). Tidal Motion in Submarine Canyons—A Laboratory Experiment. *J. Phys. Oceanography*, **13** 310–328.

Baines, P.G. & X-H Fang (1985). Internal tide generation at a continental shelf/slope junction: a comparison between theory and a laboratory experiment. *Dyn. Atmos. Oceans*, **9** 297–314.

Benjamin, T.B. (1966). Internal waves of finite amplitude and permanent form. *J. Fluid Mech.*, **25** (2), 241–270.

Benjamin, T.B. (1967). Internal waves of permanent form in fluids of great depth. *J. Fluid Mech.*, **29**, 559–592.

Bole, J.B., C.C. Ebbesmeyer & R.D. Romea (1994). Soliton Currents in the South China Sea: Measurements and Theoretical Modeling., *Proc. 26th Ann. Ocean Tech. Conf.*, Houston, Texas, USA, 2–5 May (OTC 7417).

Booker, J.R. & F.P. Bretherton (1967). The critical layer for internal gravity waves in a shear flow. *J. Fluid Mech.*, **27** 513–539.

Born, M. & E. Wolf (1959). *Principles of optics: electromagnetic theory of propagation, interference and diffraction of light.* London: Pergammon Press.

Bowman, F. (1953). *Introduction to Elliptic Functions with Applications*. London: English Universities Press.

Briscoe, M.G. (1975). Introduction to a Collection of Papers in Internal Waves. *J. Geophys. Res.*, **80** (3) 289–290.

Crandall, S.H., N.C. Dahl & T.J. Lardner, eds. (1978). *An introduction to the mechanics of solids*, 2nd edition with SI units, McGraw-Hill International, Tokyo.

Curtin, T.B. & C.N.K. Mooers (1975). Observation and Interpretation of a High-Frequency Internal Wave Packet and Surface Slick Pattern. *J. Geophys. Res.*, **80** (6) 882–894.

Dalrymple, R.A. & P.L-F. Liu (1978). Waves over Soft Muds: A Two-Layer Fluid Model. *J. Phys. Oceanography*, **8**, 1121–1131.

Davies, P.A. (1992). Aspects of Flow Visualisation and Density Field Monitoring of Stratified Flows. *Optics and Lasers in Engineering*, **16** (4-5), 311-335

Davis, R.E. & A. Acrivos (1967). Solitary internal waves in deep water. *J. Fluid Mech.*, **29**, 593–607.

Dean, R.G. & R.A. Dalrymple (1991) *Water wave mechanics for engineers and scientists*, Singapore: World Scientific.

Department of Energy (1990). *Offshore Installations: Guidance on Designs, Construction and Certification.* 4th Ed., HMSO.

Djordjevic, V.D. & L.G. Redekopp (1978). The Fission and Disintegration of Internal Solitary Waves Moving over Two-Dimensional Topography. *J. Phys. Oceanography*, **8** 1016–1024.

Dore, B.D. (1970). Mass transport in layered fluid systems, *J. Fluid Mech.*, **40**(1), 113–126

Easson, W.J., C.A. Greated, P.A. Davies, L.A. Mofor, N.H. Parks & A.J. Martin (1993). Kinematics of Internal Waves: Quarterly Report 02 (interim report to the Health and Safety Executive/Marine Technology Support Unit), The University of Edinburgh.

Ekman, V.W. (1904). On dead-water., in: Nansen, F.: *Sci. Results Norwegian N. Polar Expedition 1893–96*, **5** (15) 1–152 (17 plates).

Edinburgh Wave Power Project (1987). *Solo Duck Linear Analysis*, Report to the Wave Energy Steering Committee, UK Department of Energy.

Efthymiou, M. & C.G. Graham (1990). Environmental Loading on Fixed Offshore Platforms. *Society for Underwater Technology,* **26**: *Environmental Forces on Offshore Structures and their Prediction,* 293–320.

Evans, W.A.B. (1996a). Exact Numerical Solutions to *Large Amplitude* Internal Solitary Waves. *Proc. 6th Int. Conf. Offshore & Polar Eng. (ISOPE 1996)*, 124–130. Los Angeles, USA, 26–31 May. Golden, Colorado: International Society of Offshore and Polar Engineers.

Evans, W.A.B. (1996b). An exact integral-equation for Solitary Waves (with new numerical results for some internal properties). *Proc. Roy. Soc. Lon. A*, **452** (1945) 373–390.

Evans, W.A.B. & M.J. Ford (1996). An integral equation approach to internal (2-layer) solitary waves. *Phys. Fluids.* **8**(8). 2032–2047

Friis, H.A., J. Grue, E. Palm & P.O. Rusås (1997). A method for computing unsteady fully nonlinear interfacial waves. *Submitted for publication.*

Garrett, C. & W. Munk (1975). Space-Time Scales of Internal Waves: A Progress Report. *J. Geophys. Res.*, **80** (3) 291–297.

Gasparovic, R.F., J.R. Apel & E.S. Kaisichke (1988). An Overview of the SAR Internal Wave Signature Experiment. *J. Geophys. Res.*, **93** (C10) 12304–12316.

Gilbert, D. & Christopher G. (1989). Implications for Ocean Mixing of Internal Wave Scattering off Irregular Topography. *J. Phys. Oceanography*, **19** 1716–1729.

Gray, C. (1989). *The Development of Particle Image Velocimetry for Water Wave Studies.* Ph.D. Thesis, University of Edinburgh.

Gray, C., C.A. Greated, D.R. McCluskey & W.J. Easson (1991). An analysis of the scanning beam PIV illumination system. *Meas. Sci. Tech.*, **2** 717–724.

Greated, C.A., D.J. Skyner & T. Bruce (1992). Particle Image Velocimetry in the Coastal Engineering Laboratory. *Proc. 23rd. Int. Conf. Coastal Eng.* (B.L. Edge, ed.), **1** (15), 212–225, American Society of Civil Engineers, New York.

Hallam, M.G., N.J. Heaf & L.R. Wootton (1978). *Dynamics of Marine Structures: Methods of calculating the dynamic response of fixed structures subject to wave and current action* (Report UR8, 2nd. Ed. ), London: Ciria Underwater Engineering Group.

Hammack, J.L. (1980). Baroclinic Tsunami Generation. *J. Phys. Oceanography.* **10**, 1455–1476

Hannoun, I.A., H.J.S. Fernando & E.J. List (1988). Turbulence structure near a sharp density interface. *J. Fluid Mech.*, **189** 189–209.

Harrison, W.J. (1908). The influence of viscosity on the oscillations of superposed fluids. *Proc. Lon. Math. Soc. , Ser. 2*, **6** 396–405.

Head, M.J. (1983). *The Use of Miniature Four-Electrode Conductivity Probes for High Resolution Measurement of Turbulent Density or Temperature Variations in Salt-Stratified Water Flows*, Ph.D. Thesis, University of California, San Diego.

Helfrich, K.R. & W.K. Melville (1986). On long nonlinear internal waves over slope-shelf topography. *J. Fluid Mech.*, **167**, 285–308.

Helmis, C.G., H.A. Flocas, A.A. Papadopoulos, D.N. Asimakopoulos, P.G. Papageorgas & J.A. Kalogiros (1996). An experimental study of lee waves formation and evolution. *submitted for publication.*

Herman, R. (1992). Solitary Waves. *American Scientist*, **80** (July-August), 350–361.

Hinze, J.O. (1975). *Turbulence* (2nd Ed.), New York: McGraw-Hill.

Holloway, P.E., E. Pelinovsky, T. Talipova & B. Barnes (1997). Nonlinear Models of Internal Tide and Internal Solitary Wave Evolution over a Continental Slope. Submitted to *Proc. 7th Int. Offshore & Polar Eng. Conf. (ISOPE-97).*

Horowitz, P. & W. Hill (1989). *The Art of Electronics*, 2nd ed. Cambridge University Press.

Howard, L.N. (1961). Note on a paper of John W. Miles. *J. Fluid Mech.*, **10** 509–512.

Keane, R.D. & R.J. Adrian (1990). Optimization of particle image velocimeters. Part I: Double pulsed systems. *Meas. Sci. Technol.*, **1**, 1202–1215

Keulegan, G.H. & L.H. Carpenter (1958). Forces on Cylinders and Plates in an Oscillating Fluid. *J. Res. Nat. Bureau Stand.* **60** (5, paper 2857) 423–444

Kleuser, R. (1996). *Design and Use of a Towing Carriage for the Measurement of Oceanic Internal Waves*, Honours Project Report, Department of Mechanical Engineering, The University of Edinburgh.

Koop, C.G. & G. Butler (1981). An investigation of internal solitary waves in a two-fluid system, *J. Fluid Mech.*, **112**, 225–251

Korteweg, D.J. & G. De Vries (1895). On the change of form of long waves advancing in a rectangular canal, and on a new type of long stationary waves. *Phil. Mag.*, Ser. 5, **39**, 422–443.

Lamb, H. (1932) *Hydrodynamics*, (6th. ed. ), New York: Cambridge University Press

LeBlond, P.H. (1966). On the damping of internal gravity waves in a continuously stratified ocean. *J. Fluid Mech.*, **25** (1) 121–142.

LeBlond, P.H. & L.A. Mysak, (1978). *Waves in the Ocean*, Amsterdam: Elsevier Scientific.

Lee, C-Y & R.C. Beardsley (1974). The Generation of Long Nonlinear Internal Waves in a Weakly Stratified Shear Flow. *J. Geophys. Res.*, **79** (3) 453–462.

Leone, C., H. Segur & J.L. Hammack (1982). Viscous decay of long internal solitary waves, *Phys. Fluids*, **25**(6), 942–944

Lide, D.R., ed. (1993). *CRC Handbook of Chemsitry and Physics: a ready-reference book of chemical and physical data*, 74th ed., CRC Press, London.

Lighthill, J.R. (1978). *Waves in Fluids.* Cambridge University Press.

Lim, F.K. & R. Nielsen (1993). Design and Installation of Snorre Field TLP Rigid Riser System. *Proc. 3rd Int. Conf. Offshore & Polar Eng. (ISOPE 1993)*, 272-279. Singapore, 6–11 June. Golden, Colorado: International Society of Offshore and Polar Engineers.

Liu, A.K., J.R. Holbrook & J.R. Apel (1985). Nonlinear Internal Wave Evolution in the Sulu Sea. *J. Phys. Oceanography*, **15**, 1613–1624.

Long, R.R. (1952). Some Aspects of the Flow of Stratified Fluids: I. A Theoretical Investigation. *Tellus*, **5** (1) 42–58.

Long, R.R. (1953). A laboratory model resembling the "Bishop-wave" phenomenon. *Bulletin Amer. Meteorological Soc.*, **34** 205–211.

Long, R.R. (1954). Some Aspects of the Flow of Stratified Fluids: II. Experiments with a Two-Fluid System. *Tellus*, **6** (2) 97–115.

Long, R.R. (1955). Some Aspects of the Flow of Stratified Fluids: III. Continuous Density Gradients. *Tellus*, **7** (3) 341–357.

Long, R.R. (1956). Solitary Waves in One- and Two-Fluid Systems, *Tellus*, **8** (4), 460–471.

Long, R.R. (1965). On the Boussinesq approximation and its role in the theory of internal waves, *Tellus*, **XVII**(1), 46–52

Longuet-Higgins, M.S. (1953). Mass transport in water waves. *Phil. Trans. Roy. Soc. Lon. A* **245** 535–581

McEwan, A.D. (1983a). Internal mixing in stratified fluids. *J. Fluid Mech.*, **128** 59–80.

McEwan, A.D. (1983b). The kinematics of stratified mixing through internal wave-breaking. *J. Fluid Mech.*, **128** 47–57.

McCluskey, D.R. (1992). *An Optical Investigation of Air-Particle Flows.* Ph.D. Thesis, The University of Edinburgh.

McDougal, T.J. (1979). On the elimination of refractive-index variations in turbulent density-stratified liquid flows. *J. Fluid Mech.* **93** (1) 83–96.

Maas, L.R. & F-P.A. Lam (1995). Geometric focussing of internal waves. *J. Fluid Mech.*, **300** 1–41.

Massey, B.S. (1989). *Mechanics of Fluids*, 6th ed., London: Van Nostrand Reinhold.

Maxworthy, T. (1979). A Note on the Internal Solitary Waves Produced by Tidal Flow Over a Three-Dimensional Ridge. *J. Geophys. Res.*, **84** (C1) 338–346.

Miles, J.W. (1961). On the stability of heterogeneous shear flows. *J. Fluid Mech.*, **10** 496–508.

Miles, J.W. (1980). Solitary Waves. *Ann. Rev. Fluid Mech.*, **12** 11–43.

Morison, J.R., M.P. O'Brien, J.W. Johnson & S.A. Schaaf (1950). The Force Exerted by Surface Waves on Piles. *Petroleum Trans., AIME,* **189**.

Morrison, I.G. (1995). *The Hydrodynamic Performance of an Oscillating Water Column Wave Energy Converter.* Ph.D. Thesis, University of Edinburgh.

Mowbray, D.E. & B.S.H. Rarity (1967). A theoretical and experimental investigation of the phase configuration of internal waves of small amplitude in a density stratified liquid. J. Fluid Mech., **28** 1–16.

Neale, M.J., ed. (1973). *Tribology Handbook*, Newnes-Butterworth, London

Nergaard, A.I. (1993). A Fully Compensated High-Pressure Riser Telescope. *Proc. 3rd Int. Conf. Offshore & Polar Eng. (ISOPE 1993)*, 294-300. Singapore, 6–11 June. Golden, Colorado: International Society of Offshore and Polar Engineers.

Newman, J.N. (1977). *Marine Hydrodynamics*, Cambridge, MA: The MIT Press.

Oil & Gas Journal (1979). Hostile-environment technology advances for deep water, Arctic. 17 September, 66-68.

Ono, H. (1975). Algebraic Solitary Waves in Stratified Fluids. *J. Phys. Soc. Japan*, **39** (4) 1082–1091.

Osborne, A.R., T.L. Burch, & R.I. Scarlet (1978). The influence of Internal Waves on Deep-Water Drilling. *J. Petroleum Tech.*, **30** 1497–1504.

Osborne, A.R. & T.L. Burch (1980). Internal Solitons in the Andaman Sea. *Science*, **208** (4443), 451–460

Perry, R.B. & G.R. Schimke (1965). Large-Amplitude Internal Waves Observed off the Northwest Coast of Sumatra. *J. Geophys. Res.*, **70** (10) 2319–2324.

Phillips, O.M. (1977). *The Dynamics of the Upper Ocean* (2nd ed.), Cambridge University Press.

Pietrzak, J.D., C. Kranenburgh, G. Abraham, B. Kranenborg, & A. Van Der Wekken (1991). Internal Wave Activity in Rotterdam Waterway. *J. Hydraulic Eng. (ASCE)*, **117** (6), 738–757.

Prandlt, L. (1952). *Essentials of Fluid Dynamics*, Glasgow: Blackie & Son.

Press, W.H., S.A. Teukolsky, W.T. Vetterling & B.P. Flannery (1994). *Numerical Recipes in C: The Art of Scientific Computing*, 2nd ed. with corrections, Cambridge University Press

Queney, P. (1955). Rotor Phenomena in the Lee of Mountains. *Tellus*, **7** (3) 367–371.

Quinn, P.A. (1995). *Breaking Waves on Beaches*, Ph.D. Thesis, The University of Edinburgh.

Raffel, M. & J. Kompenhans (1995). Theoretical and experimental aspects of image-shifting by means of a rotating mirror system for particle image velocimetry. *Meas. Sci. Tech.*, **6** 795–808.

Ralph, F.M., M. Crochet & S.V. Venkateswaran (1992). A study of mountain lee waves using clear-air radar. *Quarterly J. Roy. Meteorological Soc. A.*, **118** (506) 597–627.

Roark, R.J. (1989). *Roark's formulas for stress and strain* (6th edition, Warren C. Young, ed.). McGraw-Hill, New York.

Russell, J.S. (1845). Report on Waves. *Report to the 14th (1844) meeting of the British Association for the Advancement of Science*, 311-390.

Segur, H. & J.L. Hammack (1982). Soliton models of long internal waves. *J. Fluid Mech.*, **118** 285–304.

Sherwin, T.J. (1988). Analysis of an internal tide observed on the Malin Shelf, north of Ireland. *J. Phys. Oceanography*, **18** 1035–1050.

Sherwin, T.J. (1989). *Internal Waves in the Færoe -Shetland Channel.* Submission to the North West Approaches Group Currents Overview Workshop, Godalming, Surrey, 30–31 October

Sherwin, T.J. (1991). Evidence of a Deep Internal Tide in the Færoe-Shetland Channel, in: Parker, Bruce B. (ed.). *Tidal Hydrodynamics*, 469–488, New York: Wiley

Sherwin, T.J., A.C. Dale, M.E. Inall & D.R.G. Jeans (1996). Linear and Non-Linear Internal Tides Around the European Atlantic Shelf Edge. *Proc. 6th Int. Conf. Offshore & Polar Eng. (ISOPE 1996)*, 131–137. Los Angeles, USA, 26–31 May. Golden, Colorado: International Society of Offshore and Polar Engineers.

Skyner, D.J. (1992) *The Mechanics of Extreme Water Waves*, PhD Thesis, The University of Edinburgh.

Smyth, W.D. & W.R. Peltier (1991). Instability and transition in finite-amplitude Kelvin-Helmholtz and Holmboe waves. *J. Fluid Mech.*, **228** 387–415.

Spedding, G.R., F.K. Browand & A.M. Fincham (1996). Turbulence, similarity scaling and vortex geometry in the wake of a towed sphere of a stably stratified fluid. *J. Fluid Mech.*, **314** 53–103.

Stamp, A.P. & M. Jacka (1995). Deep-water internal solitary waves. *J. Fluid Mech.*, **305** 347–371.

Stevens, C. & J. Imberger (1996). The initial response of a stratified lake to a surface shear stress. *J. Fluid Mech.*, **312** 39–66.

Stokes, G.G. (1847). On the Theory of Oscillatory Waves. *Trans. Camb. Phil. Soc.*, **8**, 441–455.

Taylor, J.R. (1992). The energetics of breaking events in a resonantly forced internal wave field. *J. Fluid Mech.* **239** 309–340.

Thomas, N.H. & T.N. Stevenson (1972). A similarity solution for viscous internal waves. *J. Fluid Mech.*, **54** 495–506.

Thorpe, S.A. (1968a). A method of producing a shear flow in a stratified fluid, *J. Fluid Mech.*, **32** 693–704

Thorpe, S.A. (1968b). On the shape of progressive internal waves. *Phil. Trans. Roy. Soc.* A, **263**, 563–614.

Thorpe, S.A. (1968c). On standing internal gravity waves of finite amplitude. *J. Fluid Mech.*, **32** (3) 480–529.

Thorpe, S.A. (1975). The Excitation, Dissipation and Interaction of Internal Waves in the Deep Ocean, *J. Geophys. Res.*, **80** (3), 328–338.

Thorpe, S.A. (1978). On the shape and breaking of finite amplitude internal gravity waves in a shear flow. *J. Fluid Mech.*, **85** 7–31.

Thorpe, S.A., A. Hall & I. Crofts (1972). The internal surge in Loch Ness. *Nature*, **237** 96–98.

Tulin, M.P., P. Wang & Y. Yao (1993). Numerical Prediction of Ship Generated Internal Waves in a Stratified Ocean at Supercritical Froude Numbers. Publication details unknown.

Turner, J.S. (1973). *Buoyancy effects in fluids*, Cambridge: Cambridge University Press

Ursell, F. (1953). The Long-Wave Paradox in the Theory of Gravity Waves. *Proc. Camb. Phil. Soc.*, **49**, 685–694.

Van Dyke, M. (1982). *An Album of Fluid Motion*, Stanford CA: The Parabolic Press.

Whale, J. (1996). *A study of the near wake of a model wind turbine using particle image velocimetry*, Ph.D. Thesis, The University of Edinburgh.

Woods, J.D. (1967). Wave-induced shear instability in the summer thermocline. *J. Fluid Mech.*, **32** (4) 791–800.

Yemm, R. (1995). *Development of constant force tank testing techniques and associated instrumentation*, Ph.D. Thesis, Vol. 1, The University of Edinburgh.